The Dynamic History of the Tharsis Region, Mars: Understanding the Magmato-Tectonic Deformation through Structural Analysis and Numerical Modelling

Stephanie Shahrzad

Submitted in accordance with the requirements for the degree of Doctor of Philosophy

The University of Leeds
School of Earth and Environment

March 2024

Intellectual Property and Publication Statement

I confirm that the work submitted is my own, except where work which has formed part of jointly authored publications has been included. My contribution and the other authors to this work has been explicitly indicated below. I confirm that appropriate credit has been given within the thesis where reference has been made to the work of others.

This thesis is submitted as an alternative style of doctoral thesis including published material. This format is appropriate as each chapter develops its own story, forming one published paper, one paper resubmitted with revisions, and one ready for submission. In this thesis, the three science chapters in the form of papers are preceded by an introductory chapter placing the papers within the context of relevant literature and setting the aims and scope of the work. The final chapter explores how the three publications can be considered together and suggestions for further work.

The following chapters are based on work from jointly authored papers, with the Contributor Roles Taxonomy (CRediT) used to define authorship details:

The work in **Chapter 2** of the thesis has been published under the following title: *Deciphering the Structural History of Ulysses Fossae, Mars, Using Fault Pattern Analysis*. Shahrzad, S., Bramham, E. K., Thomas, M., Byrne, P. K., Piazolo, S., & Mortimer, E. (2023). Journal of Geophysical Research: Planets, 128, e2022JE007633. https://doi.org/10.1029/2022JE007633. Published: 4 May 2023; originally submitted: 18 October 2022; resubmitted following review (minor corrections): 26 April 2023; accepted: 27 April 2023. Authorship details:

- S. Shahrzad (first and corresponding author): conceptualization, investigation, methodology, visualization, writing – original draft, writing – review and editing.
- E. K. Bramham, M. Thomas, P. K. Byrne, S. Piazolo, E. Mortimer: supervision, writing –review and editing.

The work in **Chapter 3** of the thesis has been resubmitted with minor edits, following the peer-review process, under the following title: *Amazonian tectonic evolution of Ceraunius and Tractus Fossae, Mars, and implications for local magmatic processes.* Shahrzad, S., Bramham, E. K., Thomas, M., Piazolo, S., & Byrne, P. K (2024). Journal of Geophysical Research: Planets. Originally submitted: 28 September 2023; resubmitted following review: 8 March 2023. Authorship details:

- S. Shahrzad (first and corresponding author): conceptualization, investigation, methodology, visualization, writing – original draft, writing – review and editing.
- E. K. Bramham, M. Thomas, S. Piazolo, P. K. Byrne: supervision, writing –review and editing.

The work in **Chapter 4** of the thesis is an unpublished manuscript in preparation to be submitted as follows (authorship list may change): *The Influence of Young's Modulus on Graben Formation during Martian Dike Intrusions: A Discrete Element Modeling Approach*. Shahrzad, S., Thomas, M., Piazolo, S., Bramham, E. K., & Byrne, P. K.

- S. Shahrzad (first and corresponding author): conceptualization, investigation, methodology, software, visualization, writing – original draft, writing – review and editing.
- E. K. Bramham, M. Thomas, S. Piazolo, P. K. Byrne: supervision, writing –review and editing.
- M. Purvance: software

Chapters 2 and 3 have been reformatted from their published versions for appearance in this thesis. Reformatting includes changes to heading, figure and table numbers, and conversion to UK English (from publication in American English) for consistency.

Acknowledgements

Firstly, I owe a huge thank you to my supervisory team, Dr. Emma Bramham, Dr. Mark Thomas, Professor Sandra Piazolo, Dr. Paul Byrne, and Dr. Estelle Mortimer. Thank you for giving me the opportunity to work on this exciting project, for the encouragement during the last few years, and for supporting me during my endeavour into the numerical modelling world.

Thank you to the NERC Doctoral Training Program for funding this project and to the Itasca Educational Partnership Program for providing a free license to *PFC2D*, and my IEP Mentor Matt Purvance for assisting all my assorted coding emergencies.

Many thanks and huge cheers to my lovely Leeds office mates of Room 8.152. Our coffee-runs, Friday beers, and occasional geology-related meltdowns made our office a treat to work in. To my fantastic Dungeons & Dragons group and my lovely once-housemates Lou and Daisy, I owe a thousand thank yous for the adventures, the midnight rants, the climbing trips, and the spontaneous musical interludes that kept me sane outside of the office.

To my wonderful and supporting friends in Denmark, thank you for cheering me on from afar. To my kind friends, Katja and AC, thank you for the baked goods, and the very PhD-related Mission Impossible and Star Wars discussions that kept me going through COVID. To the fabulous Anita, thank you for making me believe I could do this in the first place, for being there for me any time of day, and for being the only person who would think that making up a rap about faults would cheer me up - and then actually succeeding.

To the two incomparable and iconic Dr. Claire Orlov, Editor Extraordinaire and Second-half of My Martian Brain, and Dr. Maeve Murphy Quinlan, Slayer of Code and Provider of Electronic Gadgets. Who knew that applying for a PhD in Leeds would mean finding the best friends a person could wish for. I now know that no PhD would be complete without elaborate movie nights, ice-cold swims in the sea, and an assortment of elaborate rituals that makes the world make sense. I also owe you both a truly heartfelt thank you, for supporting me and coming with me to hold my hand to all my assorted Doctors and hospital visits over the years, when home felt so far away. I truly could not have gone through this without you.

Lastly, my biggest thank you to my wonderful family. To my parents, Seyed and Christine, words cannot describe my gratitude for the lifetime of love and support you have given me, for introducing me to Star Trek as a kid which sparked my love for space, and for never doubting that I could make it to the end of this PhD. Finally, thank you to my smart and talented sister, Sinead, your support and trust in me means the world.

Abstract

The iconic red planet of Mars boasts an ancient surface which shows evidence of billions of years of volcanism, tectonism, and erosion. However, despite the last few decades' exponential increase in satellite and rover data from Mars, the sources and timing of the complex surface structures are poorly constrained. One such structurally complex area is the Tharsis Volcanic Province, which is host to the largest volcanoes in the Solar System, and their associated structures. Understanding the structural history of Tharsis holds the key to defining the evolution of the volcanic, and thus planetary and climate, processes on Mars.

To improve this understanding, I investigate two representative study areas in Tharsis: Ulysses Fossae and Ceraunius Fossae. I examine this topic using two different approaches: a comprehensive structural mapping approach, and a numerical modelling approach. Using detailed structural mapping I characterized the extensional features of the study areas, as well as their timing and origins. I found that the structures mapped in Tharsis are younger than previously estimated, and that the deformation is largely driven by diking related to local volcanic and magmatic centres. I further investigate the diking-driven surface deformation process by constructing a Discrete Element 2D numerical model of a dike intruding the Martian lithosphere and find that for material with a sufficiently high Young's modulus, diking remains a conceivable origin for the extensive graben systems found on Mars' surface. Together these results paint the picture of a magmatically and structurally active Tharsis during the Amazonian, suggesting that our neighbouring red planet has not been as dormant during the later stages of its geological life, as previously assumed.

Contents

List of Figures

List of Tables

Chapter 1

Introduction

The planet of Mars is the fourth planet from the Sun, recognized by its distinct red colour from the iron oxide on its surface. Detailed isotopic analyses on Martian meteorites reveal that Mars accumulated and differentiated into a crust, mantle, and core within a few tens of millions of years after the formation of the Solar System (Barlow, 2008; Carr & Head, 2009).

Our knowledge of Mars has advanced over time as a result of the increase in missions which have visited or performed a fly-by of the planet and its two moons: Phobos and Deimos. As more information and data from Mars becomes available, questions about the geology, evolution, and evolutionary processes of the planet have become possible to answer. An area of Mars which encompasses possible insights to a myriad of geological questions, is the Tharsis Volcanic Province (also called the Tharsis region). Regional and local scale volcano-tectonic processes have shaped the area into the complex geological region we observe today, which, due to the low erosion rate on Mars, is left in near pristine condition despite the surface ages of billions of years. Tharsis is characterized by large shield volcanoes and intricate surface faulting, with the main tectonic morphology being a radiating system of grabens. These grabens are abundant, and their size and orientation vary with location across Tharsis. The formation of the major radial graben system has been attributed to processes related to crustal extension and dike propagation (e.g., Banerdt et al., 1992; Mège & Masson, 1996; Plescia & Saunders, 1982; Scott et al., 2002). Dike-induced graben formation has long been suggested for the majority of the observed extensional tectonic signatures observed in Tharsis and beyond. However, there have been limited in-depth studies on the origins, development, and timing of these grabens.

In this thesis, I will focus on the connection between tectonism and volcanism at two selected locations in the Tharsis region: Ulysses Fossae and Ceraunius Fossae (including Tractus Fossae). These two areas are believed to preserve tectonic activity associated with the large shield volcanoes within Tharsis, though no structural evolution or detailed studies on the origins of these study areas currently exist. These areas

are prime locations for further investigation of the tectonic, volcanic, and magmatic evolution of Tharsis and associated surface strain indicators, due to their locations midst the Tharsis volcanoes, the variety in ages, and their high topography, which has allowed any tectonic structures to be spared from coverage from later lava flows. Ulysses, Ceraunius, and Tractus Fossae were chosen as representative study sites for this thesis. Disregarding Tempe Terra, these areas are the largest intact "windows" into the complex structural deformation hidden under the majority of Tharsis, by the extensive lava flow coverage. Initial interest in these areas was due to their location, as all of the study areas are located close to morphologically distinct volcanoes (e.g. contained and high structure of Olympus Mons, vs. the wide-spread and flat structure of Alba Mons), as well as the linearly arranged Tharsis Montes. Considering the size of the volcanoes, Ulysses, Ceraunius and Tractus Fossae are prime locations for investigating structural deformation associated with these volcanoes. Specifically for Ulysses Fossae, the proximity to Olympus Mons means that this location may be the only one in Tharsis with records of far-field structural deformation, associated with the largest volcano in the Solar System. With the high-resolution data available for the Martian surface today, mapping and measurement of tectonic features has become possible at an unprecedented level of detail for Tharsis. This affords us an opportunity to investigate the processes involved in Tharsis' formation, which is a steppingstone to understanding the evolution of Mars, and by extension other terrestrial planets, using only surface data.

In this thesis, I use the surface expressions of strain to infer the structural history and inner workings of the Tharsis Volcanic Province, through time. Through a combination of detailed structural mapping and numerical modelling, I investigate two study areas, Ulysses Fossae and Ceraunius Fossae, and use them as a basis to infer a magmatic-tectonic evolution of the Tharsis Volcanic Province. I establish a structural history and produce stress evolution models for the faults I mapped in this study. In the final research chapter of the thesis, I delve into the dike-induced graben formation process on Mars and examine how changing lithosphere properties will affect any surface deformation observed. I accomplish this by creating a 2D numerical model of the dike intrusion process on Mars and benchmarking the results to real-world observations and measurements of Ulysses Fossae and Ceraunius Fossae.

This introductory chapter highlights the current established theories regarding the geological formation and processes of Mars, in order to provide background for the future research chapters. I provide a brief geologic history of Mars, along with an explanation of the Martian geologic timescale, as an overall reference for the discussion sections of the individual research chapters (Chapters 2–4) and the final Discussion and Conclusions section (Chapter 5) of this thesis. This includes background to the main

topic of this thesis: The evolution of The Tharsis Volcanic Province and diking as a graben formation process. The last part of the introduction highlights the remaining gaps in our knowledge of this research topic, which leads directly into the specific research aims and structure of this thesis.

1.1. Background

1.1.1. Geologic time scale on Mars

As is the case for Earth, Mars has its own corresponding geological time scale (Figure 1.1), This time scale breaks up the planet's ~4.6 Ga existence into a series of periods and epochs, which are defined from stratigraphic relationships and crater densities but lack direct age constraints (Hiesinger & Tanaka, 2020). Each period is additionally described by the dominant geological processes which took place during that period. See Figure 1.1 for an overview of Mars's geological periods. The oldest defined geological period on Mars is the pre-Noachian, which covers the interval >4.1 Ga. This period is followed by the Noachian (~4.1–3.7 Ga), which is named after the Noachis region located in the southern highlands of Mars. This period is further divided into early (prior to ~3.95 Ga), middle (3.95–3.8 Ga) and late (3.8–3.7 Ga) Noachian based on crater densities. Noachian units are generally characterized by their old, heavily eroded, and highly cratered surfaces (Barlow, 2008). Following the Noachian period is the Hesperian (~3.7–3.0 Ga), which is further divided into early (3.7-3.6 Ga) and late (3.6-3.0 Ga) Hesperian epochs. The Hesperian period is named after Hesperia Planum and is characterized by extensive volcanic activity which created the ridging plains of Mars (Barlow, 2008). Compared to the Noachian, Hesperian surfaces have significantly reduced surface cratering (Barlow, 2008). The last Martian period is the Amazonian (3.0 Ga–present), which is also further divided into the early (3.0–1.8 Ga), middle (~1.8–0.5 Ga) and late (~0.5 Ga–present) Amazonian epochs (Barlow, 2008). During this period, volcanism on Mars was limited to the Tharsis and Elysium regions and erosion rates were low.

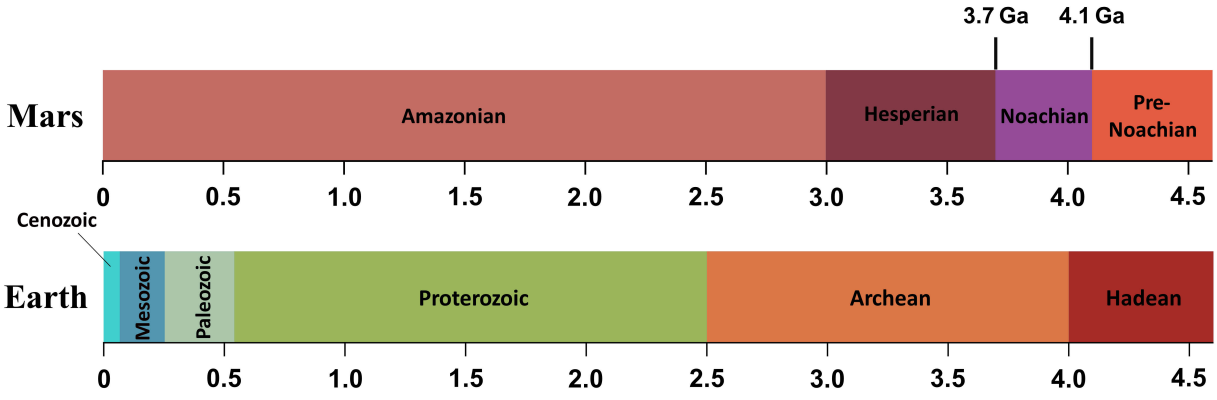

Figure 1.1: Comparison of Mars' and Earth's major geological periods.

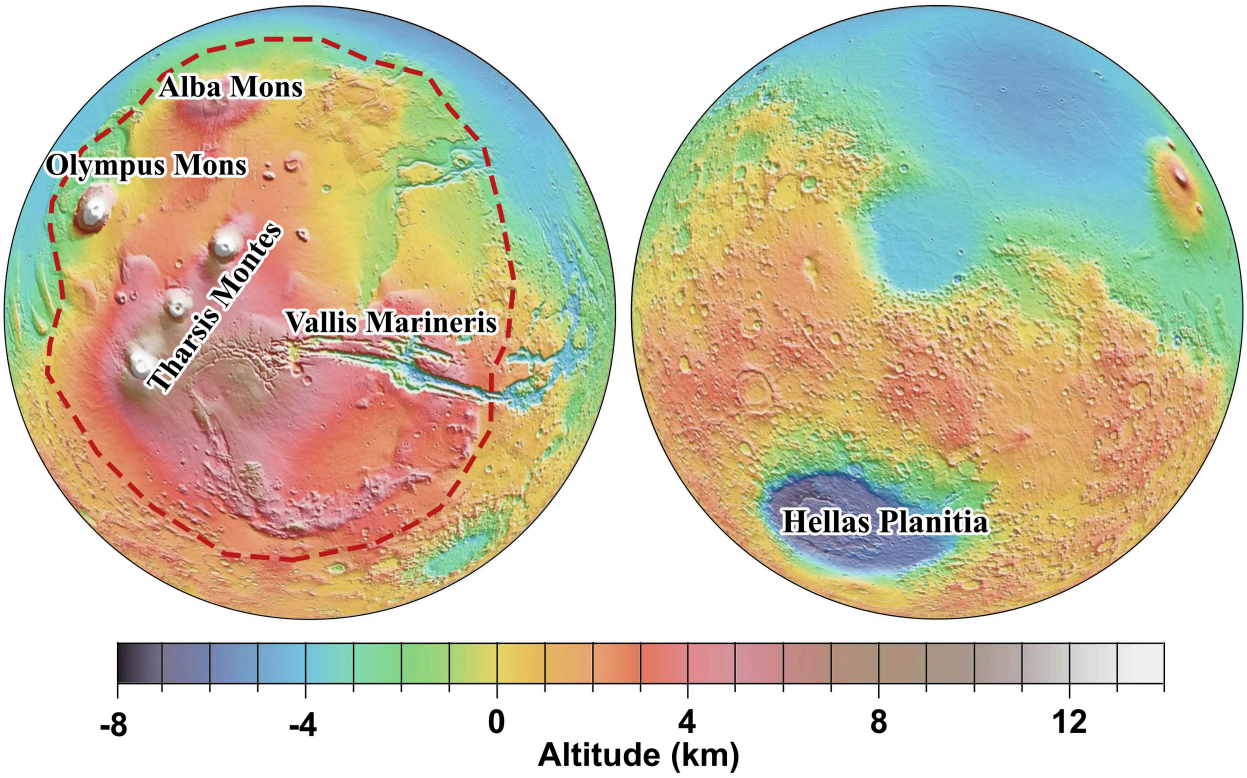

Figure 1.2: Overview of locations on the Martian hemispheres on a Mars Orbiter Laser Altimeter topographic map. The Tharsis Volcanic Province is outlined in a red dashed line. Key locations are labelled on the figure. See Figure 1.3 for a zoomed-in view.

1.1.2. Geologic history of Mars

In the following section I present a brief overview of the established geologic history of Mars, with a focus on tectonics and volcanism, for reference and context for the discussion of research chapter results. Relevant geologic events and processes are presented within their Martian geologic time periods.

Pre-Noachian (>4.1 Ga)

The early stages of Mars's geological evolution saw the development of the planet's crust, with over 70% of the crust having accumulated by 4 Ga. Initial formation of the Tharsis Volcanic Province may also have occurred at this time, though very little geomorphic evidence of this early-stage volcanism is preserved in the present day (Carr & Head, 2010).

Perhaps the most significant Martian geologic event is the formation of the global hemispheric crustal dichotomy, which resulted in elevation differences that still define the surface of the planet (Figure 1.2). Considered the oldest and largest geologic feature on Mars, the global dichotomy goes beyond the appearance of the surface to the nature of the crust itself. It is categorized into the young northern lowlands and the old southern highlands. Three main criteria differentiate between the two: difference in

elevation, difference in crustal thickness, and difference in crater densities. The southern highlands comprise about two thirds of the planet's surface, with an average crustal thickness of ~53 km. In contrast, the northern lowlands comprise of the final third of Mars's surface, and have an average crustal thickness of ~32 km (Barlow, 2008). The exact timing of formation for the global dichotomy is uncertain, but its occurrence is bookended by the formation of the crust at 4.5 Ga, and the formation of the earliest impact basins which superpose it (e.g., Utopia and Chryse basins) at 4.1 Ga (Carr & Head, 2010). The northern lowlands are surrounded by an irregular boundary which is traceable around the surface of Mars, except where a section of it is presumed buried underneath the Tharsis Volcanic Province (Andrews-Hanna et al., 2008). A variety of theories exists surrounding the origin of the dichotomy, including seafloor spreading (Lenardic et al., 2004; Sleep, 1994) and global mantle convection-driven isostatic sinking (Wise et al., 1979a). However, the prevailing model within the scientific community is the giant impact theory (e.g. Frey & Schultz, 1988; Marinova et al., 2008; Nimmo et al., 2008) which posits that the dichotomy is the result of one or more large impacts. Gravity measurements analysed by Andrews-Hanna et al. (2008) show that the dichotomy boundary has an elliptical shape, which is suggested to be explained by a giant impact. The original impact crater is dubbed the "Borealis basin", with an ellipse measuring 10,600 km by 8,500 km (Andrews-Hanna et al., 2008).

Another geological process worth highlighting in the pre-Noachian is the development of magnetic anomalies while Mars still had an active dynamo. Mission results from the Mars Global Surveyor revealed the presence of large magnetic anomalies in the southern highlands, which are absent around the young impact basins Utopia, Hellas, Isidis, and Argyre Planitia, constraining the time the early Martian magnetic dynamo was active to the Noachian (Solomon et al., 2005). A portion of these magnetic anomalies are striped in a similar fashion to the magnetic pattern produced on Earth during seafloor spreading, though at a larger scale (Nimmo, 2000). This comparison has been used as the main source of evidence to argue for a potential period of early plate tectonic activity on Mars (Carr & Head, 2010). An alternative interpretation attributes the striped magnetic anomalies to the presence of large and deep swarms of mafic dikes (Hood et al., 2007; Nimmo, 2000).

Noachian (4.1 – 3.7 Ga)

The Noachian period was dominated by high rates of cratering, erosion, and valley formation, but one of its most distinguishing features is the accumulation of the Tharsis Volcanic Province (Carr & Head, 2009). The growth of Tharsis is considered to have finished by the end of the Noachian, resulting in a topographic rise 5,000 km across and 9 km high, which occupies ~25% of Mars's surface (Carr & Head, 2010). The vast majority of Noachian volcanism was concentrated within Tharsis, and primary Noachian

volcanic deposits are still visible on the surface of Tharsis today (Carr & Head, 2010; Tanaka et al., 2014). This is contrary to the majority of Noachian terrains on the rest of the planet, which are dominated by impacts (Carr & Head, 2010). Noachian volcanic rocks are mainly low-calcium pyroxene basalts, with variable amounts of olivine (Poulet et al., 2005).

Noachian surface features have been reworked by a very high rate of erosion, resulting in craters with diameters of hundreds of kilometres, heavily eroded rims, and partly filled interiors. However, this high erosion rate was not consistent through the Noachian, as it had dropped significantly by the start of the Hesperian (Carr & Head, 2010). The majority of Noachian terrains are also marked by valley networks generally a few kilometres in length, which occur in locations with a weak regional slope and drain into local topographic lows (Carr & Head, 2010; Fassett & Head, 2011). Noachian terrains near Hellas Planitia also contain measured valley networks which are several thousand kilometres, where drainage runs north-westward from the high ground surrounding Hellas, following the regional slope down towards the Chryse-Acidalia low (Carr & Head, 2010).

A final distinguishing feature of the Noachian period is the common presence of phyllosilicates formed by aqueous alteration of basalt, including Fe-rich chlorites, nontronite, saponite, and montmorillonite (Poulet et al., 2005; Carr & Head, 2009; Fassett & Head 2010). In locations where it is possible to discern the stratigraphic relationships, the phyllosilicates are present in weathered products which have been excavated to the surface or exposed by erosion (Carr & Head, 2009).

Hesperian (3.7 – 3.0 Ga)

The Hesperian is defined by continued and episodic volcanism, canyon formation, lower rates of valley formation, and low erosion. This period corresponds to the early Archean on Earth. During the Hesperian, volcanism continued at a high average eruption rate of ~1 km^3 yr^{-1}, concentrated in the first half of the period, and resulted in the resurfacing of ~30% of the planet (Carr & Head, 2010). This volcanism took the form of ridged plains and low shield edifices. In the western hemisphere of Mars, Hesperian lava plains occurred mainly around the eastern margin of Tharsis, while in the eastern hemisphere extensive flood volcanic plains formed Hesperia Planum, Syrtis Major Planum, Malea Planum, and much of the floor of Hellas Planitia (Carr & Head, 2010). Spectra from the Thermal Emission Spectrometer onboard the Mars Global Surveyor revealed that the products of Noachian and Hesperian volcanism, which is largely constrained to the southern highlands, are all of basaltic composition (Bandfield et al., 2000). The large Tharsis shield volcanoes (including Olympus Mons and the Tharsis Montes) likely began accumulating during this period, despite their young (Amazonian) current surface ages (Werner, 2009).

Valles Marineris (Figure 1.2) is a system of canyons which cut through the Martian surface in the east of Tharsis. The main formation of Valles Marineris also occurred during the Hesperian, although the exact age of the canyons is difficult to determine. The formation of Valles Marineris was largely a result of the stresses created by the accumulating Tharsis load (Carr & Head, 2010). Since the main crustal growth of Tharsis is considered to have occurred during the Late Noachian, this marks the likely onset of canyon formation. The main opening of the canyons occurred after the Early Hesperian, as the rim of Valles Marineris consists of Early Hesperian ridged plains (Webb & Head, 2002). The opening of the main trough was followed by faulting, floor subsidence, and further erosion of the walls, which also occurred throughout the Hesperian (Carr & Head, 2010).

The significant decline in erosion rates, weathering, and formation of valleys all indicate that the surface conditions in the Noachian, which were so favourable for aqueous erosion and weathering, were now rare in the Hesperian (Carr & Head, 2010; Fassett & Head, 2011).

Amazonian (3.0 Ga – present day)

The Amazonian is the longest geological period on Mars and is dominated by ice and aeolian surface alteration processes. The majority of the geological processes that were important in earlier periods, such as impact cratering, volcanism, and tectonism, are considered to have reduced significantly.

Contrary to the widespread volcanism of the Noachian and Hesperian, Amazonian volcanism was largely constrained to the Tharsis and Elysium regions, with the continued growth of the large shields and lava plains. In contrast to the Hesperian lava plains, which typically do not display any primary flow features but shows numerous wrinkle ridges (tectonic shortening structures), the Amazonian lava plains have few wrinkle ridges but many primary flow structures, such as flow fronts and lava channels (Carr & Head, 2009). Amazonian lava is also more silica-rich than Hesperian volcanics, comparable to a terrestrial andesite. The most significant surface processes in the Amazonian are driven by the presence and movement of ice. The majority of the ice which is currently accumulated at the Martian poles is Amazonian in age and consists of thick polar layered deposits, which are composed of water-ice and silicate dust (Barlow, 2008). Thermal and compositional characteristics of the north polar permanent cap specifies that the composition is H_2O ice, while the southern polar permanent cap is H_2O ice covered by an 8 m thick CO_2 ice veneer (Barlow, 2008). Large fractions of ice are not detected from orbit at latitudes lower than 60°, though some indicators, such as patterned ground and sublimation pitting, suggest that ground ice may be present down to latitudes of 30°, which makes subsurface ice an important water reservoir on Mars (Karlsson, et al., 2015).

1.1.3. Introduction to the Tharsis Volcanic Province and regional magmatic processes

The study areas examined in this thesis are all located within the Tharsis Volcanic Province on Mars (Figure 1.3). This province is both the largest and longest-lived volcano-tectonic entity in the entire Solar System, and its complex history has yet to be fully deciphered. This section will introduce the large-scale formation and evolution theories for Tharsis and highlights the presence of diking as a significant geological process in the area. Tharsis is the largest volcanic province on Mars and occupies ~25% of the Martian surface (Barlow, 2008). The combination of volcanic and extensive tectonic structures present in Tharsis makes up an almost complete, and incredibly well-preserved, history of the geological evolution of the surface of Mars. Understanding Tharsis is therefore crucial to unravelling the tectonic, volcanic, sedimentary, erosional, and atmospheric evolution of Mars.

The defining feature of Tharsis is the vast 10 km high topographic bulge that makes up the province. Other characteristic features are a series of large shield volcanoes and small volcanic features (e.g. fissures and cones), numerous isolated structured regions and plateaus (e.g. Tempe Terra), and an extensive system of radiating graben and concentric wrinkle ridges. The surface of Tharsis is covered in young Amazonian (<3 Ga) lava flows, but the growth of Tharsis began during the Pre-Noachian to Noachian (>3.7 Ga) (Bouley et al., 2016). The region's position and large mass has enabled a reorientation of the planet with respect to its spin-axis, which is responsible for the current equatorial position of the volcanic province (Bouley et al., 2016). Tharsis is also home to a catalogue of large shield-volcanoes (Figure 1.3), with Olympus Mons and Alba Mons being the largest. However, despite being associated with the Tharsis Rise, Olympus Mons is situated right on the western end of the topographic bulge, beyond the crustal dichotomy boundary (Mège & Masson, 1996). Towards the centre of Tharsis are three extraordinarily aligned volcanoes, situated ~700 km apart from each other, which form the Tharsis Montes: Ascraeus, Pavonis, and Arsia Mons (Figure 1.3) (Barlow, 2008).

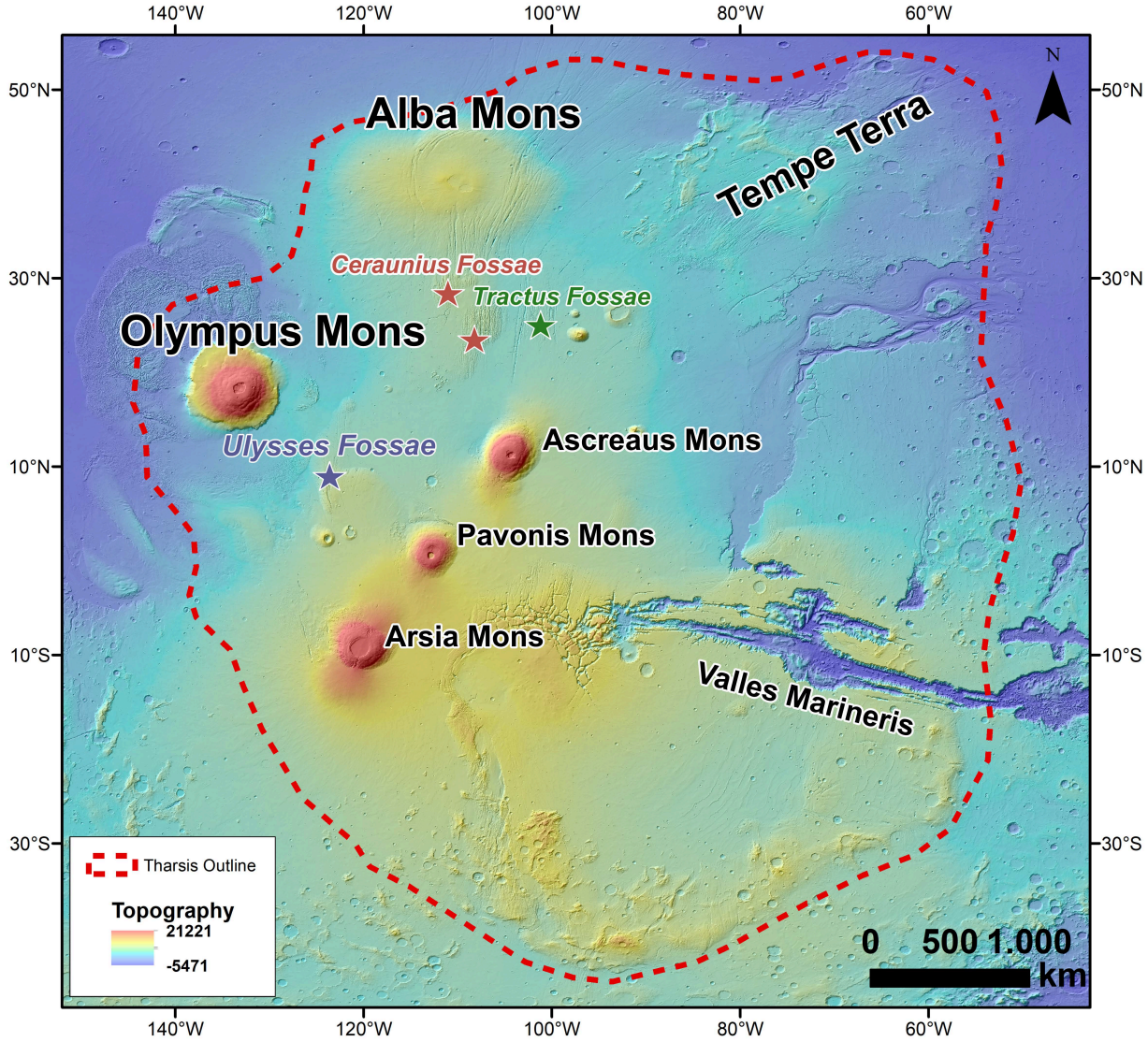

Figure 1.3: Overview of key locations in Tharsis (red dashed outline). Background image is MOLA-HRSC Digital Elevation Model (Fergason et al. 2018) overlying MOLA hillshade.

Due to it being a "single plate" planet (Solomon, 1978), volcanism on Mars (and other single plate planets, e.g., Venus) is defined as intra-plate volcanism (Wilson & Head, 1994). However, compared to Earth, where intra-plate volcanism is often expressed as volcanic island chains (e.g., Hawaii), volcanism on Mars is limited by its stagnant lid tectonic regime (Heap et al., 2017). This stagnant lid is what has enabled the creation of the large shield volcanoes on Mars, where the continuous or episodic supply of magma to the same locations over vast periods of time, has allowed the formation of the largest volcanoes in the Solar System.

1.1.4. Deep seated mantle plume as a source for Tharsis volcanic activity

The source of the volcanic activity in and around Tharsis is attributed to the presence of a single large mantle plume, or system of interconnecting plumes, underlying Tharsis, known as the Tharsis Superplume. This superplume is characterized by its abnormally long-lived and fixed deep mantle activity. A study by Baker et al. (2007) have attributed the intensity and location of the superplume to a proposed early period (within the first 500 million years) of plate-tectonic activity on Mars. In this theory, the termination of plate tectonics coincides with subduction zones beneath Tharsis and Elysium, where the subducted volatiles and potential water lead to mass melting, producing the superplume (Baker et al., 2007). However, newer studies have highlighted the likelihood that the Tharsis plume has migrated over the course of Mars's evolution. Numerical modelling and crustal thickness models show that the plume likely originated in the southern region of Mars and has migrated northwards to its most recent location in Tharsis (Cheung & King, 2014; Hynek et al., 2011). The plume model is currently the most favoured formation model for both Alba Mons and Olympus Mons. However, the position and size of both Alba Mons and Olympus Mons suggests they have been formed from a secondary plume offshoot from the large Tharsis mega-plume (Mège & Masson, 1996). A characteristic trait of the Tharsis Superplume is the initially intense episode of magmatic-tectonic activity, responsible for local and regional centres of tectonic activity, which then declined with time. This plume-related magmatic-tectonic activity includes volcanism, dike emplacement, and uplift, along with extensional and contractional tectonics resulting in vast systems of radial and circumferential extensional faults and wrinkle ridges (Dohm et al., 2007; Mège & Masson, 1996).

1.1.5. Tharsis stress models

The Tharsis topographic bulge has historically been explained by uplift of the lithosphere. The cause of this uplift was proposed to be a thermal or chemical anomaly in the mantle or crust, which led to lithospheric fracturing, followed by the emplacement of volcanic plains in the region (Carr, 1974; Wise et al., 1979b). However, later models and fault analyses introduced the mechanism of isostasy as a driver of Tharsis's development (Banerdt et al., 1982; Solomon & Head, 1982). Contrary to the uplift-driven model, isostasy models propose volcanic construction results in loading of the lithosphere, and it is the local isostatic compensation of that loading which is responsible for the topographic high of Tharsis (Solomon & Head, 1982). One such model is proposed by Banerdt et al. (1982), which outlines a 3-stage model (Figure 1.4a) where the first stage of development consists of the isostatic uplift of Tharsis as a response to intense constructional volcanism. Following this, the lithosphere thickens to a point where isostasy no longer takes place, and mass may no longer be maintained in Tharsis (Banerdt et al., 1982).

In the second stage, the constructional volcanics thus start to act as a flexural load on the lithosphere, until the final stage where the lithosphere thickness is able to support any new volcanic activity without altering the pattern of the surrounding stress field (Figure 1.4a) (Banerdt et al., 1982).

Tanaka et al. (1991) proposed a different model, involving a detached crustal cap where extended magmatism produced a thickened crust and high heat flow (Figure 1.4b). This volcanic activity produced a weak lower crust, allowing the brittle upper crust to decouple from the upper mantle in the Tharsis area (Tanaka et al., 1991). The upper mantle makes up the majority of the lithosphere and deforms separately from the upper crust layer, as a part of the rest of the global shell. The separate upper crust layer deforms independently, as a "spherical cap" with a lubricated lower surface and a peripheral boundary which is fixed to the global shell (Tanaka et al., 1991) (Figure 1.4b). This detached crustal cap is mainly deformed by circumferential extension, caused by isostatic or downslope spreading stresses along with subsidence of the lower lithosphere, the latter of which will increase the radius of the cap's curvature (Tanaka et al., 1991). A later study by Banerdt et al. (1992) suggested a flexural uplift model for Tharsis. In this scenario, Tharsis developed by buoyant uplift of the lithosphere, caused by a combination of locally thinning crust and decreasing density in the upper 350 km of the mantle (Banerdt et al., 1992). However, this was considered an unlikely scenario, given the unreasonable values for crustal thinning and density necessary for the expected radial stresses to form (Banerdt et al., 1992).

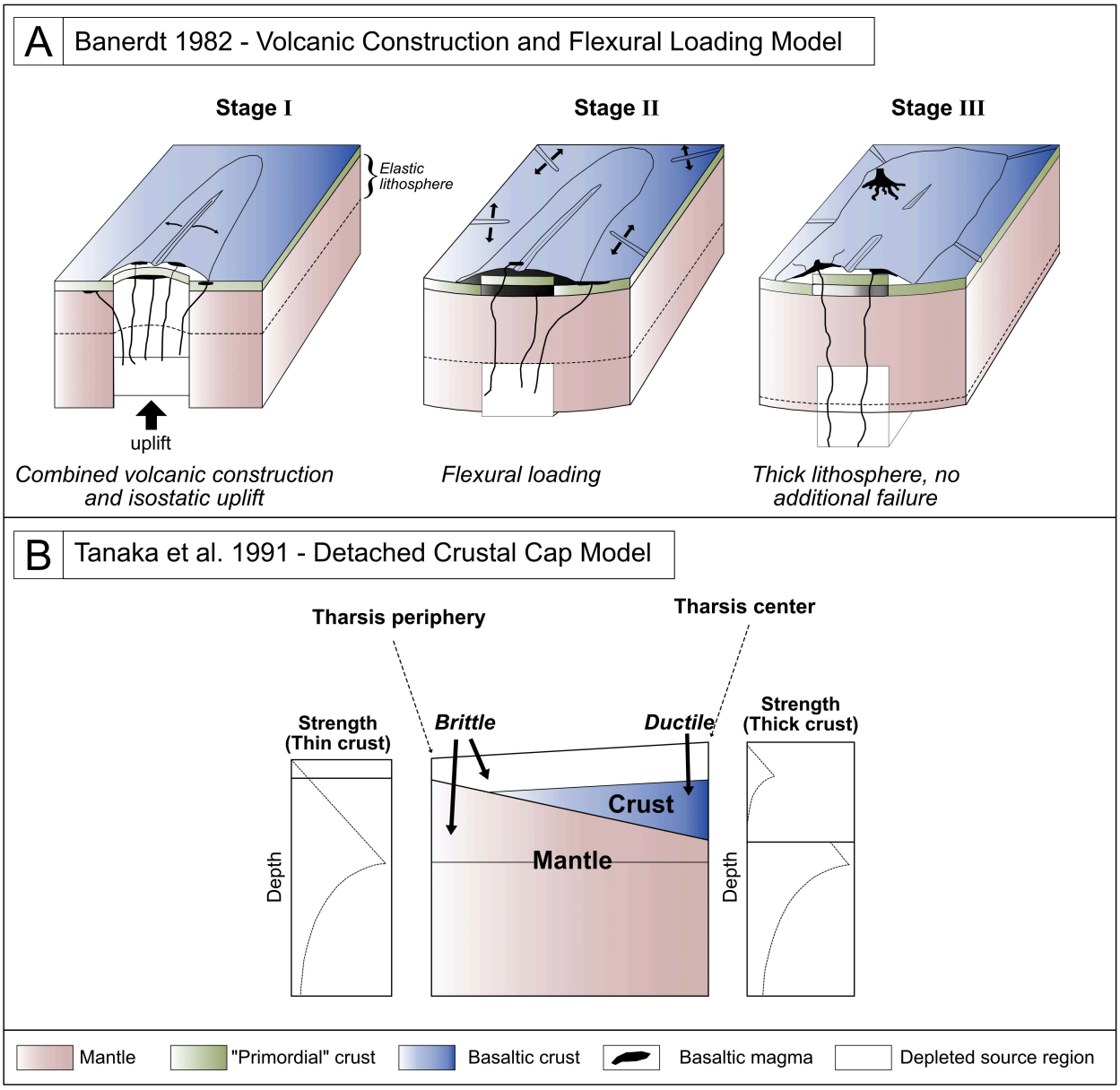

Figure 1.4: Overview of the two major Tharsis stress models. A) the three-stage Tharsis development, as hypothesized by Banerdt et al. (1982). Figure is modified from Figure 8 in Banerdt et al. (1982). Stage I: Combination of constructional volcanics and isostatic uplift. Volume increase in the mantle conversion leads to less dense crustal mineralogy, and thus construction takes place. If magmatic products move laterally outside of Tharsis, isostatic uplift will occur. Stage II: Lithosphere has thickened to a degree where isostatic compensation no longer takes place. The constructional volcanics thus behave as a flexural load on the lithosphere, leading to radial Tharsis grabens. Stage III: Lithosphere has now thickened to a point where new volcanics does not perturb the stress levels, so there is no additional failure. Activity is represented by youngest volcanic plains and shield volcanoes. B) Detached crustal cap model from Tanaka et al. (1991). Figure is modified from Figure 9 in Tanaka et al. (1991). Figure shows an idealized section through the midpoint (right) to the periphery (left) of Tharsis, highlighting the brittle and ductile areas. The strength plots on either side denotes the extensional yield strength of the lithosphere as a function of depth for the two crustal thicknesses, where straight segments show brittle yielding and curved show ductile yielding. For the thick crust in the middle of Tharsis, the lower crustal ductile zone will mechanically decouple the "detached crustal cap" (upper elastic layer), from the upper mantle.

1.1.6. The current understanding of the volcano-tectonic history of Tharsis

Along with the formation of the Tharsis bulge itself, activity from the many large volcanoes in Tharsis produced stresses which gave rise to intense surface deformation. The resulting extensional and shortening surface structures are now a defining feature of Tharsis, which has numerous exposed areas of intensely faulted terrains. Multiple studies have analysed sections of these faulted terrains and, through chrono-stratigraphy and cross-cutting relationships, are building an evolution of the crustal deformation in Tharsis (Anderson et al., 2001; Bouley et al., 2016; Dohm et al., 2007; Scott et al., 1986). Observations from these previous studies agree with the most recent geological map of Mars (Tanaka et al., 2014), that Tharsis began accumulating in the Pre-Noachian and had a major period of growth lasting to the Late Noachian (Anderson et al., 2001; Carr & Head, 2010). However, the previously ubiquitous notion that Tharsis had reached its final form by the end of the Noachian (e.g., Scott & Dohm, 1990; Scott et al., 1986; Tanaka, 1990), has been superseded since the geologic unit age revisions by Tanaka et al. (2014) re-assigned many previously Noachian terrains as Hesperian in age.

Based on this revised understanding, Bouley et al. (2018) defined a new structural history of Tharsis that established 6 stages of tectonic deformation based on mapped fault lengths, densities, and orientations. These stages are presented below, alongside corresponding activity related to the evolution of the Tharsis Superplume from Dohm et al. (2007).

Stage 1 comprises the Early-Middle Noachian epoch and represents the earliest mapped tectonic activity in Tharsis. It is characterized by a low extensional deformation rate of $\sim 4 \times 10^{-5}$ km/Myr/km^2, which occurs in the northeast in Tempe Terra (oriented N70) and in the south in Claritas and Coracis Fossae and Thaumasia Planum (oriented N180-N90) (Bouley et al., 2016). Orientation-wise, several of the structures appear to be radial to the centre of Tharsis.

Stage 2 occurs during the Late Noachian and is characterized by both extensional and contractional deformation. Similar to Stage 1, the extensional activity is concentrated around the periphery of the Tharsis bulge (i.e., western Tempe Terra, Acheron, and Claritas Fossae, and Thaumasia Planum). The shortening features are located in eastern Tempe Terra and Thaumasia Planum and are concentric to Tharsis.

Stage 3 takes place during the Early Hesperian and represents a peak in both extensional and contractional deformation. This deformation is also no longer confined to the outskirts of the Tharsis bulge, with the three main regions of extensional deformation being the northeast (Tempe Terra), the east (Valles

Marineris and Lunae Planum), and the centre-north (Ceraunius, Ulysses, and Uranius Fossae). Extensional features from this stage are also some of the longest, with lengths up to 400-600 km. The shortening activity is concentrated in the southern part of Tempe Terra, Lunae Planum, and Solis Planum. During this stage, the regions of Syria Planum, Arsia Rise, and Tempe Terra all experienced continued magmatic-tectonic activity, incipient magmatic and tectonic activity is also present in the areas around Pavonis Mons, Alba Mons, and Ulysses Paterae (Dohm et al., 2007).

Stage 4 shows the declining extensional and contractional deformation during the Late Hesperian. The extensional features are located in Noctis Labyrinthus, Noctis Fossae, and Solis Planum, as well as Tractus, Ulysses, and Fortuna Fossae, where they appear in windows surrounded by Amazonian and Hesperian volcanic units. Effusive volcanic activity is prevalent in the Late Hesperian, which includes the development of the Tharsis Montes and later Olympus Mons. In addition, extensive sheet lavas were emplaced, centred around the large shield volcanoes and Syria Planum (Dohm et al., 2007). This is followed by a transition from magmatic-tectonic activity to predominantly magmatic activity, culminating in the final instance of large-scale tectonism which is associated with Alba Mons (Dohm et al., 2007).

Stage 5 shows an even further decline in tectonic deformation in the Early Amazonian and is dominated by extensional deformation. The extensional structures appear on both Amazonian and Hesperian units (Tanaka et al., 2014) and are found across the entire Tharsis region. Radial fault patterns persist but are mainly concentrated near Alba Mons.

Stage 6 in the Middle and Late Amazonian shows very little deformation, which is consistent with Mars's overall decline in other geological activity. The appearance of normal faults is related to the formation of Olympus Mons, with other extensional features located west of Arsia and Pavonis Mons. Both Stage 5 and Stage 6 show continued growth of Olympus Mons as well as the Tharsis Montes, with some isolated occurrences of magmatic-tectonic activity associated with their construction (Anderson et al., 2001). This signifies the late-stage activity of the Tharsis Superplume, which has yet to reach its cooling threshold (Anderson et al., 2001; Dohm et al., 2007).

1.1.7. Subsurface dike emplacement as a source of extensive Tharsis graben structures

The accumulation of Tharsis and the growth of the many shield volcanoes in the region have produced a variety of tensional and compressional stress fields, which are recorded on the surface as extensive graben and wrinkle-ridge systems that are still preserved today. However, the variety of individual and combined Tharsis stress models (Section 1.1.5) are not sufficient to explain all the mapped tectonic features. Mège & Masson (1996) were among the first to implement an in-depth study into dike emplacement as being responsible for a large portion of the extensional grabens which cover Tharsis. The idea of dike emplacement as a process of radial graben formation was discussed in previous works (Davis et al., 1995; Tanaka et al., 1989; Tanaka et al., 1991), but Mège & Masson (1996) were the first to present morphological and structural evidence of widespread diking throughout the Tharsis Province. Following this paper, multiple studies have proposed the idea of giant dikes being responsible for the radiating graben systems centred on Tharsis (Ernst et al., 2001; Okubo & Schultz, 2005; E. D. Scott et al., 2002). The formation mechanism of dike-induced graben is discussed in section 1.1.8.

Okubo & Schultz (2005) examined Phlegethon, Acheron, and Tractus Catena on the southeast side of Alba Mons, with Phlegethon and Acheron Catena superposed on the flank of the volcano. All three features run largely parallel with each other and consist of large pit-crater to catenae chains (circular collapse features which appear in a linear row) of collapsed material. Examining their topographic cross-sections, these 2,000 km long structures are revealed to be the result of subsurface stalled dikes, which are radial to the centre of Tharsis (Okubo & Schultz, 2005). Similarly, a study by Wilson & Head (2002) examined a number of grabens (Claritas, Icaria, Memnonia, Sirenum, and Thaumasia Fossae) which had historically been attributed to either plume upwelling or loading of Tharsis on the lithosphere. Using a giant dike emplacement model for Mars, they concluded that the graben morphologies (i.e., widths, depths, and outcrop patterns) coincide with a dike-driven formation mechanism (Wilson & Head III, 2002). These grabens are also radial to the centre of Tharsis and interpreted to be dike-driven from a mantle plume source. These giant radiating dike systems are comparable to those we observe on Earth, such as in the Canadian shield. This region is host to a number of dike swarms, the most famous of which is the Mackenzie Dike Swarm, dated to 1270 Ma (Ernst et al., 2001). The lateral emplacement of dikes in the Mackenzie swarm has resulted in magma moving over distances up to 2,200 km, which is comparable to proposed distances for dikes on Mars. However, on Earth, these giant radiating dikes are not normally associated with surface graben formation (Ernst et al., 2001). In addition to the giant dike systems, comparatively smaller radiating dike systems are also proposed to be the source of the radiating graben

centred locally on the individual shield volcanoes in Tharsis. Examples of this are found around Alba Mons, with its extensive surrounding graben systems, and proximal to the Olympus Mons and Tharsis Montes edifices (Pieterek et al., 2022).

1.1.8. Dike-induced graben formation on Mars

There are a variety of theories regarding the actual formation mechanism of dike-induced grabens. Initial terrestrial models relied on the presence of pre-existing faults, and consisted of a widening dike in order to determine the extent of subsidence during graben formation (Mastin & Pollard, 1988; Rubin, 1992; Rubin & Pollard, 1988). For Mars, previous models rely on the ascension of the dike to generate the boundary faults necessary for graben formation. (Scott et al., 2002; Wilson & Head III, 2002).

The established model of dike-induced graben formation is as follows: a low-density, high-pressure pocket of magma will ascend from a source, through the planet's brittle lithosphere, in the form of a dike. The emplacement mechanism for igneous intrusions is dilation, where the stress governing the intrusion is influenced by the hydrostatic magma pressure which drives the upwards propagation (Park, 2000). The intrusion plane of the dike will be perpendicular to the least compressive principal stress, σ_3 (Figure 1.5a). The pressure of the magma is higher than the general horizontal pressure of the surrounding rock and will therefore cause localized tension at the tip of the dike. This tension can be sufficient to cause breakage in the surrounding lithosphere, which can continue and extend the fracture (Anderson, 1953; Rubin & Pollard, 1988). If these tension-generated fractures occur close enough to the surface, they may develop into normal faults (Gudmundsson, 2003; Rubin & Pollard, 1988; Trippanera et al., 2015). These usually occur as two bounding faults which dip towards the tip of the dike (Figure 1.5a) (Gudmundsson, 2003; Pollard et al., 1983; Rubin & Pollard, 1988). The initial normal faulting can thus facilitate graben formation, driven by the further movement of the dike or by a combination of dike intrusion and regional extension (Gudmundsson, 2020). The ascent of the dike will continue until it reaches a neutral buoyancy level, whereafter it may continue to widen horizontally, depending on the available supply of magma. This widening of the dike will also effect the final appearance and size of the graben (Paquet et al., 2007; Pollard et al., 1983; Wyrick & Smart, 2009).

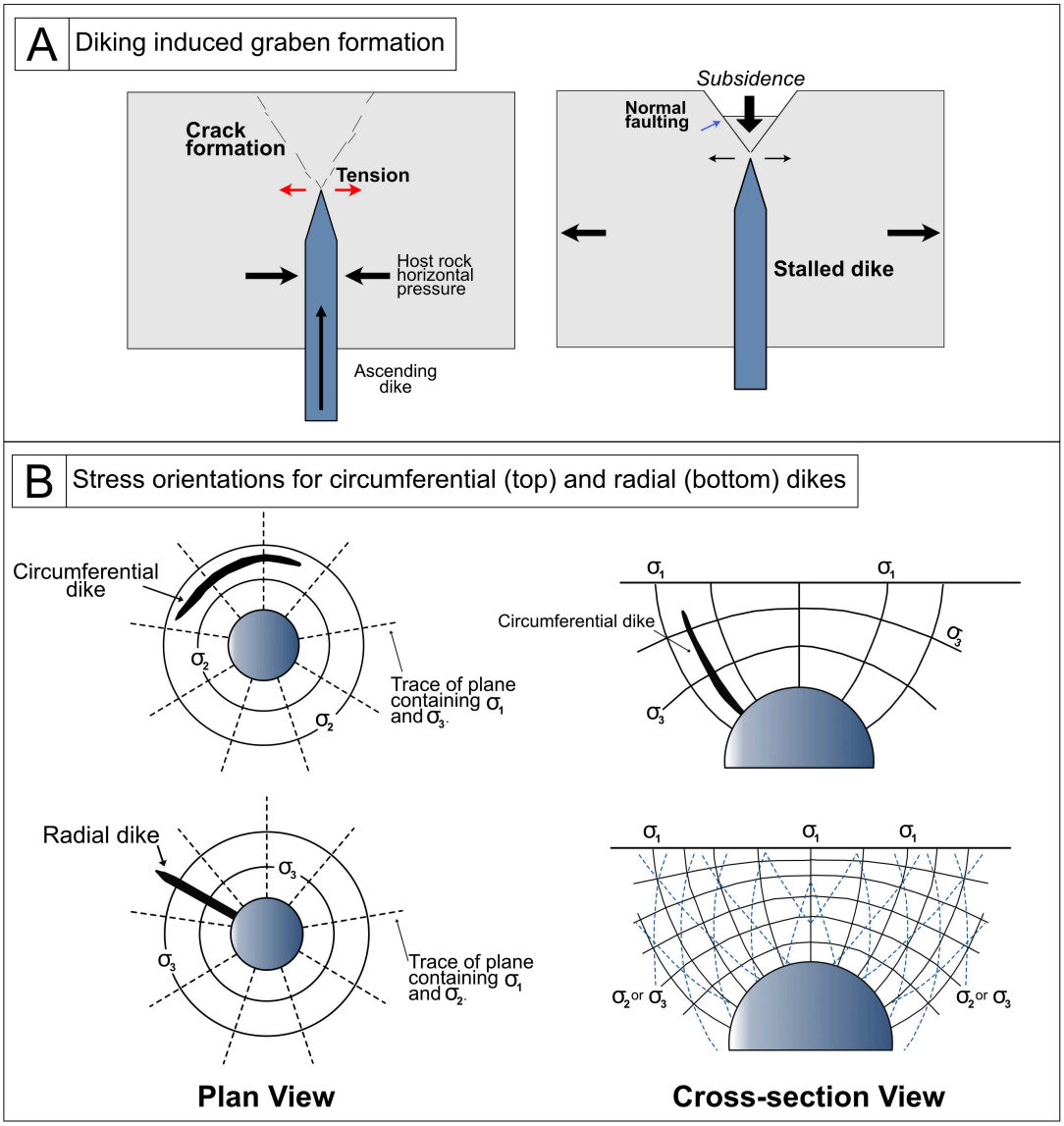

Figure 1.5: Extension by dike intrusion models. A) Dike intrusion and graben formation mechanics, highlighting the dike-tip tension induced fractures, and subsequent normal-fault and graben formation. Modified from Anderson et al. (1953). B) Radial versus circumferential diking stress in plan-view (left) and cross-section view (right). Figure modified from Park et al. (2000).

Dike-induced grabens can be challenging to distinguish from purely tectonic grabens, especially on satellite images. However, a variety of surface indicators do exist. For example, on Mars, grabens of consistent width over long distances are less likely to be tectonic and are more characteristic of dike-induced deformation (Mège & Masson, 1996). Another measurable indicator is surface topography. Numerical and analogue modelling studies of dike-induced graben formation show clear concave down topographic slopes, in contrast to the concave up slopes generated for tectonic grabens (Goudy & Schultz, 2005; Okubo & Schultz, 2005; Schultz et al., 2004) (Figure 1.6). In line with the majority of dike-induced graben formation studies, this topography indicator is a result of model-based studies, rather than observational evidence. Finally, the co-appearance of pit-crater chains is also used as an indicator of diking in or near grabens (Ernst et al., 2001; Mège & Masson, 1996). This is due to the interpretation that pit-crater chains collapse into void spaces left by magma withdrawal or outgassing (Cushing et al., 2015; Hardy, 2021).

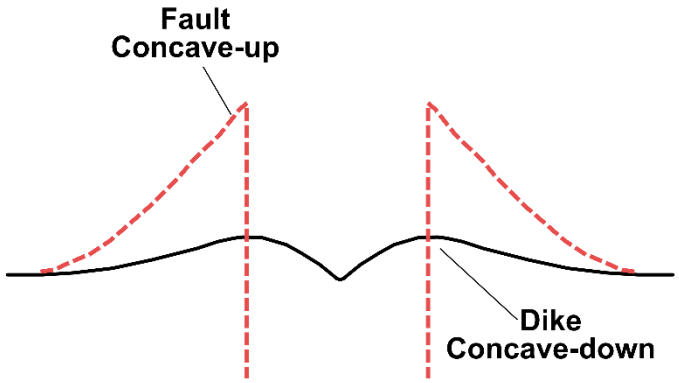

Figure 1.6: Purely tectonic induced concave up topographic signature, versus dike-induced concave down topographic examples. Figure modified from Goudy & Schultz (2005)

Physical analogue studies of dike intrusions have made it possible to use the geomorphic shape of a graben to infer depth and width of a dike (Mastin & Pollard, 1988; Mège & Masson, 1996; Rubin & Pollard, 1988). By measuring the amount of horizontal extension which has been accommodated by surface graben formation, the width and depth of the underlying dike can be estimated, though the results vary depending on the model boundary conditions (Chadwick Jr. & Embley, 1998; Ernst et al., 2001; Rivas-Dorado et al., 2022).

On Mars, diking systems are conventionally separated into radial or circumferential dikes, based on their orientations. Radial dikes radiate out from a common centre, typically a magmatic intrusion or volcanic structure. Radial dikes will propagate perpendicular to the least compressive horizontal stress (σ_3), commonly over vast distances and often fanning out with distance to the centre (Figure 1.5b) (Park,

2000; Poland et al., 2008). Some studies have suggested circumferential diking, or "cone-sheets", are responsible for the circumferential grabens surrounding some Martian volcanoes, such as Alba Mons and the Tharsis Montes (Ernst et al., 2001). However, these are more difficult to distinguish from their purely tectonic counterparts, which are typically interpreted as a result of extension related to either uplift or subsidence associated with the development of volcanic constructs (Cailleau et al., 2003; Öhman & McGovern, 2014). Figure 1.5b shows the different stress regimes responsible for radial or circumferential dike propagation.

1.2. The use of remote sensing to understand faulting on Mars.

1.2.1. Available remote sensing datasets

Examining the surface of Mars has become much more accessible with the evolution of orbiter spacecraft and rovers that have visited the Red Planet since the start of the era of Martian exploration in 1965. The work undertaken in this thesis is based on analysis of data from these remote sensing instruments.

CTX

The Context Camera (CTX) instrument is a camera which makes observations simultaneously with the higher-resolution images captured by the High-Resolution Imaging Science Experiment (HiRISE) camera, both of which are on board the Mars Reconnaissance Orbiter (MRO). The MRO reached Mars in 2006 and has been transmitting data ever since. Compared to the more localized use of the HiRISE instrument, CTX, as the name suggests, provides context for HiRISE on a more regional terrain scale. At an orbit of 400 km above the surface of Mars, CTX captures greyscale images with a span of 30 km and has a resolution of 6 meters per pixel (Malin, et al., 2007). I therefore used this data in my research to investigate large areas at a high resolution. See Figure 1.7a for image example.

MOLA-HRSC

The Mars Orbiter Laser Altimeter (MOLA) is an instrument on board the Mars Global Surveyor (MGS). The MGS was launched on the 7th of November 1996, with the mission of orbiting and subsequently mapping the surface of Mars during the mission's 3-year timespan. The MOLA instrument consists of a laser altimeter, which collected altimetry data from September 1997 to June 2001 (Fergason et al., 2018). The MOLA data has now been coupled with information from the High-Resolution Stereo Camera (HRSC), the only dedicated stereo camera orbiting Mars, to create a combined global topographic dataset.

Together this data creates the most accurate topographic representation of Mars' surface, with a resolution of 200 meters per pixel (Fergason et al., 2018). See Figure 1.7 for image examples.

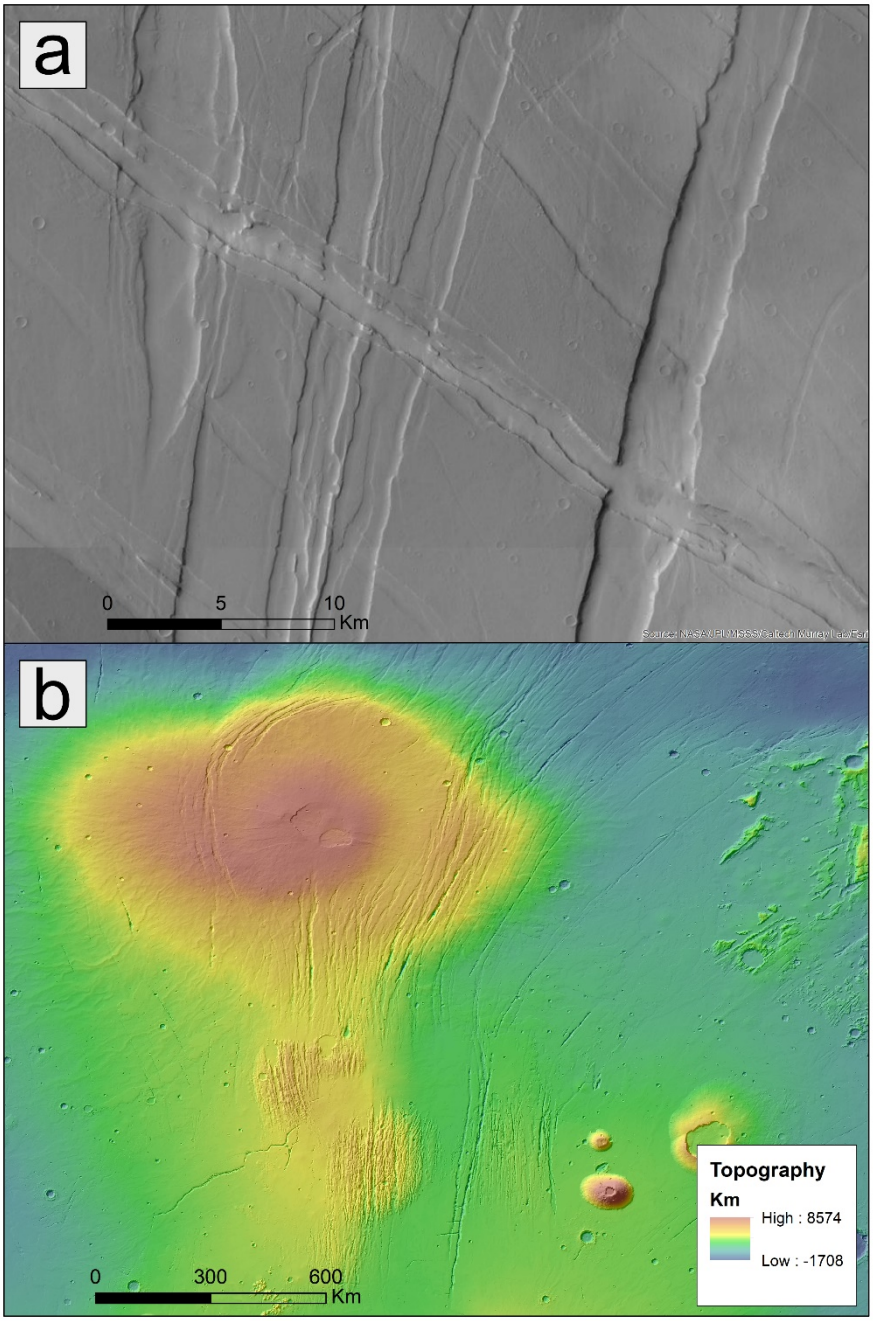

Figure 1.7: Examples of data types used in this study: a) Example of CTX data used in this study, with high-resolution fault morphology visible. b) Example of MOLA-HRSC Digital Elevation Model blend data, used in this study to infer elevation of features and constructing topographic profiles of structures.

1.2.2. Determining geological ages remotely: crater size-frequency distribution statistics

For typical terrestrial geological studies, the age of a unit is determined by radiometric dating of a representative rock sample. As it is currently impossible to gather samples from any of the Martian sites investigated in this study, another age determination method is necessary. Crater size-frequency distribution (CSFD) is a method where the number and diameter of craters are counted manually on satellite images. The relative ages of various stratigraphic units on Mars have been determined by a combination of superposition relations and crater densities. Fewer craters reflect a younger surface, while an older surface will have had a higher exposure time to impacts, and will thus have accumulated more craters (Barlow, 2008). Additionally, an older surface will also be more likely to have larger sized impact craters, as the flux of large impacting bolides has decreased with time (Michael, 2012). A single body, like Mars, is also not expected to have a uniform coverage of impact craters. Multiple resurfacing events, such as volcanic eruptions on Mars and subduction on Earth, have erased old craters and created new surfaces which are then exposed to impacts.

Counting the number of craters on a geologic unit can be used in both relative and absolute chronologies, with CSFD being the only currently known technique of remotely measuring an absolute age of a planetary surface (Fassett, 2016). Counting the number and size of craters on a homogenous geological unit produces a frequency of craters as a function of the crater diameter, to determine an absolute age. Absolute ages determined by crater counting of Martian units are labelled as "model ages", highlighting that they are not directly measured on a sample.

1.2.2.1. Impact craters: crater types and quantifiable features

When determining ages using the CSFD method, it is necessary to identify the different features of an impact crater. An impact crater is classified as a circular depression caused by an impacting bolide. A "fresh" impact crater will be circular and typically show a bright raised rim on satellite images. Surrounding it will be a blanket of ejecta material from a combination of the impactor and the impacted object. The properties of the impacted material are the dominant factor controlling the resulting shape of a crater (Melosh, 2011).

An important distinction between impact crater types is whether they are considered a primary or a secondary crater. Primary craters are created by the main impacting bolide, meaning there will be one primary crater per impacting bolide. However, during the primary impact, secondary craters are produced by the ejecta originating from primary crater formation. There is no direct correlation between the number of bolides and the number of secondary craters, as an impact can create one primary crater along

with a large, often unknown, number of secondary craters. On Mars, the maximum size of a secondary crater will be approximately 4% of the primary crater diameter (Melosh, 2011). Typically, secondary craters have a non-random spatial distribution and are concentrated in clusters, making them easier to identity.

When using CSFD as an age-dating method, different factors, including some mentioned above, contribute to various uncertainties. One of these uncertainties is the crater saturation of a surface. After a while, a surface which accumulates craters will reach its equilibrium. The surface is then saturated, so that any new impact will erase a pre-existing one, keeping the crater density of the surface relatively constant. Such a surface can thus only be measured as "very old" and thus provide no specific ages (Barlow, 2008). Of the terrestrial objects in our solar system, the majority of the Lunar highlands are affected by crater saturation. This is, however, not the case for the youngest Martian terrains, which have largely been volcanically resurfaced (Melosh, 2011). Erosion of craters is another process which makes it difficult to determine the correct number of impacts on a given surface, making it a problematic surface to date. Erosion will preferentially erase craters with a smaller diameter, which will change the slope of the curve in the lower crater diameter end of a CSFD plot, typically making the age appear older (Barlow, 2008).

The distinction between primary and secondary craters also constrains the crater counting method, as the inclusion of secondary craters would produce an artificially older age. As the secondary craters have a more clustered spatial distribution, methods exist which makes it possible to largely exclude any non-randomly distributed craters and thus prevent the inclusion of secondary craters (Michael et al., 2012)

A final point to take into consideration regarding the crater counting method, is that it works under the assumption, that the impact rate for the planetary surfaces of the inner Solar System has been decreasing at a constant rate over time. This assumption is somewhat disputed, as an observed spike in the frequency of impacts at ~3.8 Ga has been detected within the inner Solar System, which is referred to as the Late Heavy Bombardment (LHB) (Melosh, 2011).

1.2.2.2. From crater counting to absolute ages: models and methods used.

Determining an absolute model age using crater-size frequency distributions (CSFDs), is done by fitting the counted CSFD of a chosen geological unit with a known crater isochron for the relevant planet. These crater isochrons are created by combining a crater production function with a calibrated chronology function (Michael, 2013).

The Martian chronology functions were created by altering the functions created for the Moon. A lunar timescale was created first, showing the relationship between the age and the CSFD of a specific

geological unit on the Moon (Stöffler et al., 2006). This timescale was made possible using samples of the Moon's various units, which were obtained on the Apollo and Luna sample-return missions. Using these returned samples, the absolute radiogenic age of a sample could be directly related to the CSFD of the sample's source unit, deriving the exact ages for different surface-creating processes on the Moon (Stöffler et al., 2006). These calibrations were used by Neukum et al. (2001) to produce the original Lunar Chronology Function for the Moon:

$$N(1) = 5.44 * 10^{-14} (\exp(6.93T) - 1] + 8.38 \cdot 10^{-4}T \quad (1)$$

Where $N(1)$ represents the number of craters equal to and larger than 1 km in diameter per km^2 and T is the crater accumulation time in Gyr. The time-derivative of the relationship between N and T is expressed as the cratering rate: dN/dT (Neukum et al., 2001).

The Lunar Chronology Function was then scaled to fit Mars following three conditions. The first was that the population of impacting bodies should be the same between the Moon and Mars, which is indeed the case (Barlow, 2008). The second condition was that the timing of the LHB between the Moon and Mars is known, which is also the case, as the LHB is determined to begin and end simultaneously within the inner Solar System (Barlow, 2008). The third condition was that the impact flux for Mars relative to the Moon must be known (Barlow, 2008). Hartmann & Neukum (2001) determined that the average impact rate for Mars was two times higher than the Moon for asteroids of the same size. With all conditions met, the Lunar Chronology Function was scaled to fit the surface of Mars.

The production function describes the size-frequency distribution of craters produced on a surface, which has not yet reached equilibrium. It defines how many craters of a certain diameter can be expected on a surface, in relation to the number of craters with any other diameter. The general trend is that younger surfaces have smaller and fewer craters, and that older units have a larger range of crater sizes (Michael & Neukum, 2010). Figure 1.8a displays a reverse-cumulative frequency plot showing log N(> D) vs. log D, where N(> D) is the number of craters larger than D, which is directly related to the size-frequency distribution of impacting objects.

Combining the production function (Figure 1.8b) with the chronology function produces an isochron diagram, which displays the expected crater density of surfaces of different ages (Figure 1.8c). These isochrons are then used by software, such as *Craterstats v. 2* used in this study, to determine absolute model ages of surfaces on Mars (Michael, 2013).

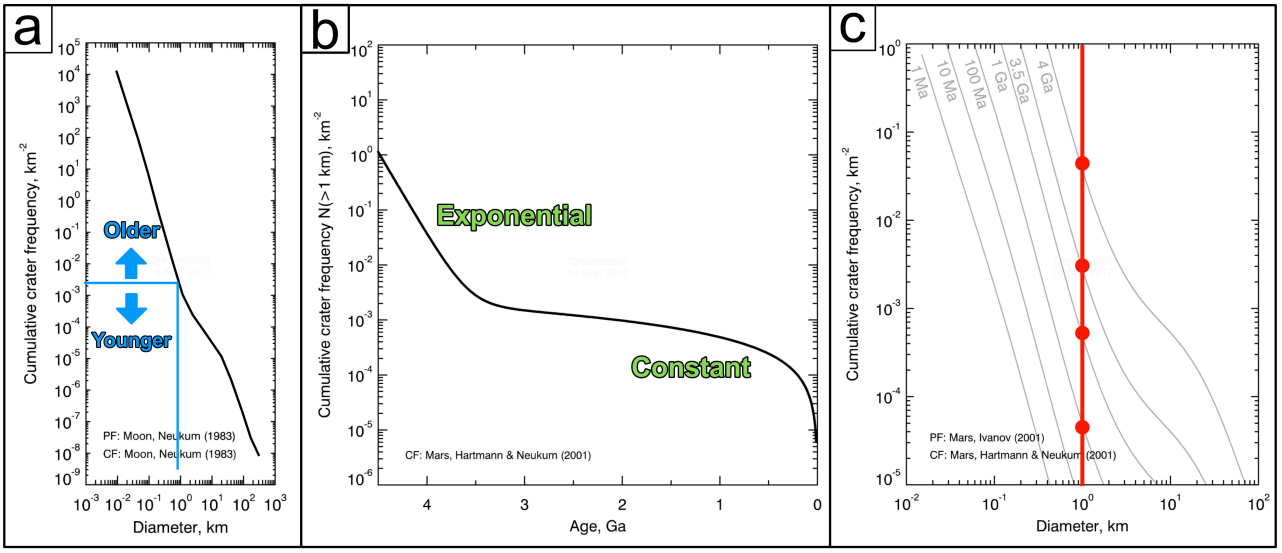

Figure 1.8: Visualization of the crater statistics functions. A) Reverse-cumulative frequency plot showing the production function. From Michael (2012). B) Simplified chronology function modified from Michael (2012). C) Isochron diagram, using Hartmann & Neukum's (2001) chronology function and Ivanov's (2001) production function, both for Mars. The red points are given by the chronology function (CF) for the different ages. The grey lines are the production function (PF), shifted either up or down to intersect the CF points.

1.3. Unresolved questions regarding Tharsis's formation and processes.

What can detailed structural studies tell us about Tharsis?

Although the origin and evolution of Tharsis and its many shield volcanoes have been areas of interest for decades, the majority of the studies have considered the large-scale evolution of the entire region – which is approximately the size of the continent of Africa – as one large study. While comprehensive, overarching studies of the region are essential, there is a significant lack of in-depth, high-resolution mapping and structural evolution models of the faulted terrains in Tharsis. Additionally, there are less than a handful of studies which consider the sources of stress for locations such as Ulysses Fossae, and other intensely faulted terrains in Tharsis.

Ulysses Fossae has only two dedicated studies, one by Scott & Dohm (1990) who mapped fault orientations on Viking photomosaics, which did not capture the complexity of faulting observed on the modern 6 m/pixel CTX image resolutions. The second study, by Fernández & Ramírez-Caballero (2019), performed a detailed kinematic analysis on a selected group of Ulysses Fossae faults, and set a solid foundation for further exploration of the Ulysses Fossae faults.

Ceraunius and Tractus Fossae, however, suffer from being included within larger studies, often related to Alba Mons (e.g., Bouley et al., 2018; McGovern et al., 2001; Tanaka, 1990), and the details within each

faulted terrain are often overlooked. Ceraunius Fossae is often attributed to Alba Mons, due to its location, but closer examination of the orientations of the faults could suggest a more complex history. There are even fewer studies which consider the more local influences on the extensional tectonic features in Tharsis. The lack of detailed analysis of Ulysses Fossae and Ceraunius and Tractus Fossae, means that we are missing information about what the local and regional sources are for the structures in these areas, and by extension Tharsis as a whole, as well as constraining the timing of these events.

How does dike-driven graben formation work on Mars?

Dike-driven graben formation is considered a primary driver of extensional tectonics on Mars. However, there are no direct measurements of dikes underneath Martian grabens. Previous studies have therefore turned to numerical modelling to aid understanding, but none of the present models include the process of intruding the ascending dike into the material, and mainly consists of a widening dike at a stalled depth (e.g. Hardy, 2016; Wyrick & Smart, 2009). In addition to lack of knowledge regarding the actual dike-induced graben formation process (e.g. fracture formation, depth of dike etc.), the actual lithospheric properties of Mars are poorly constrained. This means we lack information regarding the influence of varying lithospheric material properties has on the final surface deformation. These are crucial processes to understand in relation to the development of Tharsis, as well as to broader Martian and terrestrial planet evolution. Unravelling these questions and further defining the geological processes responsible for the structures we observed with remote sensing, will be crucially beneficial in future planetary research.

To summarize, detailed structural and tectonic studies of the Tharsis Volcanic Province on Mars are sorely lacking, and where mapping has previously been performed, the sources of stress are not consistently well defined. One important source of stress, dike-induced graben formation, is not yet fully understood. The differences in material properties and crust and mantle thickness between terrestrial planets are almost certain to have an impact on the formation of the observed surface structures, although to what extent is still unknown. We are now in an excellent position to address these knowledge gaps, having access to detailed satellite data, space mission measurements, and advanced numerical modelling software. Together these approaches can be used to decipher the evolution of the Tharsis Volcanic Province, and shed more light on the geological processes which occur on all terrestrial planets.

1.4. Study aims and objectives.

The overarching goal of my thesis is to determine the local and regional volcano-tectonic evolution of two areas of the Tharsis Volcanic Province, Ulysses Fossae and Ceraunius Fossae (including Tractus Fossae), and use this to examine the structural history of Tharsis over time. I further aim to understand the deformation processes involved in this volcano-tectonic evolution by using 2D numerical modelling to examine dike-driven graben formation on Mars and determine the processes and material properties that may affect it. To achieve these thesis aims, I have the following research objectives:

- Produce comprehensive, high-resolution maps of all extensional structures of Ulysses Fossae, Ceraunius Fossae, and Tractus Fossae on Mars, including collapse features.
- Use in-depth crater size-frequency distribution analysis to update model ages from the Tanaka et al. (2014) global geologic map of Mars for units in the study areas, using intact craters down to 1 km in diameter.
- Establish the timing and sequence of mapped structures.
- Determine the key surface features of the volcano-tectonic faults in the study areas that reflect their tectonic evolution and key controlling mechanisms.
- Investigate potential local and regional sources of magmatic-tectonic processes in the Tharsis Volcanic Province by relating the mapped features to magmatic and volcanic centres.
- Develop a simple 2D numerical model of an ascending dike intruding into the Martian lithosphere that can test both lithospheric and dike-related variables in size, velocity, and material properties.
- Examine the effects of variations in lithosphere brittleness on model results and compare model-generated surface deformation patterns to mapped structures to infer formation mechanisms and material properties.

1.5. Thesis structure

This thesis is presented as an alternative format thesis and consists of one published journal contribution (Chapter 2), one journal contribution resubmitted with minor corrections (Chapter 3), and one manuscript ready for submission (Chapter 4), resulting in three research chapters, followed by an integrative discussion and conclusion. Details with regard to the technical and scientific contributions of co-authors and publication information are provided in the Intellectual Property and Publication Statement. In the following, a brief summary of each research chapter is provided.

Chapters 2 and **3** pertain to the geological mapping and structural history of two different study areas in the Tharsis province on Mars. The focus of **Chapter 2** is the study of Ulysses Fossae, an area of extensive faulting which has been spared from coverage by extensive Tharsis lava flows due to its elevated topography. It is the only known location with far-field tectonic structures associated with Olympus Mons. In this chapter, I mapped the faults and determined their absolute and relative ages to produce a structural history of the area. I did this with an emphasis on the connections between the tectonic structures and the local and regional volcanic centres. This chapter has been published separately as a peer-reviewed journal article (Shahrzad et al., 2023).

In **Chapter 3** I performed a similar study on a different faulted area in Tharsis: Ceraunius, and Tractus Fossae. These structures have historically been associated with the Alba Mons volcano, and the structural evolution I created in this chapter serves as a useful comparison and contrast to the results and processes identified in Chapter 2.

Chapter 4 focuses on the numerical modelling portion of this thesis. Based on the new understanding provided by the results from Chapters 2 and 3, I determined diking is a primary driver of extensional tectonics in the Tharsis Volcanic Province. In this chapter I investigated this process by creating a 2D discrete element model of a dike intruding into the Martian lithosphere. I also varied the Young's modulus of the lithosphere in the model between three different values, and compared the results to a final model where graben formation was solely the result of regional tectonic extension. Finally, I compared the model results to the measurements and observations from Chapters 2 and 3.

In the concluding section, **Chapter 5,** I present an integrated discussion of the results from all three research chapters and combine these results into a suggested evolution model of the entire Tharsis area. To finish the thesis, I suggest and discuss future work recommendations.

1.6. A note on terrestrial analogues

I had originally planned to dedicate a third of my research to doing analogue fieldwork in Iceland. Earth-based analogues offer valuable opportunities to ground-truth data, validate remote sensing techniques, and improve the interpretation of structures, all of which helps enhance our understanding of geological processes on other planets. However, due to impacts of the COVID-19 pandemic, this portion of the project was removed, and the numerical modelling and additional mapping replaced it. Supervisor Emma K. Bramham, colleague Claire Orlov, and I managed to organize a brief 1-week field visit to Iceland in 2022, in order to observe the geological features and assess if a proper analogical field comparison to Mars was viable. This resulted in a few field observations, along with a plan for future geological fieldwork which would supplement the results of this thesis with ground-truthing of the remote sensing data. This is discussed further as suggested future work in Chapter 5.4.

References

Anderson. (1953). The Dynamics of Faulting and Dyke Formation with Applications to Britain. By E. M. Anderson. Second edition revised. *Geological Magazine*, *90*(4), 300–301. https://doi.org/10.1017/S0016756800065493

Anderson, R. C., Dohm, J. M., Golombek, M. P., Haldemann, A. F. C., Franklin, B. J., Tanaka, K. L., Lias, J., & Peer, B. (2001). Primary centers and secondary concentrations of tectonic activity through time in the western hemisphere of Mars. *Journal of Geophysical Research: Planets*, *106*(E9), 20563–20585. https://doi.org/10.1029/2000JE001278

Andrews-Hanna, J. C., Zuber, M. T., & Banerdt, W. B. (2008). The Borealis basin and the origin of the martian crustal dichotomy. *Nature*, *453*(7199), Article 7199. https://doi.org/10.1038/nature07011

Baker, V. R., Maruyama, S., & Dohm, J. M. (2007). Tharsis Superplume and the Geological Evolution of Early Mars. In D. A. Yuen, S. Maruyama, S.-I. Karato, & B. F. Windley (Eds.), *Superplumes: Beyond Plate Tectonics* (pp. 507–522). Springer Netherlands. https://doi.org/10.1007/978-1-4020-5750-2_16

Bandfield, J. L., Hamilton, V. E., & Christensen, P. R. (2000). A Global View of Martian Surface Compositions from MGS-TES. *Science*, *287*(5458), 1626–1630. https://doi.org/10.1126/science.287.5458.1626

Banerdt, W. B., Golombek, M. P., & Tanaka, K. L. (1992). Stress and tectonics on Mars. In *Mars* (pp. 249–297). https://ui.adsabs.harvard.edu/abs/1992mars.book..249B

Banerdt, W. B., Phillips, R. J., Sleep, N. H., & Saunders, R. S. (1982). Thick shell tectonics on one-plate planets: Applications to Mars. *Journal of Geophysical Research: Solid Earth*, *87*(B12), 9723–9733. https://doi.org/10.1029/JB087iB12p09723

Barlow, N. G. (2008). Mars, An introduction to its Interior, Surface and Atmosphere. Cambridge University Press.

Bouley, S., Baratoux, D., Matsuyama, I., Forget, F., Séjourné, A., Turbet, M., & Costard, F. (2016). Late Tharsis formation and implications for early Mars. *Nature*, *531*(7594), 344–347. https://doi.org/10.1038/nature17171

Bouley, S., Baratoux, D., Paulien, N., Missenard, Y., & Saint-Bézar, B. (2018). The revised tectonic history of Tharsis. *Earth and Planetary Science Letters*, *488*, 126–133. https://doi.org/10.1016/j.epsl.2018.02.019

Cailleau, B., Walter, T. R., Janle, P., & Hauber, E. (2003). Modeling volcanic deformation in a regional stress field: Implications for the formation of graben structures on Alba Patera, Mars. *Journal of Geophysical Research: Planets*, *108*(E12). https://doi.org/10.1029/2003JE002135

Carr, M. H. (1974). Tectonism and volcanism of the Tharsis Region of Mars. *Journal of Geophysical Research (1896-1977)*, *79*(26), 3943–3949. https://doi.org/10.1029/JB079i026p03943

Carr, M. H., & Head, J. W. (2010). Geologic history of Mars. *Earth and Planetary Science Letters*, *294*(3), 185–203. https://doi.org/10.1016/j.epsl.2009.06.042

Chadwick Jr., W. W., & Embley, R. W. (1998). Graben formation associated with recent dike intrusions and volcanic eruptions on the mid-ocean ridge. *Journal of Geophysical Research: Solid Earth*, *103*(B5), 9807–9825. https://doi.org/10.1029/97JB02485

Cheung, K. K., & King, S. D. (2014). Geophysical evidence supports migration of Tharsis volcanism on Mars. *Journal of Geophysical Research: Planets*, *119*(5), 1078–1085. https://doi.org/10.1002/2014JE004632

Cushing, G. E., Okubo, C. H., & Titus, T. N. (2015). Atypical pit craters on Mars: New insights from THEMIS, CTX, and HiRISE observations. *Journal of Geophysical Research: Planets*, *120*(6), 1023–1043. https://doi.org/10.1002/2014JE004735

Dohm, J. M., Baker, V. R., Maruyama, S., & Anderson, R. C. (2007). Traits and Evolution of the Tharsis Superplume, Mars. In D. A. Yuen, S. Maruyama, S.-I. Karato, & B. F. Windley (Eds.), *Superplumes: Beyond Plate Tectonics* (pp. 523–536). Springer Netherlands. https://doi.org/10.1007/978-1-4020-5750-2_17

Ernst, R., Grosfils, E., & Mège, D. (2001). Giant Dike Swarms: Earth, Venus, and Mars. *Annual Review of Earth and Planetary Sciences*, *29*(1), 489–534. https://doi.org/10.1146/annurev.earth.29.1.489

Fassett, C. I., & Head, J. W. (2011). Sequence and timing of conditions on early Mars. *Icarus*, *211*(2), 1204–1214. https://doi.org/10.1016/j.icarus.2010.11.014

Fernández, C., & Ramírez-Caballero, I. (2019). Evaluating transtension on Mars: The case of Ulysses Fossae, Tharsis. Journal of Structural Geology, 125, 325–333. https://doi.org/10.1016/j.jsg.2018.05.009

Fergason, R. L., Hare, T. M., & Laura, J. (2018). *HRSC and MOLA Blended Digital Elevation Model at 200m v2*. [Map]. Astrogeology PDS Annex, U.S. Geological Survey.

Frey, H., & Schultz, R. A. (1988). Large impact basins and the mega-impact origin for the crustal dichotomy on Mars. *Geophysical Research Letters*, *15*(3), 229–232. https://doi.org/10.1029/GL015i003p00229

Goudy, C., & Schultz, R. (2005). Dike intrusions beneath grabens south of Arsia Mons, Mars. *Geophysical Research Letters*, *32*. https://doi.org/10.1029/2004GL021977

Gudmundsson, A. (2003). Surface stresses associated with arrested dykes in rift zones. *Bulletin of Volcanology*, *65*(8), 606–619. https://doi.org/10.1007/s00445-003-0289-7

Gudmundsson, A. (2020). Volcanotectonics—Understanding the Structure, Deformation and Dynamics of Volcanoes. https://doi.org/10.1017/9781139176217

Hardy, S. (2016). Does shallow dike intrusion and widening remain a possible mechanism for graben formation on Mars? *Geology*, *44*(2), 107–110. https://doi.org/10.1130/G37285.1

Hardy, S. (2021). Discrete Element Modelling of Pit Crater Formation on Mars. *Geosciences*, *11*(7), Article 7. https://doi.org/10.3390/geosciences11070268

Heap, M. J., Byrne, P. K., & Mikhail, S. (2017). Low surface gravitational acceleration of Mars results in a thick and weak lithosphere: Implications for topography, volcanism, and hydrology. *Icarus*, *281*, 103–114. https://doi.org/10.1016/j.icarus.2016.09.003

Hiesinger, H., & Tanaka, K. (2020). The Planetary Time Scale. In F. M. Gradstein, J. G. Ogg, M. D. Schmitz, & G. M. Ogg (Eds.), Geologic Time Scale 2020 (pp. 443-480): Elsevier. Retrieved from https://doi.org/10.1016/B978-0-12-824360-2.00015-2

Hood, L. L., Richmond, N. C., Harrison, K. P., & Lillis, R. J. (2007). East–west trending magnetic anomalies in the Southern Hemisphere of Mars: Modeling analysis and interpretation. *Icarus*, *191*(1), 113–131. https://doi.org/10.1016/j.icarus.2007.04.025

Hynek, B. M., Robbins, S. J., Šrámek, O., & Zhong, S. J. (2011). Geological evidence for a migrating Tharsis plume on early Mars. *Earth and Planetary Science Letters*, *310*(3), 327–333. https://doi.org/10.1016/j.epsl.2011.08.020

Lenardic, A., Nimmo, F., & Moresi, L. (2004). Growth of the hemispheric dichotomy and the cessation of plate tectonics on Mars. *Journal of Geophysical Research: Planets*, *109*(E2). https://doi.org/10.1029/2003JE002172

Marinova, M. M., Aharonson, O., & Asphaug, E. (2008). Mega-impact formation of the Mars hemispheric dichotomy. *Nature*, *453*(7199), 1216–1219. https://doi.org/10.1038/nature07070

Mastin, L. G., & Pollard, D. D. (1988). Surface Deformation and Shallow Dike Intrusion Processes at Inyo Craters, Long Valley, California. *Journal of Geophysical Research: Solid Earth*, *93*(B11), 13221–13235. https://doi.org/10.1029/JB093iB11p13221

McGovern, P. J., Solomon, S. C., Head III, J. W., Smith, D. E., Zuber, M. T., & Neumann, G. A. (2001). Extension and uplift at Alba Patera, Mars: Insights from MOLA observations and loading models. *Journal of Geophysical Research: Planets*, *106*(E10), 23769–23809. https://doi.org/10.1029/2000JE001314

Mège, D., & Masson, P. (1996). A plume tectonics model for the Tharsis province, Mars. *Planetary and Space Science*, *44*(12), 1499–1546. https://doi.org/10.1016/S0032-0633(96)00113-4

Melosh, H. J. (2011). *Planetary Surface Processes*. https://doi.org/10.1017/CBO9780511977848

Michael, G. G. (2013). Planetary surface dating from crater size–frequency distribution measurements: Multiple resurfacing episodes and differential isochron fitting. *Icarus*, *226*(1), 885–890. https://doi.org/10.1016/j.icarus.2013.07.004

Michael, G. G., Platz, T., Kneissl, T., & Schmedemann, N. (2012). Planetary Surface Dating from Crater Size-Frequency Distribution Measurements: Spatial Randomness and Clustering. *Icarus*, *218*, 2486. https://doi.org/10.1016/j.icarus.2011.11.033

Nimmo, F. (2000). Dike intrusion as a possible cause of linear Martian magnetic anomalies. *Geology*, *28*(5), 391–394. https://doi.org/10.1130/0091-7613(2000)28<391:DIAAPC>2.0.CO;2

Nimmo, F., Hart, S. D., Korycansky, D. G., & Agnor, C. B. (2008). Implications of an impact origin for the martian hemispheric dichotomy. *Nature*, *453*(7199), 1220–1223. https://doi.org/10.1038/nature07025

Öhman, T., & McGovern, P. J. (2014). Circumferential graben and the structural evolution of Alba Mons, Mars. *Icarus*, *233*, 114–125. https://doi.org/10.1016/j.icarus.2014.01.043

Okubo, C. H., & Schultz, R. A. (2005). Evidence of Tharsis-Radial Dike Intrusion in Southeast Alba Patera from MOLA-based Topography of Pit Crater Chains. 1007.

Paquet, F., Dauteuil, O., Hallot, E., & Moreau, F. (2007). Tectonics and magma dynamics coupling in a dyke swarm of Iceland. *Journal of Structural Geology*, *29*(9), 1477–1493. https://doi.org/10.1016/j.jsg.2007.06.001

Park, R. G. (2000). Foundations of Structural Geology: Vol. 3rd Edition. Chapman & Hall.

Pieterek, B., Ciazela, J., Lagain, A., & Ciazela, M. (2022). Late Amazonian dike-fed distributed volcanism in the Tharsis volcanic province on Mars. *Icarus*, *386*, 115151. https://doi.org/10.1016/j.icarus.2022.115151

Plescia, J. B., & Saunders, R. S. (1982). Tectonic history of the Tharsis Region, Mars. *Journal of Geophysical Research: Solid Earth*, *87*(B12), 9775–9791. https://doi.org/10.1029/JB087iB12p09775

Poland, M. P., Moats, W. P., & Fink, J. H. (2008). A model for radial dike emplacement in composite cones based on observations from Summer Coon volcano, Colorado, USA. *Bulletin of Volcanology*, *70*(7), 861–875. https://doi.org/10.1007/s00445-007-0175-9

Pollard, D. D., Delaney, P. T., Duffield, W. A., Endo, E. T., & Okamura, A. T. (1983). Surface Deformation in Volcanic Rift Zones. In P. Morgan & B. H. Baker (Eds.), *Developments in Geotectonics* (Vol. 19, pp. 541–584). Elsevier. https://doi.org/10.1016/B978-0-444-42198-2.50036-5

Poulet, F., Bibring, J.-P., Mustard, J. F., Gendrin, A., Mangold, N., Langevin, Y., Arvidson, R. E., Gondet, B., Gomez, C., Berthé, M., Erard, S., Forni, O., Manaud, N., Poulleau, G., Soufflot, A., Combes, M., Drossart, P., Encrenaz, T., Fouchet, T., … Omega Team. (2005). Phyllosilicates on Mars and

implications for early martian climate. *Nature*, *438*(7068), 623–627. https://doi.org/10.1038/nature04274

Rivas-Dorado, S., Ruíz, J., & Romeo, I. (2022). Giant dikes and dike-induced seismicity in a weak crust underneath Cerberus Fossae, Mars. *Earth and Planetary Science Letters*, *594*, 117692. https://doi.org/10.1016/j.epsl.2022.117692

Rubin, A. M. (1992). Dike-induced faulting and graben subsidence in volcanic rift zones. *Journal of Geophysical Research: Solid Earth*, *97*(B2), 1839–1858. https://doi.org/10.1029/91JB02170

Rubin, A. M., & Pollard, D. D. (1988). Dike-induced faulting in rift zones of Iceland and Afar. *Geology*, *16*(5), 413–417. https://doi.org/10.1130/0091-7613(1988)016<0413:DIFIRZ>2.3.CO;2

Schultz, R. A., Okubo, C. H., Goudy, C. L., & Wilkins, S. J. (2004). Igneous dikes on Mars revealed by Mars Orbiter Laser Altimeter topography. *Geology*, *32*(10), 889–892. https://doi.org/10.1130/G20548.1

Scott, D., & Dohm, J. (1990). Faults and ridges—Historical development in Tempe Terra and Ulysses Patera regions of Mars. *Proc. Lunar Planet. Sci. Conf. 20th*.

Scott, D. H., Tanaka, K. L., & Kozak, R. (1986). Geologic map of the western equatorial region of Mars.

Scott, E. D., Wilson, L., & Head III, J. W. (2002). Emplacement of giant radial dikes in the northern Tharsis region of Mars. *Journal of Geophysical Research: Planets*, *107*(E4), 3-1-3–10. https://doi.org/10.1029/2000JE001431

Shahrzad, S., Bramham, E. K., Thomas, M., Piazolo, S., Byrne, P. K., & Mortimer, E. (2023). Deciphering the Structural History of Ulysses Fossae, Mars, Using Fault Pattern Analysis. *Journal of Geophysical Research: Planets*, *128*(5), e2022JE007633. https://doi.org/10.1029/2022JE007633

Sleep, N. H. (1994). Martian plate tectonics. *Journal of Geophysical Research: Planets*, *99*(E3), 5639–5655. https://doi.org/10.1029/94JE00216

Solomon, S. C. (1978). On volcanism and thermal tectonics on one-plate planets. *Geophysical Research Letters*, *5*(6), 461–464. https://doi.org/10.1029/GL005i006p00461

Solomon, S. C., Aharonson, O., Aurnou, J. M., Banerdt, W. B., Carr, M. H., Dombard, A. J., Frey, H. V., Golombek, M. P., Hauck, S. A., Head, J. W., Jakosky, B. M., Johnson, C. L., McGovern, P. J., Neumann, G. A., Phillips, R. J., Smith, D. E., & Zuber, M. T. (2005). New Perspectives on Ancient Mars. *Science*, *307*(5713), 1214–1220. https://doi.org/10.1126/science.1101812

Solomon, S. C., & Head, J. W. (1982). Evolution of the Tharsis Province of Mars: The importance of heterogeneous lithospheric thickness and volcanic construction. *Journal of Geophysical Research: Solid Earth*, *87*(B12), 9755–9774. https://doi.org/10.1029/JB087iB12p09755

Tanaka, K. L. (1990). Tectonic history of the Alba Patera—Ceraunius Fossae region of Mars. *Lunar and Planetary Science Conference Proceedings*, *20*, 515–523.

Tanaka, K. L., Golombek, M. P., & Banerdt, W. B. (1991). Reconciliation of stress and structural histories of the Tharsis region of Mars. *Journal of Geophysical Research: Planets*, *96*(E1), 15617–15633. https://doi.org/10.1029/91JE01194

Tanaka, K. L., Skinner Jr., J. A., Dohm, J. M., Irwin, III, R. P., Kolb, E. J., Fortezzo, C. M., Platz, T., Michael, G. G., & Hare, T. M. (2014). *Geologic Map of Mars* (Scientific Investigations Map) [Scientific Investigations Map].

Trippanera, D., Ruch, J., Acocella, V., & Rivalta, E. (2015). Experiments of dike-induced deformation: Insights on the long-term evolution of divergent plate boundaries. *Journal of Geophysical Research: Solid Earth*, *120*(10), 6913–6942. https://doi.org/10.1002/2014JB011850

Webb, B. M., & Head, J. W., III. (2002). Noachian Tectonics of Syria Planum and the Thaumasia Plateau. 1358.

Werner, S. C. (2009). The global martian volcanic evolutionary history. *Icarus*, *201*(1), 44–68. https://doi.org/10.1016/j.icarus.2008.12.019

Wilson, L., & Head III, J. W. (2002). Tharsis-radial graben systems as the surface manifestation of plume-related dike intrusion complexes: Models and implications. *Journal of Geophysical Research: Planets*, *107*(E8), 1-1-1–24. https://doi.org/10.1029/2001JE001593

Wilson, L., & Head, J. W. (1994). Mars: Review and analysis of volcanic eruption theory and relationships to observed landforms. *Reviews of Geophysics*, *32*(3), 221–263. https://doi.org/10.1029/94RG01113

Wise, D. U., Golombek, M. P., & McGill, G. E. (1979a). Tectonic evolution of Mars. *Journal of Geophysical Research: Solid Earth*, *84*(B14), 7934–7939. https://doi.org/10.1029/JB084iB14p07934

Wise, D. U., Golombek, M. P., & McGill, G. E. (1979b). Tharsis province of Mars: Geologic sequence, geometry, and a deformation mechanism. *Icarus*, *38*(3), 456–472. https://doi.org/10.1016/0019-1035(79)90200-8

Wyrick, D. Y., & Smart, K. J. (2009). Dike-induced deformation and Martian graben systems. *Journal of Volcanology and Geothermal Research*, *185*(1), 1–11. https://doi.org/10.1016/j.jvolgeores.2008.11.022

Chapter 2

Deciphering the structural history of Ulysses Fossae, Mars, using fault pattern analysis

S. Shahrzad[1], E.K. Bramham[1], M. Thomas[1], S. Piazolo[1], and P.K. Byrne[2]

[1]School of Earth and Environment, University of Leeds.

[2]Department of Earth and Planetary Sciences, Washington University in St. Louis.

Abstract

Ulysses Fossae is a faulted region surrounded by lava flows that sits between the major volcanoes of the Tharsis Rise volcanic province on Mars. This area is unique, as it is the only exposure of extensional faulting which can be related to the Olympus Mons volcano and one of only a few faulted areas relating to the Tharsis Montes. In order to determine the area's structural evolution through time, we mapped all identifiable faults, divided them into 10 fault groups determined by their orientation and morphology, and performed detailed crater size-frequency analysis of the geological units. We divide the fault groups into two overall types based upon their genesis: local diking and regional extension. The complex structural evolution recorded in the extensional faults in Ulysses Fossae is dominated by local dike-related activity (8/10 fault groups), along with deformation from large, regional scale extensional processes related to the development of the Tharsis province as a whole (2/10 fault groups). Strain values measured across the 10 fault groups vary between 0.4 – 2.2%, with the grabens related to regional extension accommodating larger extensional strains than the local dike-related grabens. The crater size-frequency distribution analysis of three distinct areas in Ulysses Fossae (UF Dome, UF North and UF South) revealed that the majority of the faulting in Ulysses Fossae was active during the Early Amazonian.

Plain Language Summary

The volcanoes in the Tharsis province on Mars are normally associated with deformation of the surface near them, associated with the growth and development of the volcano. However, in Tharsis, due to its significant coverage of lava, we only find volcanically associated surface deformation for some of the Tharsis volcanoes in an area called Ulysses Fossae. In this study we map and characterize the surface structures in Ulysses Fossae, which are then used to define the structural history of the area. Our work reveals that there are 10 distinct episodes of deformation in Ulysses Fossae, where the majority of the activity responsible for the surface structures, are associated with subsurface activity from nearby volcanoes. Two of the episodes also show signs of movement associated with the development of the Tharsis region as a whole. Additionally, we determined the ages of this deformation, and found that the majority of the activity takes place during the Amazonian period (~3 billion years ago) in Mars' geologic history. This shows that the volcanic systems surrounding Ulysses Fossae were active for longer than previously determined and together with the mapped structures, provides a detailed history of the different stages of activity in the area.

2.1. Introduction

The majority of tectonic structures on Mars are believed to be driven by volcanic processes (E.g. Barlow, 2008; Bouley et al., 2018; Carr & Head, 2010). While we do have an understanding of the influence of large-scale stresses in the Tharsis volcanic province (e.g. Bouley et al., 2018; Thomas & Allemand, 1993), we still lack a thorough analysis of the impact of individual volcanoes, and their interactions, on surface tectonic structures on Mars. The far-field stresses associated with volcanic centres on Mars thus remain to be fully characterized. For instance, even though the largest volcano in the Solar System, Olympus Mons, has been studied extensively (e.g. De Blasio, 2018; McGovern et al., 2004; Morris & Tanaka, 1994), it is unclear how its presence has influenced the Tharsis-related far-field stress in its surrounding region. Questions such as why there is a considerable difference between the number and size of structures related to different volcanoes, with similar plume-induced sources, remain. A complicating factor is that the majority of these volcano-related structures are only exposed in restricted patches, surrounded by Amazonian lavas. An example of this is Ulysses Fossae, which provides a "window" into some of the volcano-tectonic structures which lay beneath the extensive lavas covering Tharsis. Moreover, given how tectonically deformed the entire Tharsis Rise is (e.g. Bouley et al., 2018; Scott et al., 2002; Wilson & Head III, 2002), it is unclear to what extent given populations of extensional structures might be attributed to the several large (>2.9 x 10^{12} m^3 (Plescia, 2004)) volcanoes in the region. It is therefore likely that aspects

of the tectonic history of Tharsis, and other volcanic centres on Mars such as Elysium, are more intricate than current models acknowledge (e.g. Anderson et al., 2001; Bouley et al., 2018), where complex faulting patterns are commonly grouped together as a part of a single tectonic stage. Understanding this complexity within Tharsis is essential if we are to decipher the volcano-tectonic history of Mars as a whole, and with that its evolution through time, with accompanying geologic, biologic, and atmospheric consequences (Bouley et al., 2018). Unravelling how different faults relate to different volcanoes through time is a fundamental step to a more nuanced understanding of Tharsis' evolution.

The volcanotectonic province of Tharsis hosts 5 major volcanoes: Olympus Mons, Alba Mons, and the Tharsis Montes (Arsia, Pavonis, and Ascraeus Mons) – and therefore offers a useful case study area to explore the contribution of volcanic edifices to far-field stresses and resultant tectonic structures. The magmatic-driven processes are attributed to the Tharsis Superplume, where its five stages of pulses developed local- and regional scale centres of tectonic activity (Dohm et al., 2007). Plume associated extensional deformation in Tharsis created a suite of diagnostic landforms, with the most common being extensive fault and rift systems, and local and regional centres of magmatic driven activity, producing volcanoes and associated radial and circumferential fault systems (Dohm et al., 2007). The radial fault systems are attributed to diking from one of these local volcanic centres (e.g. Anderson et al., 2001; Dohm et al., 2007), while the commonly observed north-south oriented faults in Tharsis are attributed to isostasy in the first phase of Tharsis' evolution (Banerdt et al., 1982). The volcanic construction on Mars, a single-plate planet, allows for the volcanic material to remain vertically above the subsurface source. Isostatic uplift is then generated when the volume of erupted volcanic material moves beyond its source in Tharsis Region (Banerdt et al., 1982). According to Banerdt et al. (1982), a significant uplift will be generated, with the removal of only a fraction of volcanic material. This process thus facilitates the tensile hoop stresses identified in Tharsis, responsible for the north-south oriented faulting (Banerdt et al., 1982).

The long-lived Noachian to Amazonian tectonic activity in the Tharsis province has produced widespread extensional faulting (e. g. Mège & Masson, 1997; Scott et al., 2002; Wilson & Head III, 2002). The Alba Mons volcano, and its associated, extensive fossae systems, are perhaps the most obvious manifestation of this deformation, (e.g. Bouley et al., 2018; Wilson & Head III, 2002). The same extensive fault patterns, however, are not found surrounding other Tharsis volcanoes, such as Olympus Mons. In fact, the only exposed faulting close to Olympus Mons, and a handful of other Tharsis volcanoes, is found in the Ulysses Fossae area, east of the edifice (Figure 2.1b). Ulysses Fossae has been the target of only a few dedicated studies (Fernández & Ramírez-Caballero, 2019; Scott & Dohm, 1990), yet with the preservation of structures in this area holds the potential to unravel the complex deformation history surrounding some of the major Tharsis volcanoes (Figure 2.1b).

In this study we undertook an in-depth volcano-tectonic investigation of Ulysses Fossae to illuminate the complex deformation history of the region around the Olympus Mons volcano. We present detailed fault mapping at high spatial resolution, analysis of fault morphology and orientation, strain calculations, and new absolute model ages for geological units in Ulysses Fossae. We use these to present a history of faulting throughout the area, including tracing fault groups to their likely source. By determining, for the first time, the relative ages i.e. sequence, absolute ages, and character of faults in the Ulysses Fossae region, we are able to assess the influence and activity of the major volcanic centres in its vicinity—in particular, Olympus Mons, Pavonis Mons and Ulysses Patera.

2.1.1. The Ulysses Fossae Study Area

The heavily faulted terrain of Ulysses Fossae is located on the Tharsis Rise at 10°N, 123°W, covering 170,840 km^2. It is flanked by a number of large volcanoes, with Olympus Mons situated to the west, the three Tharsis Montes volcanoes to the southeast, and the Ulysses Patera and Biblis Patera volcanoes immediately to the south (Figure 2.1a).

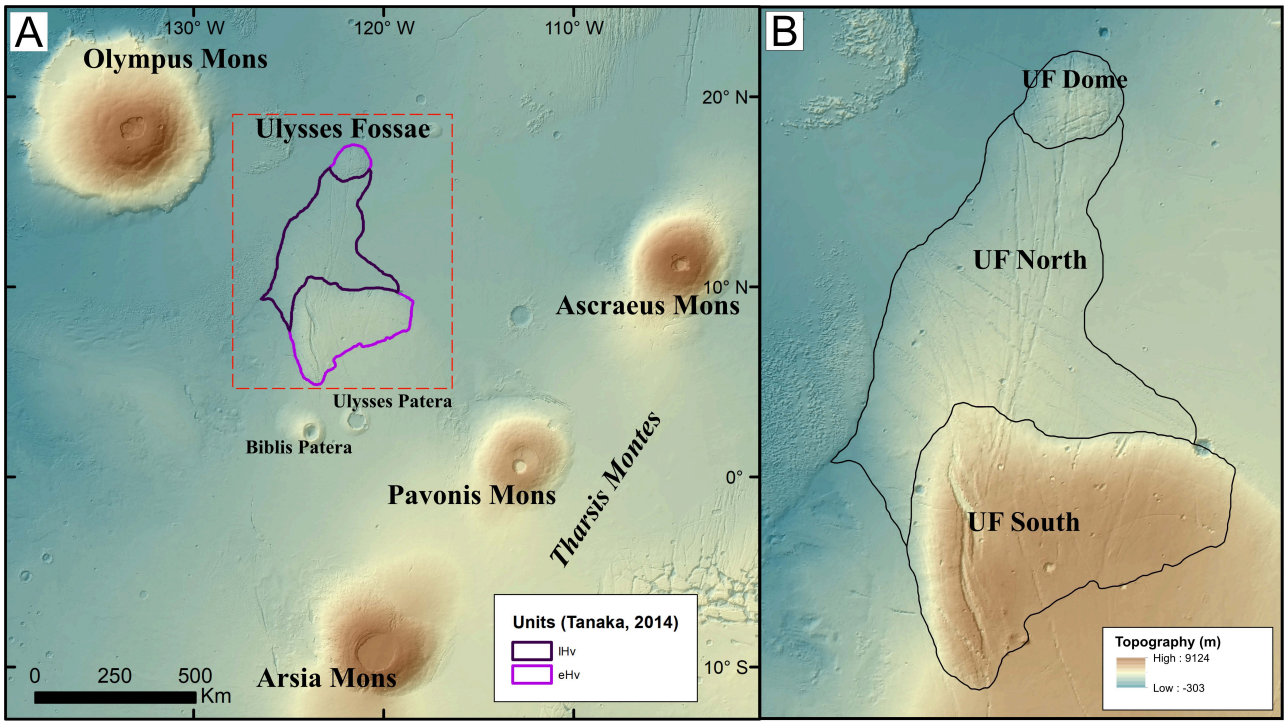

Figure 2.1: A) The location of the study area (Ulysses Fossae) and the surrounding Tharsis volcanoes. The central location of the study area in between the Tharsis volcanoes Olympus Mons, Pavonis Mons and Ulysses Patera is highlighted in a dashed red line. Note the delineation of Hesperian units lHv and eHv in purple and pink, as mapped by Tanaka et al. (2014). MOLA colorized Hillshade is used as background. B) Names for the 3 areas of Ulysses Fossae. The northern eHv unit is referred to as the "UF Dome", the lHv unit is "UF North" and the southern eHv unit is "UF South".

The geology of the region was initially mapped by Scott and Tanaka (1986) on Viking mission data, (130–300 m/pixel), and assigned to the units Hf, defined as "younger fractured material", and Nf, which is

"older fractured material". Crater size-frequency distribution calculations determined the age of the Hf unit to be Hesperian, between 3.0 and 3.7 Ga (Scott & Tanaka, 1986). In 2014 the units were remapped in a global Mars study by Tanaka et al. (2014), where two different geological units across three distinct areas were identified in Ulysses Fossae, which are the unit outlines used for this study. These units are eHv (early Hesperian) and lHv (late Hesperian), which are interpreted as undifferentiated lava, most likely from a flood lava or large volcanic lava flow (Tanaka et al., 2014). The northernmost section of Ulysses Fossae is characterized by a dome-like structure with a diameter of ~100 km (UF Dome, Figure 2.1b). Previous mapping by Scott and Tanaka (1986) described the dome as being highly deformed, older fractured terrain material, distinguishable from the younger southern terrain by a more highly faulted and fractured appearance (Scott & Dohm, 1990). In the Tanaka et al. (2014) mapping, the UF Dome is assigned unit eHv (Figure 2.1a). The second region of the eHv unit, as mapped by Tanaka et al. (2014), is to the south and hosts a large sigmoidal fault feature (UF South, Figure 2.1b). Between the two eHv units lies the late Hesperian lHv unit (UF North, Figure 2.1b), in which the main characteristic is the continuous linear normal faults crossing the terrain, without the more deformed structures apparent in the UF Dome.

The entire area of Ulysses Fossae, and in particular UF South, sits at a higher elevation than its surroundings (Figure 2.1b). This has spared Ulysses Fossae from some of the Amazonian lavas that have flooded the region, and the area has as a result been able to preserve any features which may have been covered on the rest of this region of Tharsis.

As mentioned, the sources of the faults within Ulysses Fossae have been investigated as a part of only two previous studies. A study by Scott and Dohm (1990) mapped the faults in Ulysses Fossae on Viking photomosaics at 1:2,000,000 scale and assigned their fault groups to proximal volcanoes based on their orientation and age. More recently, Fernández & Ramírez-Caballero (2019) performed a thorough investigation of the large, sigmoidal fault structure in the south of Ulysses Fossae, which they attributed to oblique rifting.

2.2. Methods and Data

2.2.1. Fault Mapping and Grouping

We mapped faults in Ulysses Fossae using images from the Context Camera (CTX) with a resolution of 6 m/pixel (Malin et al., 2007a), at a scale of ~1:250,000 to 1:100,000 in Esri ArcMap software (Figure 2.2a and 2.2b). The intention of the mapping was to capture each fault trend, and not to map every single feature. We used the unit boundaries as mapped by Tanaka et al. (2014) to define our study area and confined our fault mapping to these units. However, we captured the full length of a fault if it originated within a unit boundary but continued beyond. Fault length and strike orientation were calculated as geodesic lengths and geodesic azimuths with the Tools for Graphics and Shapes plugin for ArcGIS (Jenness, 2011). We also used the FracPaQ software package (Healy et al., 2017) to visualize fault strikes as rose diagrams. For the purposes of this study, we considered hard-linked faults as single continuous faults, whereas soft-linked faults (as defined by Polit et al. (2009)) are considered to be separate, unique faults. Any fault lengths and strikes are thus based on their mappable surface expression, and not on assumed subsurface linkage. Fault intensity is also visualized using FracPaQ where fault intensity (m^{-1}) is defined as the total length of a fault in a given area. The FracPaQ program generates a 2D grid of circular scan windows over the study area, and the mapped fault intensity is determined using the number of faults intersecting the perimeter of a scan circle (Healy et al., 2017). We use a scan circle diameter of ~13 km in order to have sufficient detail to capture the complexity of the faulting in the area, within the mapped scale. This chosen scan circle diameter produced the clearest overview of spatial intensity, and the subsequent FracPaQ produced map is used solely for visualization purposes.

Following the initial fault mapping, we assigned all the faults to groups. We based our initial grouping on similarity in strike orientation, as calculated and visualized in FracPaQ. These groupings were then subsequently refined by grouping faults with similar morphology and considering the cross-cutting relationships between faults (Figure 2.2c). This process ensured that each fault group represents a population of faults with a similar age and from a proposed similar origin.

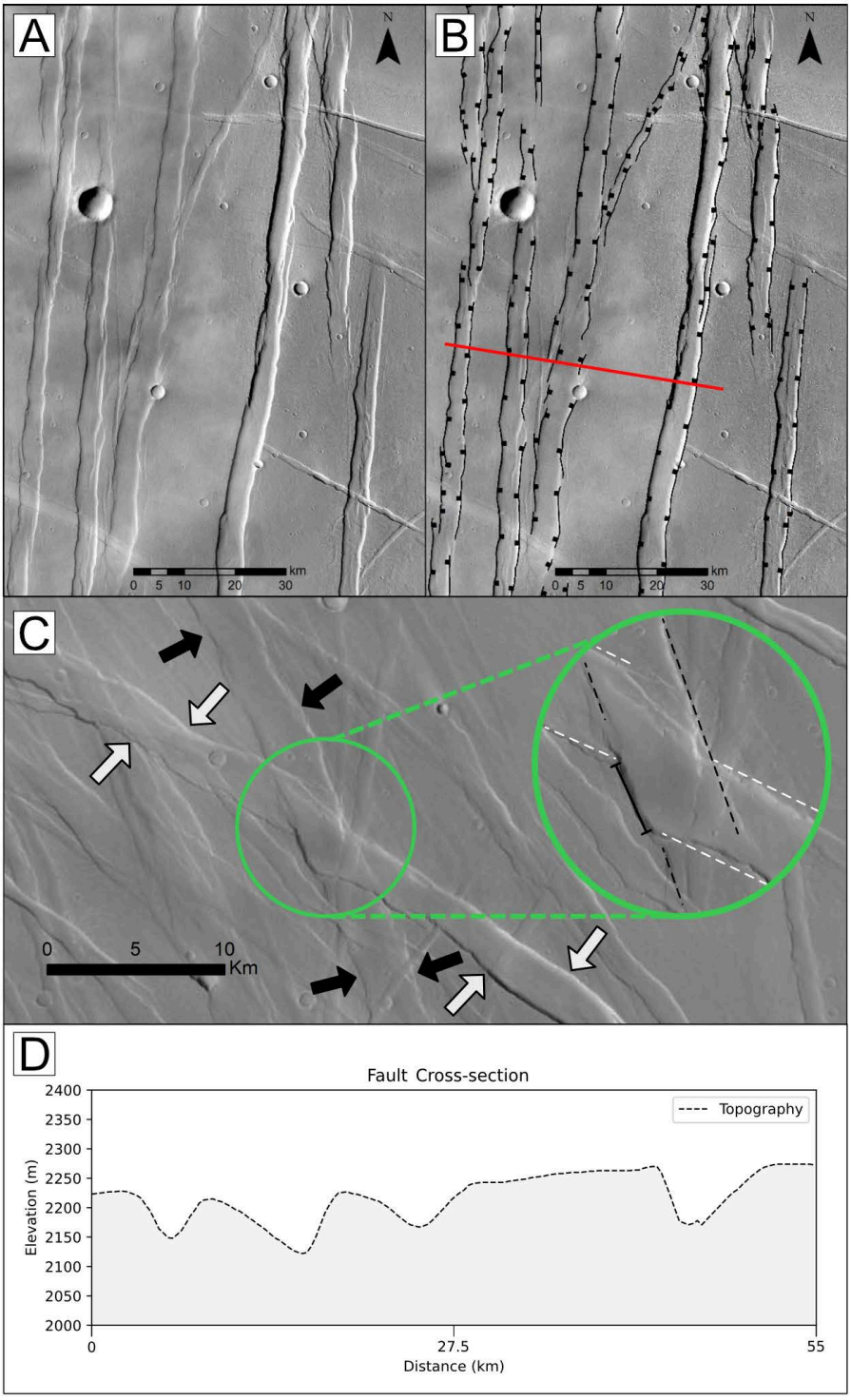

Figure 2.2: Fault mapping methodology examples. A, (unmapped) and B (mapped) show example of fault mapping, with B) showing a red line, representing the location for the cross-section in D. C) Example of relative age determination based on cross-cutting relationships. The NW-SE fault highlighted by white arrows is clearly offset (green circle) by the older faults, outlined by black arrows. Zoom in green circle highlights the displacement (black solid line). D) Example of cross-section of fault bounding grabens.

2.2.2. Chronological Sequence of Faulting

In order to establish the ages of the defined fault groups we first considered the relative ages between each fault group, and then their absolute ages. Relative ages of fault groups were determined as a function of their cross-cutting relationships, both to the geological units and to other fault groups. For example, where the path of a younger fault is kinked as a result of moving through a pre-existing, older fault (Figure 2.2c). For situations where two given fault groups did not appear to interact with each other, they were put into a relative chronological order based on their relationships to other fault groups as well as their morphology. The absolute ages of the faults were determined by their cross-cutting relationships with the geological units, which have ages assigned from our crater size-frequency distribution analysis (see Section 2.3.3). This provided a maximum age for the fault group that superposes the unit. If a fault group crossed multiple units with different ages, which was almost always the case, the youngest cross-cut unit age was assigned to the group.

2.2.3. Crater Size-Frequency Distribution Analysis

To further refine unit ages from the global-scale work of Tanaka et al. (2014), we undertook an independent crater size-frequency distribution analysis of the three Ulysses Fossae areas. We manually identified craters in CTX images and recorded their size and location using the Cratertools application in ArcMap (Kneissl et al., 2011). We only considered craters ≥1 km in diameter in our age analysis, in order to avoid the inclusion of secondary impact craters, which can artificially increase the model age (Werner et al., 2009). To ensure no 1 km craters were missed during mapping, we mapped craters down to ~800 m diameter but did not analyse craters <1 km. The Craterstats v.2 program (Michael, 2013; Michael & Neukum, 2010) was used to determine the absolute model age from crater statistics. In this study, we used the Hartmann and Daubar (2016) production function for Mars, along with the chronology function of Hartmann (2005), with the lower diameter boundary for our crater data set as 1 km. We used the differential plot type, 4^{th} root-2 binning, and a Poisson distribution fit for our statistical data (Michael et al., 2016).

2.2.4. Strain

To investigate the evolution of extension with time and further compare between fault groups, we measured the maximum finite strain for each fault group. We used topographic measurements taken from profiles (Figure 2.2d) through the blended global Digital Elevation Model (DEM) derived from the Mars Orbiter Laser Altimeter (MOLA) and High-Resolution Stereo Camera (HRSC) instruments

(Fergason et al., 2018). These elevation data have a vertical and horizontal resolution of 1 m/px and 463 m/pixel, respectively (Fergason et al., 2018).

We selected profile locations for each group so that each profile was oriented perpendicular to the main trend of the given fault group and positioned such that the profiles captured the highest fault density while avoiding craters and other non-fault structures. The number of profiles for each group was determined by the quality of the DEM data in the region covered by each group, to ensure each profile line could sufficiently resolve the mapped faults. See dataset S1 in the supplementary information for X,Y coordinates for the profiles. The topographic profiles were extracted from the HRSC-MOLA DEMs using QGIS software.

From the topographic profiles, we first calculated the extension by measuring the height of each fault scarp for the intersected graben-bounding faults, providing a throw (D_n) value. To convert throw into horizontal displacement, we assumed a 60° fault dip, consistent with Martian estimations for normal faults (e.g. Hauber & Kronberg, 2005; Polit et al., 2009). Figure 2.3b highlights an example of measuring the throw of the faults along a profile.

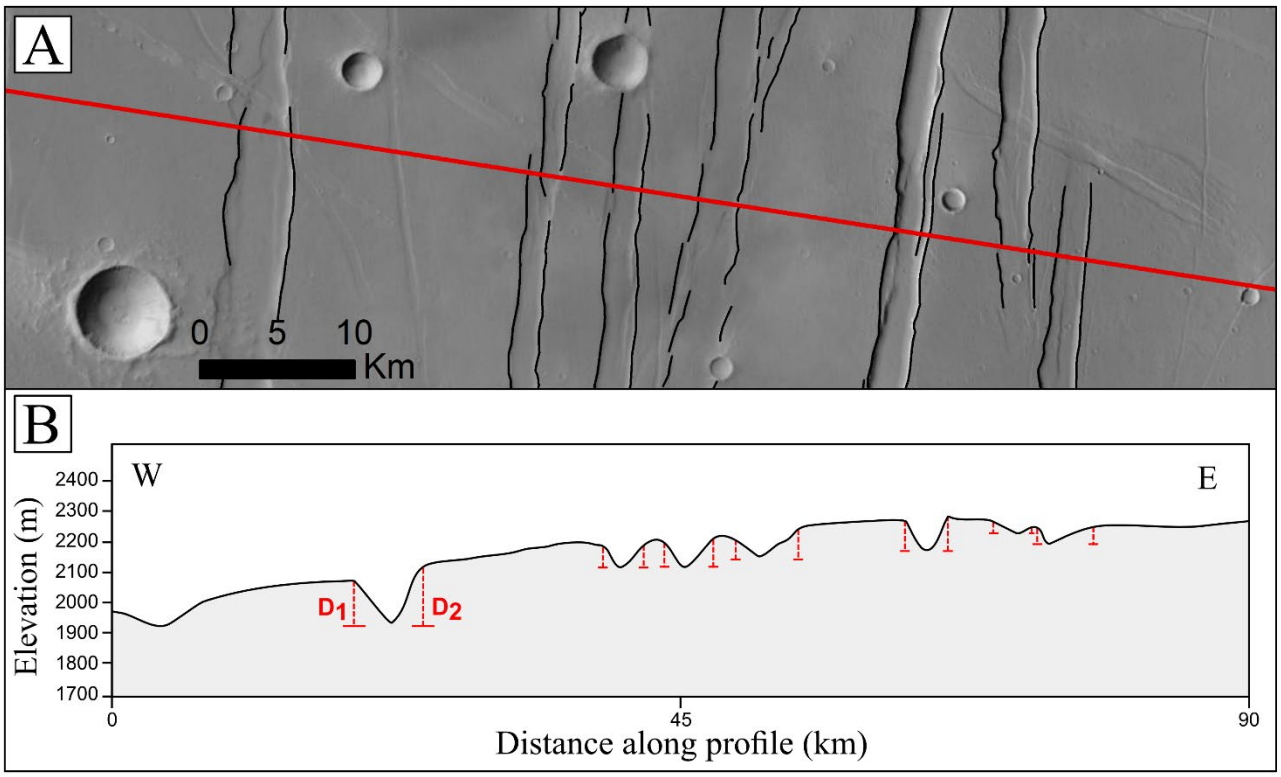

Figure 2.3: Examples of topographic measurements acquired for strain calculation. (A) Map view of faults in black, and the topographic profile location in red. (B) Example topographic profile created from the MOLA elevation data for Profile B, shown as the red line in (A). Example throw measurement approach are shown as red dotted lines on the elevation profile, and are labelled D1, D2.

Following the method by Hauber and Kronberg (2005), the cumulative extension along the mapped profiles for each fault population was calculated by:

$$e_{cum} = \frac{D_{cum}}{\tan \alpha}$$

where e_{cum} is the cumulated extension, a is the 60° fault dip and, D_{cum} is the sum of measured throws:

$$D_{cum} = D1 + D2 + \ldots + Dn$$

We then used the extension to estimate the amount of strain, ϵ, across each profile by relating the change in profile length (i.e., the extension) to the original pre-extension length by:

$$\epsilon = \frac{L_{final} - L_0}{L_0} = \frac{e_{cum}}{L_0}$$

where L_{final} is the measured length of the profile (after extension), which we determined by the shortest length that would capture as much faulting for each defined fault group as possible, and L_0 is the original length of the profile before extension:

$$L_0 = L_{final} - e_{cum}$$

Strain is a dimensionless value, so we multiply by 100 to get the strain percent value.

2.3. Results

2.3.1. Fault Mapping

We mapped a total of 5,115 faults across Ulysses Fossae, with a cumulative length of 32,253 km (Figure 2.4a). All of the faults are extensional normal faults, which are almost exclusively graben-forming. En échelon fault patterns are common, where grabens are composed of unconnected, discontinuous, but overlapping faults. This high degree of segmentation is reflected in the short average fault lengths (See supporting information Table A1 (Appendix A)), despite the fact that we observe long, continuous grabens. Spatially, the faulting is not distributed evenly, with regions of higher density in the north and through the centre of UF North (Figure 2.4). The faulting in the UF dome is an area of high fault intensity (Figure 2.4b), in that there is a larger variety of fault orientations concentrated in a small area, which are arranged in a tight cross-hatched pattern (Figure 2.4a). The faults in UF North (unit lHv) and UF South (unit eHv) (Figure 2.1b), are more widely spaced and form long, continuous grabens, which become sparse moving onto UF South. We observe two major fault orientation trends: N and NW. The N-S oriented faults appear larger, as their grabens are longer.

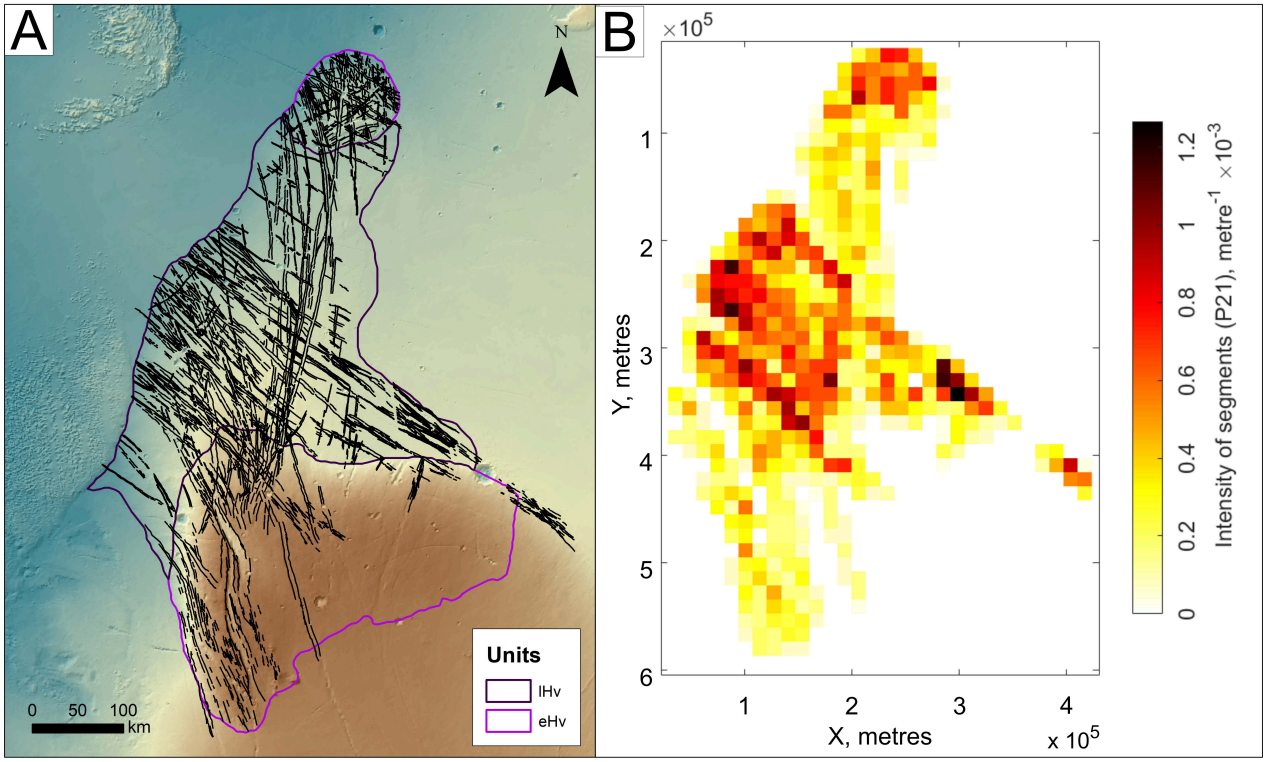

Figure 2.4: A) Mapped faults (black) in Ulysses Fossae on MOLA background. Units mapped as eHv (early Hesperian) are outlined in blue, and the unit mapped as lHv (late Hesperian) is outlined in purple. B) Fault intensity map of all mapped faults. Note the concentration of faults in UF Dome and the centre of UF North.

Using the previously described criteria, we identified 10 distinct fault groups within our mapped faults, and these were assigned the names G1 to G10 (Table A1), with G1 being oldest and G10 youngest. Faults in G1 (Table A1) trend NE and are contained within the UF Dome unit in Ulysses Fossae. Faults in G2, G3, and G5, show similar NNW orientation, and both groups G2 and G3 have slightly curved faults. Despite their similarities, the distance between the two patches of G2 and G3 warranted their separation. The faults in G4, crosscut all the previous four fault groups, making them the fifth oldest fault system in Ulysses Fossae (Table A1). G4 faults are present on all three Ulysses Fossae areas and are dominated by a largely N–S orientation, where all the faults lie within a range of 0°–20° (Figure 2.5). This fault group contains some of the longest grabens in the Ulysses Fossae system, where most have propagated along strike, compared to the faults in G2 and G3 which are more curved. Group G6 has a NNW-oriented fault population, and has sparse grabens spread over a large area (Figure 2.5). The faults making up G7 and G8 have very similar, yet discernibly different, orientations, striking noticeably NW. In both groups, the majority of the faults are located in UF North, with some presence in UF South. These are also the two most populous fault groups (Table A1), with the highest cumulative lengths of all fault groups. Faults in G9 have an average strike orientation of NE, and vary within 10-20°, from the faults in G1 (Figure

2.5), despite their difference in relative age. The final fault group, G10, trends NNW and consists mainly of the large sigmoidal grabens located in UF South. These larger grabens are also accompanied by other en échelon grabens to the east of the main structure (Figure 2.5). As mentioned, the majority of the mapped faults are purely extensional, however the G10 faults show changes in orientation with strike, accompanied by strike-slip components.

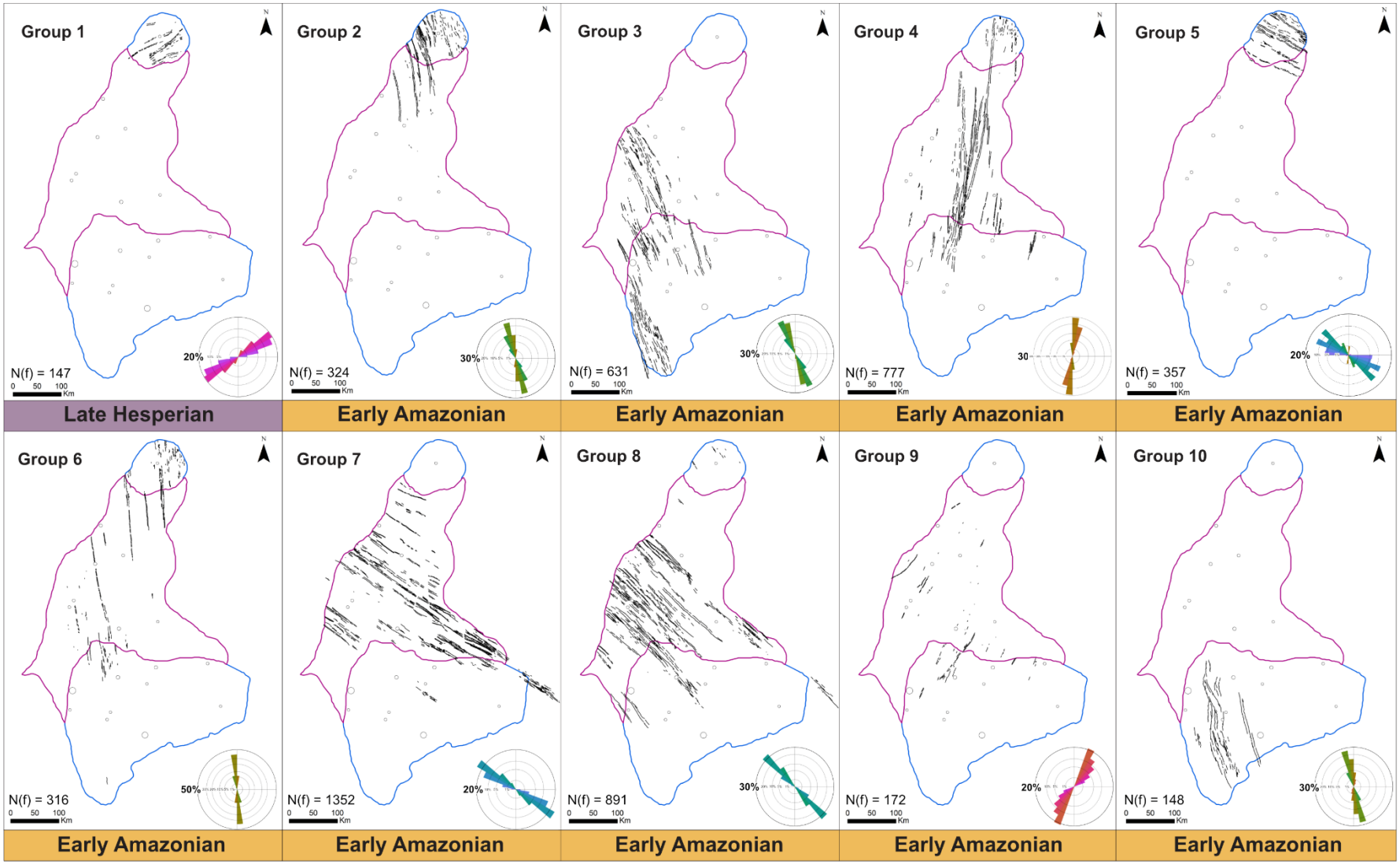

Figure 2.5: All mapped fault groups in Ulysses Fossae, with rose diagrams depicting the dominant strike orientation of each group. The groups are numbered by relative ages, with Group 1 being the oldest and Group 10 the youngest. The geological age along the bottom refers to the maximum age of the fault group based on the crater statistics derived absolute age from this study. N(f) describes number of faults in each group.

2.3.2. Crater Size-Frequency Distribution

We identified 265 craters with a diameter ≥ 1km, out of a total of 1,033 mapped craters. Based on the Hartmann (2005) chronology system, we calculated the absolute model ages for the three areas of Ulysses Fossae: UF Dome, UF North and UF South (Figure 2.1b), resulting in Late Hesperian and Early Amazonian ages for the three units (Table 2.1). An example of the Crater Size-Frequency Distribution plots is shown on Figure 2.6.

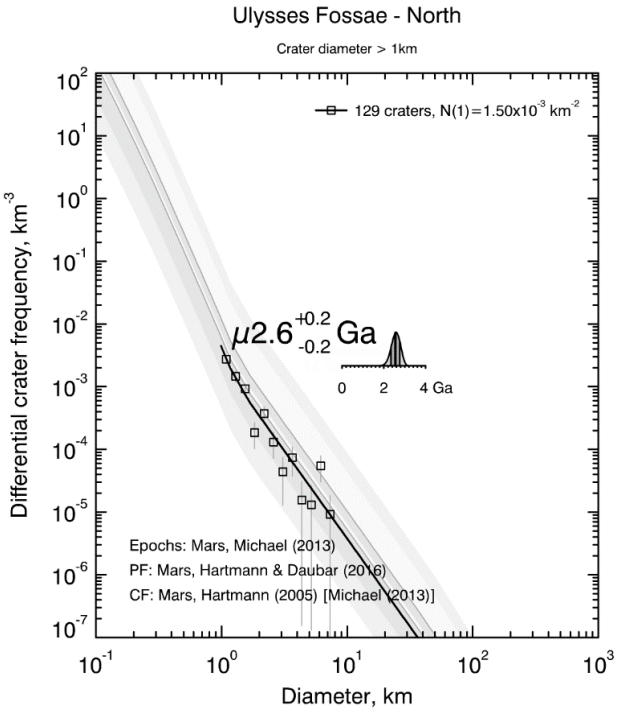

Figure 2.6: Crater Size-Frequency distribution (CSFD) plot for UF North, showing a best fit age of 2.6 Ga. See Supporting Figure A1 (Appendix A) for all 3 CSFD plots.

Area Name	Unit name	(N) Craters >1km	Unit age	Period
UF Dome	*Early Hesperian volcanic unit (eHv)*	29	3.4 +0.1/-0.3 Ga	Late Hesperian
UF North	*Late Hesperian volcanic unit (lHv)*	127	2.6 ± 0.2 Ga	Early Amazonian
UF South	*Early Hesperian volcanic unit (eHv)*	107	2.4 ± 0.2 Ga	Early Amazonian

Table 2.1: Ulysses Fossae absolute model ages. The unit age results for the three Ulysses Fossae areas (Figure 2.1B), using crater size-frequency distribution.

On the basis of our crater statistics analysis, we assign the UF Dome a Late Hesperian age of 3.4 Ga, making it the oldest in the study area. This is largely consistent with the unit age of Tanaka et al. (2014) for this area (Table 2.1). UF North and UF South are close in age and we place both units in the early Amazonian period, making them ~1 Ga younger than recognized in previously studies (Tanaka et al., 2014). Their 2.6 and 2.4 Ga ages are within uncertainty of each other, making them statistically indistinguishable. To determine their relative age, we therefore relied on assessment of the number of faults, craters, and surface structures in each. On this basis we assessed UF South as being the younger of the two units.

Closer study reveals the UF Dome area to have a more degraded appearance than UF South and UF North, with linear features generally appearing less crisp. UF Dome also has many cross-cutting fault directions, high fault intensity (Figure 2.4b), eroded features, and infilled grabens with smooth floors showing evidence of aeolian landforms formed from the infill material (Figure 2.7), all of which suggest a relatively older age for this unit. Faults with a pristine appearance that cross UF Dome belong to Early Amazonian fault groups (G2, G4, G5, and G6).

UF North and UF South differ from UF Dome in that their faults have a sharper appearance, and they lack the infill and other degraded features we see in UF Dome. The UF South unit appears the most pristine of the three areas, containing fewer craters and having a lower fault intensity (Figure 2.4b). This is evident when examining the southern extent of the mapped faults (G3–G9 on Figure 2.5), where there is a definite lack of fault traces in UF South.

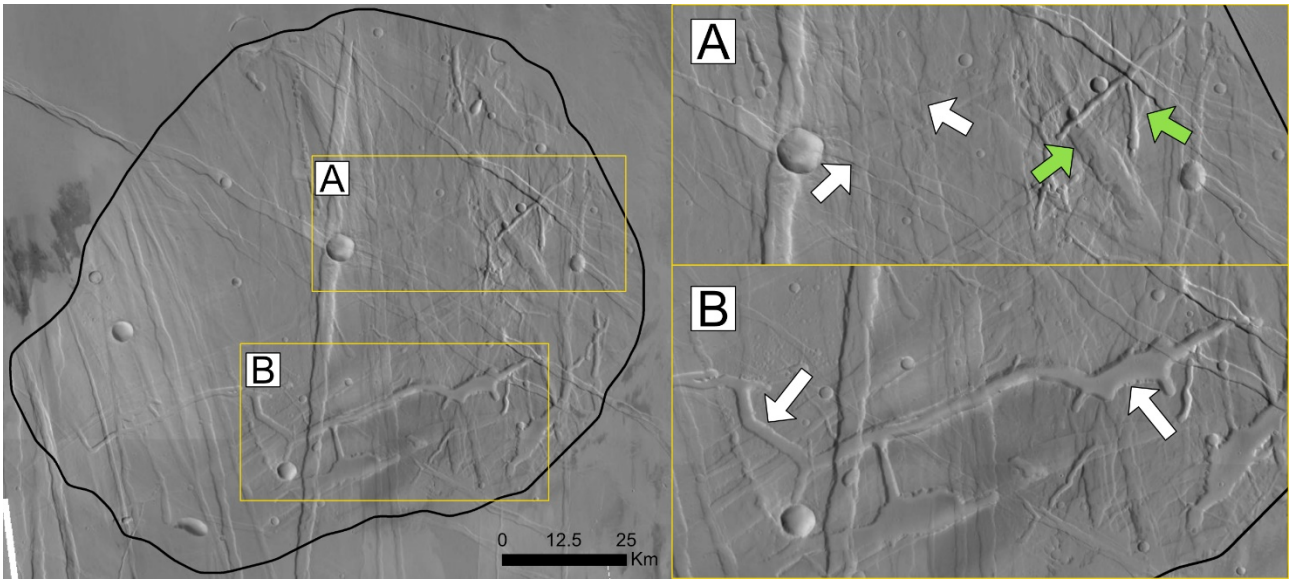

Figure 2.7: Zoom on the UF Dome in Ulysses Fossae. In Zoom A, the white arrows highlight faint fault traces, which compared to the rest of Ulysses Fossae suggests a combination of infill and erosion, hence the older age. The green arrows highlight an example of overlapping features, with faults, craters, and other altered circular features. Zoom B show an example of an eroded extensional structure, with a smooth graben floor, inferred as infilled.

From these absolute model ages, combined with relative ages determined by cross-cutting relationships, we placed the defined faults groups (Table S1) into chronological order (Figure 2.5). The vast majority of faulting (97.11%) occurs in the Early Amazonian, with only one group of Late Hesperian faults (G1). This Late Hesperian group is also NE-trending, which is not a common orientation in Ulysses Fossae.

2.3.3. Fault Group Sources

2.3.3.1. Fault Type Assignment

We assessed potential sources to the mapped fault groups using geometrical analysis. Our assigned sources fall into two categories: Regional and Local, based on the main influence on extension of the faults. In our study, fault groups were defined as *Regional* if the orientation of the faults fit the general N-S fault pattern corresponding to the E-W extensional stress expected from the isostatic development of the Tharsis Rise in this area (Carr, 1974; Melosh, 1980; Banerdt et al., 1982)).

Fault groups were classified as *Local* if the orientation of the faults did not align with the expected pattern for regional Tharsis activity (i.e., were not oriented N-S) or if their orientation could be traced back radially to a local volcanic centre. This pattern is especially obvious in cases where the faults fan outwards. We then used the orientation-based source of faulting, along with the ages of the fault groups, to define a series of stages encapsulating the volcano-tectonic evolution of Ulysses Fossae.

We identified two fault groups which fit our *Regional* criteria and we thus associate with Tharsis regional extensional stresses. These are groups G4 and G10, both of which trend primarily N-S, following the regional E-W extension. The slight curvature of faults in G4 can be attributed to an influence by local extensional stresses interacting with the regional stress field, with the Biblis Patera volcano as a possible centre of deformation.

We define six groups as having a *Local* source, with a radial relationship to a specific volcanic centre. These are groups G2, G3, G5, G6, G7, and G8, (Figure 2.8) making this the most common source of faults mapped in Ulysses Fossae. G2, G3 and G6 all have an approximately radial orientation to the southern Ulysses Patera volcano. However, in G2 and G3 some faults display slight curvature to the NW in the northern section of each group, suggesting influences from other local stress fields in this area. The faults in groups G5, G7 and G8 have a radial relationship to the three largest volcanoes in the area: Ascraeus Mons (G5), Olympus Mons (G7), and Pavonis Mons (G8).

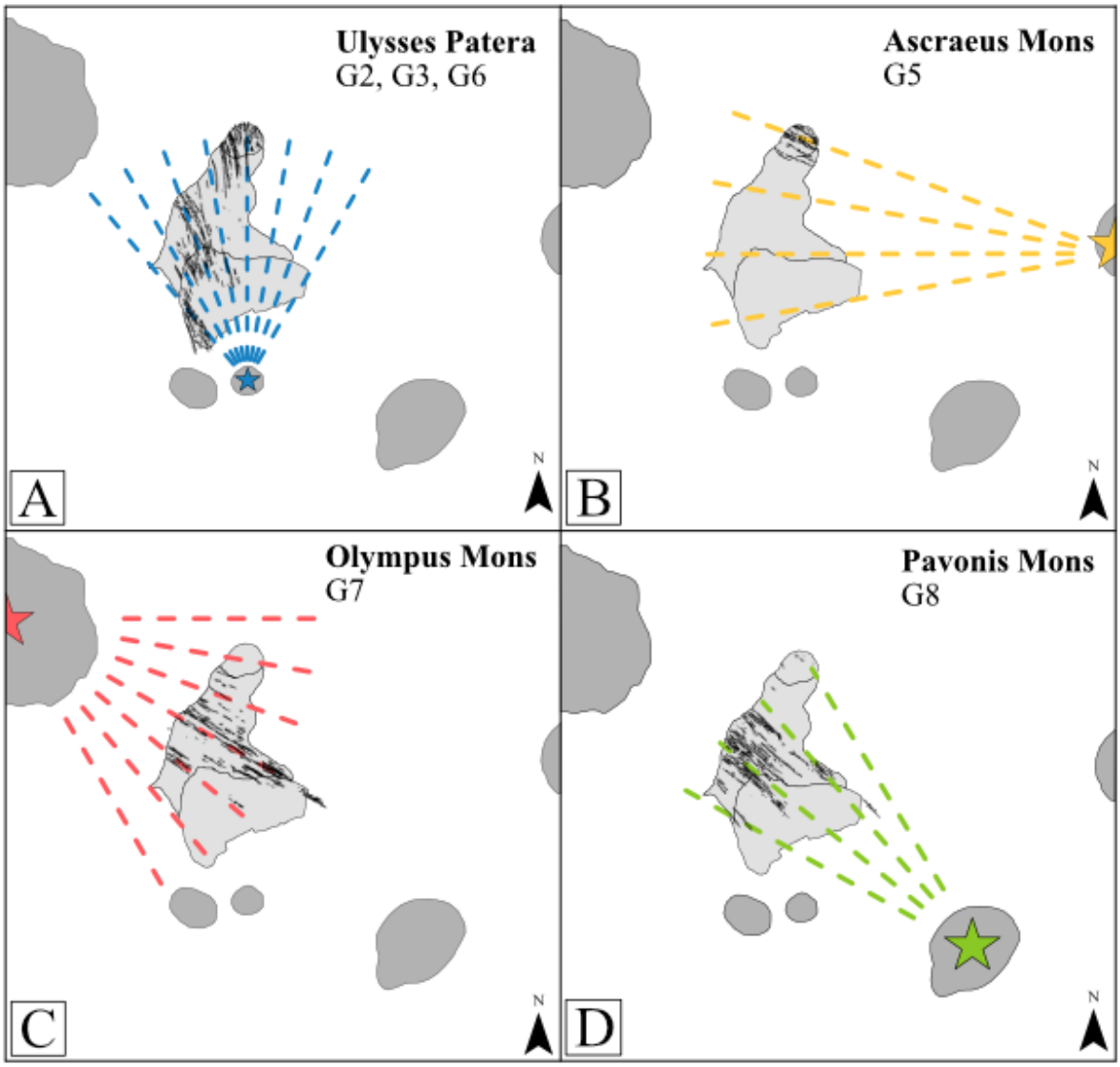

Figure 2.8: Mapped fault groups (black) with examples of radial orientations (dashed coloured lines) from a proximal volcanic centre (star) in Tharsis. A) Fault groups 2, 3 and 6 all lining up with the Ulysses Patera volcano to the south. B) Fault Group 5 lining up with radial orientations from Ascraeus Mons to the East. C) Fault Group 7 following the Olympus Mons radial orientations, and D), Group 8 faults following a radial orientation back to the Pavonis Mons volcano. Unit outlines from Tanaka (2014).

It is worth noting that the orientation of the faults in Groups 1 and 9 on average follow the NE axial trend of the three Tharsis Montes volcanoes (~650 km SE from UF) and the NNE Tempe Terra faulted terrain (1,800 km NE of UF). The definite reason for this apparent axial linear alignment of the volcanoes and Tempe Terra remains unknown, though many studies have hypothesized processes which could control the linear trend. Suggestions include mechanisms such as ancient subduction zones (Tanaka, 1990b; Sleep, 1994), impact basin-rim volcanism (Schultz, 1984) or migrating mantle plumes (Leone et al., 2022). The most broadly acknowledged model, however, consists of fracturing along a zone of weakness (Hauber et al., 2011; Wise et al., 1979), allowing magma to rise to the surface more easily.

As the Group 1 and 9 faults mapped in this study follow a similar orientation to the Tharsis Montes linear trend, this could suggest that the origin of the extension is similar to that determining the orientation of the Tharsis Montes. Though the G1 and G9 faults are located far from the axis, the comparatively small size of the faults could reflect the far-field stresses of the process. Temporally, the G1 and G9 faults are dated to the Early Amazonian, and while the construction of the Tharsis Montes began in Early Noachian, the most recent edifice ages are dated to the Amazonian (Robbins et al., 2011). This later activity is aligned with the shift from the initial widespread volcanism in the Tharsis volcanic province, to more mantle plume-driven formation of the younger, larger volcanoes in Tharsis (Orlov et al., 2023). This means that temporally, the G1 and G9 faults could be related to the forces which aligned the Tharsis Montes, however since the process(es) responsible for the Tharsis Montes alignment and associated extension are still disputed, the exact controlling mechanism for G1 and G9 remains a subject for further studies.

The faults in groups G1 and G9 are thus difficult to unambiguously assign within our classification system, as they have limited spread and do not fully fit the criteria of either source. While neither G1 nor G9 have an obviously radial relationship to any of the surrounding large volcanoes, they can potentially be attributed to the Jovis Tholus volcano, located ~200 km to the NNE of the UF Dome. We thus tentatively assign them as *Local*.

2.3.4. Strain Measurements

In Table 2.2, we show an example of the values used in strain calculations for the faults in Group 5 (See Supplementary Table A.2 for all calculations (Appendix A)). The strain percentage results for each fault group are given in Table 3; we were unable to estimate strain amounts for G5 and G9 as the MOLA-HRSC data for those structures were insufficient in resolving all the faults. The strain percent for the fault groups range from a minimum of 0.28% for G6 and a maximum of 2.20% for G10 (Table 2.3). See Supporting Figure A2 (Appendix A) for the location of the profiles used to determine strain.

	D_{cum}	e_{cum}	L_0 (m)	L_{final} (m)	ϵ	%
Profile A	859	495.9	98204	98699	0.005	0.51
Profile B	1086	627.0	90847	91474	0.007	0.69
Profile C	991	572.2	71537	72109	0.008	0.80
Profile D	561	323.9	51644	51968	0.006	0.63
Group 5 average strain %						0.66

Table 2.3: Strain amounts for each measurable fault group (G1–G10). All values are percentages. The number of profiles for each group was determined by the quality of data for their location. Group 5 and 9 yielded no usable topographic profiles.

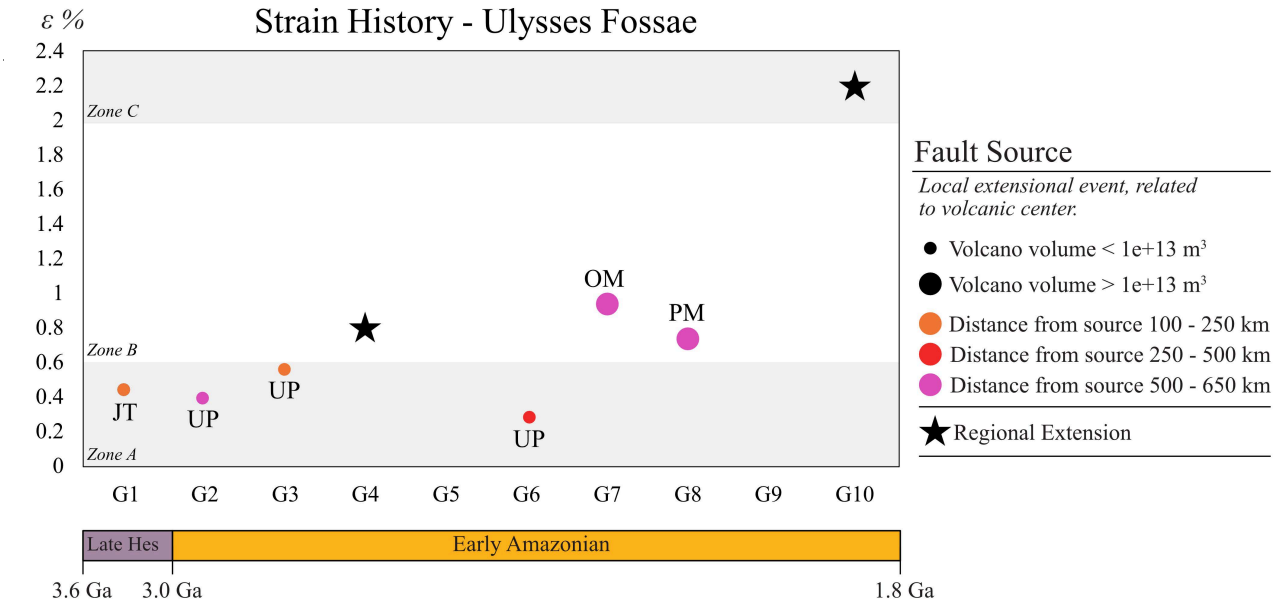

Figure 2.9: Summary of maximum estimated strain values for the different mapped fault groups through time, along with a circle or star symbol indicating their formation mechanism. No values measured for G5 and G9. Letters above or below a circle refers to the "local volcano" the faults are radial to: JT = Jovis Tholus, UP = Ulysses Patera, OM = Olympus Mons, PM = Pavonis Mons. Distance from source is determined from the centre of the volcanic structure, to the closest fault of the designated group.

Figure 2.9 shows the maximum strain value for each mapped fault group (Table 2.3) through time, along with the assigned origin for the fault group. The size of the volcano for the local fault groups (black circles in Figure 2.9) is also considered. Using this plot, we separate the fault groups into three zones (grey blocks on Fig 2.9), based on data grouping. The first zone, Zone A, consists of fault groups with strain values below 0.6%, all of which have a radial orientation to the smaller Tharsis volcanoes Ulysses Patera and Jovis Tholus. In Zone B, the strain values range between 0.6-2.0%. This zone consists of one fault group (G4) related to regional extension, and two fault groups related to local sources, with faults radially related to the largest volcanoes, Olympus Mons and Pavonis Mons. These three fault groups have the highest measured cumulative lengths. Zone C contains just one fault group (G10), which is the youngest and has the highest strain. G10 peaks at 2.2% strain, more than double the subsequent highest value of 0.94% (G7) and is related to the regional extension of Tharsis.

If all the fault groups are considered together, there is no clear trend in the amount of strain through time. However, by assessing the local and regional groups separately, some discernible trends appear. For the "locally" sourced groups, we see a change through time from faults linked to smaller, older volcanoes

to faults associated with larger, younger volcanoes, with a corresponding increase in strain. While we only have two groups to compare, the regional fault groups also show an increase in strain through time.

2.4. Discussion

2.4.1. Ages

We found our geological unit ages to be generally younger than those assigned by Tanaka et al. (2014) (Table 2.4) in their global study, and the similar Hesperian 3.5 Ga age for UF South determined by Fernández and Ramírez-Caballero (2019). For the UF Dome, our Late Hesperian age agrees with Tanaka et al. (2014), but our numerical age is slightly younger than theirs, although within uncertainty range (Table 2.44). We assign both UF North and UF South as Early Amazonian, ~1 Ga younger than the Hesperian ages from Tanaka et al. (2014) for both units (Table 2.4). Our results indicate that the youngest unit in Ulysses Fossae is UF South, while in the Tanaka et al. (2014) map this was UF North. These differences are likely due to the previous ages being a part of a global-scale study while our work is confined to Ulysses Fossae, which allows for greater, more location-specific detail.

Area name	Unit name	Unit age (2014)	Unit age (2022)	Old period (2014)	New period (2022)
UF Dome	*Early Hesperian volcanic unit (eHv)*	3.65 Ga	3.4 +0.1/-0.3 Ga	Early Hesperian	Late Hesperian
UF North	*Late Hesperian volcanic unit (lHv)*	3.55 Ga	2.6 ± 0.2 Ga	Late Hesperian	Early Amazonian
UF South	*Early Hesperian volcanic unit (eHv)*	3.65 Ga	2.4 ± 0.2 Ga	Late Hesperian	Early Amazonian

Table 2.4: Comparison of Tanaka et al. (2014) ages and this study's (2022) new cratercount ages for the three mapped Ulysses Fossae areas UF Dome, UF North and UF South (Figure 2.1b). Note the younger ages for areas UF North and UF South.

Comparing our results to the Fernández and Ramírez-Caballero (2019) study of UF South, we use a similar method of only using crater diameters >1 km and are focusing only on the local ages of Ulysses Fossae. Despite the method similarities, we produce an age which is ~1 Ga younger. This is likely due to the Hartmann (2005) chronology system, where the production function curves for 1 Ga and 3.5 Ga plot very close to each other. This means that the resulting model age is largely affected by even small variations in counted crater frequency, where variations can be caused by differences in image quality, methods and algorithms used in identifying, counting, measuring, and calculating the statistical outcome.

Our crater-statistics based ages are further supported by the fault and unit morphology of each area, where our results highlighted that UF dome appears morphologically older, and UF South appears more pristine and thus younger, fitting the model ages.

A possible explanation for the younger age of UF South determined in this study, lies in an examination of the bounds of the unit defined by Tanaka et al. (2014) (Figure 2.1b). Within this area, the topography reveals a local high in the terrain (Figure 2.1b) which continues further south, outside of the mapped Tanaka et al. (2014) borders. Given the rounded, lobate edges to the outline of this topographic high, and its proximity to the surrounding volcanoes, we interpret this feature as an Amazonian lava flow likely sourced from one of the surrounding Tharsis Montes, most likely Pavonis or Arsia Mons, based on the flow-lobe orientation. This suggests Ulysses Fossae experienced an Amazonian resurfacing event. This is further supported by the lack of fault traces and craters within the boundaries of the topographic high in UF South. This resurfacing event potentially covered some of the southern extent of the faults in G1–G9. Following this resurfacing event, another period of extension occurred and produced faults in G10 on top of the younger lava. This interpretation suggests that the crater statistics-derived 2.4 Ga model age for UF South in part reflects a resurfacing event, resulting in a younger age of the unit. This also implies that the current southern border of UF South is inaccurate, and that Ulysses Fossae does not have a defined southern border in the area, and is instead part of a larger, younger Amazonian unit which extends southwards. Figure 2.10 illustrates this suggested evolution of the UF South region.

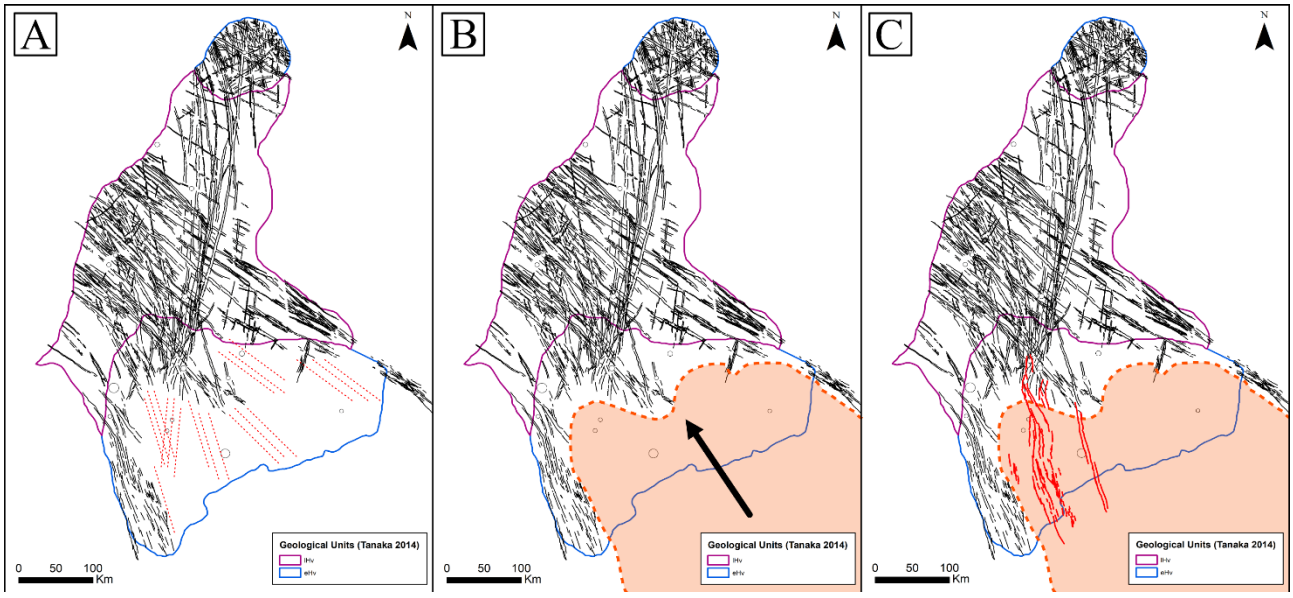

Figure 2.10: A) In black are the mapped "original" traces of the faults in Groups 1–9. Dashed red lines show inferred further continuation of the mapped fault traces, when the faulting originally occurred. B) An Amazonian resurfacing event, involving lava covering the southern section of Ulysses Fossae, as well as potentially covering some fault traces (the dashed red lines from A). C) The youngest mapped faults from Group 10 in Ulysses Fossae become active, and the faulting occurred on the more recently emplaced lava.

2.4.2. Sources of Fault Trends in Ulysses Fossae

The faults of Ulysses Fossae reflect a long period of varied extensional activity from a combination of local and regional sources. As mentioned, the N-S regional fault orientation pattern is attributed to isostasy in the first phase of Tharsis' evolution (Banerdt et al., 1982). This has implications as our results presents traces of this mechanism in the early Amazonian, suggesting either a more recent reactivation of the isostasy, which is unlikely to be confined only to the Ulysses Fossae area, or a secondary extensional event, which lead the faulting to follow any remnant N-S traces underlying the Amazonian and late Hesperian units.

Faults with radial orientations on Mars have previously been interpreted as the surface expression of dikes which terminated before reaching the surface (Mège & Masson, 1997; Scott et al., 2002). It is inferred that the dikes are controlled by the same deep magma source responsible for the origin of the Tharsis volcanoes (E.g. Cailleau et al., 2005; Dohm et al., 2007), based on their radial orientation to these volcanic centres. We attribute fault groups G1-G3 and G5-G9 as having faulting initiated by radially propagating dikes from local Tharsis volcanoes. Radial extension alone without igneous input, as part of volcano edifice growth, is unlikely as a source of the radial faulting, due to the large distance (100-800 km) between the mapped faults and the inferred radial centres. Examples of radial diking have been observed on other terrestrial planets, such as Venus and Earth, in addition to other locations on Mars, where dikes have radiated out from a volcanic centre (e.g. Cailleau et al., 2005; Grosfils & Head, 1994; Paquet et al., 2007). Both the Martian and Venusian radial diking have evidence of surface faulting, with normal faults creating grabens above the dikes. Multiple studies have linked the formation of radial faults surrounding volcanic centres to the propagation of dikes on both Venus (Ernst et al., 2001; Grosfils & Head, 1994) and Mars (Bouley et al., 2018; Cailleau et al., 2003; Mège & Masson, 1996; Mège et al., 2003; Scott et al., 2002; Wilson & Head III, 2002). The Venusian radial dikes are distinctive as the planet's consistent surface ages makes it possible to trace the laterally–extensive, dike-induced faults for several kilometres from the centre of magma supply (Grosfils & Head, 1994).

On Mars, radial grabens originating from a volcanic centre are inferred to be the surface manifestation of mantle plume-related dike intrusion complexes (Bouley et al., 2018; Schultz et al., 2004). Figure 2.11b show a cross-section along the dotted red line in Figure 2.11a and shows idealized example of a magma leading to a radial dike pattern, which are characteristically considered to flow upwards above the melting source, at which point the orientation changes, and the magma will then expand laterally toward outer regions (Mège et al., 2003; Poland et al., 2008). In instances where the least compressive stress ($\sigma 3$) is

circular surrounding a volcanic centre, such as during magma upwelling, dikes will form in a radial pattern, orthogonal to the σ3 stress orientations (Park, 2000) (Figure 2.11a).

In some instances, an upwards-propagating dike will not reach the surface, but the tensile stress generated by the now-arrested dike tip can initiate fractures, which can develop into normal faulting on the surface (Figure 2.11c and 2.11d) (Ernst et al., 2001; Gudmundsson, 2020; Mège & Masson, 1996). It is, however, the consensus that on Earth, dikes alone do not generate extensive surface faulting, such as that observed on Mars and Venus, so that dike-induced deformation has to occur in tandem with regional-scale crustal tension (Gudmundsson, 2020). This scenario is also possible on Mars for regions such as Tharsis, which have local volcanic diking sources superposed on a significant regional stress field. Consequently, the distribution of extensional faults in the Tharsis region can be treated as stress-trajectory maps (Figure 2.8), which can be traced back to their source volcano based on a plume tectonics model (Mège & Masson, 1996).

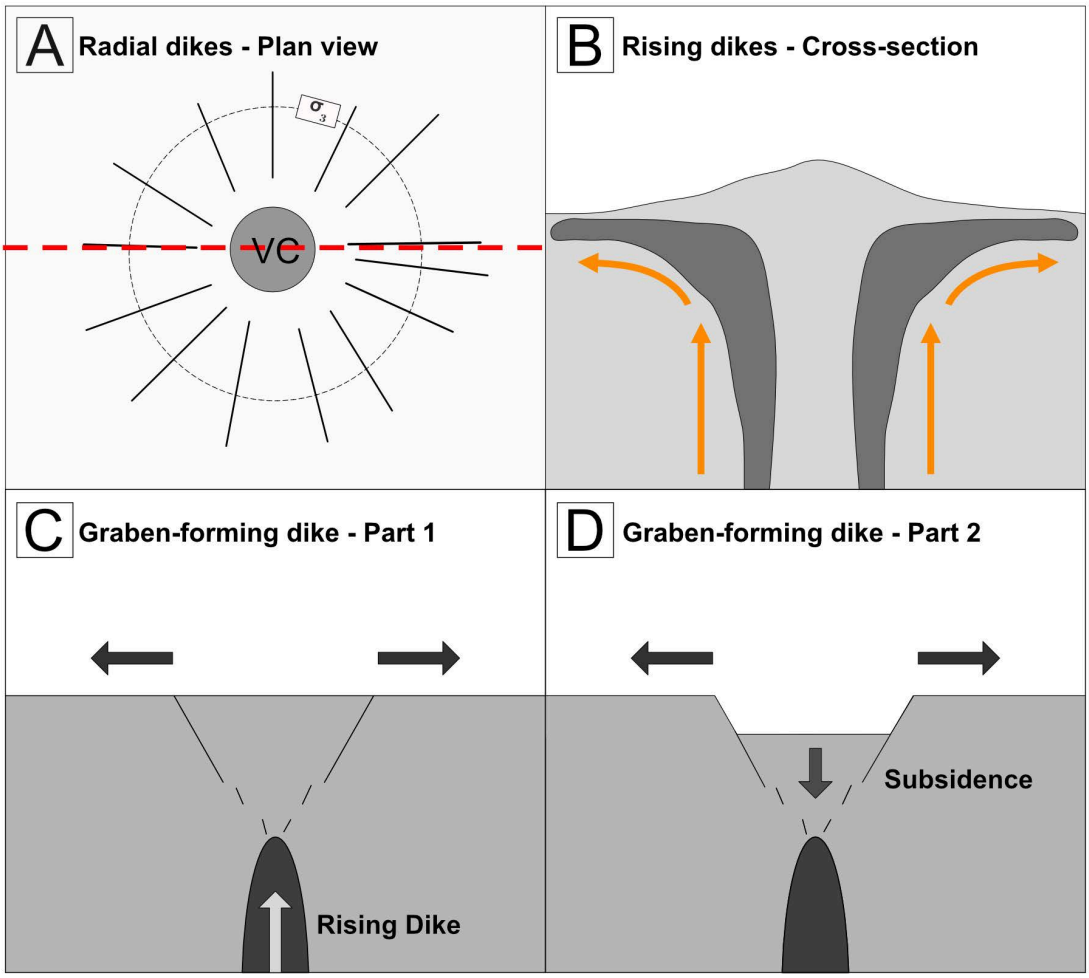

Figure 2.11: Example of radial diking with a volcanic centre. A) Plane view of radial diking from Volcanic Centre (VC). Red dashed line indicates the location of the cross-section in B), with σ_3 orientation labelled. Modified from Park (2000). B) Cross-section from A, of upwelling magma from a deep source, forming a radial orientation of dikes from the central volcano. Orange arrows indicate development of magma flow orientation. C) Part 1 of dike rising producing grabens. The rising dike produces fractures and faults, enabling the formation of grabens. D) Part 2 of the graben formation, where the material displacement from the rising dike has allowed a graben to form above the now stalled dike.

The faults mapped in this study represent a complex system where radial diking appears to be the main driver of faulting in Ulysses Fossae. As very little older material (Hesperian and Noachian) is preserved in the area, it is not surprising that the majority of tectonic activity recorded in the faults of Ulysses Fossae are related to Amazonian volcanism, and that we have minimal evidence of older, large-scale events. However, it is important to note that our attribution of fault groups as being primarily sourced from either regional extension or local dike emplacement, does not exclude the interaction of these two sources or the influence of other sources of stress. It is in fact very likely that the local and regional processes interact, particularly in cases where faulting from regional extension is influenced by diking originating from the Tharsis volcanoes, such as fault group G4. This process is also seen on Earth in the Afar rift, where dike intrusion influences an area undergoing regional extension (Calais et al., 2008), resulting in oblique fault structures (La Rosa et al., 2019).

2.4.2.1. Oblique Faulting

The faults of G10 are attributed to regional extension and largely follow an overall N-S trend. They have a unique geometry among the Ulysses Fossae faults, that reflects the influence of additional mechanisms in their development. Specifically, the curved and sigmoidal morphology of the G10 faults indicates oblique faulting processes, with signs of simultaneous strike-slip and dip-slip movement. This distinct shape of the faults in G10 is interpreted to be a result of the influence of older fault patterns in Ulysses Fossae which are reactivated during later faulting. The large size of the graben indicates large-scale regional extension, with the N-S orientation of the faults allowing for a partial reactivation of the previously established fault patterns of G3 and G4, creating the distinctive sigmoidal shape for the largest faults in the population (Figure 2.5). The extension for the G10 faults is therefore not purely orthogonal to the N-S general extension, reflecting the transtensional kinematics in UF South, similar to the interpretations of Fernández and Ramírez-Caballero (2009). The difference in elevation between UF North and UF South suggests a lava flow with a maximum thickness of ~2 km, which has allowed the extensional event for G10, to follow the patterns of G3 and G4 under the lava (Figure 2.12).

This may also be why we detect some traces of G3 and G4 faults on top of the thinner edges of UF South. The strain values calculated for G10 are significantly larger than the other groups, with a maximum strain of 2.2% (Table 3). This higher strain reflects the greater extension accommodated by the large grabens, which is potentially aided by the pre-existing structural weaknesses from the previous fault trends (Figure 2.12).

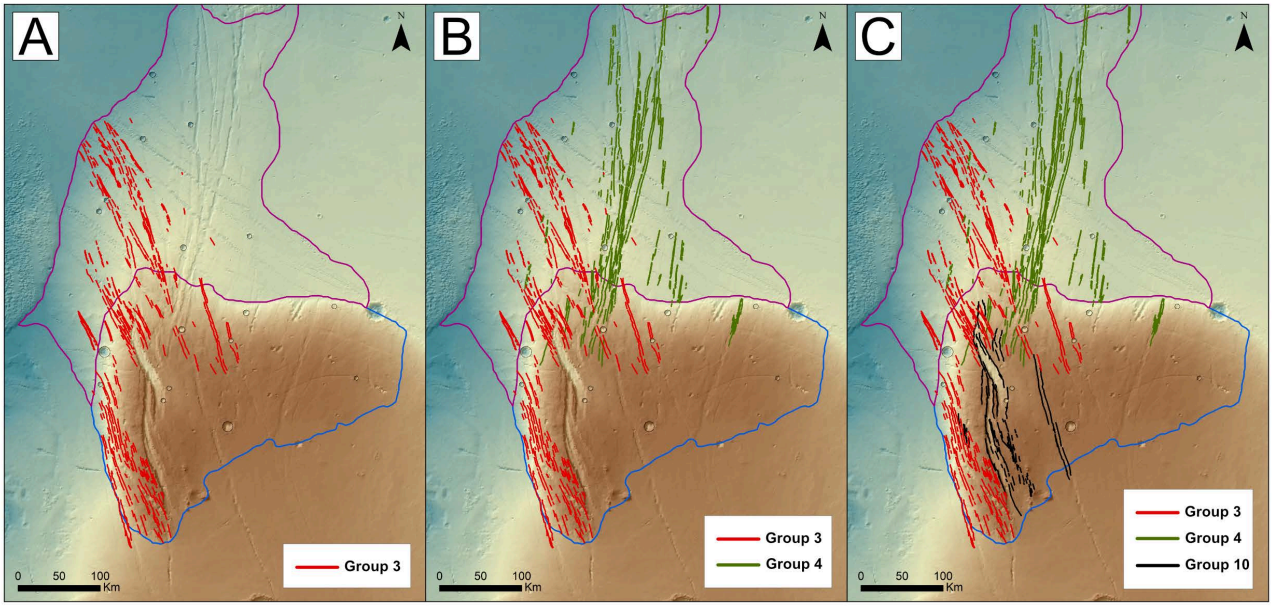

Figure 2.12: Group 3 and Group 4 faults, which influenced the orientation of the Group 10 faults, during their evolution. A) shows the oldest activity of the 2 fault groups influencing the orientation of Group 10, with Group 3 being active in the Early Amazonian. Following that in B), the faults in Group 4 become active, due to regional Tharsis extension. Finally in C) a regional E-W extension event becomes active in the southern part of Ulysses Fossae, but the pre-existing fabric of the faults from Groups 3 and 4, influences a partial reactivation of the faults, resulting in the faults in Group 10 creating a sigmoidal pattern, and not the N-S oriented faults that are expected.

It is important to note that the overall N-S Tharsis extensional trend, determined by Banerdt et al. (1982), has likely varied in orientations through time, and through the Tharsis structure. A kinematic analysis was performed on UF South faults in Fernández and Ramírez-Caballero (2019), where they determined a regional extension of NE-SW, with important local variations from E-W to NNE-SSW. This is in accordance with our interpretations of the G10 faults as a reactivation and oblique tectonic structure and is further observed in the mapped en échelon structures in Ulysses Fossae, which hints at slight stress orientation changes through the development of the faults.

2.4.3. Structural Evolution of Ulysses Fossae

Combining the fault groups, ages, and sources together, we here present an overview of the main events in the structural evolution of Ulysses Fossae, as recorded in the mapped faults and unit ages and morphology.

Stage I: Late Hesperian

The first recorded stage in Ulysses Fossae is dominated by a single event, a local NW-SE extension, potentially related to diking activity from the Jovis Tholus volcano, which produced faults in G1. These faults are exclusive to the UF Dome.

Stage II: Early Amazonian, local extension 1

The early Amazonian units in UF North, and presumably underneath UF South, were deposited, leaving the only traces of G1 preserved in the elevated UF Dome. This was followed by activity from several local volcanic centres. Diking from Ulysses Patera initiated faulting in G2 and again in G3, potentially in the presence of another local or regional stress field, resulting in the slightly curved faulting.

Stage III: Early Amazonian, regional extension.

Regional E-W extension followed this period of local events, and potentially interacted with structural weaknesses related to Biblis Patera to create the faults in G4.

Stage IV: Early Amazonian, local extension 2

The fourth stage of faulting in Ulysses Fossae is also contained within the early Amazonian and represents the main period of recorded faulting. Faults from this stage are radial to proximal volcanic centres, reflecting diking activity associated with various local volcanoes.

First, dikes from Ascraeus Mons produced the G5 faults, followed by the final activity related to Ulysses Patera diking forming the faults in G6. Following this, Olympus Mons produced radial dikes which created the faults in G7. Finally, diking activity from Pavonis Mons initiated the faults in G8. The measured strain from this period reflects the fact that the two biggest volcanoes were active (Figure 2.9).

Stage V: Early Amazonian, local extension 3

An extensional event, potentially related to diking from Jovis Tholus, produced the scattered faults of G9. This was followed by a series of lava flows which surrounded Ulysses Fossae, defining the north, east and western outlines of the UF Dome and UF North units. These flows were likely sourced from

Olympus Mons to the west, and along the eastern boundary, by regional fissure and vent systems (Tanaka et al., 2014), and as a result cover any faults which may have extended beyond the current unit boundaries.

Stage VI: Early Amazonian extension and reactivation

Another early Amazonian lava flow covers the area, this time from the south, covering any pre-existing faults. This flow was likely sourced from one of the Tharsis Montes. A regional E-W extension event facilitated the initiation of the G10 faults, which reactivated paths of faults from G3 and G4, creating a large oblique fault structure in UF South.

2.4.4. Ulysses Fossae and Tharsis development

Assuming the edifice age of the volcano to be the most recent activity of the volcano, an early Amazonian age for diking related to Olympus Mons, Pavonis Mons, and Ascraeus Mons is consistent with previous mapping of the area (Tanaka et al., 2014), which assigns an Amazonian age to each edifice. For the smaller volcanoes Ulysses Patera, Biblis Patera and Jovis Tholus, the Amazonian activity is more surprising, as their most recent surface activity is attributed to the Hesperian (Tanaka et al., 2014), though a more focused study on the volcanoes themselves has determined Amazonian ages for the Ulysses Patera's caldera, indicating more recent activity (Robbins et al., 2011). However, disregarding the volcanic edifice itself, a recent study by Richardson et al. (2021), linked a number of observed volcanic vents in Tharsis to the surrounding volcanoes, determining that the Ulysses Fossae magma system may have been active as recent as the Early-Late Amazonian (Richardson et al., 2021), validating the Amazonian ages determined in our study.

Despite 5 of our stages occurring during the Early Amazonian, we are not suggesting a contemporaneous formation of all the fault groups during that time. The fault stages are interpreted as sequential events on the basis of the different group orientations, which indicate changes in the primary stress orientations, and the numerous clear cross-cutting relationships, which indicate separate events.

The complexity of the subsurface magmatic systems related to the nearby Tharsis volcanoes, which is recorded in the variously oriented faults in Ulysses Fossae, makes it difficult to distinguish specific events within the larger scheme of the evolution of the Tharsis volcanic province. This is particularly challenging in Ulysses Fossae as most of the faulting events take place during the Amazonian, during the fifth stage of activity of the Tharsis Superplume (Dohm et al., 2007). However, this peak of sustained magmatism, with periodic pulses of diking and subsequent faulting, which is recorded in Ulysses Fossae, provides a constraint on the intense activity taking place during the Amazonian. Considering the Tharsis region as

a whole, our absolute age results do agree with recent studies' conclusions, that the period of active tectonism experienced in the Tharsis volcanic province has indeed extended into the Amazonian (Bouley et al., 2018), where we add the majority of the faults in Ulysses Fossae to this period, with the added relative distinction between the sources of tectonic activity between the Tharsis volcanoes. Previous studies by Anderson et al. (2001) and Tanaka et al. (1991), similarly identified the main fault activity in Ulysses Fossae to occur before faulting related to Olympus Mons and Pavonis Mons, in concurrence with our relative age results. However, in those studies the faults related to Olympus Mons and Pavonis Mons are not identified within the Ulysses Fossae area (Anderson et al., 2001). This also means that our results vary in terms of absolute ages, where Anderson et al. (2001) and Tanaka et al. (1991) assigns an Early Hesperian age to all Ulysses Fossae fault activity, and a Late Hesperian – Early Amazonian age to the Olympus Mons and Pavonis Mons activity.

2.5. Conclusions

Through our fault mapping of Ulysses Fossae, we identified and analysed 10 fault groups, which together illustrate several stages of structural activity in the Ulysses Fossae region. Results from relative and absolute model age analysis indicate a complex history involving radial faulting generated by dikes from the surrounding volcanoes (Olympus Mons, Ascraeus Mons, Pavonis Mons, Ulysses Patera and tentatively Jovis Tholus), later reactivation of pre-existing fault populations, and influence from the regional extension related to the Tharsis development. We determine a range of maximum strain values between 0.4 – 2.2%, where 2.2% from G10 are significantly higher than the rest of the groups, reflecting a relatively greater extension. Additionally, considered separately, both the local and regional sourced fault groups tend to increase in strain with time.

The faulting in Ulysses Fossae has occurred interspersed with Amazonian-aged lava-emplacement events and thus only records activity since ~3 Ga ago. The intense extensional faulting associated with the Tharsis volcanoes, including what appears to be multiple extensional events associated with a single volcano, Ulysses Patera, points to the Tharsis volcanotectonic systems being active for longer than previously determined. Our work provides important background necessary to further unravelling the complex tectonic history of the Tharsis volcanic province. Further work will include mapping and comparing other volcanotectonic structures in Tharsis, such as Alba Mons, to the results presented here, ultimately in order to better understand the history of volcanism and tectonism on Mars.

Acknowledgments

S. Shahrzad is funded by the National Environmental Research Council (NERC) Panorama Doctoral Training Partnership (DTP) NE/S007458/1. We thank NASA and ESA for the free access to Martian data through NASA's Planetary Data System (PDS).

Open Research

Shapefile of the mapped faults and craters in this study is available for free download from Zenodo: faults (Shahrzad, 2022a), craters (Shahrzad, 2022b). We also provide the.diam CraterTools files for input in Craterstats in Zenodo (Shahrzad, 2023). The CTX images (Malin, 2007b) used in this study can be downloaded from NASA's PDS Geoscience Node at https://pds-imaging.jpl.nasa.gov/portal/mro_mission.html and the MOLA-HRSC DEM v2 used to generate topographic profiles is available from USGS' Astropedia Catalog (Fergason et al., 2008). Software used in this research are available to download for free. FracPaQ (Healy et al., 2017) is available for download via Github, and Craterstats 2.0 is available via the Freie Universität Berlin at: https://www.geo.fu-berlin.de/en/geol/fachrichtungen/planet/software/index.html

References

Anderson, R. C., Dohm, J. M., Golombek, M. P., Haldemann, A. F. C., Franklin, B. J., Tanaka, K. L., Lias, J., & Peer, B. (2001). Primary centers and secondary concentrations of tectonic activity through time in the western hemisphere of Mars. *Journal of Geophysical Research: Planets*, *106*(E9), 20563–20585. https://doi.org/10.1029/2000JE001278

Banerdt, W. B., Phillips, R. J., Sleep, N. H., & Saunders, R. S. (1982). Thick shell tectonics on one-plate planets: Applications to Mars. *Journal of Geophysical Research: Solid Earth*, *87*(B12), 9723–9733. https://doi.org/10.1029/JB087iB12p09723

Barlow, N. G. (2008). *Mars, An introduction to its Interior, Surface and Atmosphere*. Cambridge University Press.

Bouley, S., Baratoux, D., Paulien, N., Missenard, Y., & Saint-Bézar, B. (2018). The revised tectonic history of Tharsis. *Earth and Planetary Science Letters*, *488*, 126–133. https://doi.org/10.1016/j.epsl.2018.02.019

Cailleau, B., Walter, T. R., Janle, P., & Hauber, E. (2003). Modeling volcanic deformation in a regional stress field: Implications for the formation of graben structures on Alba Patera, Mars. *Journal of Geophysical Research: Planets*, *108*(E12). https://doi.org/10.1029/2003JE002135

Cailleau, B., Walter, T. R., Janle, P., & Hauber, E. (2005). Unveiling the origin of radial grabens on Alba Patera volcano by finite element modelling. *Icarus*, *176*(1), 44–56. https://doi.org/10.1016/j.icarus.2005.01.017

Carr, M. H. (1974). Tectonism and volcanism of the Tharsis Region of Mars. *Journal of Geophysical Research (1896-1977)*, *79*(26), 3943–3949. https://doi.org/10.1029/JB079i026p03943

Carr, M. H., & Head, J. W. (2010). Geologic history of Mars. *Earth and Planetary Science Letters*, *294*(3), 185–203. https://doi.org/10.1016/j.epsl.2009.06.042

De Blasio, F. V. (2018). The pristine shape of Olympus Mons on Mars and the subaqueous origin of its aureole deposits. *Icarus*, *302*, 44–61. https://doi.org/10.1016/j.icarus.2017.11.003

Dohm, J. M., Baker, V. R., Maruyama, S., & Anderson, R. C. (2007). Traits and Evolution of the Tharsis Superplume, Mars. In D. A. Yuen, S. Maruyama, S.-I. Karato, & B. F. Windley (Eds.), *Superplumes: Beyond Plate Tectonics* (pp. 523–536). Springer Netherlands. https://doi.org/10.1007/978-1-4020-5750-2_17

Ernst, R., Grosfils, E., & Mège, D. (2001). Giant Dike Swarms: Earth, Venus, and Mars. *Annual Review of Earth and Planetary Sciences*, *29*(1), 489–534. https://doi.org/10.1146/annurev.earth.29.1.489

Fergason, R. L., Hare, T. M., & Laura, J. (2018). *HRSC and MOLA Blended Digital Elevation Model at 200m v2*. [Map] [Dataset]. Astrogeology PDS Annex, U.S. Geological Survey.

Fernández, C., & Ramírez-Caballero, I. (2019). Evaluating transtension on Mars: The case of Ulysses Fossae, Tharsis. *Journal of Structural Geology*, *125*, 325–333. https://doi.org/10.1016/j.jsg.2018.05.009

Grosfils, E. B., & Head, J. W. (1994). The global distribution of giant radiating dike swarms on Venus: Implications for the global stress state. *Geophysical Research Letters*, *21*(8), 701–704. https://doi.org/10.1029/94GL00592

Gudmundsson, A. (2020). *Volcanotectonics—Understanding the Structure, Deformation and Dynamics of Volcanoes*. https://doi.org/10.1017/9781139176217

Hauber, E., & Kronberg, P. (2005). The large Thaumasia graben on Mars: Is it a rift? *Journal of Geophysical Research: Planets*, *110*(E7). https://doi.org/10.1029/2005JE002407

Healy, D., Rizzo, R. E., Cornwell, D. G., Farrell, N. J. C., Watkins, H., Timms, N. E., Gomez-Rivas, E., & Smith, M. (2017). FracPaQ: A MATLAB™ toolbox for the quantification of fracture patterns [Software]. *Journal of Structural Geology*, *95*, 1–16. https://doi.org/10.1016/j.jsg.2016.12.003

Jenness, J. (2011). Tools for Graphics and Shapes. *Jenness Enterprises*.

Kneissl, T., van Gasselt, S., & Neukum, G. (2011). Map-projection-independent crater size-frequency determination in GIS environments—New software tool for ArcGIS. *Planetary and Space Science*, *59*(11), 1243–1254. https://doi.org/10.1016/j.pss.2010.03.015

La Rosa, A., Pagli, C., Keir, D., Sani, F., Corti, G., Wang, H., & Possee, D. (2019). Observing Oblique Slip During Rift Linkage in Northern Afar. *Geophysical Research Letters*, *46*(19), 10782–10790. https://doi.org/10.1029/2019GL084801

Malin, M. C., Bell, J. F., Cantor, B. A., Caplinger, M. A., Calvin, W. M., Clancy, R. T., Edgett, K. S., Edwards, L., Haberle, R. M., James, P. B., Lee, S. W., Ravine, M. A., Thomas, P. C., & Wolff, M. J. (2007). Context Camera Investigation on board the Mars Reconnaissance Orbiter [Dataset]. *Journal of Geophysical Research: Planets*, *112*(E5). https://doi.org/10.1029/2006JE002808

McGovern, P. J., Smith, J. R., Morgan, J. K., & Bulmer, M. H. (2004). Olympus Mons aureole deposits: New evidence for a flank failure origin. *Journal of Geophysical Research: Planets*, *109*(E8). https://doi.org/10.1029/2004JE002258

Mège, D., Cook, A. C., Garel, E., Lagabrielle, Y., & Cormier, M.-H. (2003). Volcanic rifting at Martian grabens. *Journal of Geophysical Research: Planets*, *108*(E5). https://doi.org/10.1029/2002JE001852

Mège, D., & Masson, P. (1996). A plume tectonics model for the Tharsis province, Mars. *Planetary and Space Science*, *44*(12), 1499–1546. https://doi.org/10.1016/S0032-0633(96)00113-4

Mège, D., & Masson, P. (1997). *Graben formation and dike emplacement on Earth and other planets*. *28*, 929.

Melosh, H. J. (1980). Tectonic patterns on a reoriented planet: Mars. *Icarus*, *44*(3), 745–751. https://doi.org/10.1016/0019-1035(80)90141-4

Michael, G. G. (2013). Planetary surface dating from crater size–frequency distribution measurements: Multiple resurfacing episodes and differential isochron fitting. *Icarus*, *226*(1), 885–890. https://doi.org/10.1016/j.icarus.2013.07.004

Michael, G. G., Kneissl, T., & Neesemann, A. (2016). Planetary surface dating from crater size-frequency distribution measurements: Poisson timing analysis. *Icarus*, *277*, 279–285. https://doi.org/10.1016/j.icarus.2016.05.019

Michael, G. G., & Neukum, G. (2010). Planetary surface dating from crater size-frequency distribution measurements: Partial resurfacing events and statistical age uncertainty. *Earth and Planetary Science Letters*, *294*, 223–229. https://doi.org/10.1016/j.epsl.2009.12.041

Morris, E. C., & Tanaka, K. L. (1994). Geologic maps of the Olympus Mons region of Mars. *IMAP*. https://doi.org/10.3133/i2327

Paquet, F., Dauteuil, O., Hallot, E., & Moreau, F. (2007). Tectonics and magma dynamics coupling in a dyke swarm of Iceland. *Journal of Structural Geology*, *29*(9), 1477–1493. https://doi.org/10.1016/j.jsg.2007.06.001

Park, R. G. (2000). *Foundations of Structural Geology: Vol. 3rd Edition*. Chapman & Hall.

Plescia, J. B. (2004). Morphometric properties of Martian volcanoes. *Journal of Geophysical Research: Planets*, *109*(E3). https://doi.org/10.1029/2002JE002031

Poland, M.P., Moats, W.P. & Fink, J.H (2008). A model for radial dike emplacement in composite cones based on observations from Summer Coon volcano, Colorado, USA. *Bull Volcanol* **70**, 861–875. https://doi.org/10.1007/s00445-007-0175-9

Polit, A. T., Schultz, R. A., & Soliva, R. (2009). Geometry, displacement–length scaling, and extensional strain of normal faults on Mars with inferences on mechanical stratigraphy of the Martian crust. *Journal of Structural Geology*, *31*(7), 662–673. https://doi.org/10.1016/j.jsg.2009.03.016

Richardson, J. A., Bleacher, J. E., Connor, C. B., & Glaze, L. S. (2021). Small Volcanic Vents of the Tharsis Volcanic Province, Mars. *Journal of Geophysical Research: Planets*, *126*(2), e2020JE006620. https://doi.org/10.1029/2020JE006620

Robbins, S. J., Achille, G. D., & Hynek, B. M. (2011). The volcanic history of Mars: High-resolution crater-based studies of the calderas of 20 volcanoes. *Icarus*, *211*(2), 1179–1203. https://doi.org/10.1016/j.icarus.2010.11.012

Scott, E. D., Wilson, L., & Head III, J. W. (2002). Emplacement of giant radial dikes in the northern Tharsis region of Mars. *Journal of Geophysical Research: Planets*, *107*(E4), 3-1-3–10. https://doi.org/10.1029/2000JE001431

Shahrzad, S. (2022). Ulysses Fossae Fault Catalogue [Dataset]. Zenodo. doi:10.5281/zenodo.7220699.

Shahrzad, S. (2022). Ulysses Fossae Crater Catalogue [Dataset]. Zenodo. doi:10.5281/zenodo.7220715.

Shahrzad, S. (2023). Ulysses Fossae X,Y Topographic Profile Locations [Data set]. Zenodo. doi.org:10.5281/zenodo.7681321

Shahrzad, S. (2023). Ulysses Fossae Craterstats Input [Dataset]. Zenodo. doi:10.5281/zenodo.7657313

Tanaka, K. L., Skinner Jr., J. A., Dohm, J. M., Irwin, III, R. P., Kolb, E. J., Fortezzo, C. M., Platz, T., Michael, G. G., & Hare, T. M. (2014). *Geologic Map of Mars* (Scientific Investigations Map) [Scientific Investigations Map].

Thomas, P. G., & Allemand, P. (1993). Quantitative analysis of the extensional tectonics of Tharsis Bulge, Mars: Geodynamic implications. *Journal of Geophysical Research: Planets*, *98*(E7), 13097–13108. https://doi.org/10.1029/93JE01326

Werner, S. C., Ivanov, B. A., & Neukum, G. (2009). Theoretical analysis of secondary cratering on Mars and an image-based study on the Cerberus Plains. *Icarus*, *200*(2), 406–417. https://doi.org/10.1016/j.icarus.2008.10.011

Wilson, L., & Head III, J. W. (2002). Tharsis-radial graben systems as the surface manifestation of plume-related dike intrusion complexes: Models and implications. *Journal of Geophysical Research: Planets*, *107*(E8), 1-1-1–24. https://doi.org/10.1029/2001JE001593

Chapter 3

Amazonian Tectonic Evolution of Ceraunius and Tractus Fossae, Mars, and Implications for Local Magmatic Sources

S. Shahrzad[1], E.K. Bramham[1], M. Thomas[1], S. Piazolo[1], P.K. Byrne[2], and E. Mortimer[1]

[1]School of Earth and Environment, University of Leeds.

[2]Department of Earth and Planetary Sciences, Washington University in St. Louis.

Abstract

The heavily faulted Martian terrains of Ceraunius Fossae and Tractus Fossae, south of the Alba Mons volcano, have previously only been considered as parts of larger tectonic studies of Alba Mons, and consequently the complexity of the faulting remains unclear. As these terrains are in the midst of the large Tharsis volcanoes, the study of their surface deformation has the potential to help unravel the volcano-tectonic deformation associated with the growth of Tharsis, as well as decipher details of the magma-tectonic processes responsible for graben formation. Here, we distinguish between faults and collapse structures based on image and topographic evidence. We mapped ~12,000 faults, which we grouped into three distinct fault groups based on orientation, morphology, and relative ages. These show a temporal evolution in the mapped fault orientations from NE to N-S to NW, with associated changes in stress orientations. We also mapped collapse features and categorised these into four different groups: pit-crater chains, catenae, u-shaped troughs and chasmata. Examining the four collapse structure groups reveals that they are likely four progressive stages in the erosional evolution of pit-crater chains. Together this revealed a structural history heavily influenced by lateral diking from both local (radial to Alba Mons, Pavonis Mons and Ascraeus Mons) and regional (radial to Tharsis) sources, and vertical diking from a

proposed Ceraunius Fossae centred magma source. This, along with an updated crater size-frequency distribution analysis of the unit ages, reveals a highly active tectonic and magmatic environment south of Alba Mons in the Middle Amazonian.

Plain Language Summary

The large-scale faults surrounding the dome of the Alba Mons volcano on Mars have been studied intensely, while the faulted area south of Alba Mons have received relatively little attention. Closer inspection of these southern terrains, namely Ceraunius Fossae and Tractus Fossae, reveals that this area is far more complex in structure and more recent in activity, than previously thought. In this study we mapped and measured all the faults in the study areas. In addition to the faults, the surface of the study area is covered in "collapse structures". These are circular to trough-like features, created when surface material has fallen into a subsurface cavity. We mapped and characterised these faults and collapse structures, in order to determine the history of events and which geological process created them. We found three distinct extensional faulting events, and examples of all four collapse structures: pit-crater chains, catenae, u-shaped troughs and chasmata. These events all took place within 2.4–1.4 billion years ago, during the Amazonian period. Together, these results show magmatic activity drove structure deformation, both from the surrounding Alba Mons, Ascraeus Mons and Pavonis Mons volcanoes, and also from a local large magmatic source, situated directly underneath Ceraunius Fossae

3.1. Introduction

With the advent of increasing resolution of Martian image data over the last decades, it has become possible to thoroughly investigate questions related to the tectonic regimes of Mars and determine the influence of various magmatic processes on tectonics. Though larger scale processes on Mars are generally understood, local-scale graben structures observed on Mars remain understudied. Detailed characterization of the surface structures in local areas, and their relationships to large regional or local stress variations and magmatic processes, are essential to understanding the development of the volcanic centres on Mars, and thus the evolution of the planet.

One of these volcanic centres is Alba Mons, a wide, low-relief shield volcano located on the northern edge of the Tharsis region (Figure 3.1). The Alba Mons volcano, and its associated system of extensive graben structures have been studied in detail over the last two decades (e.g. Cailleau et al., 2005; Krishnan & Kumar, 2023; McGovern et al., 2001; Öhman & McGovern, 2014). The fault systems around Alba Mons include Alba Fossae, Tantalus Fossae, Ceraunius Fossae and Tractus Fossae (Figure 3.1). The different surface expressions of the faults surrounding Alba Mons have been mapped to various degrees. However, their interpretations differ significantly and the source of the deformation is still a matter of debate, with interpretations ranging from purely magmatic to purely tectonic processes, or a combination of both (Cailleau et al., 2003; Ivanov & Head, 2006; Öhman & McGovern, 2014; Stubblefield, 2018).

The Tharsis volcanic province is the largest volcano-tectonic centre on Mars, and is host to hundreds of volcanic edifices and their associated tectonic deformation (Pieterek et al., 2022; Plescia & Saunders, 1982), as well as thousands of identified small volcanic vents (Richardson et al., 2021). In the study area south of Alba Mons, 20 dated landforms reveal that the ages of latest volcanic activity ranges between 421 Ma and 68 Ma (Pieterek et al., 2022). The region of Tharsis has been in continuous development from >3.7 Ga (e.g. Plescia, 1994; Werner, 2009), with volcanic activity measured as recently as 200 Ma ago, during the Amazonian (e.g. Hauber et al., 2011; Pieterek et al., 2022). The source of the extensive volcanism in the Tharsis province has been attributed to the activity of the Tharsis superplume (e.g. Dohm et al., 2007; Mège & Masson, 1996). The superplume, consisting of several mantle plumes, is thought to have been emplaced underneath the entire volcanic province, was acting as the driving factor in the construction of Tharsis from the Noachian through to the Amazonian. However, recent research has suggested that the magma source beneath Alba Mons, which would be responsible for the low-angle slope of the volcano and the extensive surface deformation surrounding it, is a separate, possibly independent plume from the Tharsis superplume (Belleguic et al., 2005; Cailleau et al., 2005; Öhman & McGovern, 2014). This theory has its origins in the gravity study of Tharsis by Janle and Erkul (1990), which concluded that a separate diapir is responsible for Alba Mons.

The majority of the Alba Mons studies focus on the extensive structures immediately surrounding the edifice (e.g. Cailleau et al., 2005; Ivanov & Head, 2006; McGovern et al., 2001). The notable exceptions to this are the extension and mechanical stratigraphy studies by Borrachini et al. (2005, 2006), and the recent study by Krishnan & Kumar (2023), where selected lava flows, graben, volcanic pits, and boulders were analysed to construct a geodynamic setting. The faults of Tractus Fossae have been the focus of one previous study (Spagnuolo et al., 2008), though the area is not considered in relation with the neighbouring Ceraunius Fossae. Despite these analyses, detailed fault mapping of the area south of Alba Mons is still needed in order to establish a structural history of the area.

In this study, we present a novel combination of comprehensive mapping, morphological analysis, and strain calculation for the faults in the area south of Alba Mons, along with updated absolute model ages for the associated geological units. Additionally, we mapped and categorised observed collapse structures and determined any connections to the mapped faults in order to determine the conditions that would cause the collapse features to form, as well as any progression in structure. We used these analyses as the basis for determining the likely sources of both faults and non-fault structures and produced a sequence of structural events. By coupling this sequence of events with the large- and small scale tectonic and magmatic influences responsible for shaping the current surface around Alba Mons, we were able to further illuminate the magmatic and tectonic history of the Tharsis volcanic province, and Mars as a whole.

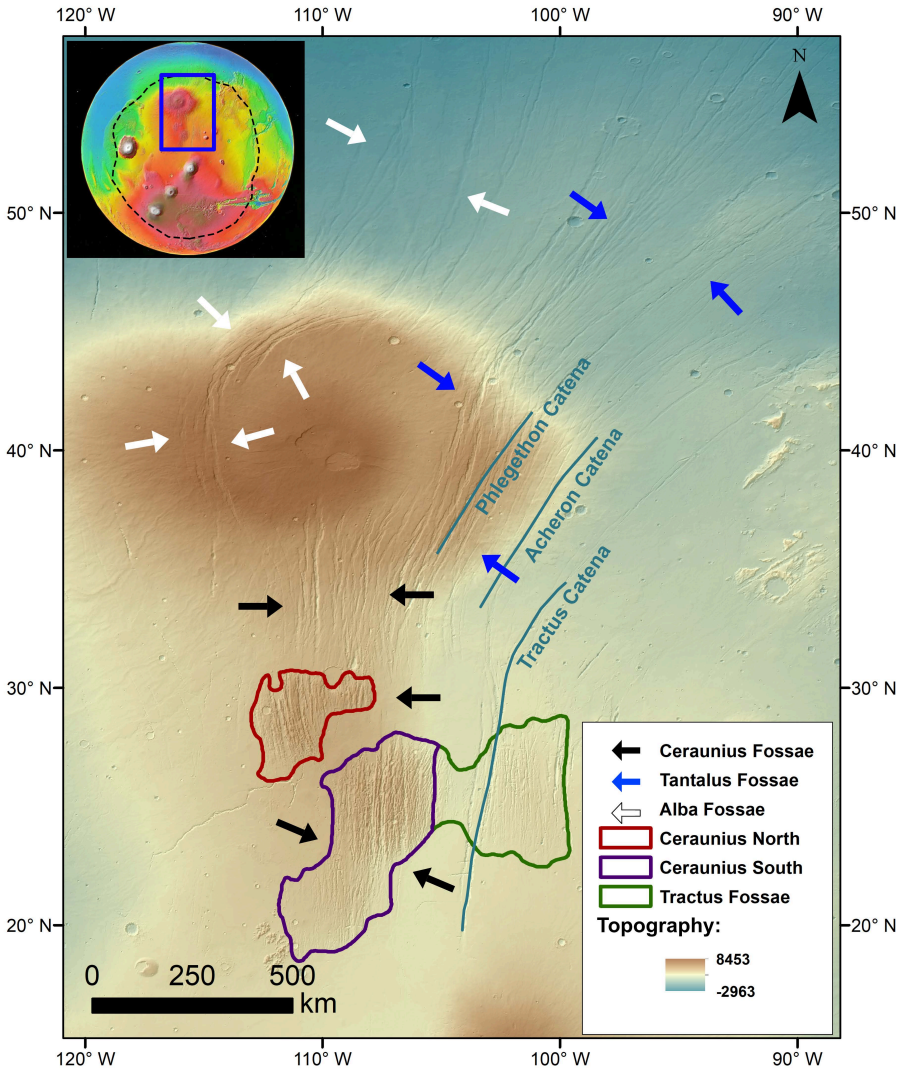

Figure 3.6: Location of features surrounding the Alba Mons volcano (See context location on top left inset of Mars, with the Tharsis Volcanic Province outlined in black dashed line). The three study areas are outlined in the legend, as mapped by Tanaka (2014). Arrows indicate the extent of three different fossae systems. The three major catenae: Tractus Catena, Acheron Catena, and Phlegethon Catena, are labelled with light blue lines. Background is Mars Orbiter Laser Altimeter (MOLA) Hillshade overlaid by merged MOLA-HRSC (High Resolution Stereo Camera) Digital Elevation model (200 m/px). (Fergason et al., 2018)

3.1.1. Geological Setting

3.1.1.1. Morphological Characteristics of the Alba Mons Volcano

Alba Mons, previously referred to as 'Alba Patera' has a diameter of ~1600 km, a ~7 km relief and a ~1° flank slope angle, making it the largest edifice of any volcano on Mars (Plescia, 2004). The northern flank of Alba Mons is located proximal to the Martian dichotomy boundary, along the margin between the southern highlands and the northern lowlands (Ivanov & Head, 2006). The summit of the volcano is host to a complex of calderas which have been dated between $3.02^{+0.32}_{-0.9}$ Ga and 450 ± 100 Ma (Robbins

et al., 2011), extensive lava flows along its flanks, and one of the largest graben complexes on Mars (Ivanov & Head, 2006). The edifice itself is surrounded by Amazonian lava flows, with some topographically raised patches of older Hesperian material to the south, at Ceraunius Fossae and Tractus Fossae (Tanaka et al., 2014). It was later suggested in a study by Pieterek et al. (2022), that the age of Ceraunius Fossae should be revisited as it is host to Amazonian-age volcanic edifices.

3.1.1.2. Graben Structures Associated with Alba Mons

Alba Mons is surrounded by complex graben systems, which are categorized into four geographical groups (Figure 3.1): Tantalus Fossae (E and NE of Alba Mons), Alba Fossae (W and N of Alba Mons), Ceraunius Fossae (S of Alba Mons), and Tractus Fossae (SE of Alba Mons). The graben can also be divided based on morphology, into the following groups: (a) north and northeast trending linear grabens and (b) concentric grabens that form the circumferential structures around the Alba Mons volcanic dome (Cailleau et al. 2003). Tantalus Fossae are linear grabens bounding Alba Mons with an average strike orientation of N/NE (blue arrows on Figure 3.1) and are considered the oldest of the graben systems. They are assumed to have been formed by a combination of regional stress and a broad uplift, due to a buoyancy zone underneath Alba Mons. This was reproduced in modelling studies by Cailleau et al. (2003) and Polit et al. (2009).

Following the formation of these linear graben, there was a change to development of the circumferential (concentric) grabens of Alba Fossae, which are prevalent on the western flank of the Alba Mons volcano (white arrows on Figure 3.1). Increasing subsidence, associated with the formation of Alba Mons, created a regime with a predominance of concentric faults in later stages of faulting (Polit et al., 2009), superimposing the subsidence related graben formation on the effects of regional extension. This was also reproduced in numerical and physical models by Cailleau et al. (2003).

3.1.1.3. Collapse Features

In addition to the faults, the southern Alba Mons area has a series of distinct, non-fault surface features which vary significantly in morphology, location, and size, and are, similar to other Martian terrains, affected by volcanism (Figure 3.2). These features include pit-crater chains, catenae, u-shaped troughs and chasmata, which we collectively refer to as "Collapse Features". Definition of these feature types have been described in previous literature on Mars (e.g. Hardy, 2021; Mège et al., 2002, 2003). Pit-crater chains (PCCs) are made of craters formed by collapse of material into subsurface voids, rather than by impacts. Such voids can be the result of various processes, but the most widely accepted ones are tension fractures, collapse of lava tubes, dike-generated volatile release, or magma withdrawal (Cushing et al., 2015; Ferrill et al., 2011; Wyrick et al., 2004). The orientation of the chain reflects the collapsed structure underneath (Mège et al., 2002). Catenae is the term for a chain of pit-craters where the craters interact with each other, either due to the initial close proximity of craters during formation, or due to further erosion of a "standard" pit-crater chain, where the isolated craters are enhanced and thus interact. U-shaped troughs are elongated troughs, which can vary drastically in orientation along strike, and terminate in a circular shape, connecting the two sides of the trough (Mège et al., 2003) (Figure 3.2c). Finally, the chasmata are generally observed as large erosional features (Figure 3.2d), possibly induced by initial pit-crater chains as well, or perhaps from collapse into larger cavities than u-shaped troughs (Mège et al., 2003). Despite this qualitative understanding, it remains unclear exactly how these four collapse features are related to each other, and how they are related to the complex magma-tectonic environment on Mars.

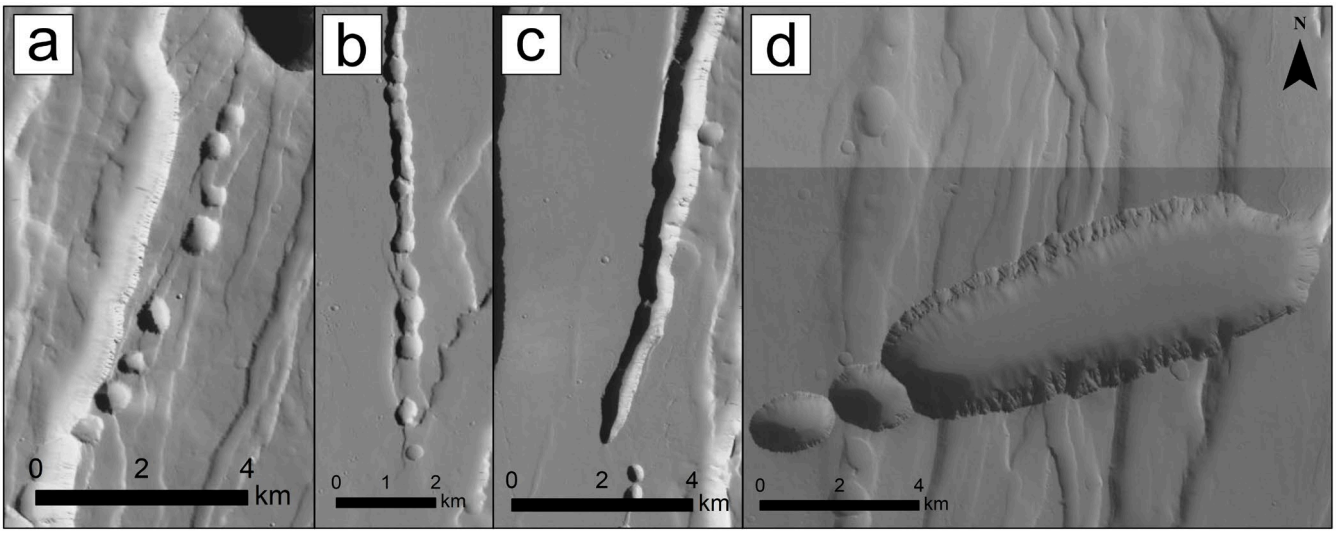

Figure 3.7: Zoom of example of variety of collapse structures found in the study areas. A) Example of pit-crater chain, feature centered at 29°39'15.17"N, 108°22'43.83"W. B) Example of catenae, feature centered at 26°55'38.14"N, 109°2'48.46"W. C) Example of a u-shaped trough, feature centered at 29°28'19.54"N, 108°28'12.44"W. D) Example of a chasma, feature centered at 19°56'3.73"N, 108°55'0.71"W. CTX background Global Mosaic credit: Esri, Caltech Murray Lab, NASA, JPL, MSSS

3.1.1.4. Expected Observations for Faulting Driven by Intrusions or Pure Tectonic Deformation.

Grabens formed by dike intrusion initiated faulting, commonly have a uniform width, depth, and length (Tanaka et al., 1991). These graben are generally narrow and symmetrical (Mège, 1999), with a radial or fan-shaped fault population geometry extending from a volcanic source (Carr, 1974; Mège & Masson, 1996). They are also often associated with other linear surface features such as pit-crater chains, chasmata and u-shaped troughs (Mège & Masson, 1996). For purely tectonic extensional faulting, we expect less narrow graben, with less symmetrical and more irregular spatial fault patterns within a population. In terms of geometry, grabens associated with volcanic loading, uplift or subsidence will show circumferential, wristwatch or hourglass patterns (Byrne et al., 2015; Cailleau et al., 2003, 2005). Non-volcanic tectonism such as flexural loading, uplift or isostatic compensation will generally be accompanied by either radial or circumferential wrinkle ridges (i.e., compression) (Banerdt et al., 1992; Tanaka et al., 1991).

3.1.2. Study Areas: Selection, General Characteristics and Previous Studies

3.1.2.1. Selection of Study Areas

We selected two fossae systems, Ceraunius Fossae and Tractus Fossae, across three geological units south of Alba Mons as our study areas for this work (Figure 3.3). While Ceraunius Fossae continues further north onto the flank of Alba Mons (Figure 3.1) we focus solely on the southern sections of Ceraunius Fossae, as defined within the Tanaka et al. (2014) mapped geological unit boundaries (Figure 3.3). Though the western border of Tractus Fossae is commonly defined by Tractus Catena, we investigate all features within the mapped lHv unit (Figure 3.3). Tanaka et al. (2014) previously mapped these three areas as separate geological units, allowing for more dependable ages constrained using the crater size-frequency distribution method. As the south of Ceraunius Fossae is divided into two units with a young lava flow separating the two areas (Figure 3.3), we refer to these regions and their faults as Ceraunius North and Ceraunius South. Ceraunius and Tractus fossae serve as examples of linear and curved faulting potentially related to Alba Mons, and possibly host a transition between the two types of faulting. At initial inspection the two areas also include a number of non-graben features with potential magmatic or volcanic origin, which we identify as the collapse features (Mège et al., 2003). Additionally, these study areas have a similar distance from their nearest volcanic edifice (of ~600 km from Alba Mons) as Ulysses Fossae (~600 km

from Olympus Mons) as described by Shahrzad et al. (2023), which allows us to compare results and ultimately broaden our understanding of the Tharsis volcanic region.

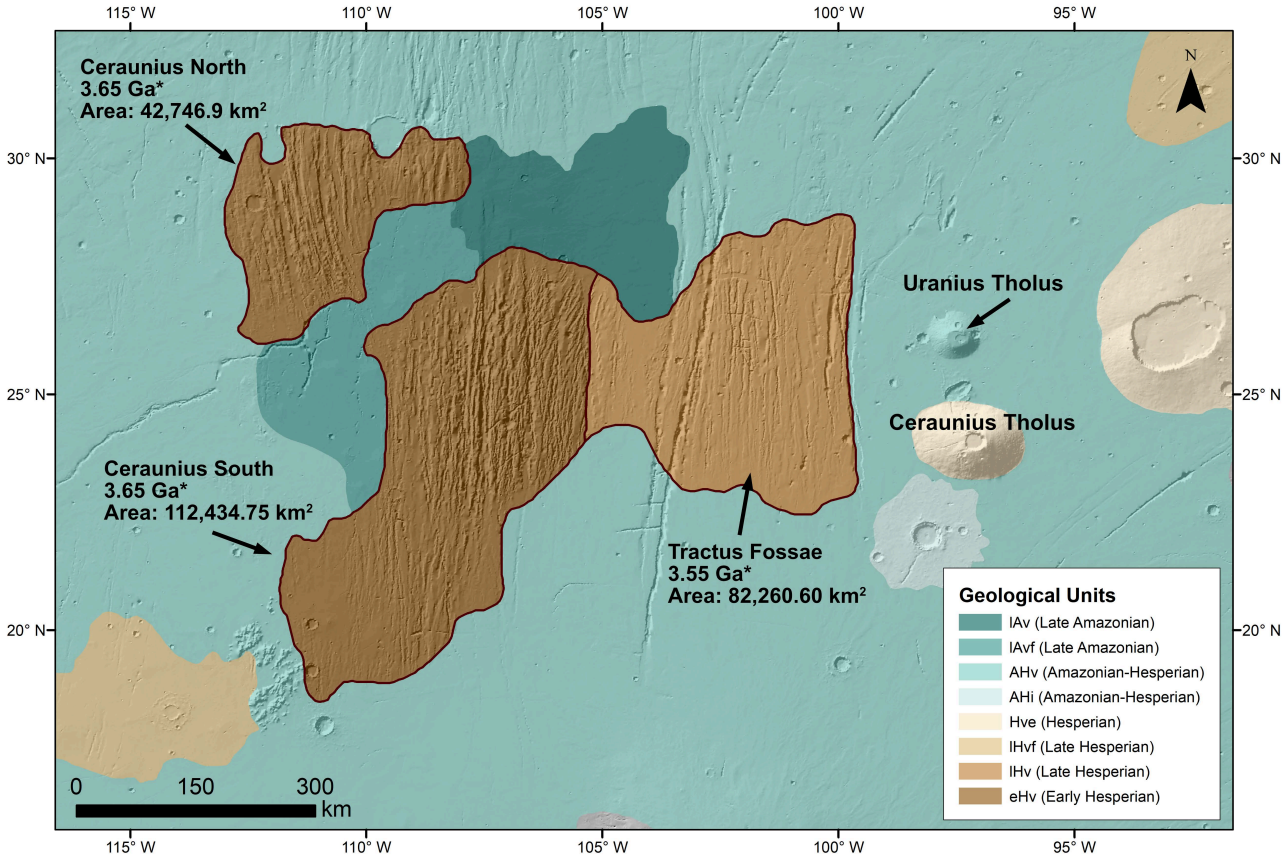

Figure 3.8: Geologic map of the three study areas, with unit outlines as defined by Tanaka et al. (2014). Note the names Ceraunius North (unit eHv), Ceraunius South (unit eHv) and Tractus Fossae (unit lHv), used to identify each unit in this study, and the area measurement for each study area. *The Tanaka et al. (2014) mapped unit age. Background image is MOLA hillshade.

3.1.2.2. General Characteristics and Previous Studies

Ceraunius Fossae North and South

The faulted terrain immediately to the south of the Alba Mons shield is a part of the *Ceraunius Fossae* system (Figure 3.1). It consists of a dense array of linear faults that appear to be oriented generally north-south, largely radial to the Alba Mons shield. The extent of our mapping of the Ceraunius Fossae fault system is contained to two raised patches of early Hesperian volcanic unit (eHv), with an absolute age of 3.65 Ga (Tanaka et al., 2014), covered by extensive faults and grabens (Figure 3.3). These elevated patches are separated by lower-elevation, younger lava flows, effectively preserving a significantly larger number of structural features than that of the surrounding flooded plains. Previous work by Tanaka (1990)

determined a two-stage sequence of faulting in the area, with an initial NE and then N-S oriented extensional events.

Tractus Fossae

The Tractus Fossae region is located immediately to the east of Ceraunius Fossae, and constitutes a unit mapped by Tanaka et al. (2014) as lHv, the late Hesperian volcanic unit. This unit is aged 3.55 Ga (Tanaka et al., 2014), and is thus considered the youngest of the three study areas. Immediately to the east of the area, the two volcanoes Uranius Tholus and Ceraunius Tholus are located, with diameters of ~60 km and ~130 km, respectively (Figure 3.1). Tractus Fossae is intensely faulted with large linear grabens, though they appear more spread out than those in Ceraunius Fossae. Tractus Fossae is also host to two large linear structures along its western border that are longer and deeper than the other graben in the area, with Tractus Catena being the only named of these. This area has only one dedicated study, by Spagnuolo et al. (2008), which identified the faulting in Tractus Fossae as being as early as the Noachian-Hesperian boundary, followed by some faulting in the Amazonian.

3.2. Methods

3.2.1. Fault Characterisation

3.2.1.1. Fault Mapping and Grouping

We mapped the faults in this study using 6 m/pixel resolution global image mosaic from the Mars Reconnaissance Orbiter's Context Camera (CTX) (Image credit: Esri, Caltech Murray Lab, NASA, JPL, MSSS) . We mapped the fault traces as separate polylines using Esri ArcMap software (v. 10.6), at a scale of 1:250,000 to 1:100,000 where we traced the upper boundary of the fault (surface breaks). For our three study areas of Ceraunius North, Ceraunius South and Tractus Fossae, we used the Tanaka et al. (2014) geologic map as unit boundaries and mapped the faults within. Any fault that started within the defined study area boundary we mapped in full even if the trace continued beyond the boundary. We aimed to map all identifiable faults at the chosen scale, in order to capture each fault trend. For fault length determinations, we only considered any fault linkage visible on the surface (hard-linked faults), and we have not made any conjectures regarding supposed sub-surface linkage of potentially soft-linked faults. We calculated the absolute lengths and strike orientations as geodesic lengths and azimuths using the Tools for Graphics and Shapes plugin for ArcGIS (Jenness, 2011). We also used the software package FracPaQ (Healy et al., 2017), to visualize fault strikes spatially and in rose diagrams, along with the mapped fault intensity. In FracPaQ, fault intensity (m^{-1}) is determined by the number of faults intersecting the perimeter of a program generated scan circle (Healy et al., 2017). We used a grid comprised of scan circles with a diameter of ~10 km, to ensure the maps captured the complexity of the faulting in the area. Following fault mapping, we separated the mapped faults into different groups defined by similar average orientation, fault morphology, and relative ages determined by their crosscutting relationships. This ensured that the faults within a group are all of similar ages and are therefore inferred to have formed through the same structural event.

3.2.1.2. Strain Measurements for Faults

We measured the strain for each defined fault group using sets of topographic profiles, created perpendicular to the main fault orientation in each group. For topography we used the global Digital Elevation Model (DEM) from the coupled Mars Orbiter Laser Altimeter (MOLA)and the High-Resolution Stereo Camera (HRSC) data (Fergason et al., 2018). The coupled MOLA-HRSC DEM data has a vertical resolution of 1 m/px and a horizontal resolution of 200 m/pixel (Fergason. et al., 2018). In QGIS software, we set the location of each topographic profile so it was perpendicular to the average fault orientation within a group and so the trace would not cross any other major topographic features,

such as craters, while still capturing as many faults as possible. This process was somewhat limited by the quality of the DEM data in certain areas, with regards to resolving individual features.

We measured the extensional strain (ϵ) by calculating the sum of measured throws (Shahrzad et al., 2023) and used a 60° fault dip (consistent with previous Martian estimations (Polit et al., 2009)), to calculate the cumulated extension (e_{cum}). The cumulated extension was then divided by the original length of the profile trace (L_0), defined as the trace length minus the sum of the heaves, to give strain.

$$\epsilon = \frac{e_{cum}}{L_0}$$

We then multiplied the result by 100 to get the strain percent value.

3.2.2. Collapse Feature Mapping

The collapse features in the three study areas were similarly mapped by marking each feature with a polyline in ArcMap, which went through the middle of the feature, recording their location and orientation. The four collapse features were identified during the mapping as follows:

Pit crater chains and catenae (see Figure 3.2a and 3.2b for examples) were the simplest to identify, as the craters make them non-ambiguous. These features are straightforward to identify on the CTX images alone, where the distinction from individual pit craters to catenae is determined by when the craters touch or directly interact with each other, while the individual craters are still identifiable. *U-shaped troughs* were more difficult to distinguish from the tectonic grabens, as they have largely similar straight linear borders. They do however vary from the grabens by several features: 1) uneven border walls, with some indications of remnant circular crater perimeter features (scalloped edges). 2) Contrary to the tectonic faults which remain parallel through their trace, the troughs terminate in a semi-circular shape where the walls connect (Figure 3.2c). As the u-shaped troughs can be a challenge to distinguish, the mapping of them is aided by comparing the CTX images with the MOLA-HRSC topographic data. As we determine u-shaped troughs as a stage in evolution of the pit-crater chains, the majority of the troughs reveal distinct pit crater chains beneath them on the topographic data, distinguishing them from the purely tectonic faults. The final collapse feature, *chasmata,* can appear similar to u-shaped troughs but are larger in size and commonly form large oval structures (Figure 3.2d) (Mège et al., 2003). They are often bounded by faults, with interiors that show evidence of large-scale mass wasting, slopes of material along the sides, and, lacking flat graben floors, distinguishing them from the defined slope breaks of the purely tectonic faults. See Figure B1 in Appendix B for examples of topographic profiles. After mapping each feature, we measured the orientation and length of the features using the Tools for Graphics and Shapes plugin in ArcMap.

3.2.3. Determining Relative and Absolute Ages

We determined the timing of the activity of the different defined fault groups as constrained by their absolute maximum ages and their relative ages. The maximum absolute ages were determined by the age of the geological unit the fault groups crosscut, which we determined in this study using crater size-frequency distributions. The vast majority of the fault groups in this study crosscut multiple geological units, and in these cases, we assigned the youngest unit age as the maximum age for the group. For the relative ages of the fault groups themselves, we used their crosscutting relationships.

3.2.3.1. Crater Size-Frequency Distribution

We obtained absolute model ages for the geological units of the three study areas (Figure 3.3), using the crater size-frequency distribution (CSFD) method in a similar approach to Shahrzad et al. (2023). We mapped all identifiable craters which had a diameter >800 m, with the aim of using all mapped craters ≥1 km in the age determination. This mapping of smaller diameters than the aim, ensured that no craters ≥1 km were missed. The crater sizes and locations were mapped in ArcMap using the CraterTools plugin (Kneissl et al., 2011). During mapping we ensured no capturing of secondary craters (clustering) or other circular features that may have been mistaken for a primary impact crater, such as pit-crater chains. We used the software Craterstats v.2 (Michael, 2013) to fit our crater data to the Martian isochrons, using the production function of Hartmann (2005) and the chronology function of Hartmann and Daubar (2016). We then fit counted craters with a lower diameter boundary of 1 km. Using Craterstats software, we also performed a randomness analysis on the craters in order to verify that secondary craters were not used to fit to the isochron. We make use of both the randomness analyses available in Craterstats. First the Standard Deviation of Adjacent Area (SDAA) method and the Mean 2nd-Closest Neighbour Distance (M2CND) method. The SDAA method constructs polygons, where the distance of any point to the associated crater centroid is less or the same as to the centroid for any other crater. The SDAA value is then the standard deviation of the area of all polygons (Riedel et al., 2021). The M2CND method determines the distance to the second closest crater centroid for each crater centroid, with the mean of these values used as the M2CND (Riedel et al., 2021). The Craterstats software produces an n_σ diagram showing the degree of clustered or ordered craters in the dataset. In this plot, values within the grey shaded area (± 3σ) are not considered clustered or ordered, and therefore show data of good quality, with no secondary craters captured, with reliable results.

3.3. Results

3.3.1. Fault Mapping

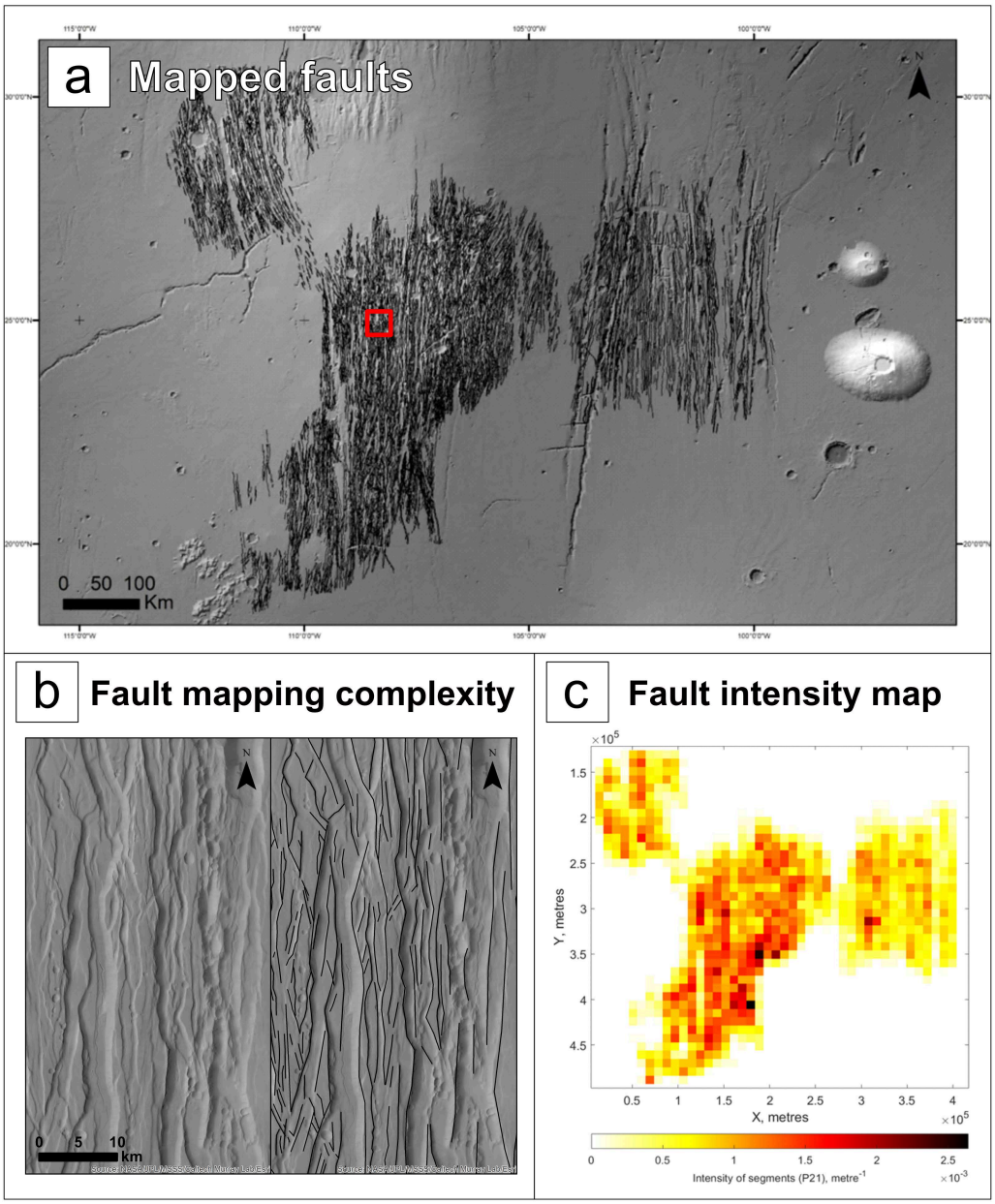

Figure 3.9: A) All mapped faults (black lines) in the study area. Red square note's location for zoom in b). Background is MOLA Hillshade overlaid by merged MOLA-HRSC DEM (200 m/px) (Fergason et al., 2018). B) Zoom on example of overprinted fault patterns. Left image is area before mapping, right image is area after mapping; black lines show the faults identified. Background Image credit: Esri, Caltech Murray Lab, NASA, JPL, MSSS. C) FracPaQ generated fault intensity map, of mapped faults.

We mapped a total of ~12,000 faults in the south of Alba Mons (Figure 3.4a), across the three study area units, the vast majority of which are graben-forming normal faults which have an average strike orientation between NNW and NNE. The faults heavily overprint each other (Figure 3.4b) and have a largely similar appearance and morphology. The majority of the graben are linear, but there is a number of faults with variations in orientation along strike, with some of them being subtly curved, e.g., the eastern faults in Ceraunius North (Figure 3.4a). We have mapped a cumulative fault length of 106,516.6 km, with the average fault length being ~8 km (see Supporting Information Figure B.2 (Appendix B) for histogram of all mapped fault lengths). Among the three geological units, the fault intensity map revealed a relatively even spatial distribution between the two flanking units Ceraunius North and Tractus Fossae, with the middle Ceraunius South unit having the highest intensity of faulting (Figure 3.4c). Common for all the grabens mapped, is the consistent width across strike, which is constantly a few km (2-4 km), resulting in relatively narrow grabens when considering their lengths.

3.3.1.1. Fault Groups

The initial approach of dividing the faults into groups based on cross-cutting relationships alone proved difficult due to the highly overprinted nature of the faulting (Figure 3.4b). This was particularly true for the N-S oriented faults in Ceraunius South, where it was challenging to distinguish if faults were changing orientation along strike within a group, or if a fault should belong to an entirely different group with a different average orientation. To allow a more detailed and consistent identification of fault groups, we expanded on our initial method. We used the general N-S orientation of the majority of the faults as the baseline for the first group, and then systematically marked any individual fault which 1) had a discernibly different average strike orientation from the N-S group (see rose diagrams in Figure 3.5) and which 2) crossed the N-S fault independently and was clearly not a branch from the N-S fault orientation group. This left us with two initial fault groups, the N-S group, and a second group of faults that did not belong to the N-S group. We then analysed the second group and used our original criteria of clear cross-cutting relationships and different strike orientation, to further divide that group into two groups, conclusively resulting in three final fault groups in our study area (Table 3.1). See Figure 3.5 for the groups.

Fault Group	(N) Faults	Cumulative Length (km)	Avg. Orientation	Unit
G1	1676	13,061	NNE/NE	CS, TF
G2	8013	76,213	N/NNE	CN, CS, TF
G3	2242	17,241	NNW/NW	CN, CS

Table 3.1: Overview of the 3 fault groups. Which units the faults in the group superpose: CN (Ceraunius North), CS (Ceraunius South), TF (Tractus Fossae).

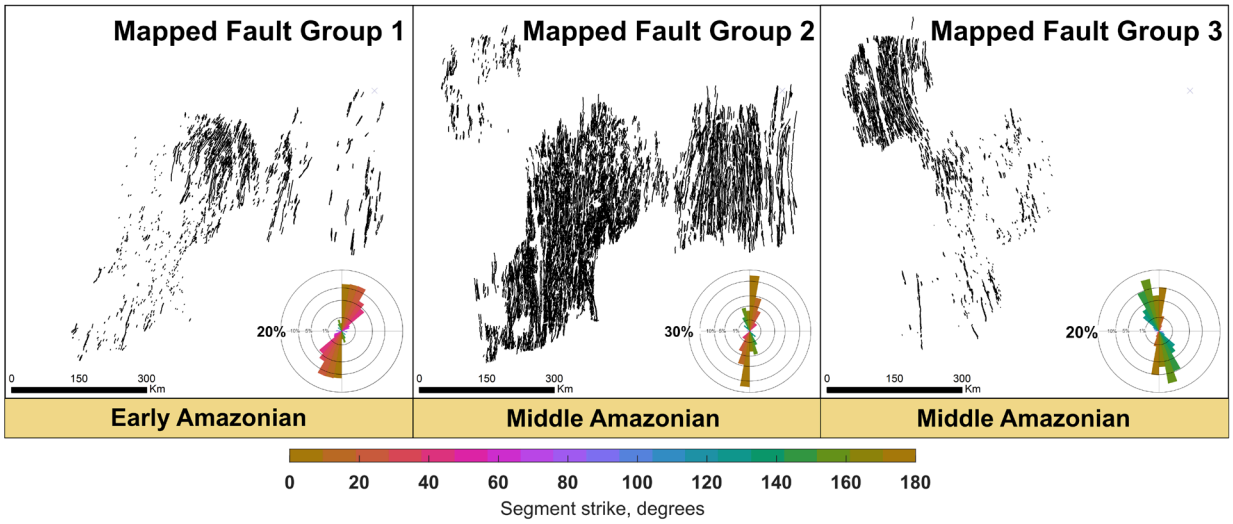

Figure 3.5: The three fault groups identified in Ceraunius Fossae and Tractus Fossae, with main fault orientations showed in the FracPaQ generated rose-diagrams. See Supporting Figure B.3 (Appendix B) for rose diagrams for each fault group, separated into each study area.

Group 1 is a relatively sparse group of faults, which crosscut the Tractus Fossae and Ceraunius South units. The main strike orientation is towards NNE, with some subtly curved faults within the Ceraunius South section of faults, which start with a NNE orientation, and then curves more towards the NE, the further north the trace goes. The faults in Group 1 have very few interactions with the Group 3 faults, so we therefore use the Group 2 faults to determine relative ages. The orientations of faults in Group 1 overlapped with the faults in Group 2 and were therefore distinguished from each other using cross-cutting relationships. In places where the two groups interact the faults in Group 1 are consistently crosscut by the faults in Group 2, making the Group 1 faults the oldest of the two groups.

Group 2 consists of faults with a largely N-S orientation, and the majority of them (the Ceraunius South faults) are radial to the main Alba Mons edifice. It is by far the most populous group, containing ~70% of all the mapped faults. The faults in this group are mostly linear, but due to heavy overprinting the faults appear to braid or branch in between each other (Figure 3.4b). The faults are largely contained within the unit boundaries, but Group 2 is the only group with faults which crosscut all three study areas and thus interacts with the two other fault groups.

The faults in Group 3 appear to crosscut the faults in Group 2 and are therefore the youngest of the three groups. These faults appear only on Ceraunius North and Ceraunius South and have almost no interactions with Group 1. However, similar to Group 1, a portion of faults in this group are also curved, though their orientation is mirrored from Group 1. In Group 3, the curved faults, which are located in the eastern part of Ceraunius North, curve from a NW to NNW orientation the more north the fault trace appears. The linear faults in the south and west maintain an NNW orientation through strike. The faults in Group 3 also show two very wide graben features, where the largest normal fault-bounding graben is ~10 km in width.

3.3.2. Strain

We measured the strain across all three defined fault groups, and determined maximum strains of 2%, 3.2% and 2.3% for Groups 1, 2 and 3 respectively. As both Groups 1 and 3 had a comparable number of faults (Table 3.1), with the faults spread over a similar area, the resemblance in strain % is not surprising. The strains for Group 2 are the highest, corresponding with the largest number of faults.

3.3.3. Absolute Ages

We determined the ages of the three units in Ceraunius Fossae and Tractus Fossae using CSFD and plotted the ages in Craterstats v.2. The crater data was constrained using a $4t^h$ root-2 binning, and a Poisson distribution fit (Michael et al., 2016). These mapped craters resulted in three best-fit Amazonian model absolute ages for the units, with Ceraunius North exhibiting a ~1 Ga younger age than the other two units (Table 3.2). The CSFD plots and associated n_σ plot for each of the three study areas, are shown in Figure 3.6. Generally, there is an acceptable fit of crater data to the isochrons, with some of the larger crater bins slightly separating from the isochron fit for Ceraunius North and South, but as they are still within their error bars, we consider these ages in the discussion section. The randomness analysis using the SDAA and the M2CND techniques, both fall within the ± 3σ area, and we therefore do not consider any of the crater data used to determine these absolute model ages to be too clustered or ordered to fit to the isochrons.

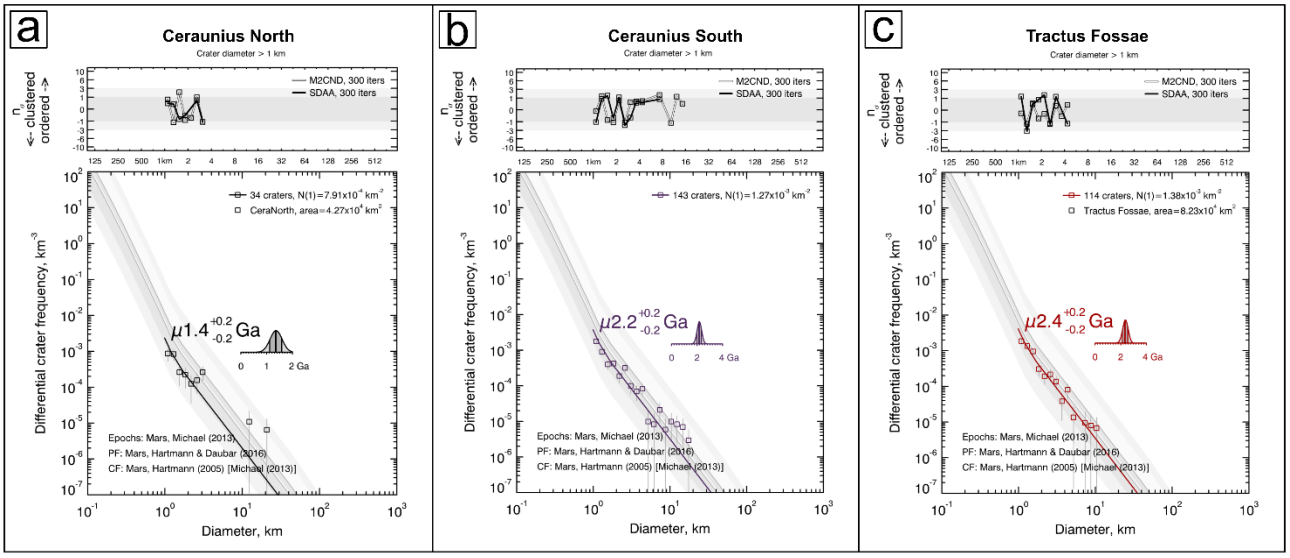

Figure 3.6: Crater Size-Frequency distribution (CSFD) plots produced in Craterstats v. 2 for A) Ceraunius North, B) Ceraunius South and C) Tractus Fossae. Note the n_σ plot above each isochron plot, presenting the results of the two Craterstats' randomness analysis methods.

Area Name	Unit name*	(N)Craters >1km	Unit age	Period
Ceraunius North	*Early Hesperian volcanic unit (eHv)*	34	1.4 ± 0.2 Ga	Middle Amazonian
Ceraunius South	*Early Hesperian volcanic unit (eHv)*	143	2.2 ± 0.2 Ga	Early Amazonian
Tractus	*Late Hesperian volcanic unit (lHv)*	115	2.4 ± 0.2 Ga	Early Amazonian

Table 3.2: Overview of the results of crater size-frequency distribution model ages for the three geological units in this study: Ceraunius North, Ceraunius South and Tractus Fossae. * Unit name is according to the Tanaka et al. (2014) mapping.

These results all suggest a maximum age for the mapped faulting in our study areas to be Amazonian, with the oldest material being Early Amazonian. This is the case for the faults in Group 1 (Figure 3.5), which crosscuts both Ceraunius South and Tractus Fossae, but not Ceraunius North. Due to the group being crosscut by Group 2 which is then crosscut by Group 3, we determine the Group 1 faults as the oldest of the mapped faults. Group 1 is then chronologically followed by Group 2 and then Group 3, where both groups are crosscutting the youngest unit, Ceraunius North, which has a Middle Amazonian age of 1.4 Ga (Table 3.2). For groups 1 and 3, the southern section of faults is highly fragmented, and shorter than the northern faults of similar orientation. We attribute this to the high degree of overprinting

of faults, where the high intensity faulting (Figure 3.4b) is obscuring the actual fault traces of any not N-S oriented faults.

3.3.4. Collapse Structures

During our mapping we came across four distinct types of collapse features, as described in the methods section. These were mapped separately, and we present an overview of the structures in Figure 3.7: The spatial distribution of mapped collapse features varies slightly across the three study areas, with Ceraunius North hosting 23.4% of the total collapse structures, 49.9% in Ceraunius South, and 26.7% in Tractus Fossae. Tractus Fossae is also host to the longest collapse structures, with average lengths of ~16 km, and the longest feature, a u-shaped trough, measuring 146 km long.

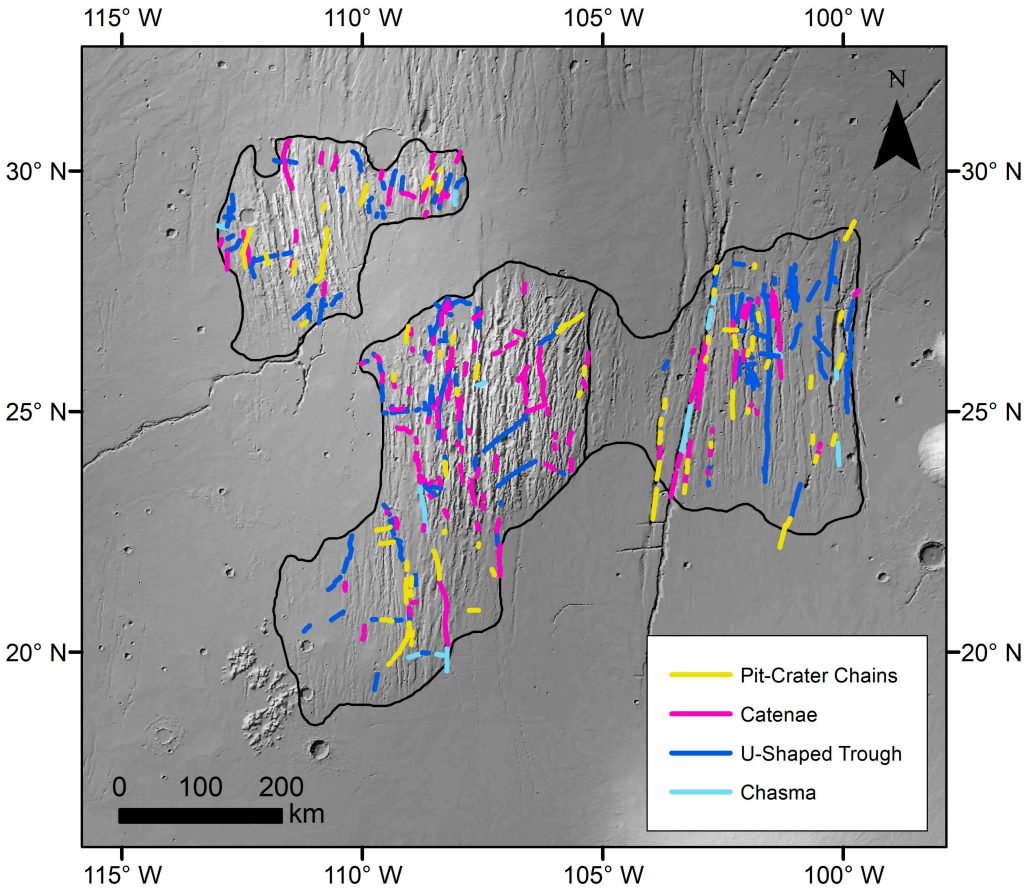

Figure 3.7: Location of mapped collapse features in the three study areas. Features are colour coded by type, as shown in the legend. Background is MOLA Hillshade overlaid by merged MOLA-HRSC DEM (200 m/px) (Fergason et al., 2018).

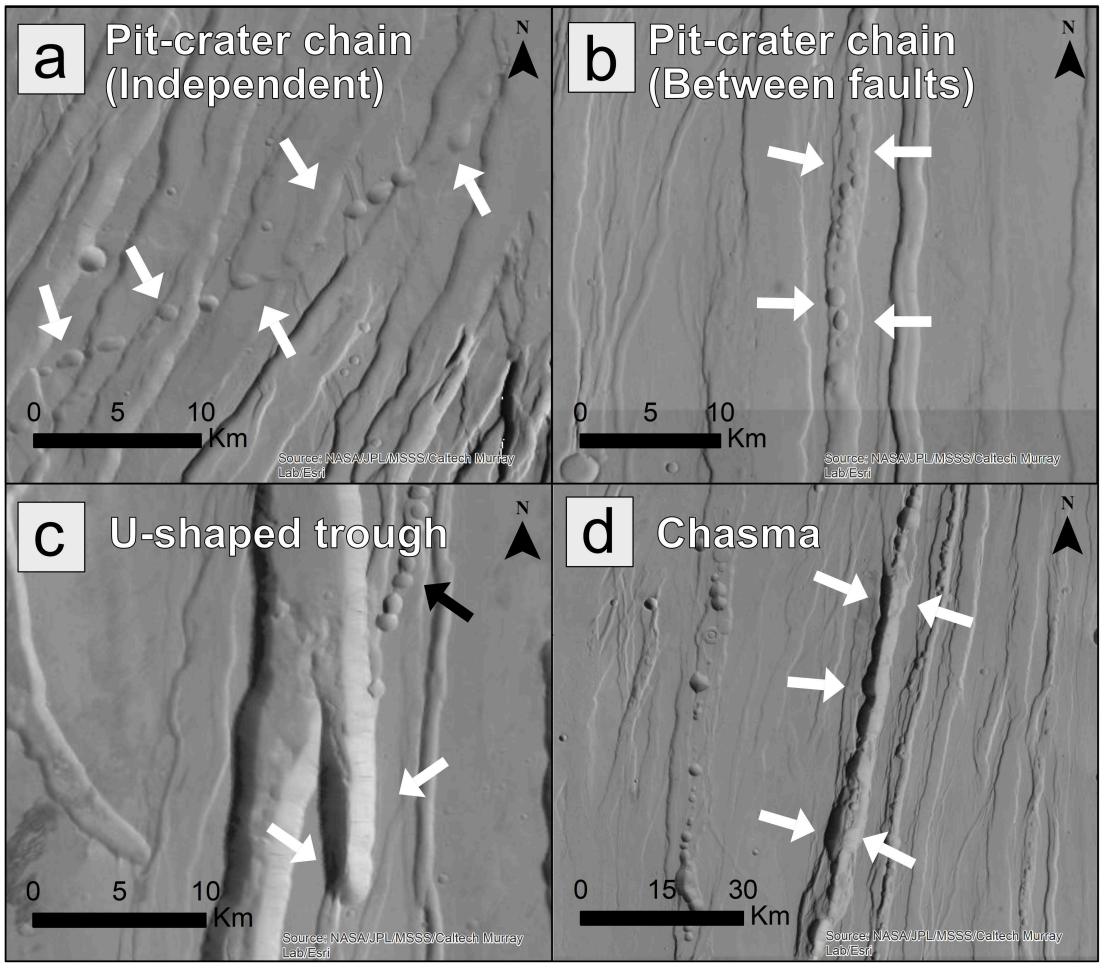

Figure 3.8: Example of a) independent pit-crater chains (Type 1). Feature centered at 26°51'13.03"N 105°38'22.07"W. B) Example of a pit-crater chain located between two faults (Type 2). Feature centered at 24°15'14.42"N 102°45'42.03"W. C) U-shaped trough example (white arrows). The black arrow shows a pit-crater chain. Image centered at 25°55'13.23"N, 100°10'0.38"W. D) Example of chasmata in Tractus Fossae (white arrows). Feature centered at 24°58'57.47"N, 103°12'27.86"W. CTX Mosaic Credit: Esri, Caltech Murray Lab, NASA, JPL, MSSS

We mapped a total of 81 pit-crater chains and 168 catenae (Table 3.3) across Ceraunius North, Ceraunius South and Tractus Fossae area. We found both pit-crater chains and catenae amongst all three mapped fault groups either dotted through the landscape independently from the faults or are located nested in between two graben-bounding faults (Figure 3.8a and 3.8b). The craters in the pit-crater chains vary between circular and oval in shape, with the long axis of the oval corresponding to the orientation of the chain itself. A portion of the pit-crater chains which are located within grabens show fault driven formation characteristics (e.g., en echelon distribution along strike, asymmetric pits etc.). The mapped pit-crater chains and catenae largely follow the N-S orientation of the majority of the faults in Group 2, however there are instances of short pit-crater chains with a NNE/NE orientations (Figure 3.7). The mapped u-shaped troughs appear as independent linear troughs, or as branches from the large graben-forming faults, where they usually occurred perpendicular to the main fault strike orientation. In cross section the troughs show steeply sloped sides (see Supporting Information Figure S1c), and, unlike the linear grabens, the troughs terminate in u-shapes, as in the example in Figure 3.8c. These features are found in all three study areas, but their large, striking, and complex appearance is the most evident in Tractus Fossae (Figure 3.7). The final mapped collapse features are the chasmata, which appear as a combination of the pit-crater chains and the u-shaped troughs with their sharp but circular edges (Figure 3.8d). These are generally the largest features of the four identified groups and can be up to 70 km long and are found on all three study areas (Table 3.3).

Feature name	Number of features	Prevalent Orientations	Cumulative length	Average length	Characteristics
Pit-Crater Chains	81	N-S/NNE	895.3 km	11.1 km	Separate craters in chain. Majority located within grabens, with some independent chains.
Catenae	168	N-S/NNE	1625.7 km	9.4 km	Crater chain, with craters interacting with each other.
U-shaped Trough	181	N-S/NE/E-W	2263.3 km	12.4 km	Non-tectonic troughs. Show underlying pit-crater chains in topographic data.
Chasmata	17	N-S/E-W	272.2 km	16 km	Large mass-wasting chasms, often oval shaped.

Table 3.3: Overview of mapped collapse features, separated into the four different types.

Comparing the linear features mapped on the CTX images with the MOLA-HRSC blend topographic maps, the u-shaped troughs and chasmata both reveal instances of what appear to be craters, or circular areas within the linear collapse features, which are much lower than the rest of the feature (Figure 3.9).

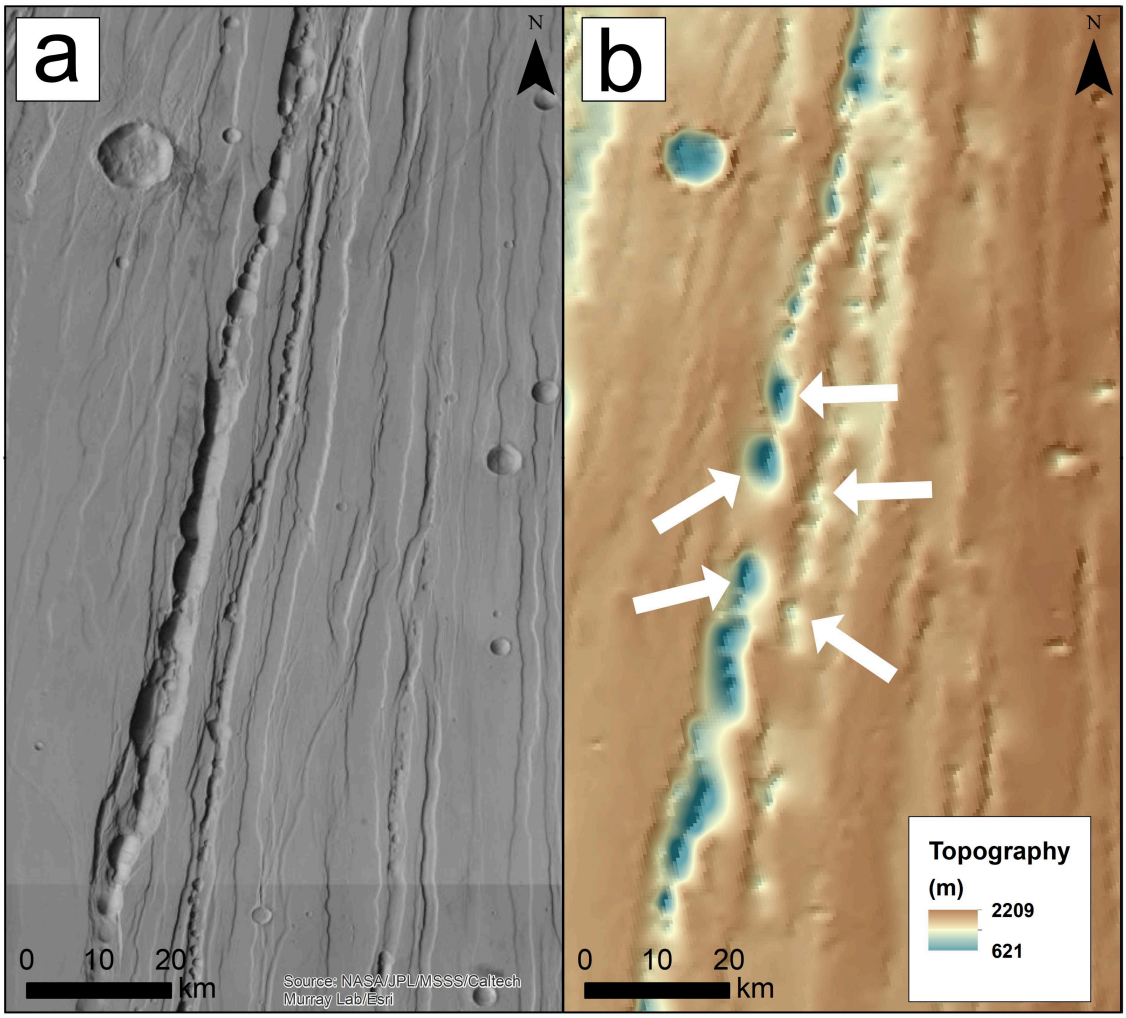

Figure 3.9: A) Example of linear structures on CTX global mosaic image (Credit: Esri, Caltech Murray Lab, NASA, JPL, MSSS), which on b) MOLA-HRSC blend topographic data, overlaid with MOLA hillshade of the same area, shows defined elongated crater morphologies of various sizes. MOLA-HRSC blend credit: Fergason et al., 2018.

In summary, the collapse features are all observed either within narrow grabens, positioned parallel to narrow grabens, or perpendicular to narrow grabens. This relationship with graben is especially true for the pit-crater chains, however they do also occasionally deviate from the orientation of the graben. In cases where the independent pit crater chains and the grabens interact, the crosscutting relationships always suggest that the pit crater chains are younger, though the time between the two is undefined.

3.4. Discussion

3.4.1. Determining the Fault Groups

Fault mapping in our three study areas revealed a series of highly dense graben formations (Figure 3.4C). The faults are predominantly linear (Figure 3.5) though the northern section of Ceraunius North and Ceraunius South host faults which exhibit a slight curvature, their shape suggesting a different extensional environment from the linear faults. Results from our work agrees with previous studies (Cailleau et al., 2005; Tanaka, 1990) in that the first stage of faulting consisted of the NE striking faults, followed by a N-S oriented graben formation. We also define a third stage of activity, younger than the NE and N-S orientations, with our Group 3 NW oriented faults.

3.4.2. The Revised Ages of Ceraunius and Tractus Fossae

The absolute model ages calculated in this study using CSFD on the three study area units, all resulted in Amazonian ages. This makes Ceraunius North 1 Ga younger than the other two units, and all three study areas 1-2 Ga younger than the previously reported ages by Tanaka et al., (2014) (Table 3.4).

Area Name	Unit name	Prev. age	Unit age	Period
Ceraunius North	*eHv*	3.65 Ga	1.4 ± 0.2 Ga	Middle Amazonian
Ceraunius South	*eHv*	3.65 Ga	2.2 ± 0.2 Ga	Early Amazonian
Tractus Fossae	*lHv*	3.55 Ga	2.4 ± 0.2 Ga	Early Amazonian

Table 3.4: Comparison of previous (Tanaka et al., 2014) CSFD ages, and the ones calculated in this study (Unit age).

Similar to the revised Ulysses Fossae ages (2.6 ± 0.2 Ga and 2.4 ± 0.2 Ga) determined by Shahrzad et al. (2023), our CSFD ages for southern Alba Mons are part of a significantly more detailed study of the craters in this specific area, when compared to ages from the global Tanaka et al. (2014) (Table 3.4). This focus on just three specific units, enables more specific statistics, when determining the ages of the units. The ages found in this study thus expectedly deviate from which the previously determined ages (Table 3.4). However, the 1.4 Ga age for Ceraunius North is an outlier, and we considered the possibility of flooded craters potentially artificially lowering the age of Ceraunius North. However, after considering the morphology of the mapped craters, we did not observe sufficient evidence to attribute the exceptionally young unit age to flooded craters alone, though it remains a definite possibility. Considering the appearance of the three study areas, the younger age for Ceraunius North found in the results is not reflected in the appearance of the grabens, which are similar to the two other study areas.

With the long-term magma source in a single plate planetary system, it is likely that volcanoes have been periodically active in Tharsis between their Hesperian construction and their most recent caldera and resurfacing ages, which for some volcanoes continued into the Late Amazonian (Werner, 2009). For Pavonis Mons, the main edifice was constructed 3.65 Ga ago (Werner, 2009), with the most recent caldera CSFD ages as young as 130 Ma (Robbins et al., 2011) and 80 Ma (Werner, 2009). Ascreaus Mons was likewise constructed in the Hesperian, 3.65 Ga ago, with the most recent CSFD determined ages between 50-100 Ma from the flanks of the volcano. Additionally, there are CSFD determined Early - Middle Amazonian ages of craters and resurfacing events for the Tharsis Montes, where a study by Werner et al. (2009) determined a strong Middle Amazonian resurfacing event for Pavonis Mons 1.2 Ga ago. This, along with Hesperian, Early, Middle and Late Amazonian flank and caldera ages for Ascreaus Mons, and Hesperian and Middle and Late Amazonian flank and caldera ages for Pavonis Mons, show evidence of a long-lived episodic history of volcanism for the Tharsis Montes. This is also the case for the giant radiating Tharsis dikes (e.g. Acheron, Phlegethon and Tractus Catena), for which emplacement ages range between Noachian and the Amazonian, based on the stratigraphic relationships between the structures (Wilson & Head, 2000). For Ceraunius Fossae specifically, a study by Krishnan and Kumar (2023) determined a continuous history of volcanic eruptions during the entirety of the Late Amazonian. Though the majority of the studied lava flows were dated to the Late Amazonian, Krishnan and Kumar (2023) also identified Early to Middle Amazonian lava flows in Ceraunius Fossae. Again, this age is likely the reflection of the most recent activity, which marks the end of a long-lived period activity from a Ceraunius Fossae centred magmatic source. This is all consistent with the inferred longevity of the episodic magmatic and volcanic activity in Tharsis (e.g. Bleacher et al., 2009; Wilson et al., 2001). In terms of graben activity, studies by Ivanov & Head (2006) and more recently Krishnan & Kumar (2023) also looked at the Ceraunius Fossae grabens, as a part of larger studies of the Alba Mons area. The former study determined a late Hesperian to early Amazonian age for radial graben formation in Ceraunius Fossae (Ivanov & Head, 2006).

Comparing these studies to our cratercounting results, it seems reasonable to suggest that the magmatic systems associated with Tharsis, and specifically the Tharsis Montes and Ceraunius Fossae, were active during the three ages determined in this study. The scarcity of Early to Middle Amazonian eruptive magmatic activity on the surface is likely a result of the extensive Late Amazonian volcanism (Christoph & Garry, 2017; Krishnan & Kumar, 2023; Pieterek et al., 2022) covering earlier structures. It may also

reflect a period during the Early and Middle Amazonian, where the majority of the magmatic activity was confined to the subsurface.

3.4.3. Fault Formation Mechanism

With defined groups and ages, we examine the morphology and appropriate stress fields which would be responsible for the orientation of the faults in order to evaluate the sources of the mapped faults. The mapped orientations of the faults suggest three distinct stress fields, one responsible for the three different orientations of faults in Ceraunius North, Ceraunius South and Tractus Fossae (Figure 3.5). The morphology of the faults in groups 1 and 2, and the linear faults in Group 3 (i.e., narrow grabens, uniform width and depth along strike, equal spacing between faults in the same group) along with their location in the highly active Tharsis volcanic province, enables our interpretation of mapped faults in our study forming as a result of diking (see Shahrzad et al., 2023, for a description of dike-induced graben formation mechanism). This is contrary to a purely tectonic extension origin, which usually manifests as much larger with fewer grabens over such an area (Fernández & Ramírez-Caballero, 2019; Shahrzad et al., 2023). This interpretation is also aided by the orientation and location of collapse features, which follow the paths of grabens in the groups. This is, however, not the case for the eastern curved faults in Group 3. These faults are wider spaced, and do not have any collapse features within the graben traces. We therefore reject a dike-origin for these faults and suggest a purely tectonic origin for the curved Group 3 faults. The formation of these features is further discussed in section 4.4.3.

On Earth, these types of large scale igneous dike systems are observed as a part of large igneous provinces (LIPs) (Ernst et al., 2019), in areas such as the giant radiating Mackenzie dike swarm (a part of the Mackenzie Large Igneous Province on the Canadian Shield) and the Liberian dike swarm associated with the Central Atlantic Magmatic Province (Marzoli et al., 2018). Additionally, examples of dike-induced surface structures have been identified, where both dike geometry and the topography of paleosurfaces has been recognized. These examples are found in the Franklin-Natkusiak event in Canada (Rainbird, 1993), the Proterozoic event in Baltica (Alapieti, 1982), and most recently in 3D seismic reflection data in offshore NW Australia (Magee et al., 2023). Terrestrial dike swarms as a part of LIPs can reach similar distances to Martian dike swarms of >3000 km. However, the duration for their emplacement is limited within a few million years (Ernst et al., 2001). We expect the Martian dike emplacement to have had a longer duration (> 5 Ma), as the single-plate structure of the planet allows for magmatic activity to persist for much longer at the same locations.

3.4.4. Cavities Causing Observed Collapse Structures, Originating from Diking Processes

We mapped a significant amount of collapse structures (pit-crater chains, catenae, u-shaped troughs and chasmata) in Ceraunius (North and South) and Tractus Fossae. Common for all four features are their relative younger ages, as all the features crosscut the faulting in the area. We consider the process that may have created them, and the connection to the surrounding faulting and their origins.

Our mapping revealed that the chasmata and u-shaped troughs both show patterns of pit-crater chains when examining the MOLA-HRSC topography in addition to the CTX images (Figure 3.9). Combining this with the erosional evolution from pit-crater chains to catenae, we consider the four collapse structures as 3-4 steps in the erosional evolution of an initial pit-crater chain (Figure 3.10a), an evolution initially suggested by Wyrick et al. (2004). This implies a common initial formation mechanism for all the structures, which evolves with time through different stages, resulting in with either a u-shaped trough or a chasma.

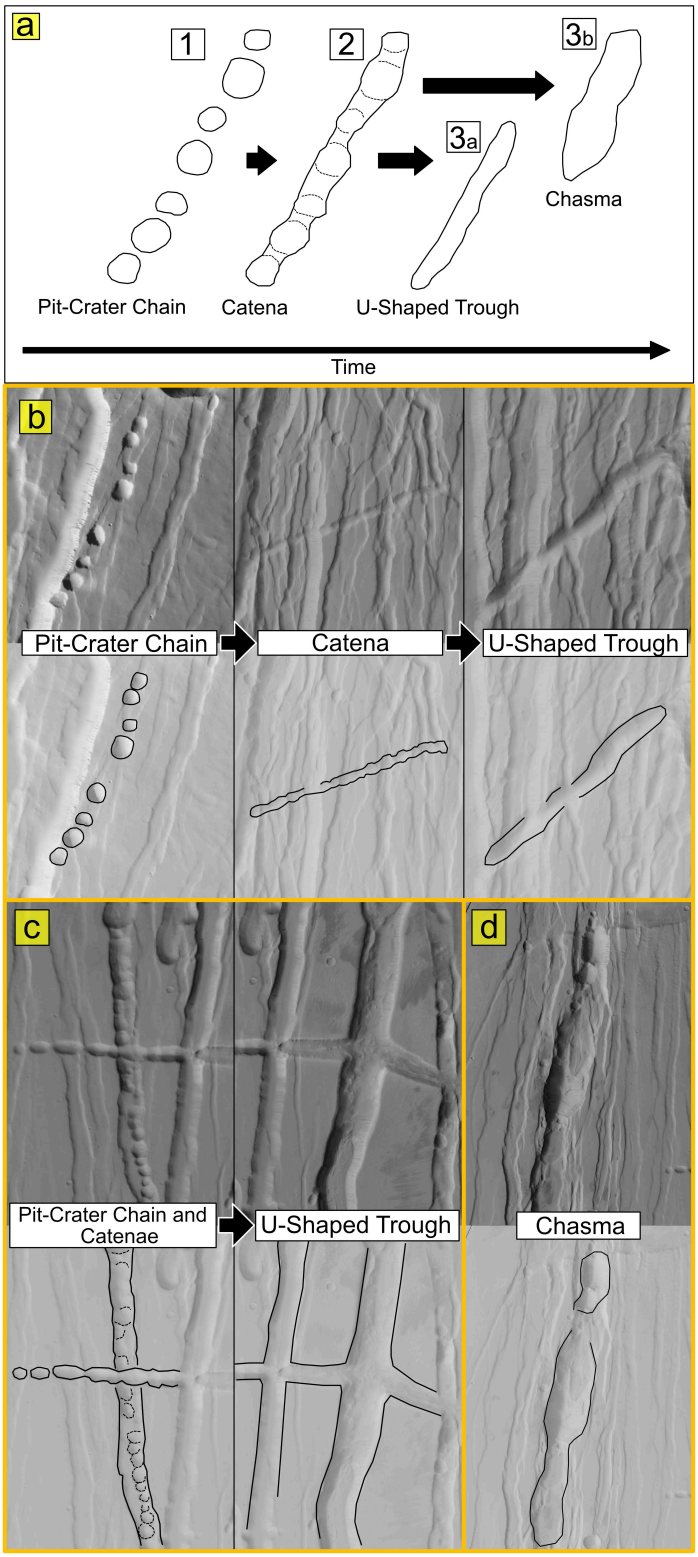

Figure 3.10: Overview of collapse structure evolution. A) evolution from pit-crater chain to either u-shaped trough or chasma. B) Examples of proposed pit-crater chain (feature centered at 29°39'32.34"N, 108°22'43.84"W) to catena (feature centered at 25°4'16.94"N, 106°24'2.90"W) and to u-shaped trough (feature centered at 24°18'32.85"N, 107°18'39.24"W) evolution, with CTX image on the left, and interpretation on the right. C) Example of more complex trough development through intersecting pit-crater chain and catenae, with image centered at 26°41'23.8"N, 102°16'51.67"W. End result example of development is the complex troughs centered at 26°40'54.34"N, 102°0'44.84"W D) Example of Chasma, with feature located at 26°59'14.42"N, 102°46'2.56"W. CTX background Global Mosaic credit: Esri, Caltech Murray Lab, NASA, JPL, MSSS

Previously, the collapse features have been explained by a collapse of material into subterranean cavities (Hardy, 2021). However, it is still disputed by which mechanism the cavities are created under the Martian surface. There are several proposed origins for cavity formation, with the most common two being 1) cavities due to the rapid withdrawal, or volatile outgassing of magma in a dike (Mège et al., 2003; Scott et al., 2002), and 2) cavities produced by dilational faulting in cohesive material (Ferrill et al., 2011; Wyrick et al., 2004). To explore the feasibility of these origins, we consider our mapped collapse features.

3.4.4.1. Pit-Crater Chains and Catenae

Similar to Mège et al. (2003), we consider the catenae as an alignment of interacting pit-craters in a chain, and thus consider their formation from the same mechanism (Figure 3.10a and 3.10b). Our mapping showed two different types of pit-crater chains (PCCs) and catenae.

The first variety of pit-crater chains and catenae are found within the mapped grabens and follow their orientation along strike (Figure 3.8b). The second variety of mapped PCCs and catenae do not appear within grabens, although the majority still follow the fault orientations. However, there are some examples of independent PCCs and catenae which do not follow the nearby fault orientations (Figure 3.8a). The size and shape of the craters are equally variable between the two types, but their orientations differ significantly. The PCCs from type 1, follow the exact orientation of the mapped grabens and are often located on the graben floor right along the side of a graben-bounding fault (See Figure 3.8b). These PCCs and catenae all follow the orientations of faults in Group 1, 2, and the linear faults in Group 3 (Table 3.4).

The remaining mapped PCCs and catenae are not bounded by any faults, yet they still follow the orientations of the fault in Group 1 or 2, either N-S or NNE. Due to the lack of surface faults or fractures associated with them, we cannot attribute these collapse features to extensional dilation fractures alone, based on the previous criteria (Cushing et al., 2015). However, we do still determine them to be diking-induced, where the dikes producing the non-graben bound PCCs and catenae did not evolve sufficiently in order to induce any surface grabens.

Of the two common PCC formation theories: dike-induced and dilational faulting (e.g. Ferrill et al., 2011; Hardy, 2021; Wyrick et al., 2004), let us consider both theories. As mentioned, the PCCs display fault driven formation characteristics, which would suggest a tectonic origin. While the mapped PCCs are located in large-scale extensional environments, we have determined the source of the extensional faulting in the study area to be largely dike-driven. Dilational faulting is considered a purely tectonic process (Wyrick et al., 2004), where extension in a heterogeneous layered material, allows unconsolidated material to fall into cavities developed in an underlying layer of more competent material. For the diking-

related formation, volatile outgassing, magma withdrawal or interactions with the cryosphere from an arrested dike-tip, can produce cavities for the overlying material to collapse into (Scott et al., 2002; Wyrick et al., 2004). Depending on the ascending dike's development, this could occur coevally or post dike-induced graben formation. Both these options would explain the observed PCC formation. As we have determined pervasive diking in the area (i.e., the mapped graben), instances of magmatic activity (e.g., Early to Late Amazonian lava flows mapped by Krishnan & Kumar (2023)), we consider it more likely for the formation of the mapped PCCs to be due to or related to the diking in the area. Whether the cavities are a result of dilational faulting produced by the arrested dike tips, or from another process, e.g., rapid withdrawal of magma or volatile outgassing, we cannot determine. However, we do reject that our mapped pit-craters are a result of explosive eruptions from the ascending dikes, as we see no evidence of lava flow or eruptions associated directly with the mapped PCCs. As the mapped PCCs are consistently younger than the grabens, we suggest that the PCC formation is related to later episodes of diking, where the magma has largely followed the paths of the graben-forming dikes. These later episodes may have ascended to an even shallower depth than the previous dikes in order to create the cavities closer to the surface, and either 1) created further extensional faulting within the wider original grabens, where the path was already weakened, or 2) magma degassed in the subsurface, potentially due to interactions with ice or water, creating the cavity that enables the PCC formation.

3.4.4.2. U-shaped Troughs and Chasmata

The orientation of the U-shaped troughs varies immensely, with some following the fault pattern and some changing orientation along strike. This may reflect erosion between Type 1 and Type 2 pit-crater chains and catenae, as the example shown in Figure 3.10c. A recent study of Noctis Labyrinthus found that a volatile-rich layer (i.e. water ice) can facilitate the development from pit-craters to trough structures, specifically by the sublimation of a thermokarst layer (Kling et al., 2021). Further inspection of the mapped u-shaped troughs and chasmata in our study do show few (<5) instances of potential thermokarstic terrain (e.g. shallow, irregular depressions (Rodriguez et al., 2016)), but they are not pervasive enough to base our interpretation on. The intense erosion that has facilitated the u-shaped troughs and chasmata may then be attributed to the intense magmatic activity forming large and cohesive pit-crater chains, and the elevation of the units compared to the surroundings, having enabled more active erosion of the collapse features on the unit.

We interpret the chasmata as another end member of the PCC and catenae evolution chain, either as a 4th step following u-shaped trough formation, or as a 3rd step, following catenae formation, bypassing the u-shaped trough formation (Figure 3.10a and 3.10d). This is a result of intense erosional formation,

characterised by the large structure and evidence of mass-wasting along the interior of the chasmata. This facilitates the growth of the structure, when the slopes become destabilised and induce landslides, widening the cavity (Mège et al., 2003). The large size (Table 3.4) of the mapped chasmata could also reflect a larger subsurface cavity than the PCCs, catenae and u-shaped troughs.

3.4.5. Considering the Origin of the Mapped Fault Groups

Assuming dike-related tectonic activity for the majority of our faults, we can thus identify two factors in their formation: the stress field the dikes have propagated in, and the source of the magma. As the study areas are located in an extremely large and active volcanic zone, there are a high number of magmatic and stress-field candidates.

3.4.5.1. Regional and Local E-W Stress Trajectories

Our initial approach is to broaden the scope and using a similar method to Shahrzad et al. (2023), we investigate the graben orientations, and determine if they are radially fanning from any volcanic centres. Mapping out geodesic radial paths from approximate volcanic centres near the study area (Alba Mons, Olympus Mons, the Tharsis Montes, etc.) shows no clear relationship between the mapped faults to a single volcanic centre, particularly regarding the most prevalent fault group, Group 2 (Table 3.1). In a general sense, we can assign the N-S oriented faults in Ceraunius Fossae to lie in a radial orientation to Alba Mons, but this is not the case for the N-S faults in Tractus Fossae, where the closest radial orientation is from Ascraeus Mons (Figure 3.11). However, considering the lack of pervasive fault orientation and volcanic centre relationships, what we have instead, are many interacting stress fields from different orientations. These are both regional and local in scale, and in our study area, they all appear to produce N-S oriented faults structures. This means that there is either an E-W regional extensional field overpowering all other extension orientations, or that the local and the regional stress fields are reinforcing each other. We therefore reconsider the main N-S orientation of the majority of our faults (Table 3.1) and determine the presence of a prevalent regional E-W extension regime over the entire study area.

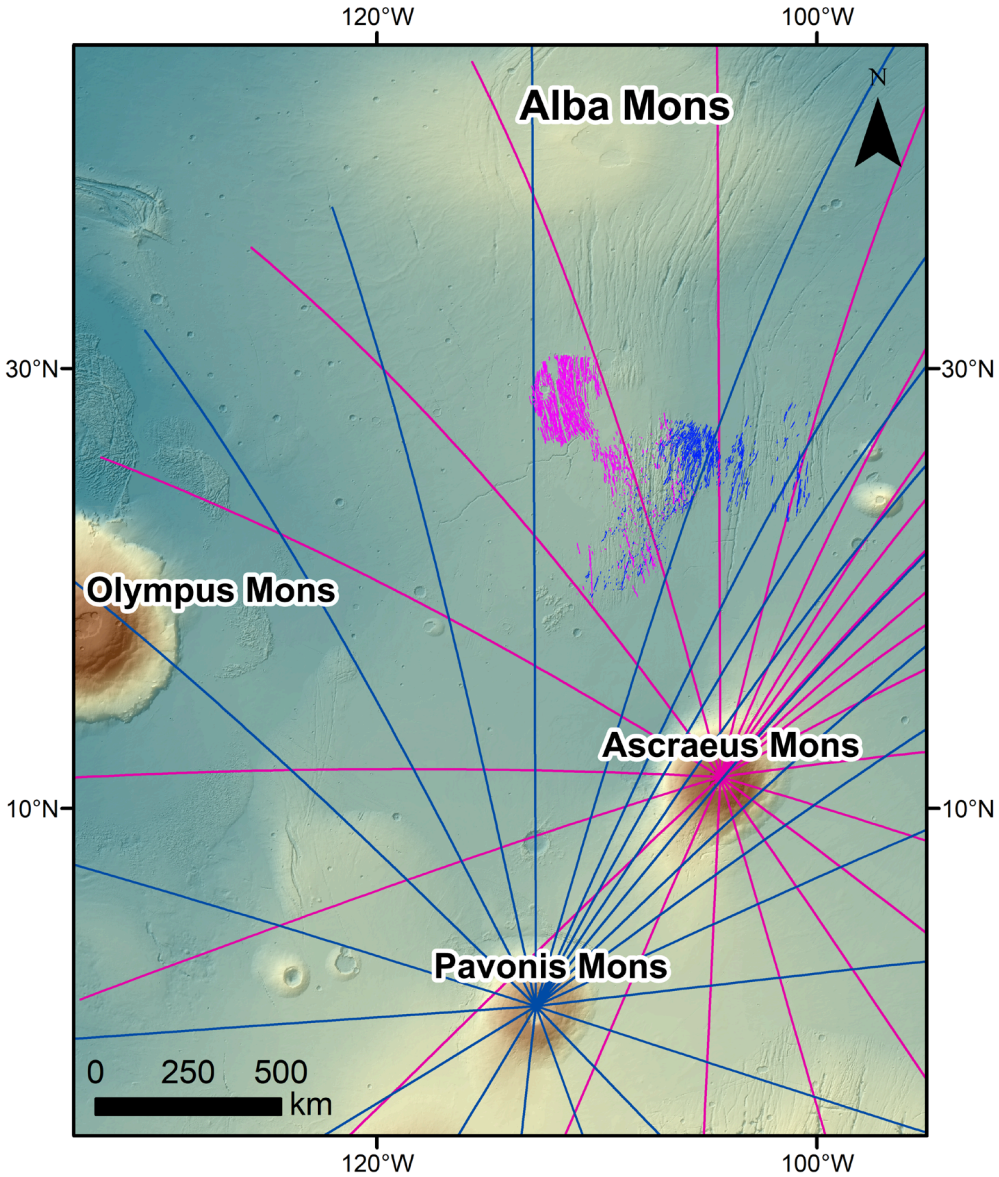

Figure 3.11: Projected geodesic radial faulting orientations from the two main volcanic edifices Pavonis Mons (blue) and Ascraeus Mons (pink), in relation to mapped fault groups, with Group 1 in blue and Group 3 in pink.

The source of this E-W extension is likely regional stresses from the large-scale development of Tharsis, with potential assistance from any local extension from Alba Mons and Ascraeus Mons (Figure 3.11). This regional Tharsis extension, and the associated N-S oriented grabens, has previously been attributed to a regional E-W Tharsis-wide extension driven by a stress field centred in Syria Planum, located to the south of the study areas (Plescia & Saunders, 1982; Tanaka, 1990). In the Tanaka (1990) study the evolution is determined to originate with an initial isostatic doming, producing radial grabens proximal to the deformation centre, which is then followed by a period of flexure, producing the distal grabens we see in Ceraunius and Tractus Fossae (Tanaka, 1990). As we consider these features to be dike-

related, Syria Planum could be a potential magma source, though we consider a more proximal source, such as Ceraunius Fossae or Alba Mons, more likely.

3.4.5.2. Magmatic source

With this regional E-W extension in mind, we consider the source of magma for the propagating dikes. Further examining the study area in the context of the surrounding area, several features can be highlighted. First, both Ceraunius North and Ceraunius South (and to some degree Tractus Fossae), are at an elevated topography to the surrounding lava plains (Figure 3.12a). Second, Bouguer gravity maps of Mars (Genova et al., 2016) reveal two low density zones within Ceraunius North and South, with the lowest value of -288 mGal located in Ceraunius North (Figure 3.12b). Negative gravity anomalies can suggest underlying hotter and/or lower density crustal material and is as such a useful indicator for the presence of plumes. Lastly, examining the global crustal thickness map of Mars (Genova et al., 2016) which accompanies the gravity data, we observe a zone of relatively higher crustal thickness (~20 km thicker) associated with the topographic highs (Figure 3.12c). The localised increase in ascending partial melts may be responsible for the increased the thickness of the crust. This is however assuming that the current measured crustal thickness is similar to the thickness ~1.4 Ga. Note that these anomalies are not apparent for Tractus Fossae.

Together, along with the mapped dike-related faulting, these observations suggest a zone of magma,

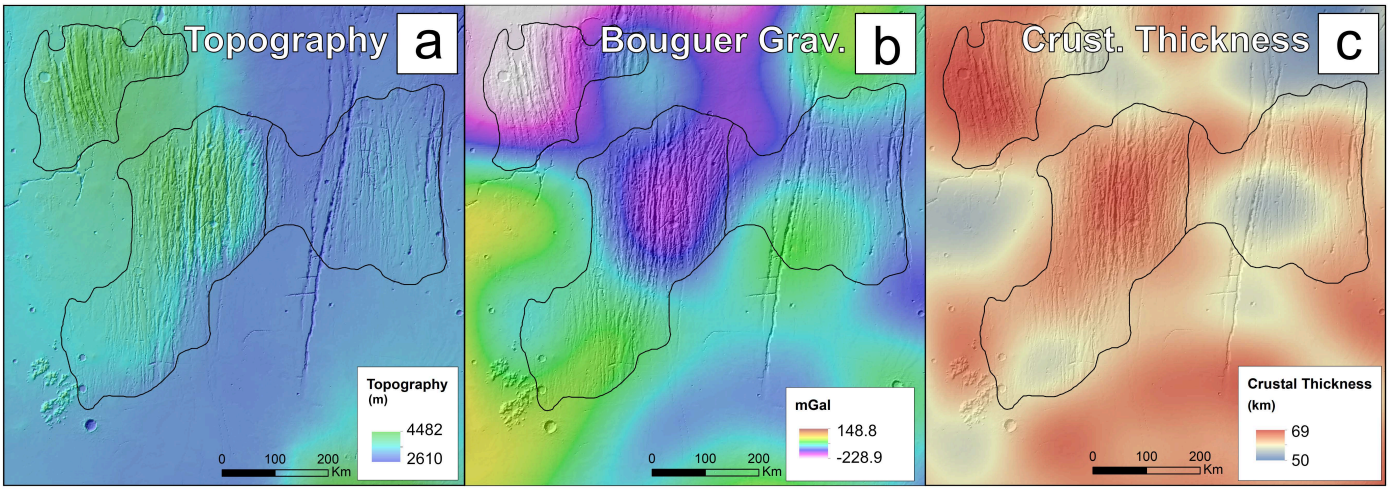

Figure 3.12: A) MOLA Hillshade overlaid by merged MOLA-HRSC Digital Elevation model (200 m/px) (Fergason et al., 2018) topographic map of Mars. B) Bouguer gravity anomaly map for Mars (centred on study area) from Genova et al. (2006). C) Crustal thickness map of Mars from Genova et al. (2006).

located underneath the Ceraunius Fossae area. These observations are also consistent with a more recent study by Plesa et al. (2023) which suggested several zones containing high melt fraction portions on Mars, which may still be active today. One of these identified high melt fraction (7-8 %) zones is located beneath Ceraunius Fossae, and is particularly pronounced in the scenario of a Mars with a crustal density

difference between the Northern and Southern hemisphere (Plesa et al., 2023). This zone of magma is potentially a plume off-shoot from the Alba Mons plume, or a zone of magmatic underplating. Both instances would be able to produce the vertically propagated dikes we have mapped in this study.

The 2023 study by Krishnan and Kumar examined boulders, pit-crater chains, lava flows, and select grabens in the Alba Mons area. Their findings concluded that magmatic underplating under Ceraunius Fossae was responsible for the small shield volcanism found in the area. Based on their surface ages, the study determines that the activity of this magma source has been migrating south during the Late Amazonian (Krishnan & Kumar, 2023). However, we suggest that the migration of the subsurface magmatic plumbing may have begun even earlier than this, emplacing dikes, and subsequent grabens from the Early-Middle Amazonian. This set the framework and was followed by the extensive period of surface eruptions in the Late Amazonian, identified by Krishnan and Kumar (2023). This magmatic reservoir is likely an off-shoot or otherwise related to the larger Alba Mons plume (Krishnan & Kumar, 2023; Pieterek et al., 2022). Extension values also support a more directly intense extensional environment immediately above the recognized magma source, with 3.2% extension in Ceraunius South compared to the maximum 1.20% in the NS faults in Tractus Fossae. Considering the orientation of our mapped graben features, we suggest a pattern of vertically propagating dikes, radial above a centralized Ceraunius Fossae magma source. Figure 3.13 illustrates a potential Ceraunius Fossae centred magma source, in this case by underplating, as suggested by Krishnan & Kumar (2023). Another region of Tharsis has also been suggested to host a magmatic underplating source, in the southeast of Tharsis, west of the Tharsis Montes (Richardson et al., 2021). This particular magma source has been determined to be active within the last 500 Ma years (Richardson et al., 2021), supporting the longevity of the Tharsis magmatic activity.

A Ceraunius Fossae centred magma source scenario would explain the mapped N-S oriented grabens in Ceraunius Fossae but does not entirely justify the dike-induced grabens in Tractus Fossae. Though deformational centres related to magma chambers can vary laterally, for example, with an asymmetric magma chamber (Gudmundsson, 2020), we suggest a combination of E-W radial stresses on the surface above the magma chamber, along with any E-W radial extension fields radiating from the Alba Mons and Ascraeus Mons volcano-tectonic centres, are responsible for the N-S oriented faults in Tractus Fossae. The overlapping E-W stress fields from Alba Mons, Ascraeus Mons and likely, Syria Planum, reinforced each other and facilitated the vertical diking in Tractus Fossae from a Ceraunius Fossae

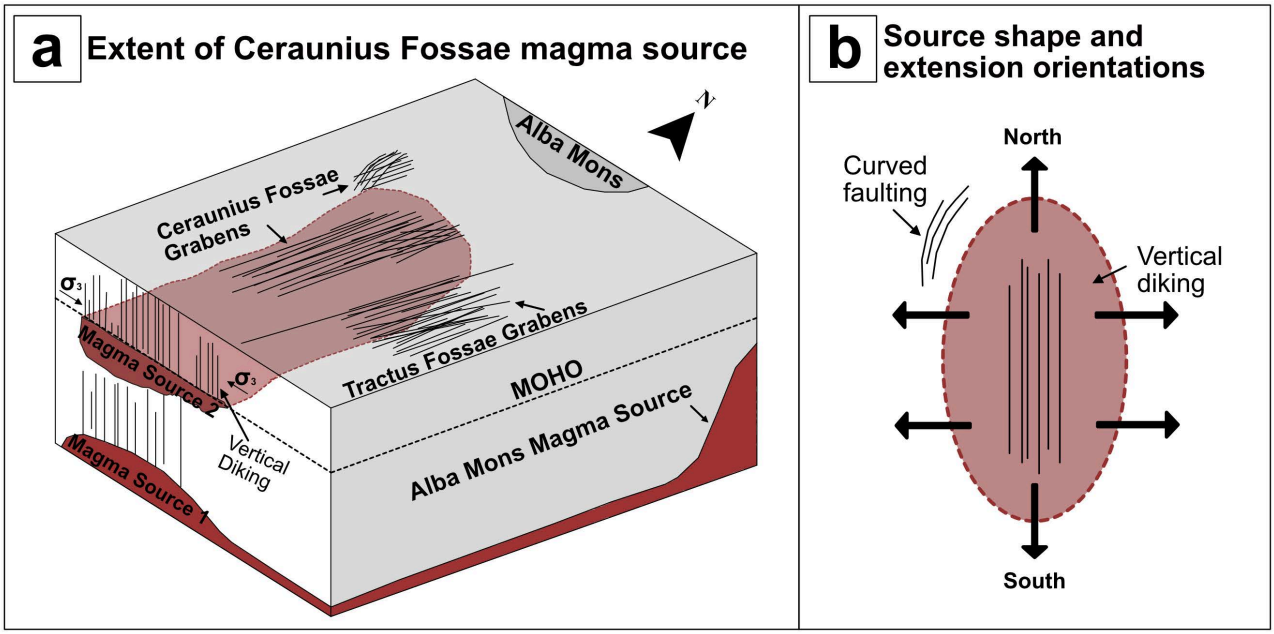

Figure 3.13: a) Diagram of suggested Ceraunius Fossae magma source. Magma source 1 is the deep source feeding the shallower Magma Source 2, which in this model is magmatic underplating, but could also be a plume off-shoot from an Alba Mons plume. Vertical diking and thus the N-S grabens above the red Magma Source 2 area, is a result of the E-W extension from the magma source, combined with a regional E-W extension. This results in N-S faulting immediately above (Ceraunius North and South) and east (Tractus Fossae) of the supposed Magma Source 2. b) Shows a simplified suggestion of the magma source shape, and the surface faults the orientations of extension produced.

3.4.5.3. Sources of Extensional Stresses for Each Fault Group

Considering these stress trajectories and potential magma sources presented, we determine the source of extensional stresses for the mapped fault groups.

Group 1: An exact source for the stresses responsible for Group 1 is difficult to determine with certainty, as the combination of location and orientation can result from a number of extensional events. The faults in Group 1 follow an NNE orientation. We have determined the extension to be dike-induced, which

corresponds to orientation of the largest collapse features mapped in this study. With this in mind, we consider the orientation of features surrounding Alba Mons. Acheron and Phlegethon Catena, located on the SE flank of Alba Mons (Figure 3.1), are both parallel in orientation to the mapped Group 1 faults, with an NNE strike. These two Catenae are considered the surface expressions of dikes (Raitala, 1988; Scott et al., 2002). This is also the case, as suggested for Tractus Catena (see location on Figure 3.1), which we have also identified as a collapse structure in this study. A study by Mège et al. (2003) likewise suggested a dike-induced origin for the catena. The similar orientation and collapse-induced morphology between the mapped faults in our study and the origins for Acheron, Phlegethon, and Tractus Catena, suggests a correlation between their origins. This would put Group 1 faults in the same system of Tharsis radial dikes which have driven the formation of large grabens with similar orientation, during the Middle Amazonian (Okubo & Schultz, 2005; Scott et al., 2002). In addition to the Tharsis-radial scale diking, we also consider the effect of large volcanic edifices, located within ~1000 km radius from the study area. Considering the radial patterns using the volcanic edifices as an approximate centre of deformation, Group 1 faults have a best fit with projected radial orientations from Pavonis Mons (Figure 3.11). Robbins et al. (2011) determined a Pavonis Mons summit caldera age as young as 130 ± 20 Ma, which together with the Early Amazonian Pavonis Mons activity recorded by Bouley et al. (2018), suggest a (likely periodical) history of magmatic activity which continued through the Amazonian. This corresponds to the early Amazonian maximum age for Group 1 determined in this study. We therefore propose an origin for the Group 1 faults, related to NNE diking and oriented by Pavonis radial stresses, which may have been emphasised by crustal weakening associated with previous large-scale Tharsis radial diking.

Group 2: The Ceraunius Fossae part of Group 2 grabens (Figure 3.5) is the result of vertical diking, likely from a local plume or magmatic underplating source (Figure 3.13a). For reasons discussed above, Tractus Fossae appears different as it lacks the evidence of a low-density anomaly underneath and is thus not considered to be located directly above the magma source. The extensive N-S diking in Group 2 is likely the result of several interacting stress fields, namely the regional Tharsis E-W extension, and E-W extension related to Alba Mons and Ascraeus Mons, though we still consider an Alba Mons plume, or the potential Ceraunius Fossae underplating, the source of the dikes, with the surrounding extensions explaining the dike orientations. A highlighted feature of this group is the high density of faulting (Figure 3.4c) in Ceraunius South. We consider it a likely overprinting of several stages of largely N-S oriented faulting, which are near-impossible to distinguish from each other.

Group 3: The majority of the faults mapped in this group are in Ceraunius North, and it contains both linear and a portion of curved faults. Curved faults are found in several places on Mars, such as the Alba Fossae around Alba Mons (Öhman & McGovern, 2014), and around other volcanoes such as Labeatis Mons (Orlov et al., 2022). Common for these, is that the structures all curve around a volcanic centre, which is not the case for the northern Group 3 faults. As discussed above, we do not consider these faults dike related, a theory which is strengthened by the lack of collapse feature which follow the orientation of the faults. As there are no signs of a buried volcanic structure near the faults, we consider their origin a more likely result from interacting stress fields. However, instead of reinforcing each other, as in the case with Tractus Fossae, they change the orientation of the structure. Figure 3.13b shows a suggestion on how this may occur. Here we assume an elongated magma source, where the bounding extensional stresses results in curved grabens. Curved grabens are also indicative of either loading or deflation associated with a volcanic centre (Cailleau et al., 2003; Mège & Masson, 1996). On Earth, this is referred to as a "wristwatch pattern", and can be found around volcanoes such as Fantale in the Afar rift, and Hengill in Iceland (van Wyk de Vries & Matela, 1998). As mentioned, we do not observe any structure the faults would be circumferential to, but deflation of a volcanic centre (e.g., by cooling or magma withdrawal), consequently covered by more recent lava flows, remains another possibility. The reason for the limited spatial occurrence of the curved Group 3 faults, may reflect a more shallow portion of the magmatic source driving the extension, aided by any pre-existing weaknesses as a result from the evolution of Alba Mons (Cailleau et al., 2003). Additional modelling of the proposed Ceraunius Fossae magma source would be needed to confirm this.

The linear NNW trending faults in this group have collapse features in the same orientation, and within the grabens, and their radial orientation to the nearby Ascraeus Mons suggests diking related activity as the source of these faults. Ascreaus Mons is located an approximate 800 km from the centre of Ceraunius North (Figure 3.11), which would reflect the travel distance of potential radial dikes. In Tharsis, radiating dikes have been determined to travel as far as 1000 km (Scott et al., 2002), with a maximum distance of 3000 – 4000 km (Wilson & Head, 2000) from their source. We find similar examples on Earth, where the largest fanning dike swarm, the Mackenzie swarm, contains dikes that have travelled nearly 2500 km (Ernst et al., 2001). The linear and curved faults in Group 3 appear side-by-side, so their slight change in orientation cannot be distinguished temporally.

3.4.6. Stages of Deformation South of Alba Mons

We have identified four main stages of structural activity in Ceraunius Fossae and Tractus Fossae, all occurring in the Amazonian. Based on their ages and orientations we propose the following stages of evolution of the southern area of Alba Mons (Figure 3.14).

1. Following an Amazonian lava emplacement, laterally propagating radial dikes from a volcanotectonic centre near the mid of the Tharsis bulge reflect the first recorded extension activity in Ceraunius South and Tractus Fossae. WNW-ESE extension facilitates NNE trending faults (Group 1) in Tractus Fossae and Ceraunius South (Figure 3.14a). These diking induced grabens are likely sourced from either Pavonis Mons or a centre in Tharsis itself.
2. Previous regional E-W extension related to the isostatic loading of Syria Planum, has likely weakened the crust in Ceraunius Fossae and Tractus Fossae, and thus aided the emergence of Alba Mons plume/Ceraunius Fossae underplating sourced vertical diking-induced faulting (Figure 3.14b). This E-W extension that allowed the intensity of the N-S faulting (Group 2), was likely amplified by radial stresses from Alba Mons and Ascraeus Mons.
3. Activity from the Ceraunius Fossae magma source, perhaps related to late-stage deflation in accordance with diminishing activity, creates a set of curved faults (in Group 3) to the south of Alba Mons (Figure 3.14c).
4. Any low-lying lands are covered with the most recent Amazonian lava flows (unit AHv on Figure 3.3) (Tanaka et al., 2014), isolating the raised patches we map in this study (Figure 3.14d). Smaller instances of tectonic activity may have continued after this period, with few (~12) identified grabens within the study area, dated between 1.9 Ga and 45 Ma, based on their contact with dated lava flows (Krishnan & Kumar, 2023).

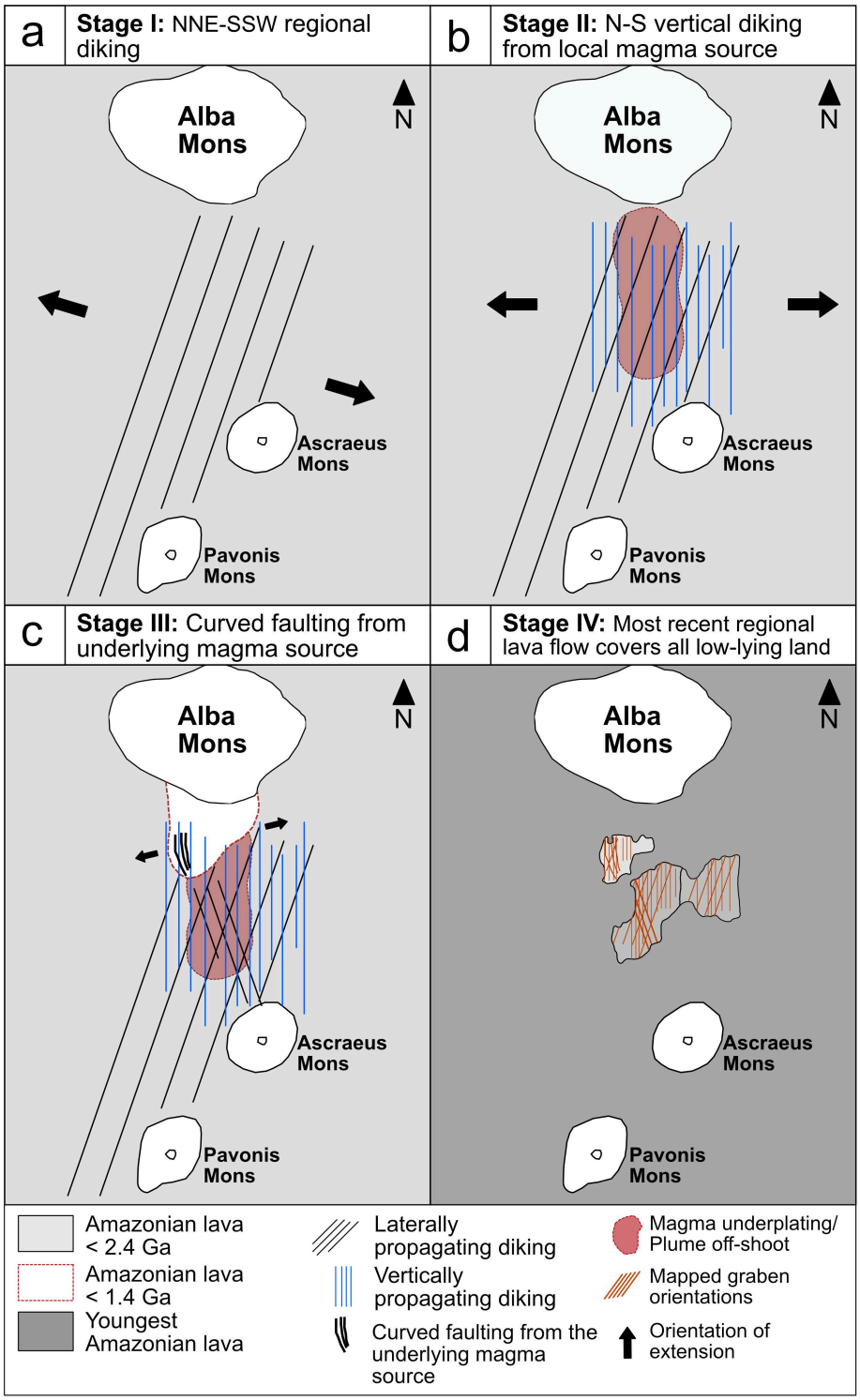

Figure 3.14: The four main stages of tectonic activity in the southern Alba Mons, all occurring during the Amazonian. A) Stage I, initial NNW/SSE extension, due to Tharsis bulge centered diking, which results in NNE oriented grabens (Group 1). B) Stage II, activity from Ceraunius Fossae centered magma source, combined with regional (Syria Planum centered) and local (Alba Mons and Ascraeus Mons) E-W extension produces N-S oriented vertical diking (Group 2). C) Stage III, interacting stress fields from the Ceraunius Fossae magma source, together with Ascraeus Mons diking produces linear and curved faulting (Group 3). D) The most recent Amazonian lava flow covers all low-lying terrain.

3.4.7. Implications for Magma Reservoir Location

Results from the fault mapping and grouping reveals three main stages of extensional activity in Ceraunius and Tractus Fossae, occurring during the Amazonian. Overall, the area south of Alba Mons shows intense surface deformation, the majority of which is associated with the magmatic activity localized here. We observe extensional faulting as a result of diking, and collapse features such as pit-crater chains, which we consider the result of arrested dikes interacting with the surface. As mentioned in the introduction, the magma that fed the extensive diking and subsequent extensional faulting and collapse structures around the surface of Alba Mons, is suggested to originate from a separate source, independent from the Tharsis superplume.

Other highly faulted volcanotectonic areas, such as Ulysses Fossae (Fernández & Ramírez-Caballero, 2019; Shahrzad et al., 2023) and Noctis Labyrinthus (Kling et al., 2021), display similar pit-crater chain and catenae morphology as the ones we have mapped south of Alba Mons in this study. However, the complexity of troughs varies between the three locations on a range. Ulysses Fossae show the least amount of trough complexity, where the few instances of collapse structures are isolated PCCs and troughs, with only a few contained compound trough structures in the northern part (Shahrzad et al., 2023). An increase in complexity is found in the examples in this study, where Ceraunius and Tractus Fossae show more "developed" structures, interlinking u-shaped troughs, catenae and PCCs. Then the intricate chaotic terrain and interacting troughs in Noctis Labyrinthus define the majority of the structures there (Kling et al., 2021), and show the most complex collapse structures between the three examples.

Particular for the Alba Mons hotspot, a study by Ivanov & Head (2006), concluded that the magma reservoir feeding the Alba Mons lobes must be located at a relatively shallow depth (high topographic level), compared to other Tharsis volcanoes. Additionally, Mège et al. (2003), investigated representative areas of Alba Patera and Noctis Labyrinthus, and found that magma reservoirs might lie at ~1 km and ~5 km depth, respectively. These findings could indicate that the source of magma was relatively close to the surface, compared to the rest of the Tharsis volcanoes and could thus have an influence on the amount and longevity of the diking, and the subsequent high-density faulting and collapse structures, which compared to Ulysses Fossae, is more prevalent in Ceraunius and Tractus Fossae, as well as Noctis Labyrinthus. This magma source may have remained stable throughout the Amazonian, with potential remnants of this reservoir still located underneath Ceraunius Fossae at present day, as suggested by Plesa et al. (2023). Other Tharsis volcanoes such as the Tharsis Montes show pit-crater chain structures on the flanks of the volcanoes, but given the distance from the main volcano for the faults in Noctis Labyrinthus (Kling et al., 2021) and Ceraunius and Tractus Fossae, a relatively more shallow magma source (and near-surface volatile layers) could be the reason for the complexity of the collapse structures in those locations,

compared to Ulysses Fossae (Shahrzad et al., 2023). There, the comparative "lack" of complex collapse features from the majority of the Tharsis-superplume related volcanoes, could reflect a deeper magma source. However, this is just one possible explanation and further modelling of the potential magmatic reservoirs are necessary to confirm or refute it.

3.5. Conclusions

- In this study we mapped and measured ~12,000 faults and determined their ages of activity based on crater size-frequency distributed ages, as being active during the Amazonian period, late in Mars' history.
- Grouping the faults based on orientation and morphology reveals three distinct stages of extensional activity recorded in the study areas, with a change from NE to N-S to NW oriented faults and associated perpendicular extensional strain orientations, through time.
- We determine the majority of the faulting to be dike-induced (groups 1, 2 and some of 3), with both regional (Tharsis) and local (Alba Mons, Ascraeus Mons and Pavonis Mons) centres of deformation. We determine the curved western faults in Group 3 to be purely tectonic and a result of the stresses from a local magmatic source.
- Additionally, the mapped collapse structures are also considered related to diking and are consistently younger than the mapped faults.
- The magmatic activity from a local Ceraunius Fossae magma source (either from an Alba Mons plume off-shoot, or magmatic underplating), has highly influenced Ceraunius and Tractus Fossae, with dike-induced graben formation and associated pit-crater chains, catenae, u-shaped troughs and chasmata dotting the landscape. This potentially shallow and recent (< 1.4 Ga) magmatic activity was inducive to the mapped surface deformation, which was amplified by the regional Tharsis E-W extension, with influence from radial stresses from local volcanoes.

Open Research

Mapped faults, collapse features, and craters from this study are available to download free from Zenodo: faults (Shahrzad, 2023a), collapse features (Shahrzad, 2023b), craters (Shahrzad, 2023c). The CTX global mosaic (Credit: Esri, Caltech Murray Lab, NASA, JPL, MSSS) used in this study can be downloaded from The Murray Lab's website at https://murray-lab.caltech.edu/CTX/ and the MOLA-HRSC DEM v2 used to generate topographic profiles is available from USGS' Astropedia Catalog (Fergason et al., 2018). The software used in this research is available to download for free: Craterstats 2.0 is available from the Freie Universität Berlin at https://www.geo.fu-berlin.de/en/geol/fachrichtungen/planet/software/index.html and FracPaQ (Healy et al., 2017) is available for download via GitHub.

References

Alapieti, T. (1982). The Koillismaa layered igneous complex, Finland: Its structure, mineralogy and geochemistry, with emphasis on the distribution of chromium.

Banerdt, W. B., Golombek, M. P., & Tanaka, K. L. (1992). Stress and tectonics on Mars. In H. H. Kieffer, B. M. Jakosky, C. W. Snyder, & M. S. Matthews (Eds.), Mars (pp. 249–297). University of Arizona Press

Belleguic, V., Lognonné, P., & Wieczorek, M. (2005). Constraints on the Martian lithosphere from gravity and topography data. Journal of Geophysical Research: Planets, 110(E11). https://doi.org/10.1029/2005JE002437

Bleacher, J. E., Glaze, L. S., Greeley, R., Hauber, E., Baloga, S. M., Sakimoto, S. E. H., Williams, D. A., & Glotch, T. D. (2009). Spatial and alignment analyses for a field of small volcanic vents south of Pavonis Mons and implications for the Tharsis province, Mars. Journal of Volcanology and Geothermal Research, 185(1), 96–102. https://doi.org/10.1016/j.jvolgeores.2009.04.008

Byrne, P. K., Holohan, E. P., Kervyn, M., van Wyk de Vries, B., & Troll, V. R. (2015). Analogue modelling of volcano flank terrace formation on Mars. Geological Society, London, Special Publications, 401(1), 185–202. https://doi.org/10.1144/SP401.14

Cailleau, B., Walter, T. R., Janle, P., & Hauber, E. (2003b). Modeling volcanic deformation in a regional stress field: Implications for the formation of graben structures on Alba Patera, Mars. Journal of Geophysical Research: Planets, 108(E12). https://doi.org/10.1029/2003JE002135

Cailleau, B., Walter, T. R., Janle, P., & Hauber, E. (2005). Unveiling the origin of radial grabens on Alba Patera volcano by finite element modelling. Icarus, 176(1), 44–56. https://doi.org/10.1016/j.icarus.2005.01.017

Carr, M. H. (1974). Tectonism and volcanism of the Tharsis Region of Mars. Journal of Geophysical Research (1896-1977), 79(26), 3943–3949. https://doi.org/10.1029/JB079i026p03943

Christoph, J. M., & Garry, W. B. (2017). Spatial and Temporal Relationships Among Low Shield Volcanoes in the Ceraunius Fossae Region of Tharsis: The Last Gasp of Martian Volcanism. *Presented at 48th Annual Lunar and Planetary Science Conference* (2017), 2798

Cushing, G. E., Okubo, C. H., & Titus, T. N. (2015). Atypical pit craters on Mars: New insights from THEMIS, CTX, and HiRISE observations. Journal of Geophysical Research: Planets, 120(6), 1023–1043. https://doi.org/10.1002/2014JE004735

Dohm, J. M., Baker, V. R., Maruyama, S., & Anderson, R. C. (2007). Traits and Evolution of the Tharsis Superplume, Mars. In D. A. Yuen, S. Maruyama, S.-I. Karato, & B. F. Windley (Eds.), Superplumes: Beyond Plate Tectonics (pp. 523–536). Springer Netherlands. https://doi.org/10.1007/978-1-4020-5750-2_17

Ernst, R. E., Liikane, D. A., Jowitt, S. M., Buchan, K. L., & Blanchard, J. A. (2019). A new plumbing system framework for mantle plume-related continental Large Igneous Provinces and their mafic-ultramafic intrusions. Journal of Volcanology and Geothermal Research, 384, 75–84. https://doi.org/10.1016/j.jvolgeores.2019.07.007

Ernst, R., Grosfils, E., & Mège, D. (2001). Giant Dike Swarms: Earth, Venus, and Mars. Annual Review of Earth and Planetary Sciences, 29(1), 489–534. https://doi.org/10.1146/annurev.earth.29.1.489

Fergason, R. L., Hare, T. M., & Laura, J. (2018). HRSC and MOLA Blended Digital Elevation Model at 200m v2. [Map] [Dataset]. Astrogeology PDS Annex, U.S. Geological Survey. Retrieved from https://arcg.is/1OOm9K

Fernández, C., & Ramírez-Caballero, I. (2019). Evaluating transtension on Mars: The case of Ulysses Fossae, Tharsis. Journal of Structural Geology, 125, 325–333. https://doi.org/10.1016/j.jsg.2018.05.009

Ferrill, D. A., Wyrick, D. Y., & Smart, K. J. (2011). Coseismic, dilational-fault and extension-fracture related pit chain formation in Iceland: Analog for pit chains on Mars. Lithosphere, 3(2), 133–142. https://doi.org/10.1130/L123.1

Genova, A., Goossens, S., Lemoine, F. G., Mazarico, E., Neumann, G. A., Smith, D. E., & Zuber, M. T. (2016). Seasonal and static gravity field of Mars from MGS, Mars Odyssey and MRO radio science. Icarus, 272, 228–245. https://doi.org/10.1016/j.icarus.2016.02.050

Gudmundsson A. Magma Movement through the Crust: Dike Paths. In: *Volcanotectonics: Understanding the Structure, Deformation and Dynamics of Volcanoes*. Cambridge University Press; 2020:325-378.

Hardy, S. (2021). Discrete Element Modelling of Pit Crater Formation on Mars. Geosciences, 11(7), Article 7. https://doi.org/10.3390/geosciences11070268

Hauber, E., Brož, P., Jagert, F., Jodłowski, P., & Platz, T. (2011). Very recent and wide-spread basaltic volcanism on Mars. Geophysical Research Letters, 38(10). https://doi.org/10.1029/2011GL047310

Healy, D., Rizzo, R. E., Cornwell, D. G., Farrell, N. J. C., Watkins, H., Timms, N. E., Gomez-Rivas, E., & Smith, M. (2017). FracPaQ: A MATLAB™ toolbox for the quantification of fracture patterns. Journal of Structural Geology, 95, 1–16. https://doi.org/10.1016/j.jsg.2016.12.003

Ivanov, M. A., & Head, J. W. (2006). Alba Patera, Mars: Topography, structure, and evolution of a unique late Hesperian–early Amazonian shield volcano. Journal of Geophysical Research: Planets, 111(E9). https://doi.org/10.1029/2005JE002469

Jenness, J. (2011). *Tools for graphics and shapes: Extension for ArcGIS (version 2.1.85)*. Jenness Enterprises. Retrieved from http://www.jennessent.com/arcgis/shapes_graphics.htmKling, C. L., Byrne, P. K., Atkins, R. M., & Wegmann, K. W. (2021). Tectonic Deformation and Volatile Loss in the Formation of Noctis Labyrinthus, Mars. Journal of Geophysical Research: Planets, 126(11), e2020JE006555. https://doi.org/10.1029/2020JE006555

Kneissl, T., van Gasselt, S., & Neukum, G. (2011). Map-projection-independent crater size-frequency determination in GIS environments—New software tool for ArcGIS. Planetary and Space Science, 59(11), 1243–1254. https://doi.org/10.1016/j.pss.2010.03.015

Krishnan, V., & Kumar, P. S. (2023). Long-Lived and Continual Volcanic Eruptions, Tectonic Activity, Pit Chains Formation, and Boulder Avalanches in Northern Tharsis Region: Implications for Late Amazonian Geodynamics and Seismo-Tectonic Processes on Mars. Journal of Geophysical Research: Planets, 128(1), e2022JE007511. https://doi.org/10.1029/2022JE007511

Magee, C., Love, V., Fayz, K., Andrews, B., Rivas-Dorado, S., Jackson, C., Orlov, C., & Bramham, E. (2023). Quantifying Dyke-Induced Graben and Dyke Structure Using 3D Seismic Reflection Data and The Role of Interpretation Bias. Tektonika, 1. https://doi.org/10.55575/tektonika2023.1.2.25

Malin, M. C., Bell, J. F., Cantor, B. A., Caplinger, M. A., Calvin, W. M., Clancy, R. T., Edgett, K. S., Edwards, L., Haberle, R. M., James, P. B., Lee, S. W., Ravine, M. A., Thomas, P. C., & Wolff, M. J. (2007). Context Camera Investigation on board the Mars Reconnaissance Orbiter. Journal of Geophysical Research: Planets, 112(E5). https://doi.org/10.1029/2006JE002808

Marzoli, A., Callegaro, S., Dal Corso, J., Davies, J., Chiaradia, M., Youbi, N., Bertrand, H., Reisberg, L., Merle, R., & Jourdan, F. (2018). The Central Atlantic Magmatic Province (CAMP): A Review (pp. 91–125). https://doi.org/10.1007/978-3-319-68009-5_4

McGovern, P. J., Solomon, S. C., Head III, J. W., Smith, D. E., Zuber, M. T., & Neumann, G. A. (2001). Extension and uplift at Alba Patera, Mars: Insights from MOLA observations and loading models. Journal of Geophysical Research: Planets, 106(E10), 23769–23809. https://doi.org/10.1029/2000JE001314

Mège, D. (1999). Dikes on Mars: (1) What to Look For? (2) A First Survey of Possible Dikes During the Mars Global Surveyor Aerobreaking and Science Phasing Orbits. Paper presented at Fifth International Conference on Mars, Pasadena, California. (6207).

Mège, D., Cook, A. C., Garel, E., Lagabrielle, Y., & Cormier, M.-H. (2003). Volcanic rifting at Martian grabens. Journal of Geophysical Research: Planets, 108(E5). https://doi.org/10.1029/2002JE001852

Mège, D., A. C. Cook, E. Garel, Y. Lagabrielle, and M. H. Cormier (2002), Surface collapse and volcanic rifting on Mars (abstract), *Proc. Lunar Planet. Sci. Conf. 33rd*, 2042.

Mège, D., & Masson, P. (1996). A plume tectonics model for the Tharsis province, Mars. Planetary and Space Science, 44(12), 1499–1546. https://doi.org/10.1016/S0032-0633(96)00113-4

Michael, G. G. (2013). Planetary surface dating from crater size–frequency distribution measurements: Multiple resurfacing episodes and differential isochron fitting. Icarus, 226(1), 885–890. https://doi.org/10.1016/j.icarus.2013.07.004

Michael, G. G., Kneissl, T., & Neesemann, A. (2016). Planetary surface dating from crater size-frequency distribution measurements: Poisson timing analysis. Icarus, 277, 279–285. https://doi.org/10.1016/j.icarus.2016.05.019

Öhman, T., & McGovern, P. J. (2014). Circumferential graben and the structural evolution of Alba Mons, Mars. Icarus, 233, 114–125. https://doi.org/10.1016/j.icarus.2014.01.043

Okubo, C. H., & Schultz, R. A. (2005). Evidence of Tharsis-Radial Dike Intrusion in Southeast Alba Patera from MOLA-based Topography of Pit Crater Chains. 1007.

Orlov, C. J., Bramham, E. K., Thomas, M., Byrne, P. K., Piazolo, S., & Mortimer, E. (2022). Structural Architecture and Deformation History of Tempe Terra, Mars. Journal of Geophysical Research: Planets, 127(11), e2022JE007407. https://doi.org/10.1029/2022JE007407

Pieterek, B., Ciazela, J., Lagain, A., & Ciazela, M. (2022). Late Amazonian dike-fed distributed volcanism in the Tharsis volcanic province on Mars. Icarus, 386, 115151. https://doi.org/10.1016/j.icarus.2022.115151

Plesa, A.-C., Wieczorek, M., Knapmeyer, M., Rivoldini, A., Bozdag, E., Walterova, M., Knapmeyer-Endrun, B., Kim, D., Broquet, A., Stähler, S., Mittelholz, A., Breuer, D., Johnson, C., Hauber, E., Panning, M., Spohn, T., Lognonne, A. P., Smrekar, S., & Banerdt, B. (2023). InSight's Constraints on the Interior of Mars: Geodynamical Models and Observations. 2806, 2212. https://www.hou.usra.edu/meetings/lpsc2023/pdf/2212.pdf

Plescia, J. B. (1994). Geology of the Small Tharsis Volcanoes: Jovis Tholus, Ulysses Patera, BibIls Patera, Mars. Icarus, 111(1), 246–269. https://doi.org/10.1006/icar.1994.1144

Plescia, J. B. (2004). Morphometric properties of Martian volcanoes. Journal of Geophysical Research: Planets, 109(E3). https://doi.org/10.1029/2002JE002031

Plescia, J. B., & Saunders, R. S. (1982). Tectonic history of the Tharsis Region, Mars. Journal of Geophysical Research: Solid Earth, 87(B12), 9775–9791. https://doi.org/10.1029/JB087iB12p09775

Polit, A. T., Schultz, R. A., & Soliva, R. (2009). Geometry, displacement–length scaling, and extensional strain of normal faults on Mars with inferences on mechanical stratigraphy of the Martian crust. Journal of Structural Geology, 31(7), 662–673. https://doi.org/10.1016/j.jsg.2009.03.016

Rainbird, R. H. (1993). The Sedimentary Record of Mantle Plume Uplift Preceding Eruption of the Neoproterozoic Natkusiak Flood Basalt. The Journal of Geology, 101(3), 305–318. https://doi.org/10.1086/648225

Raitala, J. (1988). Composite graben tectonics of Alba Patera on Mars. Earth, Moon, and Planets, 42(3), 277–291. https://doi.org/10.1007/BF00058491

Richardson, J. A., Bleacher, J. E., Connor, C. B., & Glaze, L. S. (2021). Small Volcanic Vents of the Tharsis Volcanic Province, Mars. Journal of Geophysical Research: Planets, 126(2), e2020JE006620. https://doi.org/10.1029/2020JE006620

Riedel, C., Michael, G. G., Orgel, C., Baum, C., van der Bogert, C. H., & Hiesinger, H. (2021). Studying the Global Spatial Randomness of Impact Craters on Mercury, Venus, and the Moon With Geodesic Neighborhood Relationships. Journal of Geophysical Research: Planets, 126(3), e2020JE006693. https://doi.org/10.1029/2020JE006693

Robbins, S. J., Achille, G. D., & Hynek, B. M. (2011). The volcanic history of Mars: High-resolution crater-based studies of the calderas of 20 volcanoes. Icarus, 211(2), 1179–1203. https://doi.org/10.1016/j.icarus.2010.11.012

Rodriguez, J. A. P., Zarroca, M., Linares, R., Gulick, V., Weitz, C. M., Yan, J., Fairén, A. G., Miyamoto, H., Platz, T., Baker, V., Kargel, J., Glines, N., & Higuchi, K. (2016). Groundwater flow induced collapse and flooding in Noctis Labyrinthus, Mars. Planetary and Space Science, 124, 1–14. https://doi.org/10.1016/j.pss.2015.12.009

Scott, E. D., Wilson, L., & Head III, J. W. (2002). Emplacement of giant radial dikes in the northern Tharsis region of Mars. Journal of Geophysical Research: Planets, 107(E4), 3-1-3–10. https://doi.org/10.1029/2000JE001431

Shahrzad, S., Bramham, E. K., Thomas, M., Piazolo, S., Byrne, P. K., & Mortimer, E. (2023). Deciphering the Structural History of Ulysses Fossae, Mars, Using Fault Pattern Analysis. Journal of Geophysical Research: Planets, 128(5), e2022JE007633. https://doi.org/10.1029/2022JE007633

Shahrzad, S. (2023a). Ceraunius Fossae and Tractus Fossae, Mars, Fault Catalogue [Dataset]. Zenodo. https://doi.org/10.5281/zenodo.8376744

Shahrzad, S. (2023b). Ceraunius Fossae and Tractus Fossae Crater Catalogue [Dataset]. Zenodo. https://doi.org/10.5281/zenodo.8376774

Shahrzad, S. (2023c). Ceraunius Fossae and Tractus Fossae Collapse Features Catalogue [Dataset]. Zenodo. https://doi.org/10.5281/zenodo.8376769

Spagnuolo, M. G., Figueredo, P. H., & Ramos, V. A. (2008). Reinterpretation of Tractus Fossae region as an asymmetric rift system on Mars. Icarus, 198(2), 318–330. https://doi.org/10.1016/j.icarus.2008.08.007

Stubblefield, R. K. (2018). Extensional Tectonics at Alba Mons, Mars: A Case Study for Local versus Regional Stress Fields. [Master of Science, North Carolina State University]. http://www.lib.ncsu.edu/resolver/1840.20/36604

Tanaka, K. L. (1990). Tectonic history of the Alba Patera—Ceraunius Fossae region of Mars. Lunar and Planetary Science Conference Proceedings, 20, 515–523.

Tanaka, K. L., Golombek, M. P., & Banerdt, W. B. (1991). Reconciliation of stress and structural histories of the Tharsis region of Mars. Journal of Geophysical Research: Planets, 96(E1), 15617–15633. https://doi.org/10.1029/91JE01194

Tanaka, K. L., Skinner Jr., J. A., Dohm, J. M., Irwin, III, R. P., Kolb, E. J., Fortezzo, C. M., Platz, T., Michael, G. G., & Hare, T. M. (2014). Geologic Map of Mars (Scientific Investigations Map) [Scientific Investigations Map].

van Wyk de Vries, B., & Matela, R. (1998). Styles of volcano-induced deformation: Numerical models of substratum flexure, spreading and extrusion. Journal of Volcanology and Geothermal Research, 81(1), 1–18. https://doi.org/10.1016/S0377-0273(97)00076-0

Werner, S. C. (2009). The global martian volcanic evolutionary history. Icarus, 201(1), 44–68. https://doi.org/10.1016/j.icarus.2008.12.019

Wilson, L., & Head, J. (2000). Tharsis-radial graben systems as the surface manifestation of plume-related dike intrusion complexes: Models and implications - art. no. 5000. Journal of Geophysical Research Atmospheres, 107. https://doi.org/10.1029/2001JE001593

Wilson, L., Scott, E. D., & Head III, J. W. (2001). Evidence for episodicity in the magma supply to the large Tharsis volcanoes. Journal of Geophysical Research: Planets, 106(E1), 1423–1433. https://doi.org/10.1029/2000JE001280

Wyrick, D., Ferrill, D. A., Morris, A. P., Colton, S. L., & Sims, D. W. (2004). Distribution, morphology, and origins of Martian pit crater chains. Journal of Geophysical Research: Planets, 109(E6). https://doi.org/10.1029/2004JE002240

Chapter 4

The Influence of Young's Modulus on Graben Formation during Martian Dike Intrusions: A Discrete Element Modelling Approach

Abstract

The Martian surface is covered in extensive networks of vast graben systems, spanning hundreds of kilometres in length. While certain graben populations stem from tectonic extension, a considerable portion is attributed to diking-induced deformation. Despite theories proposing this process for both Mars and Earth, limited field observations and numerical modelling results exist regarding the creation of grabens solely through dike activity, independent of regional extension. In this study, we investigate this process on Mars, with a focus on the poorly constrained lithospheric properties of the planet. We examine the resulting surface deformation after dike-injection into a Martian lithosphere of varying properties. To do this, we construct a 2D numerical model of the Martian lithosphere using *PFC2D* software, in order to simulate the process of dike-intrusion. We vary the Young's modulus with three different values: 5.4 GPa, 50 GPa and 100 GPa, in order to assess the variation of resulting surface deformation structures. We find that ascending dikes can form grabens in the Martian lithosphere if the Young's modulus is ≥50 GPa. The lowest Young's modulus value of 5.4 GPa does not produce a surface graben, but surface faulting is present, as is trough formation. We confirm that surface-reaching faulting is initiated at the dike-tip, where the fracture initiation depth is larger for the 100 GPa model than the 50 GPa model. Our results, combined with observations from separate studies suggest that the average Young's modulus for the Martian lithosphere may be higher than previously assumed.

4.1. Introduction

The surface of Mars is covered by regions of extensive parallel graben systems, the majority located in volcanic areas such as the massive 1000 km scale Tharsis Volcanic Province, which covers ~25% of the planet's surface. Previous studies have mapped and categorized these vast extensional fault systems, for example Tempe Terra (Orlov et al., 2022), Ulysses Fossae (Fernández & Ramírez-Caballero, 2019; Shahrzad et al., 2023), Ceraunius and Tractus Fossae (Shahrzad et al., 2024), and Alba Mons (Cailleau et al., 2005). Detailed studies of these Martian fault systems which use satellite data to generate detailed topographic maps, perform high-resolution morphological image analyses, characterize fault geometry, and measure strain, suggest that a significant portion of extensional grabens are directly related to subsurface dikes from local or regional-scale volcanic centres. Dike-driven faulting and subsequent graben formation is therefore considered a main driver for the extensional fault systems on Mars, specifically in volcanic provinces i.e., Tharsis and Elysium (e.g. Okubo & Schultz, 2005; Scott et al., 2002; Shahrzad et al., 2023).

Previous studies of Martian graben systems involving seismic and geodetic monitoring, found that diking-related surface faulting did not occur before the dike ascension, but that it was the intrusion of the dike itself which initiated the surface faulting (Rubin, 1992; Rubin & Pollard, 1988). Even though this does not mean that near-surface dikes will always produce extensional faults or grabens, in cases where it does, the faulting always occurs before the dike reaches the surface (Chadwick Jr. & Embley, 1998). The most common model for graben formation associated with an ascending dike is based on the following evolving stress-fracture-fault relationships. During the dike ascent σ_1 is vertical and σ_3 is horizontal (Figure 4.1, Gudmundsson, 2020). As the dike ascends it will create fractures in the host rock when the tensile stress generated from the advancing dike tip overcomes the yield strength of the rock. The internal pressure from the dike will compress locally the surrounding rock and the elastic displacements which are produced, are oriented away from the dike (Pollard et al., 1983). For an ascending dike close to the free surface, this will generate fractures at an angle from the tip. These will, with further ascent, result in continuing horizontal tension developing into normal faults on the surface with a graben positioned above the ascending dike (Figure 4.1, Ernst et al., 2001; Gudmundsson, 2020; Mège & Masson, 1996). If no subsequent eruption occurs, the arrested dike tip will be located at a depth which is estimated to be half the width of the produced graben, based on field observations and numerical models (Bazargan & Gudmundsson, 2019).

Both numerical and analogue model studies of dike-induced graben formation suggest a topographical difference between diking- and tectonically-induced grabens, where diking produces concave down topographic slopes, in opposition to the concave up slopes modelled for tectonic grabens (Okubo & Schultz, 2005; Schultz et al., 2004).

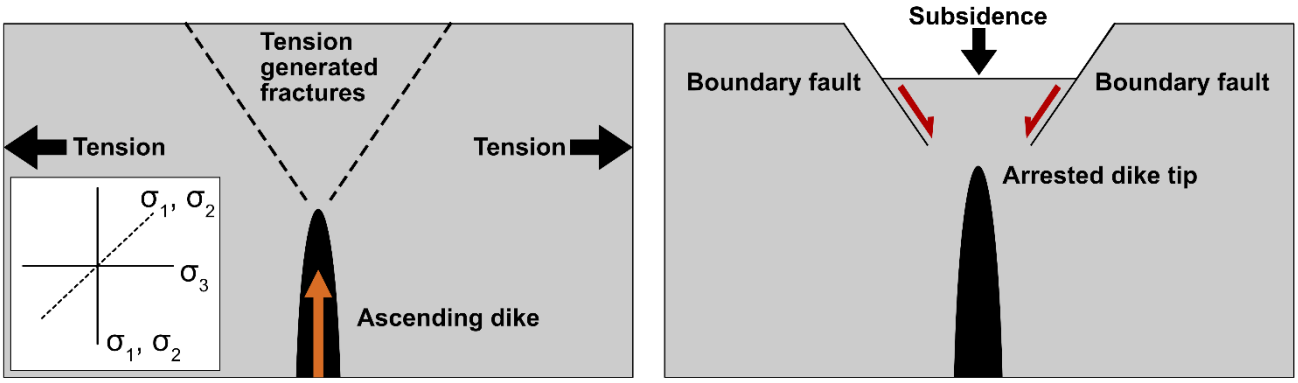

Figure 4.1: Diagram illustrating schematically the stresses involved during diking-induced graben formation. Modified from Rivas-Dorado et al. (2021), and Gudmundsson (2020).

Though the model proposed in Figure 4.1 illustrates a process based on Earth observations and measurements where dikes and faults are more accessible for direct measurements and analyses, there are remarkably few documented examples of dikes directly creating grabens on Earth. One of these is a recent study by Magee and Jackson (2020), where they used seismic reflection data to argue for two dike-induced graben bounding faults reaching a paleo surface in NW Australia (Magee & Jackson, 2020). The sparsity of examples on Earth highlights the apparent discrepancy between the proposed theoretical models for terrestrial bodies and field examples. In contrast, dike-induced deformation is considered one of the main extensional tectonic processes on other terrestrial planets, such as Mars and Venus (Ernst et al., 2001) as these systems are characterized by high levels of past igneous activity evident in ample signatures of volcanism and local large scale magmatic bodies (e.g. Orlov et al. 2023).

Even though the described general model of graben formation associated with an ascending dike is accepted within the community, questions remain regarding the nature of fracture propagation from the ascending dike, the relationship between dike width and ascending speed, and how the dike influences the final surface topography in materials of different rheological properties. The final question in particular is significant, as remote sensing surface analysis is the main type of data available to study the surface of other terrestrial planets and moons. If characteristics of surface topography can be linked to material properties, these characteristics can be used to derive such properties. To gain such understanding, the following questions need to be answered: Are there any resulting surface structures if the dike is stalled before breaching the surface, and is there a difference in the depth and width of any

resulting structure with varying lithosphere rheological parameters? These queries remain unresolved not only on Mars but on other planetary bodies and thus warrants further study.

Though the mantle-crust distribution of Mars is similar (although at a smaller scale) to Earth, the properties of the crust and the upper most part of the mantle i.e. the lithosphere, are considered to vary significantly between each of the terrestrial planets. A Martian lithosphere with a higher stiffness, at larger thickness, as suggested in Heap et al. (2017), is potentially a main contributing factor for the increased likelihood of ascending dikes related to graben formation. Heap et al. (2017) argue that the lower Martian gravity of 3.71 m/s^{-2} decreases the lithostatic pressure ($P = \rho g h$), which as a result will, at any given depth, be lower on Mars than on Earth. Considering the lower confining pressure along with the cold nature of the Martian crust (Solomon & Head, 1990), this results in a significantly deeper brittle to ductile transition zone on Mars. Such a deeper brittle-ductile transition zone (BDTZ) means, theoretically, that dikes on Mars would not have to penetrate as shallowly into the crust in order to induce surface-breaking fractures and subsequent extensional faulting. Other than depth of the brittle-ductile transition zone, the thickness of crust that the dike must ascend through may also have an impact on the resulting surface deformation. At the same time, the lack of significant chemical differentiation as well as low temperature may favour dikes that approach, but not reach the surface. The majority of dikes are thought not to have reached the surface on Mars (Okubo & Schultz, 2005; Scott et al., 2002).

As there is no way to perform fieldwork or collect samples from the Martian sites presently, numerical models are essential, especially for planetary science where direct observations are difficult to conduct. Numerical modelling is by far the most suitable approach to investigating diking-induced graben formation and determining the influence of different lithospheric parameters on the formation of surface graben formation. While there are a number of numerical models exploring dike induced graben formation in the Earth environment (e.g. Koehn et al., 2019), few numerical modelling simulations of dike-induced graben formation are specific to Martian conditions. The existing models for dike-induced graben formation on Mars are based on discrete element models (DEM) using discrete elements or particles to simulate the local and bulk behaviour of the systems in question. In DEM, particles and their interaction with each other during different simulation scenarios are monitored, making such models well suited to model granular material and any discontinuities due to fracture or failure (Coetzee, 2017).

The few existing DEMs of dike-induced deformation on Mars consist of a so called "bonded assembly". Here, the initial state of the models consists of a dike represented by a rectangle of rigid material, which is already emplaced at the arrested dike depth. Dike intrusion is then simulated by widening the dike horizontally in order to investigate any resulting surface graben formation (Hardy, 2016; Wyrick & Smart,

2009). Interestingly, although using a similar approach, results are contrasting. Wyrick and Smart (2009) find it unlikely that the widening of a dike alone on Mars can create surface grabens, while Hardy (2016) show that any of the tested final dike widths will yield the extensional faulting and subsidence required for graben formation on Mars.

Our study expands upon these previous Mars focused studies, by incorporating a simple simulation of the actual ascent of a dike represented by a wedge-shaped object. In particular, we investigate the influence of varying a Martian lithosphere elastic property parameter, as well as an initial investigation into the effects of maximum dike width, on the final surface-expression above an ascending dike. We use a two-dimensional DEM approach to simulate a dike injection into a section of the brittle lithospheric Martian crust. In the model, the material is assumed to be purely elastic. In order to investigate the resulting surface deformation for variations in the Martian lithosphere over time, we vary the Young's modulus through the different numerical simulations. Using discrete modelling makes us able to accurately display the complex surface structures observed in detail by the Martian orbiting satellites (Carr & Head, 2010).

4.2. Numerical Model Method

4.2.1. Particle Flow Code in 2D

We use the modelling software Particle Flow Code (PFC*2D*) developed by Itasca (Itasca Consulting Group, 1999) to model the two-dimensional impact of an intruding dike, moving through a Martian lithosphere of varying thickness and elastic constants i.e. Young's modulus. The Young's modulus is a scalar property of an elastic material relating compressive stress to axial strain. PFC is a numerical model which is capable of describing the mechanical behaviour of assemblies of discs (in 2D) and spheres (in 3D) (Cundall & Strack, 1979). The PFC model acts as a synthetic material which consists of an assembly of rigid grains that interact at their contacts. A PFC model where the particles are assigned a contact model, is referred to as a "bonded assembly". This bonded model can then simulate the movement and interaction of the many finite-sized particles (or balls), which together act as a collection of individual particles, replicating the movement and deformation of a rigid, elastic body (Potyondy, David, 2019). Particles will interact with each other using the bonds between them, which are defined by their individual contact models. It is in the assigned particle bonds that material properties are expressed. For this study we use the softbond model (Potyondy, 2019). Damage in the overall bonded material will be reflected as bond-breaking events. It is important to note that the purpose of each particle in this case is not to

represent an individual crystal or a block of rock, but rather act as a discrete element for the purpose of computation (Harnett et al., 2018).

PFC has previously been used to describe volcanic systems, even on other planets, setting precedent for its use for this study. Examples include using PFC to model the stress evolution during caldera collapse (Holohan et al., 2015), the tectonic evolution of chasma walls on Mars (Imre, 2004), and modelling Martian pit crater formation (Smart et al., 2011).

The soft-bond contact model in PFC works similarly to a linear parallel bond model, where the contacts are a finite size point which lies between the contacting particles in a cross-section (Figure 4.2 below). These bonds can transmit both a force and a moment, allowing for accurate mechanical responses of the simulated rock. It is possible for the bonds to fail if the strength of the bonds is exceeded by shear or tension. However, differently from the linear parallel bonded model, in a soft-bond model following failure, the bonds are not immediately removed. Here, the bonds can enter a regime of softening which continues until it reaches a threshold value (failure criteria) where the bonds are considered broken, and thus removed (Potyondy, David, 2019). This makes the soft-bond model capable of simulating the failure behaviour of the large-sized lithosphere section used in this study (Chong et al., 2021).

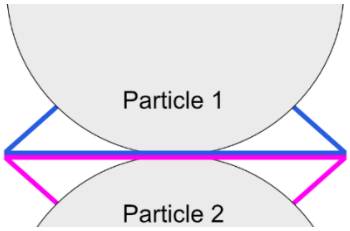

Figure 4.2: Soft-bond model diagram. To particles are bonded at the interface between the two, with the grey balls reflecting the particles, and the pink and blue lines showing the parallel bonds. Modified from Potyondy (2019).

The contact force and moment for the soft-bond model are updated according to the model's force-displacement law:

$$F_c = F + F^d$$

$$M_c = M$$

Where, F is the linear force, F^d is the dashpot force and M is linear moment. In the soft-bond model F is comprised of normal and shear movement and is therefore resolved into their respective forces. The linear moment, M, is comprised by a twisting and a bending moment. These are updated according to the following:

$$F = -F_n \hat{n}_c + F_s$$

$$M = M_t \hat{n}_c + M_b$$

Where, a normal force, $F_n > 0$ is tension. When the material is bonded it behaves in a linear elastic mode until either shear or tensile strength limit is exceeded (Potyondy, 2019).

4.2.2. Model Set-up.

To investigate the surface deformation caused by intruding dikes, we create a simplified 2D model of the upper Martian lithosphere in PFC. The model consists of 3 main components: the bonded assembly, an intruding dike, and servo-walls. To assess different Martian lithosphere scenarios, we are varying the Young's modulus.

Material properties: Bonded Granular Assembly

The main component of the model is a bonded assembly of particles, which when bonded together in the soft-bonded model, will serve as a block of the Martian lithosphere. At model initiation, we generate the bonded assembly with a random particle packing. We assume the Martian lithosphere to be basaltic, based on spacecraft and meteorite data (McSween et al., 2009), and assign the bond contact values with the macro properties of tholeiitic basalt. . Simulating real world processes requires calibrations of the physical properties of the material we are simulating. As we do not have access to Martian rocks to calibrate, we use pre-calibrated values of basalt, as presented in Holohan et al. (2015), to convert from macro to micro properties. This work has been widely accepted and validated in previous studies, making the values for basalt a reliable reference for our simulations. Using these established and well-validated properties for basalt ensure that the outcome of the model has real-world significance, even under Martian conditions. The PFC particle bond properties: tensile- and shear strength values used in this study were thus adapted from values from Holohan et al. (2015), which are based on the model material calibration performed in Holohan et al. (2011). There, virtual compression, and tension tests confirmed the micro-property values we apply to the PFC bonds in our study (Table 4.1).

Bond Property	*Symbol*	*Value*	*Unit*	*Source*
Young's Modulus	E^*	5.4 – 100	GPa	Heap et al. (2020)
Normal-to-shear stiffness ratio	k^*	2.5	-	Holohan et al. (2015)
Tensile strength	σ_c	5.0e+06	MPa	Holohan et al. (2015)
Cohesion	c	5.0e+06	MPa	Holohan et al. (2015)
Friction angle	φ	30	Degrees	
Friction coefficient	μ	0.5	-	Holohan et al. (2015)
Normal critical damping ratio	β_n	0.5	-	

Table 4.1: Overview of bond properties used in the numerical model in this study.

In Holohan et al. 2011, the particle bond values are based on volcanic rock masses which were estimated using simulated biaxial tension and compression tests at a range of confining pressures. These tests were

designed to examine the behaviour of an assembly of bonded particles, in order to approximate the bulk elasticity and material behaviours of a real rock mass. They conducted 10 realizations of each test, on material samples with a size of 360 x 180 m. The resulting stress-strain curves from the tests showed, that the modelled material exhibited deformation behaviour characteristic to real rock deformation, such as initial elasticity and consequent yielding, strain hardening, failure and strain softening (Holohan et al., 2011). The resulting bulk modulus values, which are the ones used in our study, fall within the expected range for "natural" rock masses, and overlap in the lower end of material (Holohan et al., 2011). There is, however, an exception for the USC (Unconfined Compressive Strength) and tensile strength, which show lower values than the "natural" rock values. This is typical for DEM models which use circular particles (Potyondy, 2019), and can be mitigated to an extent, either by using the "clump" feature to make the particle shape irregular, or by adding additional dampening of particle rotation. However, each of these mitigations come with either a severe increase in model run time and subsequent unrealistically high volumetric strains or will hinder the movement of fracture-bound blocks. In addition, published literature values are usually on intact rock strength, from tests conducted on small scale, defect free samples. This is not a representation of a "natural" system, where the rock-mass scale properties are often considerably weaker. Similar to the conclusion in Holohan et al. (2011), we therefore continue with the standard DEM approach and acknowledge that the USC and tensile strength values deviate somewhat from real rock behaviour.

The size of the model, and thus the bonded assembly, is determined by considering the depth of elastic lithosphere, as well as the size of the resulting deformation we expect. The thickness of the Martian elastic lithosphere (T_e) has, like many other Martian properties, been estimated using gravitational data and numerical modelling. The majority of the numerical modelling studies are based on the flexural loading of a volcanic edifice on the surface of Mars, where the lithospheric flexure will be influenced by the lithospheric parameters. These studies provide models and estimates of the lithosphere thickness, of a specific location on Mars, at the time of loading (e.g. Belleguic et al., 2005; Comer, 1985; Watters, 2003). Over time, the same location on Mars will have a range of elastic lithosphere thickness values, with location thicknesses varying between 2 and 150 km depending on their location on Mars (McGovern, 2004). For computational efficiency considering the number of particles in the model, we use a thickness of 25 km for the dikes to propagate from. The width the model is assigned as 3 times the depth, and is thus 75 km.

To allow for a timely computation, we utilize a gradation of particle sizes from the centre, coarsening outward (Figure 4.3a). This is so that the central area where we are expecting the main surface deformation to occur can be modelled in most detail. For size-scale reference purposes regarding the

final surface structure appearance, we define a "representative model graben cross section" (Figure 4.3b), with a representative depth and width value from the Shahrzad et al. (2024) study of the grabens south of Alba Mons, Mars. The majority of the mapped grabens in the Shahrzad et al. (2024) study have been suggested to be of dike-induced origin based on extensive fault mapping (Shahrzad et al., 2024).

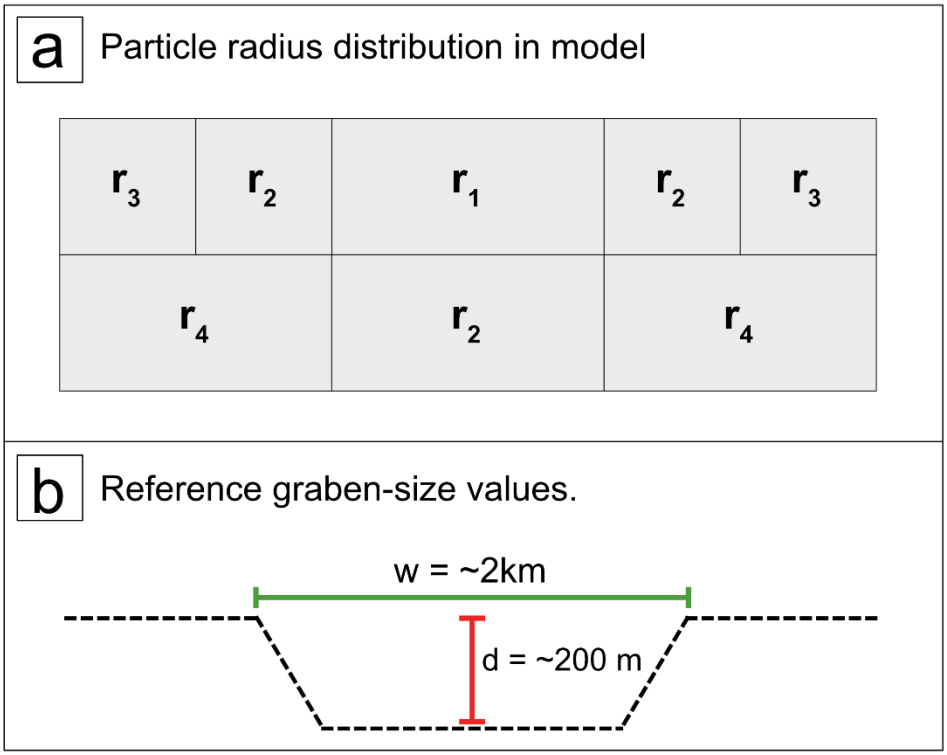

Figure 4.3: A) diagram of particle size distribution in the model, with "r" = particle radius. r1=8-20, r2=20-80, r3=80-100, r4=100-140. B) Reference graben cross-section with average width and depth values from Shahrzad et al. (2023)

For the purposes of this model, we consider the crust as a homogeneous and isotropic material, which is reflected in the bonded assembly setup. The layers incorporated in output diagrams are purely graphic, to aid visualization of the mechanical deformation and do not interfere with any produced stress-fields. Together, this bonded assembly setup is the initial state of the model and reflects a cohesive basaltic rock-mass where we investigate its behaviour under Martian gravity (3.71 m/s^{-2}) with varying Young's modulus.

Boundary Conditions: Free Top Surface, Frictionless Botom, and Servo-Walls on Sides.

The bonded assembly is positioned on a frictionless surface allowing unhindered movement of material along the bottom model boundary (Figure 4.4). However, since we are modelling a section of the lithosphere, the vertical boundaries along the right and left side of the bonded assembly are used to

simulate the confining pressure of surrounding rock. We therefore assign the PFC *servo function* to these walls, which allows material to move horizontally during dike intrusion while at the same time maintaining a constant lithostatic pressure in the bonded assembly (Potyondy, 2019). This is implemented by dividing each side wall into 3 sections with depth and calculating the average expected lithostatic pressure for each wall section, where the depth is the middle of each wall (Figure 4.4).

The Intruding Dike.

Similarly to previous models of Martian diking (Hardy, 2016; Wyrick & Smart, 2009) we model the dike as a simplified solid object. This is done in order to reflect the high fluid pressure of the ascending magma and volatile exsolution, with the ascent driven by the density difference between the magma and surrounding rock (Wilson & Head, 1981). We use a wedge-shaped object to represent horizontal widening of the dike during its ascension (Figure 4.4), and the narrower tip during dike propagation (e.g., Mastin & Pollard, 1988; Rubin, 1992). Analogue experiments have shown that during ascent, a "crack-tip" is generated above the ascending magma, and further crack growth will occur as the dike ascends (Mastin & Pollard, 1988). Similarly, previous numerical models of ascending dikes on Earth model the behaviour of the dike as cracks in material (Koehn et al., 2019), where the propagation produced appropriate stress fields for the potential surface deformation we are investigating (Mastin & Pollard, 1988; Pollard et al., 1983). This behaviour follows Griffith's energy criterion, where the dike-induced crack will propagate if the available energy overcomes the resistance i.e. yield strength of the surrounding material (Rubin, 1993). The zone of influence from the crack tip upon the surrounding rock is dependent on the driving pressure in the crack and will vary if the pressure is constant or is increased towards the tip (Mastin & Pollard, 1988). We keep this "apparent" pressure constant between the model variations to ensure consistency. During the numerical simulation, the dike will ascend to a depth where it will stall when it reaches a depth representing the neutral buoyancy level. In this model, the stalled dike depth is set to 2 km, based on estimations on neutral buoyancy depth of Martian dikes from previous studies,

with a variation between 500 m – 3.3 km (Perrin et al., 2022; Rivas-Dorado et al., 2022). A diagram of the combined model setup with all its components is shown in Figure 4.4.

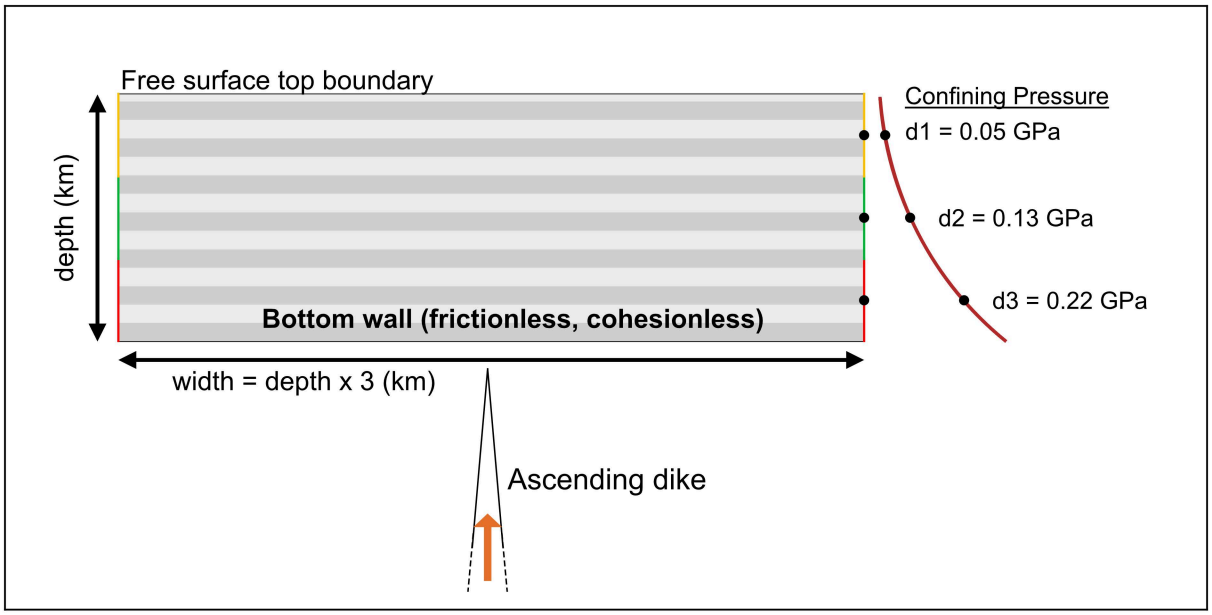

Figure 4.4: Diagram illustrating schematically the model set up a) Diagram of the initial conditions of the numerical model, with the 3 main components: bonded assembly, intruding dike, and servo walls. Horizontal grey bands do not represent any change in values and are only there for deformation visualization. d1, d2 and d3 represent the depth used to calculate the confining pressure for each section of the servo wall.

4.2.3. Model runs: Models A, B, C, and D.

We performed 3 model runs designed to investigate the link between material properties and the morphological nature of grabens formed. In particular, we examine dike driven extension and systematically vary a rheological property of Mars' lithosphere, specifically the Young's modulus. The Young's modulus (E) is defined by the ratio of longitudinal stress to axial strain in a linear elastic material, defining the stiffness of the material. A rock with a high Young's modulus is thus less deformable (i.e., stiff), and the initial part of the complete stress–strain deformation curve of the rock will appear steep in laboratory studies. The opposite is the case for a rock with a low Young's modulus, which is more deformable, and the initial part of the complete stress–strain curve will be gentle (Hudson and Harrison, 1997). Test conducted on different rock types show how Young's modulus varies in different rock types, though there is a large bias in literature towards experiments on sedimentary rocks, with igneous rocks having little to no studies. It is, however, clearly determined that sandstone has a higher Young's modulus than siltstone, followed by mudstone. In terms of igneous rocks, there is no clear distinction between the rock types, as there is large variation in Young's modulus within a singular rock type. An example is andesite, which has recorded Young's modulus values between 1 GPa up to 50 GPa (Heap et al., 2020).

The most distinct correlation is found between Young's modulus and porosity, where Young's modulus increases as porosity decreases. This correlation is found in both sedimentary and volcanic rocks (Heap et al., 2020). Contrarily, increased porosity weakens the rock and reduces the Young's modulus. Additionally, Young's modulus increases as confining stress increases, meaning that Young's modulus is expected to increase with depth (Tesauro et al., 2012). This factor is likely related to the porosity and microcracks, which both decreases the stiffness of rocks. The increase in pressure (depth) can close microcracks and can thus increase the Young's modulus as the stiffness increases, as evidenced in sample deformation experiments (Heap et al., 2020). However, this is only the case for rocks with pre-existing microcracks, where an increase in pressure will likely not affect the Young's modulus of a fully intact/crack-free rock (Heap et al., 2020). The lower gravitational acceleration on Mars ($g = 3.71$ m/s^2 versus $g = 9.81$ m/s^2 on Earth) will mean that for equivalent depths between the two planets, Mars will have a lower confining pressure ($P=\varrho gh$). Thus, the lithosphere's Young's modulus is always expected to be lower on Mars, at corresponding depths.

This parameter has been suggested to be crucially different between Earth's and Mars's lithosphere (Belleguic et al., 2005; Grott & Breuer, 2008). Additionally, this property is expected to have changed during Mars' evolution, from thin and ductile to thick and brittle, as the mantle has cooled over time and the depth of the brittle-ductile transition has increased to larger depths (Grott & Breuer, 2008; Heap et al., 2017). We thus expect differences in Young's modulus to highlight any planetary (between Mars and Earth) or temporal (over the course of Mars' evolution) differences in dike-induced graben formation.

As with other Martian rock mechanical properties, the Young's modulus is estimated based on terrestrial laboratory test and numerical modelling (e.g. Grott et al., 2005; Musiol et al., 2016). Previous literature have used values between 15 GPa (Polit et al., 2009) – 120 GPa (Musiol et al., 2016), with the most commonly used value being 100 GPa (e.g. Belleguic et al., 2005; Broquet & Wieczorek, 2019; Comer, 1985; Grott et al., 2005). In this study we use a lower value of Young's modulus of 5.4 GPa, from a recent study by Heap et al. (2020), who performed an extensive study on laboratory experiment on terrestrial basaltic rocks. We then vary the value to $E = 50$ GPa as an intermediate value and have a maximum of E=100 GPa (Table 2), increasing the Young's modulus with each run. See below for an overview of the different model runs (Table 2).

In addition to the three main models (A, B, and C), we also tested an example using a dike width similar to that of the smallest proposed Martian dike widths, to compare the results to models A, B and C. There

are no direct measurements of dike widths on Mars, but due to the material properties of the lithosphere, they are generally considered to be considerably larger than dikes on Earth. Estimations of dike widths on Mars are based on numerical models of surface deformation (D_w = 600 – 2000 m) (Hardy, 2016; Wyrick & Smart, 2009), numerical models based on Martian magnetic anomalies (D_w = 20-2000 m) (Nimmo, 2000), calculations based on area balance of topographic profiles (Dw = <60 m) (Rivas-Dorado et al., 2021), and on calculations and models based on surface graben widths (Dw = 30 – 1000 m (Ernst et al., 2001) and Dw = >400 m (Wilson & Head, 2002). As there is currently no method of reliably measuring dike widths on Mars, we utilize the previous modelling results as a reference for the variety of sizes in Martian dike widths. In order to attempt to narrow this wide range of numbers, we add an additional model, Model D, to the runs, in an attempt to define a lower boundary of dike width for graben-forming dikes.

For Model D, we chose a dike width of 200 m, a width which is often within the range of cited narrowest Martian dike widths (see examples above). We tested this dike width in the intermediate Young's modulus material of 50 GPa (Table 4.2).

Model Run	*Young's Modulus, E, (GPa)*	*Max. dike width*	*Mode of deformation*
Model A	5.4	**2 km**	**Dike intrusion**
Model B	50	**2 km**	**Dike intrusion**
Model C	100	**2 km**	**Dike intrusion**
Model D	50	**200 m**	**Dike intrusion**

Table 4.2: Model run overview with model variable values.

4.3. Results

We ran all four of our models to a dike-tip depth of 2 km and monitored the material displacement throughout the simulations. At the final stage of the numerical models, three dike-intrusion models managed to produce material fracture (normal and listric faulting for Models A, B, and C) and for Models B and C, subsequent graben formation of different sizes. Model D showed no immediate material fracture.

4.3.1. General deformation behaviour:

*In Model A (*E = 5.4 GPa), Figure 4.5 presents three snapshots of the model during the dike intrusion process where the dike-tip depth varies. At a dike-tip depth of 20 km (Fig. 4.5a), the dike has generated two petal shapes of material which are moving upwards with more displacement than the surrounding lithosphere. The rest of the lithosphere displays an initial large asymmetry with the right side of the model displaying a higher negative displacement than the rest of the lithosphere, likely due to the random packing of particles. Once the dike has reached a depth of 10 km (Fig. 4.5b), the initial defined pockets of higher displaced material have developed into elongated petal shapes, originating from the dike-lithosphere interface. There is no noticeable deformation on the surface of the model. This changes when the dike-tip reaches a depth of 7.5 km (See Supplementary Figure C.1 (Appendix C)), where faulting at the surface is initiated. 6 fractures are generated at the surface, with 3 on either side of the dike, all with a largely consistent depth of ~700 m. At this point the fractures are largely vertical, with no apparent angle. At the final dike-tip depth of 2 km, the intrusion has generated 9 surface-breaking faults in total (5 to the left of the dike and 4 to the right), all contained within the smaller particle radius region (See Figure 4.3a for reference).

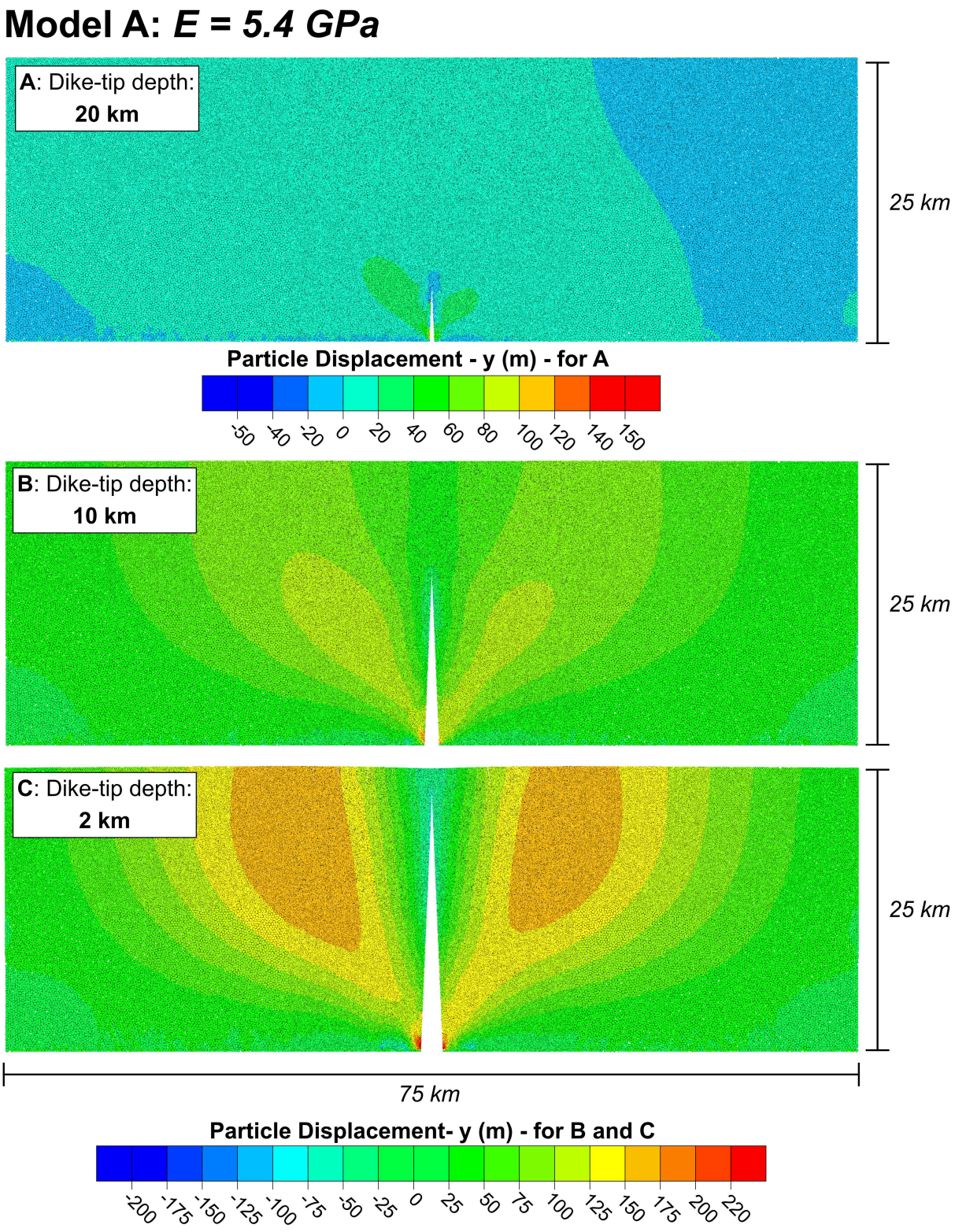

Figure 4.5: Examples for three different dike-tip depths for Model A, where E = 5.4 GPa. Note that Figure 4.5a has a different vertical displacement scalebar from Figure 4.5b and 4.5c.

The results of *Model B (*E = 50 GPa) are shown in Figure 4.6. At a dike-tip depth of 20 km (Fig. 4.6a) the surrounding lithosphere is responding to the stresses generated by intruding dike. Different from the petal shape generated in Model A, the material displacement is shaped as a large wedge, at an angle of 15°-20° from the tip of the dike at the initial intrusion point, which changes to ~11°, 9 km from the surface (Figure 4.6). There is a final shift to ~7° at 3 km (Supplementary Figure C.2 (Appendix C)). At this point, the dike is inducing material displacement along ~15.8 km of the surface. Large-scale surface-breaching brittle deformation of the lithosphere starts occurring at a dike-tip depth of ~15km (See Supplementary S1), and by dike-tip depth of 10 km (Figure 4.6b), the material breakage has developed into sets of large fractures reaching the surface. There is a slight asymmetry of material displacement, with a wedge of material on the left side of the dike, which has had more down-going movement relative to the rest of the lithospheric material. In the final stage of the model on Figure 4.6c, the dike has reached the final intrusion depth of 2 km. The dike intrusion has produced a well-developed graben, with two bounding normal faults, and a number of interior normal and potential listric faults in different orientations (Figure 4.6c). The graben has a width of ~8.8 km, and the floor is mostly symmetric, with a peak in the middle, largely centred on the peak of the underlying dike tip. The highest amount of material displacement is localized in the two wedges on either side of the dike (Figure 4.6c).

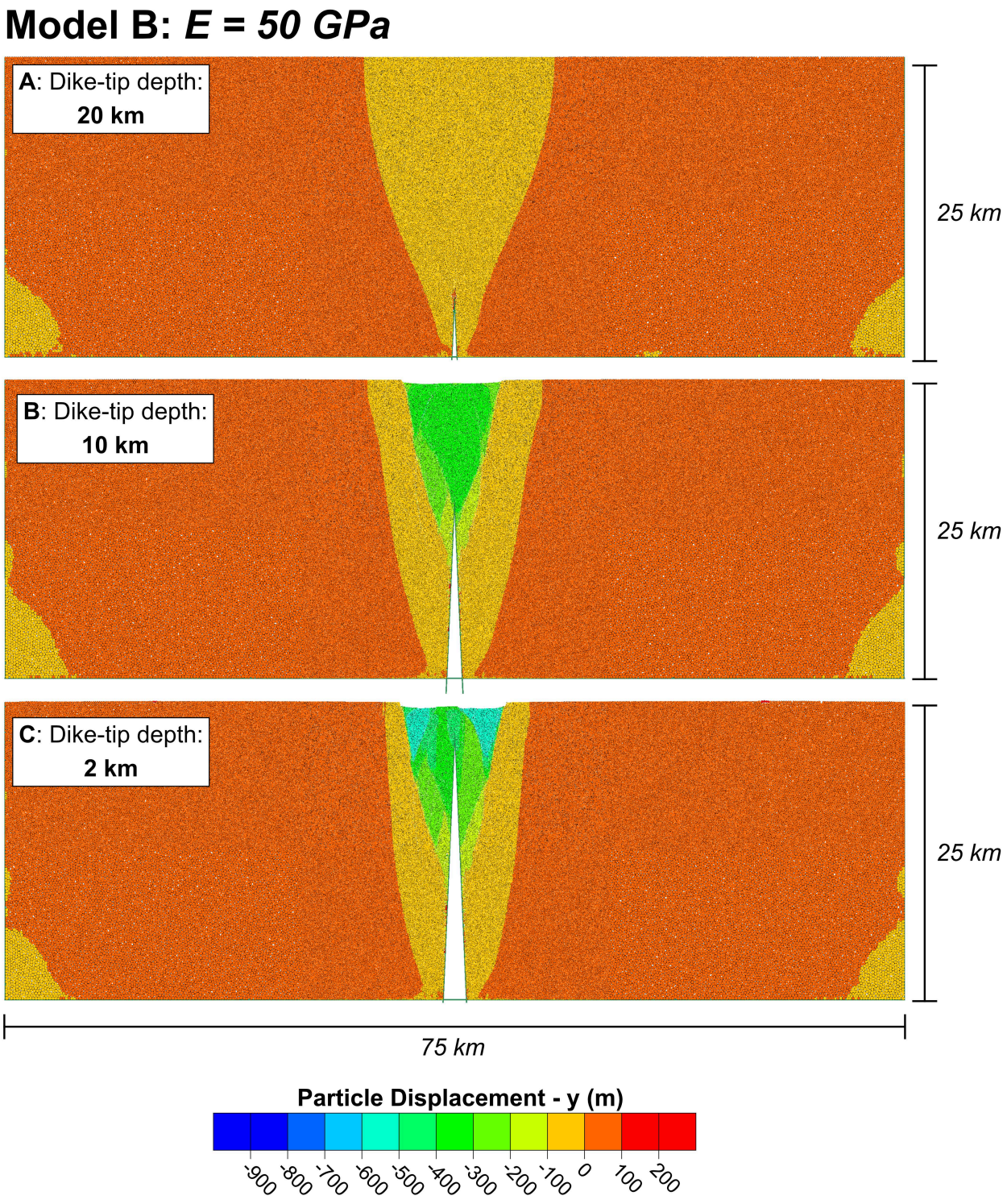

Figure 4.6: Examples for three different dike-tip depths for Model B, where E = 50 GPa.

In *Model C,* (E = 100 GPa), at a dike-tip depth of 20 km, the dike has generated a similar displacement pattern for the overlying material, as Model A and B, for a similar depth. Here, a wedge shape of material centred on the dike-tip has been moved up more relative to the surrounding lithosphere, where material has also been moved up. This displacement reaches the surface and, similarly to Model B, starts an angle of ~20° from the tip of the dike at the initial intrusion point, which changes to ~10°, and finally reaches ~7° at the surface. Surface-breaking faulting starts at a dike-tip depth of ~18km. This develops as the simulation continues as the dike intrudes, where Figure 4.7b shows a network of well-defined faults creating distinct blocks of the material. While the right-side asymmetry is present in the later stages for Model B, it is significantly more pronounced in Model C. Here the faulting has separated the blocks of material, allowing the hanging wall to move down the normal fault, creating a ~4.2 km nested graben within the larger 10.2 km graben induced by the dike. This is also evident on the final topography of the graben floor.. The dip of the final graben bounding faults are consistently ~70° for the faults across both Models B and C. See supplementary Figure C.3 (Appendix C) for all 9 model captures.

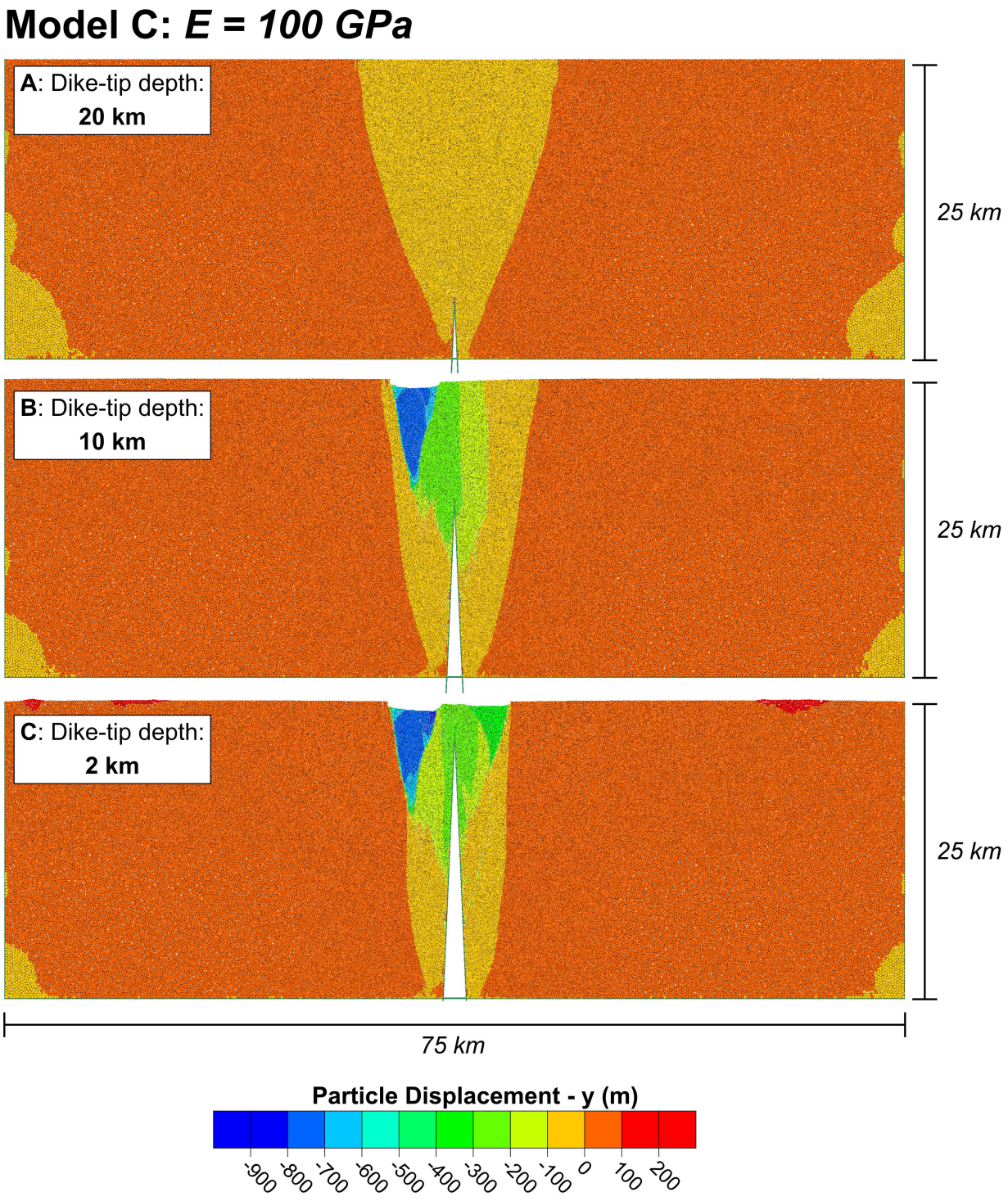

Figure 4.7: Examples for three different dike-tip depths for Model C, where E = 100 GPa.

In the final model, *Model D*, we ran a "comparison" model width a narrower dike width (see Figure 4.8). At the first overview it is clear that this model is not producing the same subsurface faulting or even surface fractures, as observed on Models A, B, and C. The slight material displacement caused by the uprising of the dike, which begins at a dike depth of 22.5 km (Figure 4.8a), is slowly and slightly increasing through the runtime of the model, with the negative material displacement originating from the tip of the stalled dike. While no material fracture is immediately evident, the model does show the same type of asymmetry in material displacement as the later stages of Models B and C. The final area of material displacement on the surface on Figure 4.8c is approximately 7 km in width.

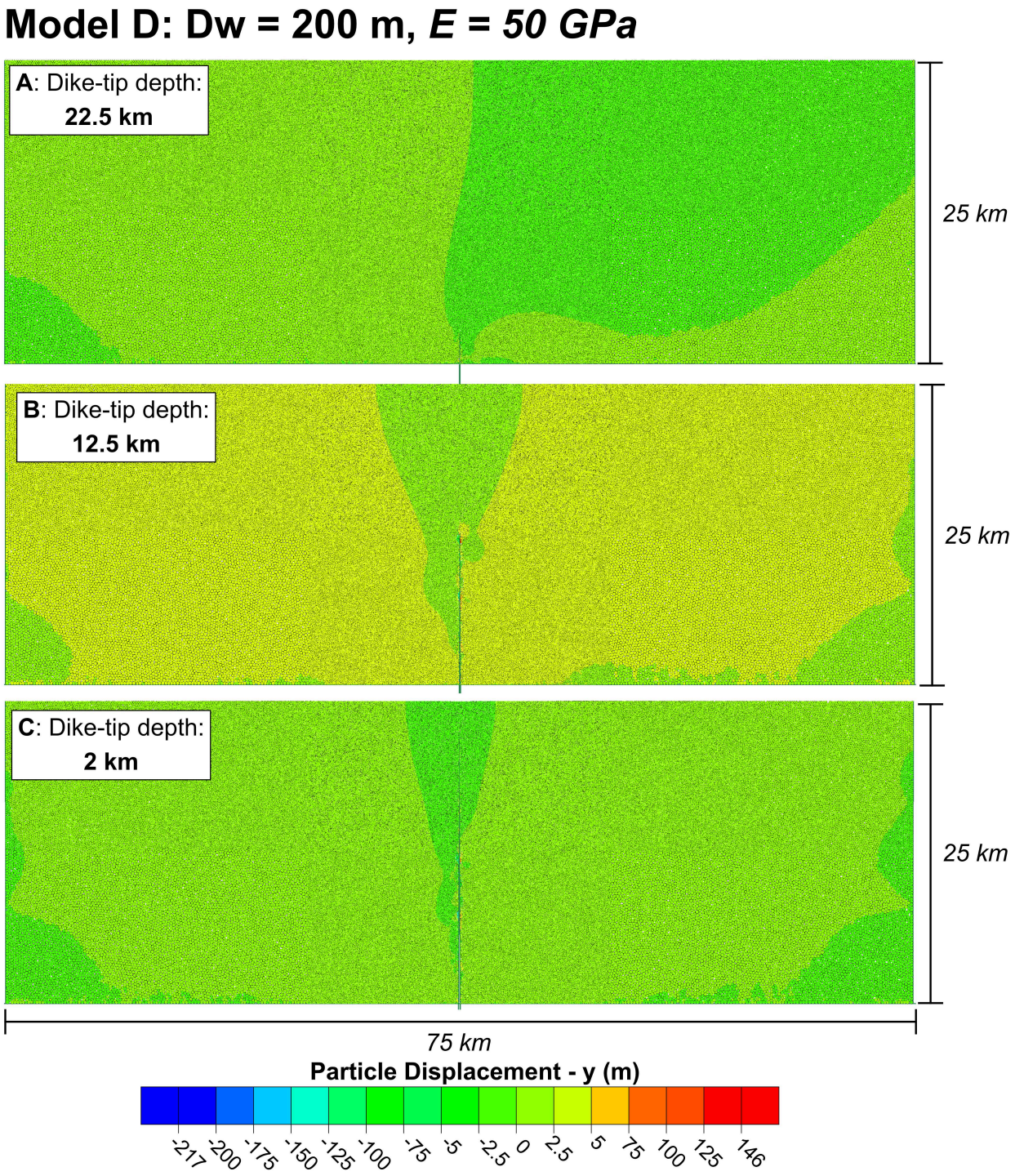

Figure 4.8: Examples for three different dike-tip depths for Model D, with a dike width (Dw) of 200 m and E = 50 GPa. Note the different particle displacement legend values from Models B and C.

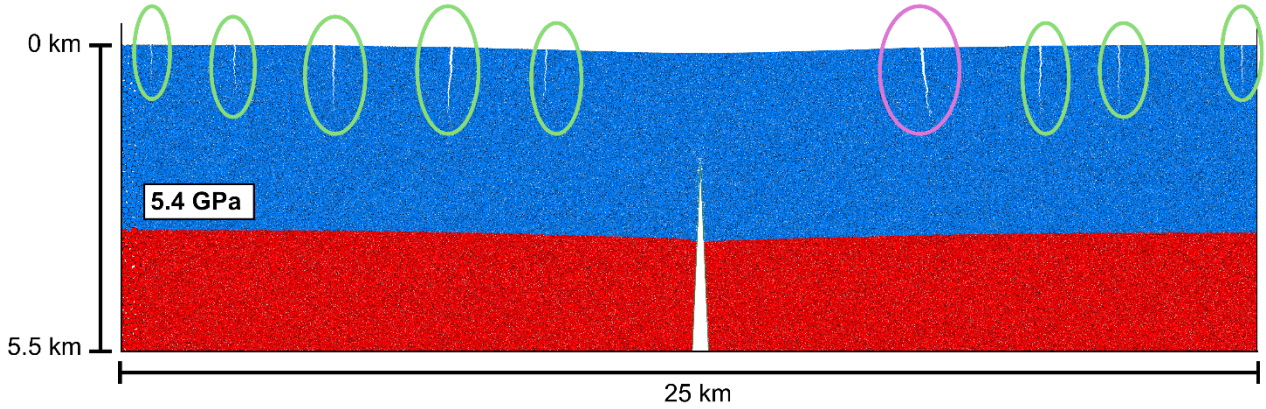

Figure 4.9: Zoom on the final surface fractures for Model A, at a 2 km dike-tip depth. Note the asymmetric fracturing. The green circles highlight the largely vertical fractures, while the pink circle highlights the fracture which dips away from the dike. Red and blue material colours are for observing material movement and does not reflect a change in lithospheric properties.

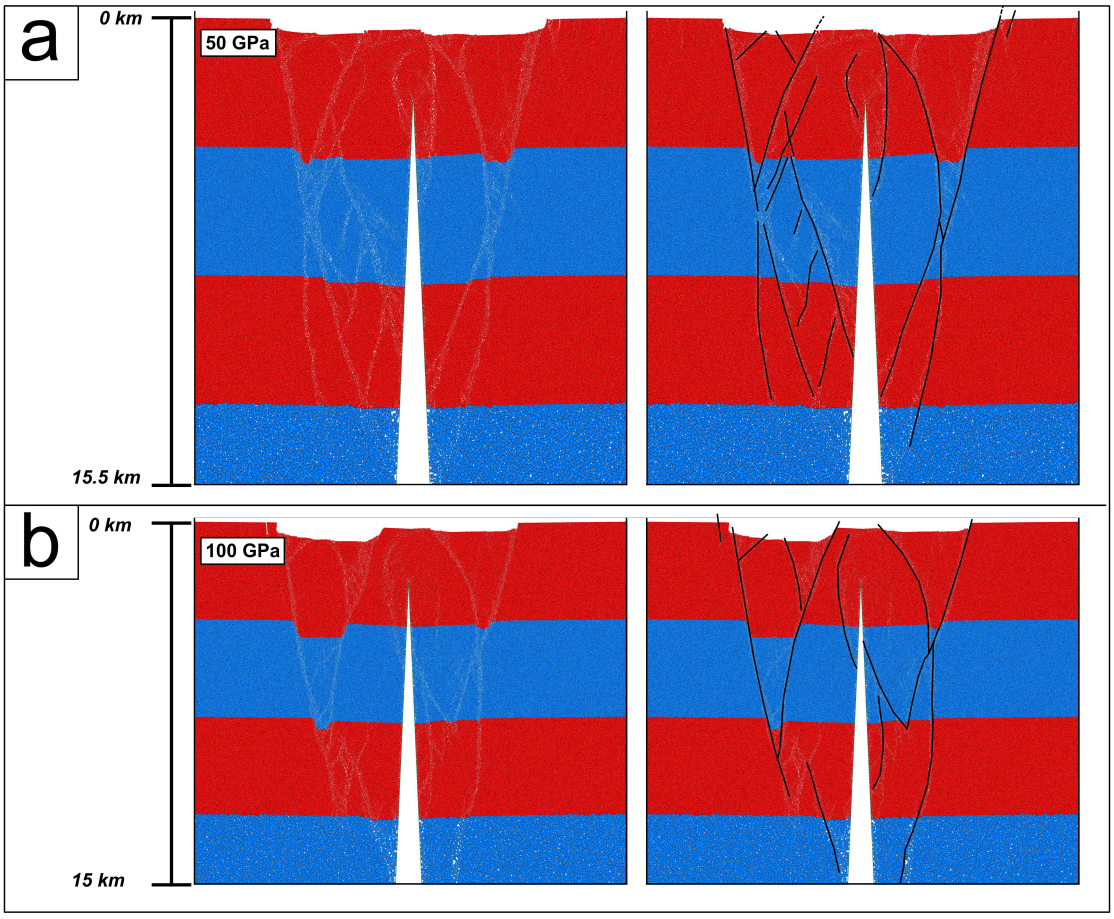

Figure 4.10: Final fractures generated by the top for a) Model B and b) Model C, for a dike-tip depth of 2 km. Image on the left is a screengrab of the fractured material and the image on the right has the material break marked in black lines for better visibility. Red and blue colours are for observing material movement and does not reflect a change in lithospheric properties.

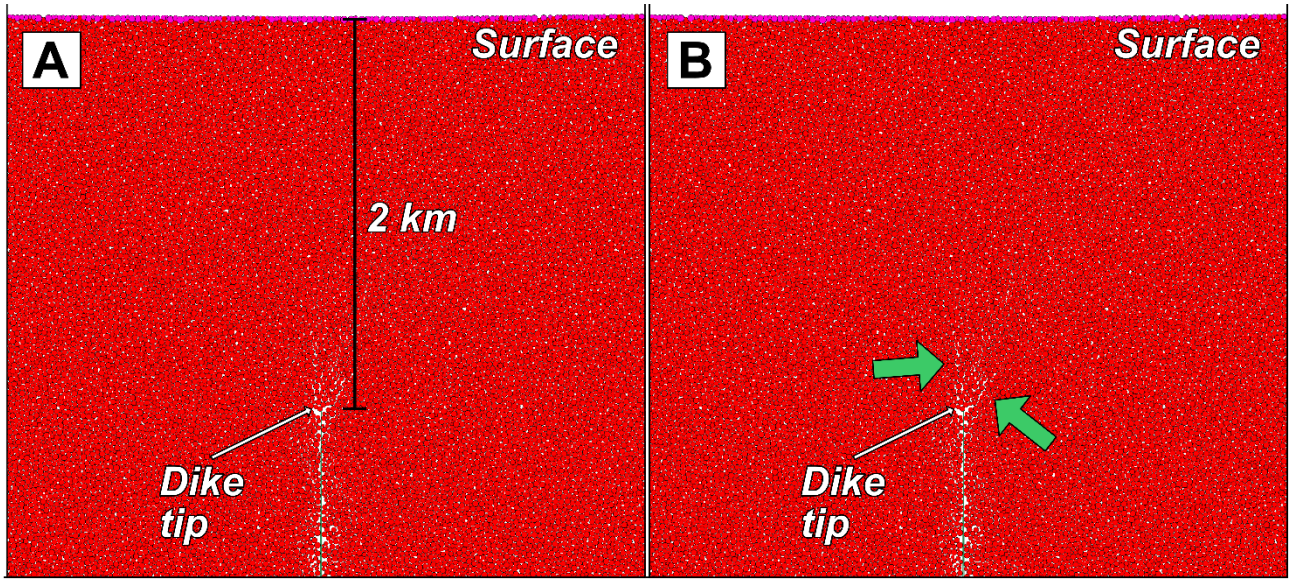

Figure 4.11: Zoom on material for the final state of Model D. The colour of the material does not reflect any values, they are simply highlighting the particles.

4.3.2. Detailed fracture and surface topography

Taking a closer look at the fractures generated during the dike ascent, the differences between Model A and Models B and C become even clearer. Model A shows no internal brittle deformation along the intruding dike, though material is being displaced upwards. The extensional fractures formed in the material are exclusively contained to the surface (Figure 4.9). These fractures reach a depth of (max) 1.6 km, and while they are not graben forming, a depression has begun forming above the arrested dike tip (Figure 4.5c and Fig. 4.9). Models B and C both show initial listric faulting, which is generated at the tip of the dike, and propagate upwards to break the surface. These primary faults develop as a slightly asymmetric set of 2 faults, with one of each side of the dike tip. This is supplemented with a network of further linear normal faults and additional listric faults (Figures 4.10a and 4.10b). The main difference between Models B and C is the depth from which the faults propagate from, with surface-breaking faulting in Model C starting ~3 km deeper than Model C (Supplementary Figure C.3 (Appendix C)). Additionally, the zoom on Figure 4.10 highlights the difference in amount of faulting, where Model B (Figure 4.10a) shows a higher number of more fragmented faulting, while Model C (Figure 4.10b) contains less, and more cohesive faulting.

Model D did not produce any identifiable subsurface fractures or faults of the same scale as the previous three models. Examination of the model surface also show no indicated material fracture. However, when zoomed in at the very tip of the stalled dike at 2 km depth (see Figure 4.11a), it is possible to identify the initiation of one or two cracks in the subsurface (see Figure 4.11b), originating as the dike tip.

To closely monitor resultant surface deformation and surface topography characteristics, we constructed surface topography plots for the final state of each of the first three models (Figure 4.12). The difference between the three models with their different brittleness values is clear, with the lowest brittleness on Figure 4.12a showing a smooth concave up curve, centred above the intrusion. The intermediate Young's modulus for Figure 4.12b shows actual brittle deformation, with surface breaks creating a graben with a peak on the graben floor. The final profile (Figure 4.12c) shows Model C, where a graben has also formed, though a few hundred meters deeper than the graben in Model B (Figure 4.20b). The resulting graben has a noticeable asymmetric appearance reflecting the nested graben visible on Figure 4.7. Note for Model B and Model C, the surrounding surface, which is not in the grabens, has increased in elevation by several hundred meters relative to the original surface.

For the additional Model D, the final topography (Figure 4.13) reflects the lack of structures and relatively smaller material displacement observed on the model results (Figure 4.8). We can however observe the formation of a small trough above the stalled dike, with an approximate depth of 36 m. The surface topography also displays what appears to be a few fractures in the surface, particularly around the 50-70 km distance (Figure 4.13). However, inspecting the surface of the model results (Figure 4.8), these are more likely due to the surface topography code identifying slightly different particles than the surface ones, as no material fractures can be identified at these locations.

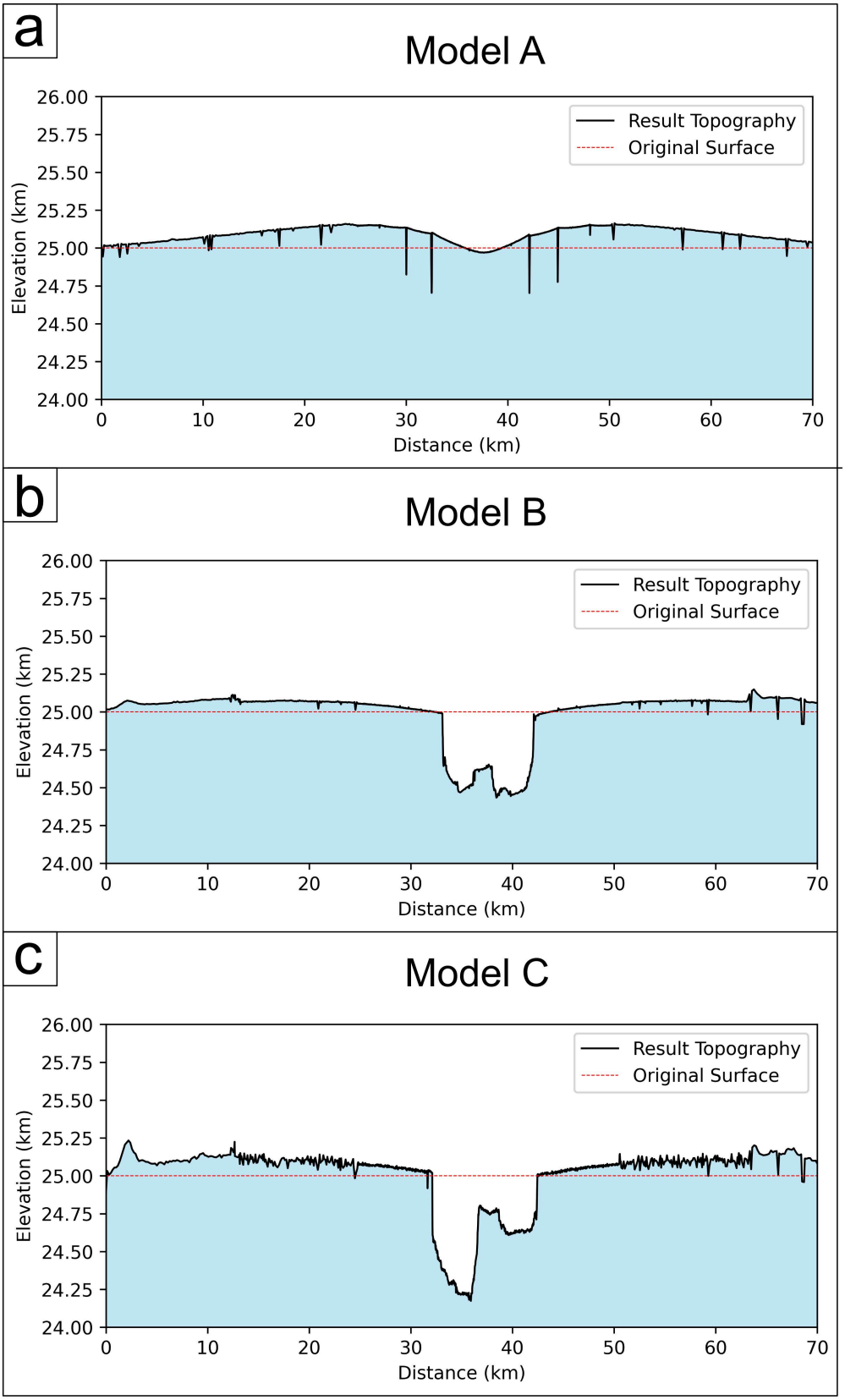

Figure 4.12: Topographical profiles for Model A, Model B, and Model C, at final dike-tip depth of 2 km. Black line denotes the final surface, while the red dashed line shows the original surface, pre dike-injection.

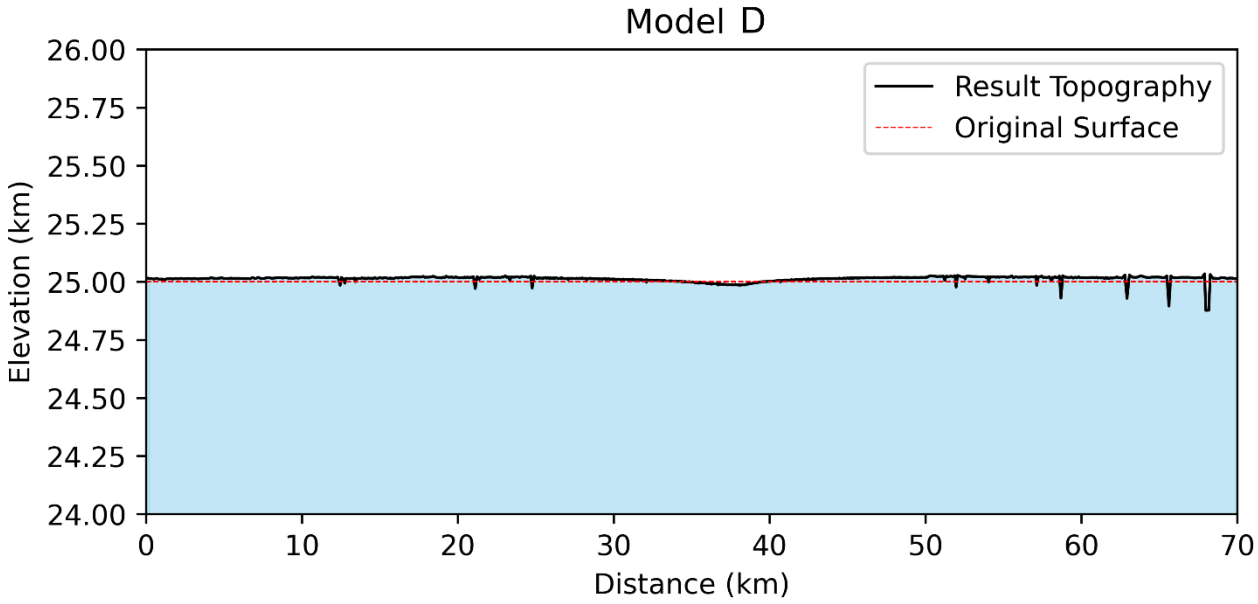

Figure 4.13: Final surface topography versus original topography surface of Model D, with dike width = 200 m and E =50 GPa.

4.4. Discussion

4.4.1. Fracture development across the four different models.

Changing the Young's modulus of the model yielded significantly different results for Model A and Models B and C. For Model A, throughout the intrusion of the dike, there is not a lot of brittle deformation occurring, though material is being displaced (Figure 4.5). The fracturing of the lithosphere is initiated at the surface, and not at the tip of the dike, as proposed in most models of dike-induced graben formation. Compared to the other models (see Supplementary Figure C1), the horizontal displacement along the upper ~5 km of the model lithosphere, far outweighs the vertical displacement. This could suggest that they are not generated by the tension produced at the tip of the dike, but rather by extension due to the movement of material towards the boundary of the model by the slight widening of the intruding dike. As the surface has the lowest lithostatic pressure, this is where the faulting is concentrated. Both Models B and C show an initial development of a set of two listric faults, generated at the tip of the ascending dike, which reach the surface of the lithosphere. In accordance with the slight widening of the intruding dike, accommodation space is created, and further normal faulting occurs, some constrained in the subsurface, while others break the surface. This allows for the movement of material (Figure 4.10), which at the end of both Models B and C develops into the large final graben structure (Figure 4.14) with faulting within. These initial listric faults are a deviation from the idealized assumption of an initial two graben-bounding normal faults (Figure 4.1).

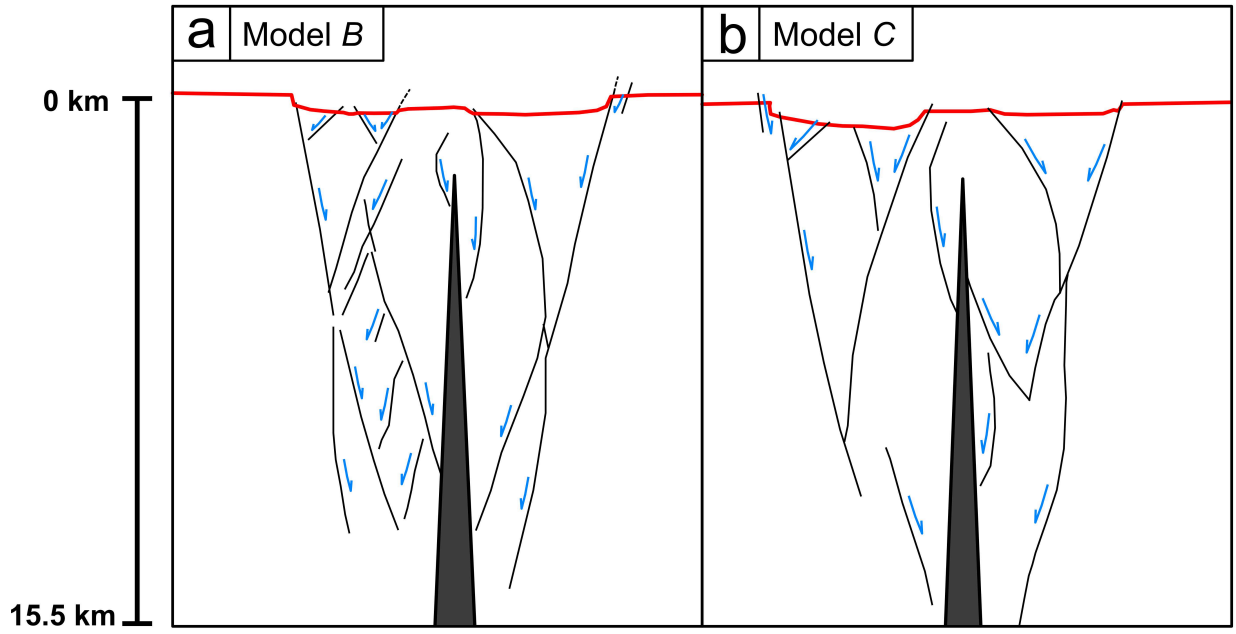

Figure 4.14: Schematic of the faults produced during Model runs B (left) and C (right), from the results on Figure 4..

Rather, in our models, the dike-generated listric faults facilitate the initial surface break, allowing further normal faulting to develop at the surface. Though Models B and C are very similar in comparison with the resulting structures from Model A, the main difference is found in the scale of the final features, and in particular the initial depth where surface-breaking faults are generated. As hypothesized in Heap et al. (2017), the higher Young's modulus allowed fractures to propagate to the surface from a larger depth in the 100 GPa model compared to the 50 GPa model.

For Model D, we ran a model with a dike width of 200 m in material with E = 50 GPa, in order to test the effects of a narrow dike on graben formation. While the ascent of the dike did initiate some material displacement (Figure 4.8), no faults or identifiable surface fracturs were generated. A few fractures were observed near the stalled dike tip, which may have developed further into faulting if the thinner dike had propagated closer to the surface. It is however expected that a shallower dike depth will produce a smaller graben width (Rivas-Dorado et al., 2021).

4.4.2. Relating Model A, B and C results to other numerical studies:

We compare our results to other numerical models regarding dike-induced surface deformation on Mars. In Wyrick and Smart (2009), they use a discrete element model setup of the Martian crust. They simulate the widening of an already intruded dike in order to assess the surface deformation and find that the dike-widening only produces a trough consisting of contractional folds, and not a graben, in material with varying heterogeneity. However, a study by Hardy et al. (2016), similarly testing dike-widening as the graben-formation mechanism, produces extensional faulting and subsequent grabens using more "consolidated material". While it is not possible to perform a direct comparison of our results to these two studies, as the modelled material properties are not available, based on the results from our Models A, B and C, it appears safe to assume that the model of Hardy et al. (2016) has used a stiffer material than Wyrick and Smart (2009). This is consistent with the Wyrick and Smart results more closely resembling our Model A topographic profile results (Figure 4.12a), with a slight upwards displacement of material on either side of the dike, resulting in a slight trough shape directly above the dike. We do, however, not see any contractional or folding structures within the lithospheric material in Model A (Figure 4.5).

The fact that the grabens formed in Models B and C (Figure 4.14) require a relatively small widening of the dike to form, in accordance with Hardy et al. (2016), could account for how we observe hundreds of kilometre long grabens on Mars, which are spaced very closely together, often with spacing less or equal to the individual graben widths (Shahrzad et al., 2023). This is challenging to explain if significant in-situ widening of the dike is required to create any surface deformation, as modelled in Wyrick and Smart (2009) and Hardy et al. (2016).

While the previous models concern themselves with diking-induced surface structures of Mars, we also compare our results with another study, where Martian lithosphere parameters was assessed by simulating different geologic processes using numerical modelling. A study by Taylor et al. (2020) varies lithospheric and edifice properties when using finite element modelling to simulate the gravitational loading of a volcanic edifice on the Martian lithosphere. In their results, they find that a Young's modulus of 17.8 GPa was the best fit for their results. This is a distinctly low value, considering the average values used to model Mars are usually in the 50-100 GPa range. This value is closer to the 5.4 GPa suggested for terrestrial volcanic material in Heap et al. (2020).

While the average Martian dike-induced topography (Figure 4.13) is a closer fit to the 50 GPa and 100 GPa models, a natural assumption is then that the Martian lithosphere has a significantly higher Young's modulus than theoretically assumed (due to the lower gravitational acceleration than Earth's). This is consistent with the assumptions made in numerous numerical models (E.g. Belleguic et al., 2005; Comer, 1985; Kronberg et al., 2007; Musiol et al., 2016). However, if we take a closer look at the differences between the results from Models B and C, despite doubling the Young's modulus, the overall morphology of the deformation is extremely similar, with a few km size differences in graben width and depth. While we do observe dike-induced grabens of this size on Mars (Shahrzad et al., 2023), the average graben width is around 2 km for dike-induced grabens in Tharsis (Figure 4.3b). Additionally, Models B and C are such a large departure from the results of Model A, despite increasing the Young's modulus by approximately the same amount. Combining this with the 17.8 GPa Young's modulus from Taylor et al. (2020), this could suggest that there is a threshold value of Young's modulus in the lower range (~20 GPa), where the lithosphere starts allowing sufficient brittle deformation to occur during dike-injection, to produce the structures we observe on the surface of Mars.

The final graben width is not significantly larger for Model C compared to Model B, which is consistent with previous studies, where relationships between graben width (G_w) and dike-tip depth (D_d) are used to assign values to these variables. As the dike-tip depth is consistently 2 km, we show that the 100% increase of Young's modulus between the two graben-forming models, only increases the graben width by 15.9% (1.4 km). This gives us an average G_w/D_d ratio of 4.75 for the grabens in Models B and C. Comparing this to estimations from other studies, values range from 1.18 (Rivas-Dorado et al., 2021), 3.42 (Wilson & Head III, 2002) and ranges between 3.52 to 6.24 in a numerical study by Wyrick and Smart (2009). Our results are in the high end, but we consider it a more accurate representation of the connection between G_w and D_d than some previous studies, as their estimates rely on final surface deformation as a result of dike widening.

4.4.3. Relating resulting fracture patterns and surface topography from Models A, B, and C to Mars:

For the current Martian lithosphere, properties such as thickness and density are considered heterogeneous across the *current* Martian lithosphere, which similarly to Earth, displays higher and lower values depending on the location, where multiple studies have determined a variety of crustal densities and lithosphere thicknesses beneath the major Martian terrains, with values in T_e ranging from <12 km for Noachis Terra (McGovern et al., 2002) to 105 km for Ascreaus Mons (Belleguic et al., 2005). However, when considering the development of the planetary lithosphere as a whole, the Martian lithosphere has had a defined evolution through time. The initial state of the Martian lithosphere in the Noachian is considered thin, which was then followed by a rapid growth of the elastic lithosphere in the Hesperian, as the mantle cooled over time to its present determined temperature, slightly lower than that of Earth (Baratoux et al., 2011; Grott & Breuer, 2008).

Though Mars is considered to have a lower Young's modulus along with a deeper brittle/ductile transition than Earth, due to the lower surface gravitational acceleration affecting the rock porosity (Heap et al., 2017), limitations from lack of actual rock samples has meant that the material properties for the Martian lithosphere is poorly constrained. Numerical models of Mars have previously used a large variety of values to represent the Young's Modulus. Values range from 15 GPa (Polit et al., 2009) to 100 GPa (Belleguic et al., 2005; Comer, 1985; Grott et al., 2005; Watters, 2003). Intermediate values such as 40 or 50 GPa (Cailleau et al., 2005; Musiol et al., 2016) and 80 GPa (Kronberg et al., 2007) have also been used for modelling the Martian crustal lithosphere.

We make a more direct comparison by assessing our final surface topographies to a sample of 10 grabens mapped in the Ceraunius Fossae area in the Tharsis volcanic province on Mars (Shahrzad et al., 2024) (Figure 4.15). The profiles used in the plot in Figure 4.15 are all from structures which have been determined to be diking induced, during an independent study of the extensional features in the area (Shahrzad et al., 2024). As the topographic profiles are of varying absolute lengths, we also plot an average profile using the average Y (elevation) value over a common, representative X (distance), to compare the graben structures.

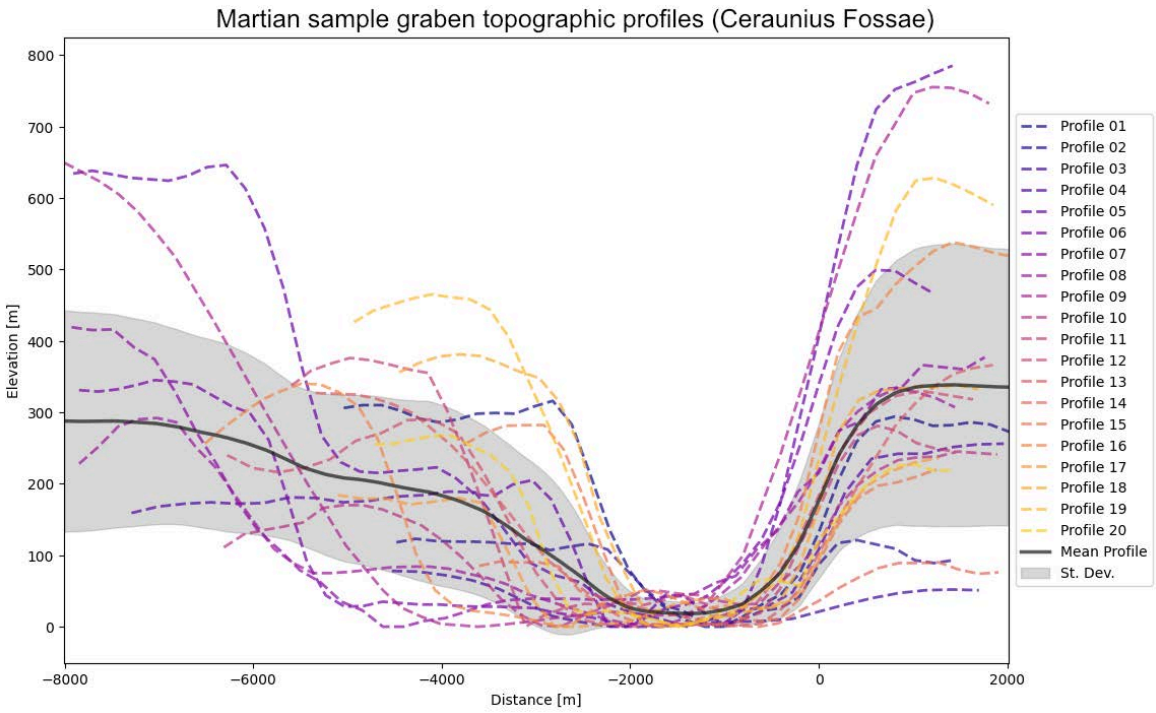

Figure 4.15: Plots of a sample of 20 topographic profiles taken across diking-induced grabens in Ceraunius Fossae, Mars. The grabens are from a study in Shahrzad et al. (2024). We use the MTPT code (Murphy Quinlan, 2024) to plot the profiles, where the lowest points are aligned, and the maximum slope is also aligned, in order to compare the graben shapes more accurately. We plot an average graben topographic profile based on the measured sample group.

When plotting the average measured graben shape, it is clear that the topographic profiles most closely resemble the results from Models B in particular, as well as C. The individual grabens in Figure 4.15 and the numerical model results display two graben bounding faults, and a relatively flat graben floor, with a slight peak in the middle. The average measured topography from Ceraunius Fossae (Figure 4.15) likewise show the asymmetric graben floor we produce in Models B and C. However, the small sample size in profiles makes it difficult to determine if this is a prevalent behaviour in the Martian dike-induced grabens. The similarity with the topographic profile from Model C (Figure 4.10c), could suggest that the asymmetric Martian grabens may have formed in material with a higher Young's modulus, than those with flat graben floors. This avenue can be further explored in future work, with a larger sample size of measured Martian topographic profiles of dike- and non-dike induced grabens. Another thing to notice is the scale of the grabens. The grabens produced in Models B and C (Figure 4.10) are larger than the average fault width from the Tharsis sample grabens (~2-4.5 km). As we show a small difference in graben width between Models B and C, this difference is likely a result of the shallow dike (2 km) used in our models, while the mapped grabens may have formed as a result of deeper stalled dikes.

The similarities in graben shapes between the results from Models B and C and the average measured profiles from Ceraunius Fossae highlights how a Young's modulus of $\geq$ 50 GPa is a reasonable assumption to use when modelling the Martian lithosphere, and in particular regions in Tharsis.

Based on the results from Models B and C, we propose a variation of the model of fault development and subsequent graben formations for Mars, for lithospheres with Young's modulus is at least ≥ 50 GPa. In this model, the initial dike-tip generated faults are listric, and subsequent normal faulting facilitated by the dike forms the boundaries for the final graben structure (Figure 4.16).

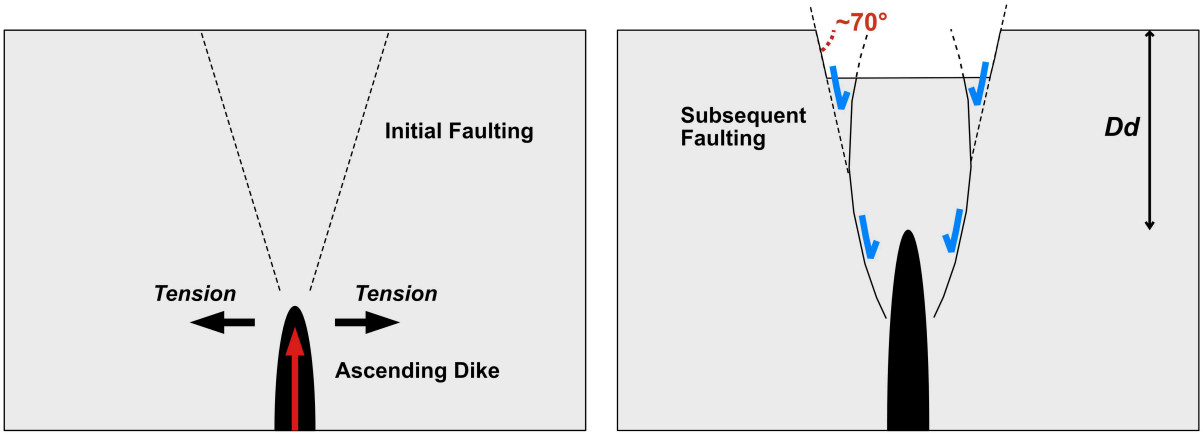

Figure 4.16: Proposed new model of simplified fault development and subsequent graben formation during dike ascent in the Martian lithosphere.

The ~70° dip of the graben bounding faults in both Models B and C is slightly higher than the average 60° degrees assumed for Martian faults (Polit et al., 2009). The higher value is likely a reflection of the depth of the faults generated, with the 70° dip originating from a slightly lower depth. As this dip is fairly consistent between the 50 GPa and 100 GPa model, the Young's modulus does not have an immediately apparent relationship with the fault dips but may instead reflect a difference in fault dips between diking-induced faulting and purely tectonic extensional faulting.

4.4.4. Relating the results to Earth

Additionally, we consider the differences in dike-induced grabens between Mars and Earth. Other than the examples mentioned in the introduction (e.g. Ernst et al., 2001; Magee & Jackson, 2020), it is difficult to find examples of diking induced grabens on Earth's surface, despite the theory being well proved in analogue and numerical studies (Gudmundsson, 2006; Rubin, 1992; Rubin & Pollard, 1988). While structures may have been erased due to the active tectonism and plate activity on Earth, the active magmatic activity on Earth should, in theory, produce results similar, though at a different scale, to the dike-induced grabens of Mars.

According to the results from Models A, B and C, the higher Young's modulus on Earth should result in extensive and large graben structures on Mars, as a result of dike-injection. As mentioned, this does not appear to be the prevalent case on Mars, as there are limited observations of dikes underlying grabens.

What this means is that as a parameter, Young's modulus is not a sole controlling factor for dike-induced graben formation across different terrestrial planets. This opens up an avenue for testing additional parameters, which are discussed in Section 4.4.5.

A final thing to consider, is that the dike-induced graben structures mapped on Mars are regularly 2-3 billion years old at the time of their emplacement. Relating this to the lack of evidence from current Earth observations, may suggest that the Young's modulus for the Martian lithosphere, at the time the graben formations, was higher than that of the current Earths.

4.4.5. Sizes of dikes on Mars

While the inclusion of Model D in this study is only the beginning of a potential modelling study focusing on the different widths of the dikes on Mars, the results from this model can be used as a starting point to narrow down the wide range of potential Martian dike widths cited in literature (e.g. Ernst et al., 2001; Hardy, 2016; Rivas-Dorado et al., 2021; Wilson & Head III, 2002). Of the 2 km dike width models, Model B and C, both yielded final graben widths between 8.8 - 10.2 km. While these are larger than the average measured graben width in this study (~2 - 4.5 km), we do have examples of grabens with similar sizes across all three study areas, with the largest grabens in Ulysses Fossae on Mars measuring 7-10 km, with 7-11 km wide grabens in Ceraunius Fossae, and the slightly lower 6-7 km maximum graben widths in Tractus Fossae (Shahrzad et al., 2023; Shahrzad et al., 2024). The 2 km dike models therefore show the upper limit of fault structures identified in previous study areas on Mars (Shahrzad et al., 2023; Shahrzad et al., 2024). To assess the impact of the width of the dike on the final surface structure, we ran Model D, which showed the opposite end of the spectrum of potential Mars dike widths. The resulting material showed no evident faulting or large fractures, but did show negative material displacement, where the formation of a small trough had begun on the surface. While the area of displacement was quite large (~7km) on the surface, the results from the previous graben-forming models (Model B and C), showed that the actual area of fault-bounded graben formation is smaller than the area of negative material displacement, though the difference is very small in the high Young's modulus model, Model C.

While this "test" run does show that dike width has a considerable impact on whether or not there is surface-graben formation, it cannot be excluded that a graben might have formed if the 200 m dike propagated to a shallower depth, or if the material had a higher Young's modulus, though the 2 km dike was able produce a large graben structure at E = 50 GPa (Model B). A graben formed in these circumstances in the model, however, would again be expected to be much narrower (Rivas-Dorado et al., 2021) and not match the observed width of grabens covering the Martian surface.

So why are the dikes on Mars so large?

As the 200 m dike in Model D did not produce any structures of the scale as those mapped on Mars, and the 2 km width dike in Models B and C *did* (Shahrzad et al., 2023; Shahrzad et al., 2024), we can assume that the dikes on Mars are likely in the larger end of the 200 – 2000 m width range. This is considerably larger than the dikes on Earth, which on average range in widths <10 m (Ernst et al., 2001). Our results are also consistent with the results from Hardy et al. (2016), where a 300 m dike manages to produce a "graben" of ~2.6 km width. If scaled linearly, a 1800 m dike would produce a graben with and approximate width of 7.8 km, close to the results in our Models B and C.

While these widths of dikes can seem very large, it is important to consider that Mars has many large structures, such as the iconic colossal shield volcanoes, where the largest of them, Olympus Mons, has an edifice height of ~22 km and an area of ~ 303,000 km^2. The size of these large features is attributed to the lack of plate-tectonics on Mars, which has enabled a constant supply of magma for the volcanoes to build their large shields (Musiol et al., 2016).

A study by Heap et al. (2017) highlighted how the low surface gravity, and therefore lower lithostatic pressure, has affected the Martian lithosphere. For any given depth, the lithostatic pressure will be substantially lower on Mars than on Earth. As lower pressure favours a brittle failure mode, the depth of the brittle-ductile transition is deeper on Mars. Since fractures close as lithostatic pressure increases, the lower pressure on Mars means that the fracture density and average fracture aperture will be greater on Mars at any given depth (Heap et al., 2017). Additionally, the depth of Mode I fractures (opening mode in Griffith's criterion), will also increase with the low pressure. As a result of this, the ease of dike propagation and fracture generation on Mars is likely greatly enhanced, along with the weak lithosphere resulting in wider dikes than Earth, for any given depth (Heap et al., 2017). Combining this with the high rates of magma discharge during the Late Noachian, Hesperian and Amazonian (Carr & Head, 2010), highlighting the vast supply of magma, could be a potential explanation for the wide Martian dikes and huge volcanic structures. Other terrestrial planets without plate tectonics are likewise considered to produce larger dikes, such as on Venus. Dikes on Venus are likewise considered to be significantly larger than Earth, with dike width estimates in the same range as those for Mars (200 - 1500 m) (Ernst et al., 2001; Petford, 2000).

A final consideration could also be given to the number of dikes required to create a graben, while our models show that a single large dike is capable of replicating structures mapped on Mars, and previous studies explain how dikes on Mars can grow much larger than on Earth (as well as the large sizes of other

volcanic structures on Mars), a 2 km wide dike might seem very large in comparison to Earth. The reason for this could be that it is inface not a single dike, but a swarm of smaller (though still larger than Earth) dikes which create the grabens together. As Models B and C show, the faulting is generated at the dike tip, making the swarm theory unlikely, but it is impossible to fully rule out this theory without direct subsurface measurements of the dikes on Mars.

In lieu of measured dike widths on Mars, we intend to use the results of this model as a starting point for future studies which will test a larger variation of dike-widths between the 200 – 2000 m range and assess their impact on surface-graben formation on Mars, along with determining what the average dike width, and which lithospheric material properties that can produces the average Martian graben width of ~2-4 km.

4.4.6. Applications for further studies.

Contrasting previous models with instantaneous emplacement of a dike, this progressive intrusion model allows us to monitor detailed fracture initiation and development during dike emplacement, along with any changes that material properties have on the process. This also makes a significant improvement in monitoring and understanding the resultant material displacement and graben formation, as the model simulates the entire process from dike-tip fracture formation at depth, to the final surface graben.

Our models show how factures and subsequent graben formation occurs during the ascent and slight widening of a dike into a Martian lithosphere, with increasingly higher Young's modulus value. While our results show a clear difference between low- intermediate- and high values, the jump in deformation style between Model A and B, warrants further testing of Young's modulus in the 5-4 GPa to 50 GPa range, to get a higher resolution on when the lithosphere adopts the deformation style we observe on the surface of Mars. Additionally, the Young's modulus is but one of many lithosphere parameters which could potentially influence the final surface deformation during a dike-intrusion. Other contributing factors to the final surface deformation during dike intrusion, could be planetary gravity and the thickness of the lithosphere. Due to the time-limitations of this model we maintain a constant elastic lithosphere thickness and Martian gravity. However, the study by Taylor et al. (2020) found that when testing Young's modulus and lithosphere thickness in relation to loading the lithosphere, the same deformation was produced by a thick lithosphere with a low Young's modulus and a thin lithosphere and a high Young's modulus. Testing whether this is also the case for the dike-induced deformation in our models is a natural next step, and simple to execute using the current code, with the caveat of exceptionally long model run-times (weeks/months) depending on the chosen thicknesses. Additionally, the effect of altering other lithosphere properties, such as the average density or Poisson's ratio, as well as varying the maximum

dike thickness, could likewise have an effect on final structures and are thus interesting to test in the future. Lastly, while our model showed definite graben formation as a result of diking, comparing these results to a model of 1) pure tectonic extension and 2) dike-intrusion simultaneously to regional extension, will aid in future discussions about diking indued surface deformation.

These initial results and future variations of this model can help us fully categorize the relationship between lithosphere properties, subsurface processes and resulting surface structures. This will shed further light into dike-induced faulting in terrestrial planetary lithospheres and can be a valuable aid in determining approximate lithosphere properties, based on remote-sensing surface structures on other planets.

4.5. Summary and Conclusions

In summary, we present a novel numerical modelling result, of a dike-intrusion producing dike-tip generated faulting and subsequent surface graben formation on Mars, as hypothesized. We show a difference in created surface structures between low, intermediate, and high Young's modulus values, with the high (100 GPa) and intermediate (50 GPa) models showing graben formation. The fact that there is a lack of dike tip-generated faulting in our model with a Young's modulus of 5.4 GPA suggests that the Martian lithosphere is approximately an order of magnitude higher than suggested for the terrestrially derived Young's modulus of 5.4 GPa (Heap et al., 2020). We also show initial results on how dikes on Mars require a significantly larger width than terrestrial dikes, in order to induce surface deformation

Our models show that:

- Ascending dikes can form grabens, without the aid of an overarching regional extensional stress-field, particularly if the Young's modulus of the lithosphere is ≥50 GPa.
- Fractures initiated by diking starts deeper in the higher Young's modulus models and can propagate all the way to the surface.
- The Young's modulus alone is not a controlling factor in dike-induced surface deformation across different terrestrial planets.
- Modelled dikes with a maximum width of 2 km can generate graben sizes similar to examples measured on Mars.

Our results highlight the importance of including the mechanics of the *intrusion* of the dike in future numerical studies, as our model show the intrusion facilitates the initial surface breaking faults necessary for further graben formation.

References

Baratoux, D., Toplis, M. J., Monnereau, M., & Gasnault, O. (2011). Thermal history of Mars inferred from orbital geochemistry of volcanic provinces. *Nature*, *472*(7343), 338–341. https://doi.org/10.1038/nature09903

Bazargan, M., & Gudmundsson, A. (2019). Dike-induced stresses and displacements in layered volcanic zones. Journal of Volcanology and Geothermal Research, 3*84*, 189–205. https://doi.org/10.1016/j.jvolgeores.2019.07.010

Belleguic, V., Lognonné, P., & Wieczorek, M. (2005). Constraints on the Martian lithosphere from gravity and topography data. *Journal of Geophysical Research: Planets*, *110*(E11). https://doi.org/10.1029/2005JE002437

Broquet, A., & Wieczorek, M. A. (2019). The Gravitational Signature of Martian Volcanoes. *Journal of Geophysical Research: Planets*, *124*(8), 2054–2086. https://doi.org/10.1029/2019JE005959

Cailleau, B., Walter, T. R., Janle, P., & Hauber, E. (2005). Unveiling the origin of radial grabens on Alba Patera volcano by finite element modelling. *Icarus*, *176*(1), 44–56. https://doi.org/10.1016/j.icarus.2005.01.017

Chadwick Jr., W. W., & Embley, R. W. (1998). Graben formation associated with recent dike intrusions and volcanic eruptions on the mid-ocean ridge. *Journal of Geophysical Research: Solid Earth*, *103*(B5), 9807–9825. https://doi.org/10.1029/97JB02485

Chong, S., Li, W., & Meng, Q. (2021). A Dynamic Strain-Rate-Dependent Contact Model and Its Application in Hongshiyan Landslide. *Geofluids*, *2021*, 1–23. https://doi.org/10.1155/2021/9993693

Coetzee, C. J. (2017). Review: Calibration of the discrete element method. *Powder Technology*, *310*, 104–142. https://doi.org/10.1016/j.powtec.2017.01.015

Comer, R. P. S. (1985). Mars—Thickness of the lithosphere from the tectonic response to volcanic loads. *Reviews of Geophysics*, 61–92.

Cundall, P. A., & Strack, O. D. L. (1979). A discrete numerical model for granular assemblies. *Géotechnique*, *29*(1), 47–65. https://doi.org/10.1680/geot.1979.29.1.47

Ernst, R., Grosfils, E., & Mège, D. (2001). Giant Dike Swarms: Earth, Venus, and Mars. *Annual Review of Earth and Planetary Sciences*, *29*(1), 489–534. https://doi.org/10.1146/annurev.earth.29.1.489

Fernández, C., & Ramírez-Caballero, I. (2019). Evaluating transtension on Mars: The case of Ulysses Fossae, Tharsis. *Journal of Structural Geology*, *125*, 325–333. https://doi.org/10.1016/j.jsg.2018.05.009

Grott, M., & Breuer, D. (2008). The evolution of the martian elastic lithosphere and implications for crustal and mantle rheology. *Icarus*, *193*(2), 503–515. https://doi.org/10.1016/j.icarus.2007.08.015

Grott, M., Hauber, E., Werner, S. C., Kronberg, P., & Neukum, G. (2005). High heat flux on ancient Mars: Evidence from rift flank uplift at Coracis Fossae. *Geophysical Research Letters*, *32*(21). https://doi.org/10.1029/2005GL023894

Gudmundsson, A. (2006). How local stresses control magma-chamber ruptures, dyke injections, and eruptions in composite volcanoes. *Earth-Science Reviews*, *79*(1), 1–31. https://doi.org/10.1016/j.earscirev.2006.06.006

Gudmundsson, A. (2020). *Volcanotectonics—Understanding the Structure, Deformation and Dynamics of Volcanoes*. https://doi.org/10.1017/9781139176217

Hardy, S. (2016). Does shallow dike intrusion and widening remain a possible mechanism for graben formation on Mars? *Geology*, *44*(2), 107–110. https://doi.org/10.1130/G37285.1

Harnett, C. E., Thomas, M. E., Purvance, M. D., & Neuberg, J. (2018). Using a discrete element approach to model lava dome emplacement and collapse. *Journal of Volcanology and Geothermal Research*, *359*, 68–77. https://doi.org/10.1016/j.jvolgeores.2018.06.017

Heap, M. J., Byrne, P. K., & Mikhail, S. (2017). Low surface gravitational acceleration of Mars results in a thick and weak lithosphere: Implications for topography, volcanism, and hydrology. *Icarus*, *281*, 103–114. https://doi.org/10.1016/j.icarus.2016.09.003

Heap, M. J., Villeneuve, M., Albino, F., Farquharson, J. I., Brothelande, E., Amelung, F., Got, J.-L., & Baud, P. (2020). Towards more realistic values of elastic moduli for volcano modelling. *Journal of Volcanology and Geothermal Research*, *390*, 106684. https://doi.org/10.1016/j.jvolgeores.2019.106684

Holohan, E. P., Schöpfer, M. P. J., & Walsh, J. J. (2015). Stress evolution during caldera collapse. *Earth and Planetary Science Letters*, *421*, 139–151. https://doi.org/10.1016/j.epsl.2015.03.003

Itasca Consulting Group. (1999). *PFC2D: Particle Flow Code in 2 Dimensions*. Itasca.

Koehn, D., Steiner, A., & Aanyu, K. (2019). Modelling of extension and dyking-induced collapse faults and fissures in rifts. *Journal of Structural Geology*, *118*, 21–31. https://doi.org/10.1016/j.jsg.2018.09.017

Kronberg, P., Hauber, E., Grott, M., Werner, S. C., Schäfer, T., Gwinner, K., Giese, B., Masson, P., & Neukum, G. (2007). Acheron Fossae, Mars: Tectonic rifting, volcanism, and implications for lithospheric thickness. *Journal of Geophysical Research: Planets*, *112*(E4). https://doi.org/10.1029/2006JE002780

Magee, C., & Jackson, C. A.-L. (2020). Seismic reflection data reveal the 3D structure of the newly discovered Exmouth Dyke Swarm, offshore NW Australia. *Solid Earth*, *11*(2), 579–606. https://doi.org/10.5194/se-11-579-2020

Mastin, L. G., & Pollard, D. D. (1988). Surface Deformation and Shallow Dike Intrusion Processes at Inyo Craters, Long Valley, California. *Journal of Geophysical Research: Solid Earth*, *93*(B11), 13221–13235. https://doi.org/10.1029/JB093iB11p13221

McGovern, P. J., Solomon, S. C., Smith, D. E., Zuber, M. T., Simons, M., Wieczorek, M. A., Phillips, R. J., Neumann, G. A., Aharonson, O., & Head, J. W. (2002). Localized gravity/topography admittance and correlation spectra on Mars: Implications for regional and global evolution. *Journal of Geophysical Research: Planets*, *107*(E12), 19-1-19–25. https://doi.org/10.1029/2002JE001854

McSween, H. Y., Taylor, G. J., & Wyatt, M. B. (2009). Elemental Composition of the Martian Crust. *Science*, *324*(5928), 736–739. https://doi.org/10.1126/science.1165871

Murphy Quinlan, M. (2024). Martian Topographic Profiles Toolbox (0.1.0). Zenodo. https://doi.org/10.5281/zenodo.13745338

Musiol, S., Holohan, E. P., Cailleau, B., Platz, T., Dumke, A., Walter, T. R., Williams, D. A., & van Gasselt, S. (2016). Lithospheric flexure and gravity spreading of Olympus Mons volcano, Mars. *Journal of Geophysical Research: Planets*, *121*(3), 255–272. https://doi.org/10.1002/2015JE004896

Okubo, C. H., & Schultz, R. A. (2005). *Evidence of Tharsis-Radial Dike Intrusion in Southeast Alba Patera from MOLA-based Topography of Pit Crater Chains*. 1007.

Orlov, C. J., Bramham, E. K., Thomas, M., Byrne, P. K., Piazolo, S., & Mortimer, E. (2022). Structural Architecture and Deformation History of Tempe Terra, Mars. *Journal of Geophysical Research: Planets*, *127*(11), e2022JE007407. https://doi.org/10.1029/2022JE007407

Perrin, C., Jacob, A., Lucas, A., Myhill, R., Hauber, E., Batov, A., Gudkova, T., Rodriguez, S., Lognonné, P., Stevanović, J., Drilleau, M., & Fuji, N. (2022). Geometry and Segmentation of Cerberus Fossae, Mars: Implications for Marsquake Properties. *Journal of Geophysical Research: Planets*, *127*(1), e2021JE007118. https://doi.org/10.1029/2021JE007118

Polit, A. T., Schultz, R. A., & Soliva, R. (2009). Geometry, displacement–length scaling, and extensional strain of normal faults on Mars with inferences on mechanical stratigraphy of the Martian crust. *Journal of Structural Geology*, *31*(7), 662–673. https://doi.org/10.1016/j.jsg.2009.03.016

Pollard, D. D., Delaney, P. T., Duffield, W. A., Endo, E. T., & Okamura, A. T. (1983). Surface Deformation in Volcanic Rift Zones. In P. Morgan & B. H. Baker (Eds.), *Developments in Geotectonics* (Vol. 19, pp. 541–584). Elsevier. https://doi.org/10.1016/B978-0-444-42198-2.50036-5

Potyondy, David. (2019). Material-Modeling Support for PFC. *Itasca Consulting Group, Inc.*

Rivas-Dorado, S., Ruiz, J., & Romeo, I. (2021). Subsurface Geometry and Emplacement Conditions of a Giant Dike System in Elysium Fossae, Mars. *Journal of Geophysical Research: Planets*, *126*(1), e2020JE006512. https://doi.org/10.1029/2020JE006512

Rivas-Dorado, S., Ruíz, J., & Romeo, I. (2022). Giant dikes and dike-induced seismicity in a weak crust underneath Cerberus Fossae, Mars. *Earth and Planetary Science Letters*, *594*, 117692. https://doi.org/10.1016/j.epsl.2022.117692

Rubin, A. M. (1992). Dike-induced faulting and graben subsidence in volcanic rift zones. *Journal of Geophysical Research: Solid Earth*, *97*(B2), 1839–1858. https://doi.org/10.1029/91JB02170

Rubin, A. M. (1993). Tensile fracture of rock at high confining pressure: Implications for dike propagation. *Journal of Geophysical Research: Solid Earth*, *98*(B9), 15919–15935. https://doi.org/10.1029/93JB01391

Rubin, A. M., & Pollard, D. D. (1988). Dike-induced faulting in rift zones of Iceland and Afar. *Geology*, *16*(5), 413–417. https://doi.org/10.1130/0091-7613(1988)016<0413:DIFIRZ>2.3.CO;2

Schultz, R. A. (1993). Brittle strength of basaltic rock masses with applications to Venus. *Journal of Geophysical Research: Planets*, *98*(E6), 10883–10895. https://doi.org/10.1029/93JE00691

Schultz, R. A., Okubo, C. H., Goudy, C. L., & Wilkins, S. J. (2004). Igneous dikes on Mars revealed by Mars Orbiter Laser Altimeter topography. *Geology*, *32*(10), 889–892. https://doi.org/10.1130/G20548.1

Scott, E. D., Wilson, L., & Head III, J. W. (2002). Emplacement of giant radial dikes in the northern Tharsis region of Mars. *Journal of Geophysical Research: Planets*, *107*(E4), 3-1-3–10. https://doi.org/10.1029/2000JE001431

Shahrzad, S., Bramham, E. K., Thomas, M., Piazolo, S., Byrne, P. K., & Mortimer, E. (2023). Deciphering the Structural History of Ulysses Fossae, Mars, Using Fault Pattern Analysis. *Journal of Geophysical Research: Planets*, *128*(5), e2022JE007633. https://doi.org/10.1029/2022JE007633

Smart, K. J., Wyrick, D. Y., & Ferrill, D. A. (2011). Discrete element modeling of Martian pit crater formation in response to extensional fracturing and dilational normal faulting. *Journal of Geophysical Research: Planets*, *116*(E4). https://doi.org/10.1029/2010JE003742

Solomon, S. C., & Head, J. W. (1990). Heterogeneities in the thickness of the elastic lithosphere of Mars: Constraints on heat flow and internal dynamics. *Journal of Geophysical Research: Solid Earth*, *95*(B7), 11073–11083. https://doi.org/10.1029/JB095iB07p11073

Tesauro, M., Audet, P., Kaban, M. K., & Cloetingh, S. (2012). The effective elastic thickness of the continental lithosphere: Comparison between rheological and inverse approaches. *Geochemistry, Geophysics, Geosystems*, *13*(9). https://doi.org/10.1029/2012GC004162

Tesauro, M., Kaban, M. K., & Cloetingh, S. A. P. L. (2013). Global model for the lithospheric strength and effective elastic thickness. *Tectonophysics*, *602*, 78–86. https://doi.org/10.1016/j.tecto.2013.01.006

Watters, T. R. (2003). Lithospheric flexure and the origin of the dichotomy boundary on Mars. *Geology*, *31*(3), 271–274. https://doi.org/10.1130/0091-7613(2003)031<0271:LFATOO>2.0.CO;2

Wilson, L., & Head III, J. W. (1981). Ascent and eruption of basaltic magma on the Earth and Moon. *Journal of Geophysical Research: Solid Earth*, *86*(B4), 2971–3001. https://doi.org/10.1029/JB086iB04p02971

Wilson, L., & Head III, J. W. (2002). Tharsis-radial graben systems as the surface manifestation of plume-related dike intrusion complexes: Models and implications. *Journal of Geophysical Research: Planets*, *107*(E8), 1-1-1–24. https://doi.org/10.1029/2001JE001593

Wyrick, D. Y., & Smart, K. J. (2009). Dike-induced deformation and Martian graben systems. *Journal of Volcanology and Geothermal Research*, *185*(1), 1–11. https://doi.org/10.1016/j.jvolgeores.2008.11.022

Chapter 5

Integrated Discussion and Conclusions

This final chapter summarises the key results produced in each of the three previous research chapters. Following this, I discuss the wider implications of the research results presented, on the previously determined ages of Martian extensional activity, the significance of magmatic processes on the surface appearance of the Tharsis Region, and the overall role of diking in the process of graben formation. I end this chapter with a reflection on the future work in this area of research, both in terms of the structural history and the numerical modelling.

5.1. Summary of findings and resultant implications

This thesis contains 3 research chapters, where research chapters 2 and 3 presents results regarding the structural evolution of the two largest volcano-tectonic areas on Mars in the Tharsis volcanic Province. Research Chapter 4 investigates the dike-induced graben formation process on Mars, using numerical modelling.

5.1.1. Structural evolution in the Tharsis Volcanic Province

This section will present the results and discussion of the mapping and structural evolution of the Tharsis Region, presented in Chapters 2 and 3.

5.1.1.1. Chapter 2 – Widespread Amazonian Extensional Activity associated with Tharsis Volcanoes.

In Chapter 2, *Deciphering the Structural History of Ulysses Fossae, Mars, Using Fault Pattern Analysis*, I presented the structural history of the area of Ulysses Fossae on Mars, using surface data from the orbiting satellites: Mars Express and the Mars Reconnaissance Orbiter. Ulysses Fossae stands as an elevated isolated feature, offering a unique vantage point to explore the faulted terrain that lies beneath the more recent Amazonian lava flows from the prominent Tharsis volcanoes. By investigating the morphology and cross-cutting

relationships of ~5000 mapped faults, I identified 10 different groups of faults, each grouped by a similar orientation, morphology, and relative age.

A key result of this work is that the area of Ulysses Fossae records 10 distinct extensional events, which are each associated with magmatic activity from (1) local volcanoes (*Olympus Mons, Ascraeus Mons, Pavonis Mons and Ulysses Mons),* and (2) from large-scale regional extension. The implication of this is that the main driver for extensional grabens in Ulysses Fossae, is due to radial diking activity with local volcanic centres, highlighting the highly active magmatic systems in the area. Additionally, using detailed crater-size frequency distributions, this work significantly reduced the previously determined ages of this magmatic activity in the area, by ~1 billion years. Together, this new understanding of a younger and more active structural activity in this area has implications on previous evolutionary models of the Tharsis region and Mars as a whole. This is further discussed in Section 2.1.2.

The results from this study conclude that lateral, radial diking from local magmatic centres is the main driver of surface deformation in Ulysses Fossae. To investigate if this is process is limited to Ulysses Fossae or whether there is a wider pattern of Tharsis volcano-tectonic behaviour, the next Research Chapter addresses the structural history and extensional process of another large tectonic centre on Mars: Ceraunius Fossae.

5.1.1.2. Chapter 3 – Structural History of Ceraunius and Tractus Fossae

Chapter 3, *Amazonian tectonic evolution of Ceraunius and Tractus Fossae, Mars, and implications for local magmatic processes,* addresses the structural evolution of the areas south of the Alba Mons volcano: Ceraunius- and Tractus Fossae. The detailed mapping of surface structures in these areas resulted in a total of ~11,000 mapped graben-forming normal faults. The grabens mapped here are wider than the average Martian grabens, and display depths of ~200 m with flat graben floors. Additionally, the surface was also deformed by a significant amount of non-fault collapse structures, which are identified as pit-crater chains, catenae, u-shaped troughs and chasmatas (Figure 3.2 in Chapter 3). Together, these mapped surface structures, along with crater-statistics derived unit ages, enabled the establishment of the structural evolution of this area, allowing the pinpoint of the magmatic sources responsible for the extensional tectonics in the area. A key outcome of this work is the identification of three distinct extensional events, with main orientations ranging through time from NE to NS to NW. This is contrary to the previously assumed purely N-S fault producing E-W extensional field. Similar to Ulysses Fossae (Shahrzad et al., 2023), I measure the extensional activity as much younger than previous studies (Tanaka et al., 2014), with all the extensional activity taking place during the Amazonian. The results from this paper provides direct additional evidence of lateral and vertical dike-induced surface deformation, for

both faults and collapse structures, in the Tharsis Region on Mars, along with novel support for the recent theory of a contained magma supply (either a plume off-shoot or underplating) located directly beneath Ceraunius Fossae.

The main limitation from this work concerns the true nature of the process forming the collapse structures. Morphologic and topographic data analysed in this study suggest that all four collapse structures are part of an erosional evolutionary development trough time. Pit-crater chains, catenae, u-shaped troughs, and chasmatas are in this study interpreted as an evolutionary chain of morphological features (See Figure 3.10 in Chapter 3), and the formation process of these is determined to be from the influence of diking. This interpretation is supported by other evidence of intense magmatic activity in the area; however, some previous studies prefer an alternative origin for the collapse structures. The proposed mechanisms for pit-crater chains are numerous and include collapsed lava tubes, dikes of different types (exsolved volatiles, hydrosphere/cryosphere interaction, Plinian-style eruptions), collapsed magma chamber, karst dissolution, extension fractures and dilational faulting (Wyrick et al., 2004). Dilational normal faulting, or dike induced cavities are the most common formation mechanisms interpretations. Determining their origin would make pit-crater chains and associated collapse structures a very helpful aid when surveying terrestrial planet surfaces. This is the case whether they are indicative of faulting, diking or other magmatic activity, or of interactions with water. This is likely to remain unsolved, until more detailed subsurface data is available for the specific locations. Section 5.4 of this chapter delves into further data and research which would benefit uncertainties such as this.

5.1.1.3. Insights drawn from Chapter 2 and 3 results: Timing and underlying processes.

The results summarized here from Chapter 2, combined with the structural evolution and identification of magmatic processes from Chapter 3, provides a new understanding of a much younger and active magmatic system in the Tharsis Region on Mars than previously assumed. Results have implications for the timeline of geologic events on Mars, along with redefining the major structural processes that were active during this period. These topics are discussed further in *Section 5.1.2*. The results from Research Chapters 2 and 3, both conclude that the majority of the extensional faulting in the Tharsis Region is dominated by lateral and vertical diking from the local volcanic (*e.g., Olympus Mons, Alba Mons, Tharsis Montes*) and magmatic centres (*Ceraunius Fossae*). These results are based on the satellite image- and topography-based mapping and is supported by previous research on other large-scale Tharsis tectonics (e.g. Ernst et al., 2001; Okubo & Schultz, 2005; Schultz et al., 2004). In lieu of access to geophysical

measurements on the surface of Mars, the following final research chapter addresses the process of dike-induced graben formation, using a numerical modelling approach.

5.1.2. Chapter 4 - Lithosphere Parameter Impacts on Dike-Induced Graben Formation

Chapter 4, *The Influence of Young's Modulus on Graben Formation during Martian Dike Intrusions: A Discrete Element Modelling Approach*, focuses on examining a key result from Chapters 2 and 3, namely that extensive diking is the main driving process behind the extensional faulting in the Tharsis Volcanic Province on Mars. In this chapter, I present a 2D numerical model of a deep-sourced dike intruding into a Martian lithosphere of varying mechanical properties. There are many variables that affect the mechanical properties of a planet's lithosphere, but I focus on investigating the influence of Young's modulus, in relation to the Martian lithosphere over time, on the resulting surface deformation. Under Martian gravity, I vary the Young's modulus between 5.4 GPa, 50 GPa and 100 GPa for each of the three model runs. A key result of this work that the three models show is, that in the 50 GPa and 100 GPa models, an intruding dike is capable of 1) initiating surface breaking fault, originating from the dike tip, and 2) as the dike continues to intrude the lithosphere, the faulting will develop into a graben. An implication of this, is that previously assumed assistance from overarching regional extensional stresses, or extensive widening of the dike after emplacement, are *not* processes which are required for diking to produce graben; if the Young's modulus of the lithosphere is high enough ($\geq$ 50 GPa according to the model results), the intruding dike can produce graben structures unaided. This is a contrast to the results from the 5.4 GPa model, where the final surface deformation is limited to near-vertical surface-breaking faults, and enough upwards and downwards material displacement to produce a trough-like structure. Another key finding is apparent when comparing the models' resulting surface structures to topographic examples of diking-induced grabens measured on Mars; while the structures are of a different scale, the morphology of the Mars graben examples more closely resemble the results of the 50 GPa and 100 GPa models, suggesting Young's modulus values in that range are suitable assumptions for the Martian lithosphere, at least for the time the structures were emplaced, ~2 Ga ago.

5.1.2.1. Reflections on numerical modelling

The main limitation of this work is the simplified nature of the 2D numerical model. Though not fully understood on Mars, terrestrial dike ascent is a complex process of varying dike morphology, temperature, and velocity (Bazargan & Gudmundsson, 2019; Daniels et al., 2012; Hou, 2012; Rubin, 1995). The computational solve time for large discrete element models, such as the one discussed in

Chapter 4, is significant, and therefore a simple model was developed, resembling previous numerical modelling in this area. A discrete element modelling approach was deemed the most appropriate to simulate any surface deformation. In this study, the dike is represented by a rigid material, in order to simulate the tip-fracture process, while a truer-to-nature model would likely treat the intruding dike as a fluid material. This could potentially have an impact on resulting surface structures but is more relevant when modelling the actual dike ascension process. In this numerical model, the section of lithosphere is assumed homogeneous, for ease of computation. Though this is not unusual among Martian lithosphere numerical models, due to uncertainties on exact ranges and values (e.g. Taylor et al., 2020; D. Y. Wyrick et al., 2015), Mars is more likely to have a mechanically layered heterogeneous crust, which in turn has influence on dike development (Gudmundsson, 2003; Schöpfer et al., 2017).
The design of this final numerical model is primed to further investigate other lithospheric- and dike parameter variations, which are discussed in the Future Work in Section 5.1.6.

5.2. Implications for the understanding of Tharsis' structural and magmatic evolution

The following section will gather the key outcomes of this thesis and discuss the implications of them, with reference to the timing and processes related to the structural and magmatic evolution of Tharsis, as recoded in the study areas from Chapters 2 and 3: Ulysses Fossae, Ceraunius Fossae and Tractus Fossae.

5.2.1. Revised younger activity and crater-statistics derived ages.

A key outcome of the work of this thesis, is a new understanding of when structural activity took place in the Tharsis Region on Mars. The end of the Hesperian period on Mars (~3 Gyr) has historically marked the assumed termination of the majority of the Martian volcanic and associated tectonic processes. The average rate of volcanism for the following Amazonian period decreased by an order of magnitude, and the accumulation and movement of ice became the prevalent processes of that period (Carr & Head, 2010). Though the surface of Mars is covered in Amazonian lavas, compared to the activity in the Hesperian, we therefore historically do not associate the Amazonian with volumetrically large magmatic activity and associated generated structural deformation. Previous global stratigraphic studies considered Ulysses Fossae, Ceraunius Fossae, and Tractus Foss a Noachian terrain (Scott et al., 1986), where revised studies assigned these as Early and Late Hesperian units, and considered the narrow grabens and fault that crosscut it Early Hesperian as well (Tanaka et al., 2014).

The results from the detailed crater counts and size-frequency distribution statistics in Chapters 2 and 3, show that the previous ages for each location was overestimated by a minimum of 1 Ga, with the highest discrepancy between the previous and revised age is for Ceraunius North.

Location	*Unit name**	*Prev. age**	*New age*
North Dome	eHv	3.65 Ga	3.4 +0.1/-0.3 Ga
UF North	lHv	3.55 Ga	2.6 ± 0.2 Ga
UF South	eHv	3.65 Ga	2.4 ± 0.2 Ga
Ceraunius North	eHv	3.65 Ga	1.4 ± 0.2 Ga
Ceraunius South	eHv	3.65 Ga	2.2 ± 0.2 Ga
Tractus Fossae	lHv	3.55 Ga	2.4 ± 0.2 Ga

Table 5.1: Overview of the six geological units studied in this thesis. * Unit age and name from Tanaka et al., 2014.

As discussed in the respective research chapters, the younger unit ages means that volcanic, and associated volcano-tectonic, processes were active until a billion years later than previously determined. However, these new younger ages measured in this study, have a knock-on effect on the rest of the established Martian stratigraphy. Examining the units surrounding the 6 measured in this study (See Table 5.1 above), highlights that the examined units are older, as the surrounding units are all superposed on top of the study areas. This makes the surrounding units younger by rule of superposition. With the exception of smaller volcanic flows preserved in the vicinity, the immense *AHv* unit covers the majority of the Tharsis plateau. This unit, named the *Amazonian and Hesperian volcanic unit,* is comprised of stacked, gently sloping lobate flows, which are tens of meters thick, and hundreds of kilometres long (Tanaka et al., 2014). Though this unit definition is slightly arbitrary, with it consisting of multiple different flows grouped together, the unit as a whole is considered younger than the units found in the study areas. This suggests that the young age results from Research Chapters 2 and 3 are not solely showing the tail-end of Amazonian volcano-tectonic processes, but coupled with the overlying *AHv* unit suggests that

extensive volcanism did not cease by the end of the Hesperian but did in fact continue far into the Amazonian, by at least another billion years of activity.

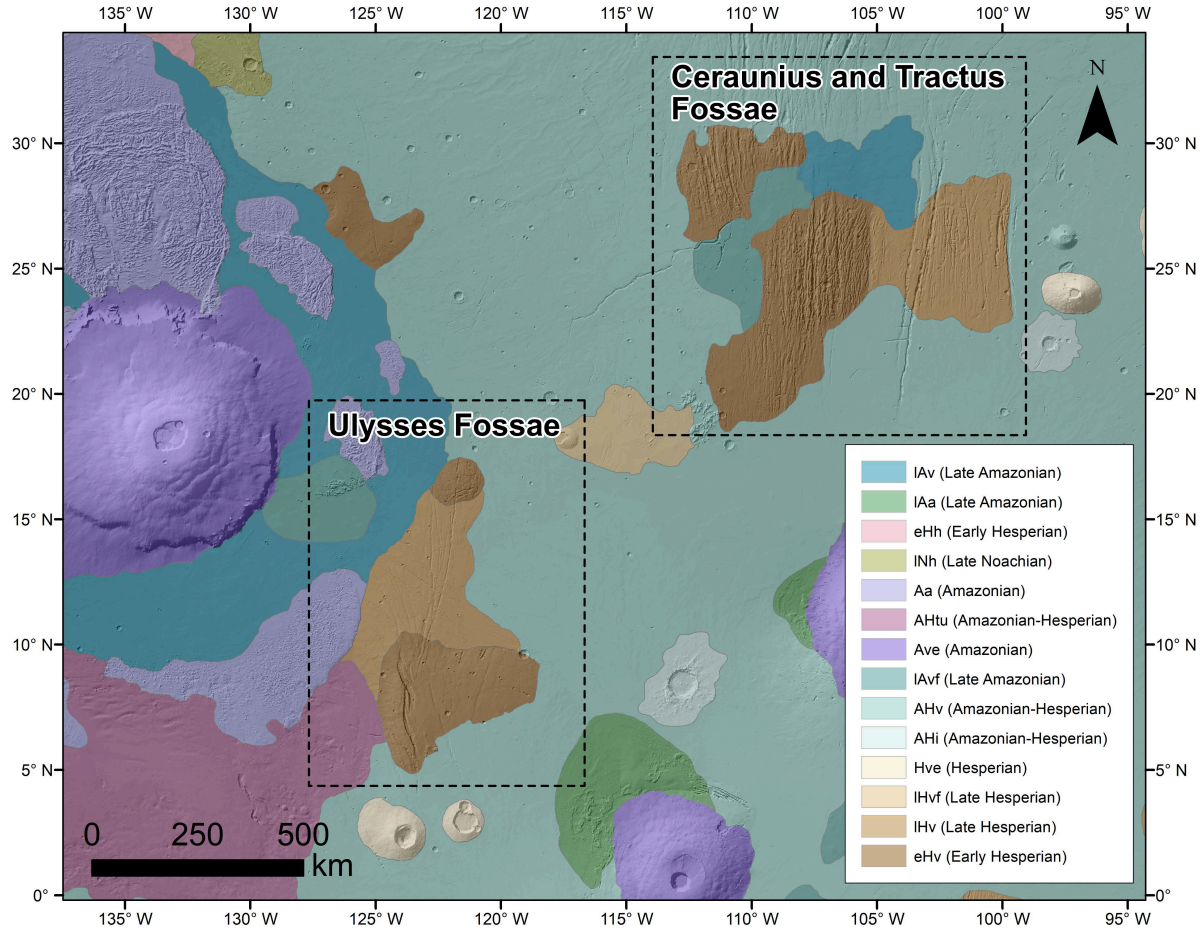

Figure 5.1: Geological unit context map for the two study areas: Ulysses Fossae and Ceraunius Fossae. Mapped units are from Tanaka et al. (2014).

Further examining the ages on the 2014 Global Map of Mars (Tanaka et al., 2014) in comparison with more local studies of crater-statistics derived ages, highlights the differences in study resolutions. A part of the reason for this discrepancy, lies the nature of previous absolute model age determinations on Mars. As mentioned in Chapter 1, the lack of location specific samples from Mars, means that any absolute model age determinations, using remote sensing on terrestrial planets, are based on crater-size frequency distributions. For most of Mars's research, the 2014 Tanaka et al. global map of Mars has been considered the standard baseline for geological unit ages and boundaries. While this approach was essential for initial Martian surface studies, these global or quadrangle approaches to the crater-size-frequency distribution are bound to have missed craters or combined unit data, which possibly should not be combined, simply

due to the sheer size of the global studies. This is particularly the case for the Tharsis Region, as the many overlapping lava flows have resurfaced older material, making it a challenge to correctly identify plan view geological unit boundaries.
Higher resolution, location specific tectonic studies are still scarce in the Martian scientific literature. However, the nature of these studies positions them ideal to improve the previously globally determined ages and stratigraphic relationships. The global-scaled unit ages are largely based on crater counting statistics, which would benefit greatly from closer studies, where stratigraphic details and individual unit boundaries are not missed.

The main limitation of this work entail using the ages of the geological units to date the extensional activity in the study areas. Using the unit age approach, I only assign a maximum age the fault structures, and there are only a few places where units provide both upper and lower temporal bounds to fault formation. However, this is currently the only method of remotely assigning any ages to these faults.
During the peer-review process for Chapter 2, a reviewer raised the question of further specifying the ages of the mapped grabens, instead of relying on the unit ages; an additional approach to this would be to apply the buffered crater counts method. Buffered Crater Counting (BCC) is a different approach to the standard crater counting method, where a buffer area is placed around the area of interest, and all counted craters with rims or ejecta within the buffered area, regardless of whether their centres are within the boundary, are included in the count (Fassett & Head, 2008; Kneissl et al., 2015); notably the BCC method also works for linear features, such as faults. This method has the potential to determine how much younger the mapped fault sets are than the unit they crosscut, if the data is resolvable. Additional analysis with BCC, which provides a minimum age constraint, was however unnecessary for my purposes given the maximum ages I determined using standard-practice crater size-frequency distribution statistics in Chapters 2 and 3 were already significantly younger than existing mapped ages. Additionally, this method is largely suited for discerning the ages of separate fault groups, and since the mapped faults in Chapters 2 and 3 are all heavily overprinting each other, I did not find this method suitable.

The crater-statistics derived ages are, per definition, highly sensitive to any slight statistical variations, in addition to the manually counted craters. As of yet there are no method standards for the automation of crater detection, though recent research shows improvement in the area. Previously, crater-identification computer vision techniques, included recognizing light and shadow patterns, circle finding, and edge detection; however, more recent techniques involves the use of Convolutional Neural Networks (CNN), which is predicted be able to automatically identify craters from image and annotation data alone, without

requiring the predefined identification features mentioned above (DeLatte et al., 2019). As of now we are limited to manually identifying craters and unit boundaries, which comes with its own set of challenges; secondary craters are the main concern when mapping craters on a terrestrial planet surface, where multiple secondaries are identifiable by the atypical clustering of craters, but isolated secondaries may be impossible to identify. No definitive statistical method has been devised to solve this issue, but performing a spatial randomness analysis of the satellite images used to count the craters on, can assist in eliminating any clustering of craters (Shahrzad et al., 2019).

Further examination of detailed Martian geology offers valuable insights, and as planetary structural geologists, we already conduct comprehensive analyses of planetary surfaces and are in a perfect position to incorporate crater statistics to our studies. By integrating more targeted and in-depth crater statistics for geological units, we can significantly enhance our understanding of Martian stratigraphy and the absolute and relative timing of previous and ongoing geological processes.

5.2.2. Identifying the effects of diking on Terrestrial Planets

From the results summaries, it is established that the main driver for extensional surface deformation in the Tharsis region are subsurface arrested dikes, both lateral and vertically propagating radial dikes. The subsurface diking process is believed to be similar if not identical to systems found on Earth, despite the apparent inconsistencies in surface expressions. While dikes are defined as vertical structures, the propagation of the structure itself can occur both vertically and laterally. The vast majority of the surface-expressions of diking mapped in Chapters 2 and 3 are laterally propagating vertical dikes; the majority of these radiate out from a local volcano, where the exceptions to this are the Tharsis radial dikes. For the local volcanoes, the radial dikes propagate outwards in a mostly fan-shaped geometry from the centre (See Figure 1.6). Vertical dikes are identified on most terrestrial planets (Earth, Venus and Mars in particular), and they propagate vertically, both within volcanic structures (e.g., Vesuvio and Piton de la Fournaise), as well as along rift zones, such as Iceland (Urbani et al., 2018). There are several factors which determine whether dikes will propagate solely vertically or if they will have a laterally propagating component; an analogue modelling study by Urbani et al. (2018) determined that the effects of crustal layering, among other structures and processes, to be the main driving factor between the two dike propagation types. They found that rigidity layering, where a weaker layer was underlying a stiffer layer, predominantly favoured lateral dike propagation, while a stiffer layer underlying a softer layer favour vertical dike propagation (Urbani et al., 2018). Both laterally and vertically propagating radial dikes have been considered prevalent on Mars, Venus and on Earth.

As presented in this thesis, the surface effects of dikes are defined using fault morphology and orientations, topographic measurements, and in some cases, the appearance of co-morphologies associated with diking, such as collapse structures. In addition to the results from this study, other Martian locations have hypothesized radial diking (Elysium, Syrtis Major), based on surface deformation. Due to the lack of samples and instruments on Mars, numerical modelling is also used to model the occurrence of dikes, based on the surface structures, as introduced in Chapter 4.

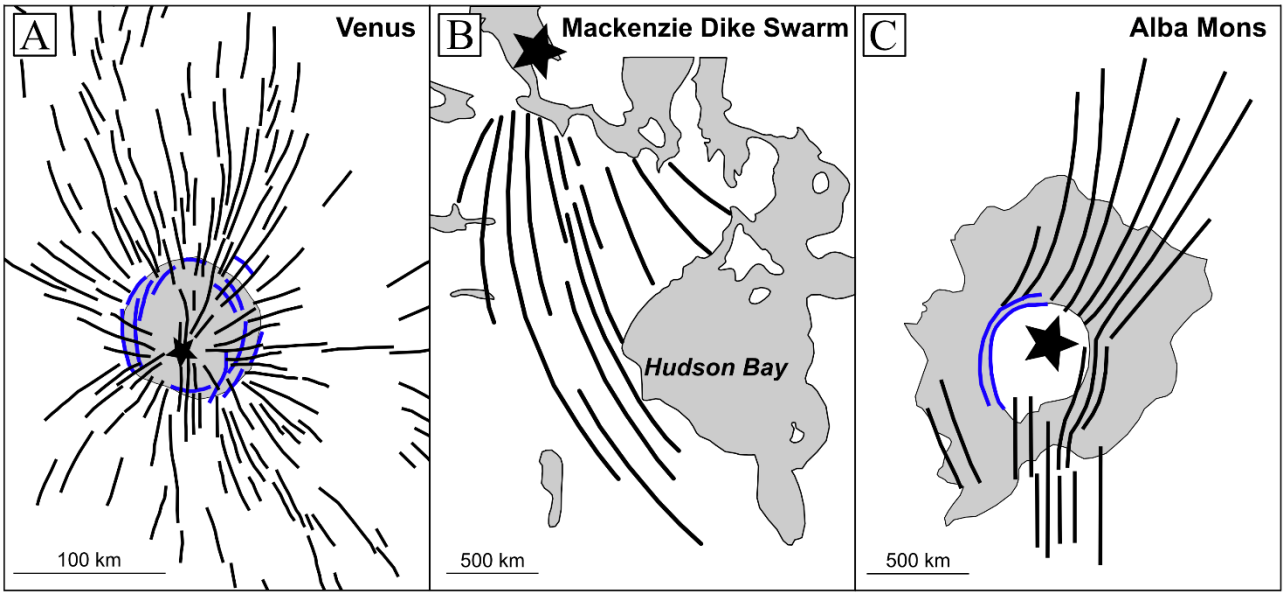

Figure 5.2: Examples of radial diking on terrestrial planets, with black stars denoting the centre of activity. A) Radially fanning lateral diking located at 8°S, 243.5°E on Venus. Modified from Grosfils & Head (1994) B) The radiating Mackenzie Dike Swarm on the western Canadian Shield on Earth. Figure modified from Cailleau et al. (2005). C) Proposed circumferential (blue) and radial (black) diking surrounding the Alba Mons volcano on Mars. Figure modified from Cailleau et al. (2005)

On Earth we observe radial diking associated with the major laterally propagating dike swarms, such as the Mackenzie dike swarm (Figure 5.2b) and the Central Atlantic reconstructed swarm – the latter also known as the Central Atlantic Magmatic Province (CAMP) (Ernst et al., 2001). Vertical propagation of dikes on Earth, such as the Grenville Swarm in Canada, and the Krafla volcano in Iceland (Trippanera et al., 2015), is a process usually located within a rift zone, with a laterally elongated magma source. Similar to Mars, the dikes in a terrestrial dike swarm vary in length, with values ranging from tens of km to >2000 km (Ernst et al., 2001). However, on Earth these dike swarms are confined to the basement, with little to none confirmed surface-expressions of dikes (Ernst et al., 2001). Despite numerous models confirming the process of dike-induced surface deformation (Mastin & Pollard, 1988; Rubin, 1992, 1995), and the results from Chapter 4 validating the process for Mars, there are little to none direct observations of dikes directly underlying grabens on Earth (Gudmundsson, 2003). This discrepancy in theoretical models and field observations on Earth is further discussed in the final paragraph of this Section.

Earth's sister planet, Venus, with its almost identical planet size, also features numerous mapped cases of fractures which are assumed to be related to radial lateral diking on its surface (Figure 5.2a). The lack of significant surface erosion on Venus reveals that the surface is covered with volcanoes, with a recent estimate of ~85,000 identified edifices, ~99% of which are <5 km in diameter (Hahn & Byrne, 2023). Similar to Mars, radial surface fractures around volcanoes are observed and interpreted as deformation induced by the presence of subsurface dikes (Galgana et al., 2013). These structures are primarily identified by their geometry, which is identical to diking patterns observed and measured on Earth. In addition to geometry, other geomorphic evidence, such as the presence of collapse features (e.g. pit crater chains), alignment of small shield volcanoes along fractures and evidence of lava flow which has emanated from the fractures (Ernst et al., 2001). The presence of the majority of or all of these indicators distinguishes dike-generated surface fractures from purely tectonic generated, though it does not exclude a process where diking is taking place within a larger regional tectonic field.

The occurrences of giant radiating dikes on Mars, Earth, and Venus, are similar in dike length, width, and radiating geometry between the three planets, indicating a common origin process (Figure 5.2). As summarized, Martian and Venusian dikes are identified based on the observed geometry and geomorphology of surface fractures and faults (see Chapters 2 and 3), while terrestrial dikes can be measured and observed directly on both surface and subsurface. Additionally, Earth differentiates itself from Venus and Mars, by the presence of plate tectonics. The shifting of tectonic plates on Earth's surface disrupts the original geometric pattern of dike swarms, and often leads to the removal or modification of the central region from which these dikes emanate, particularly since they are commonly situated along continental breakup margins (Ernst et al., 2001). This means that using modern detection tools, such as magnetics and gravity, dike emplacement on Earth is well documented, but related surface effects are more difficult to detect, due to plate tectonics and erosion. The opposite problem is true for Mars and Venus, where there are no plate tectonics, and surface erosion is minimal (for Mars and $<10^{-3}$ mm/yr for Venus (Campbell et al 1997). Here, the grabens on the surface are well preserved (See the mapping results in Chapters 2 and 3), while subsurface dike detection is the challenge. Plate tectonics and erosion are therefore also the likely reasons why there are such few examples of grabens associated with subsurface diking on Earth. Few locations with potential are found in large igneous provinces. Victoria Island in the Canadian arctic has several narrow grabens identified, buried in the Natkusiak volcanic sequence. No direct dike is detected, the grabens follow the same 150 trend as the nearby Franklin dikes (Rainbird, 1993). Another case is found in northern Finland, in the Koillismaa sequence, where gravity traces might have revealed the sedimentary infilling of a paleo-graben, which is associated with a stalled feeder dike (Alapieti, 1982). Finally, a recent 2023 study by Magee and Jackson, examined seismic

reflection of the Exmouth Dyke Swarm in offshore NW Australia. Here, they find dikes, and normal faulted grabens, which converge on the upper tip of the stalled dikes (Magee & Jackson, 2020).

In summary, the theoretical models for dike-induced surface deformation have very few field-observational or measurement evidence on Earth; other terrestrial planets such as Mars and Venus show plenty of the predicted surface evidence, but due to data access limitations, lack the direct measurements of stalled dikes underlying the grabens. Results from Chapter 4 show how dike-induced graben formation is indeed possible on Mars, while also indicating that the lithospheric parameter of Young's modulus, is not the sole controlling factor for the lack of structures on Earth. The future work suggested in Section 5.1.7.1, highlights other material properties which may influence dike-induced graben deformation, which along with the conclusions regarding Young's modulus from Chapter 4, can help narrow down the factors controlling graben formation on different planets.

5.2.2.1. Dike, and subsequent fault behaviour, in the study areas

Stalled Subsurface Dikes

A factor to take notice of, is that the vast majority of dikes on Mars appear to have stalled before breaching the surface. The arrest of Terran dikes in the subsurface has been attributed to a myriad of factors, such as buoyancy, magma supply rate, extent of external stress fields and dike-dike interactions (Rivalta et al., 2015). While these factors undoubtedly all have an influence on the propagation of Terran and Martian dikes, considering the consistency of arrested dikes on Mars, dike arrest is likely related to planet-wide parameters, such as lithospheric properties. More specifically, stress heterogeneities due to abrupt changes in the elastic properties of different lithospheric layers has been found to cause the arrest of dikes at shallow crustal depths in numerical and physical analogue studies (Gudmundsson, 2011; Maccaferri et al., 2010; Rivalta et al., 2015; Taisne et al., 2011). Explicit examples of this comes from the Maccaferri et al. (2010) study which ran numerical models of dikes propagating in layered media and found that how the was influenced by the energy release of a dike during propagation. Results from this study found that rigidity changes at an interface causes a "deviation" of the fluid (magma) filled fractures orientation when crossing it (Maccaferri et al., 2010). If the fractures travel from a high-rigidity layer to a low rigidity layer, they will be deflected in a vertical direction. In this case, the dike will continue to accelerate until it reaches the interface whereafter it will suddenly decelerate, though dike arrest will not occur. These findings are also supported by analogue gelatine experiments (Rivalta et al., 2005). If the opposite scenario occurs, and a dike travels from a low-rigidity layer to a high-rigidity layer, the fractures will refract horizontally. In this scenario, it is possible for the energy released from the crack tip at the

interface to be lower than the energy needed to create a new crack surface, resulting in arrest of the dike right before, or at the interface itself (Rivalta et al., 2015).

As mentioned, the relationship between dike-induced graben width and the depth of dike tip has been referenced often in planetary dike-studies, as a comparison between data, and as a tool to estimate the depth of the dike-tip using the graben width (e.g. Rivas-Dorado et al., 2021; Wilson & Head III, 2002). For the following example, we use the average relationship suggested by Pollard et al. (1983), where the graben width is equal to two times the dike depth. Considering the average of measured graben widths in our study (4-5 km) would thus suggest a consistent dike arrest depth of ~2-2.5 km. Combining this with consistency of stalled subsurface dikes on Mars could suggest the presence of a lithospheric boundary layer which reflects a change from a low-rigidity layer of the lithosphere to a high-rigidity lithospheric layer around a depth of ~2-5 km depth in the Tharsis study areas. Future studies could with great interest model the boundaries and potential sources for this hypothetically "shallow" layer rigidity change in the Martian lithosphere.

Lack of fault reactivation

Another observation in this thesis, is the limited fault reactivation in the fault populations in the study areas at Ulysess Fossae, Ceraunius Fossae, and Tractus Fossae. This lack of reactivation may be unusual or unexpected given the amount of faulting that has occurred at these locations and the prevalence of fault reactivation in other parts of the Tharsis region, such as Tempe Terra (Orlov et al., 2022), Noctis Labyrinthus (Bistacchi et al., 2004), and Valles Marineris (Vallianatos & Sammonds, 2011).

For fault reactivation to occur, two criteria must be met: 1) the existing fault plane must be optimally oriented to slip in the new stress regime, and 2) the new driving stress must overcome the frictional sliding strength of the existing fault (Morris et al., 1996). A lack of fault reactivation in the three study areas suggests that one or both of these criteria were not met in subsequent deformation events after initial fault formation.

Given that many of the fault populations mapped in the study areas share similar orientations, and thus similar extension directions, it is likely that the pre-existing fault planes should have been sufficiently aligned to later stress fields to reactivate in those conditions. Thus, the first criteria is likely met and stress field orientation is unlikely to be the reason for the lack of reactivation.

If a new driving stress cannot overcome the strength of pre-existing faults this may be because the stress is weak and/or the faults are strong. A number of factors may increase the frictional strength of faults, including thermal annealing by intrusives, precipitation by fluid flow, and the presence of some granularity or asperities (Bellahsen & Daniel, 2005; Morris et al., 1996). While we cannot confirm the

presence of these conditions without fieldwork and samples, high fault strength remains a possible cause of the lack of reactivation.

Local variations in the Martian lithosphere, such as thickness and temperature may have had an influence on the lack of reactivation at the study areas, and the relative strength of the faults. However, considering the size of Mars and the likely highly heterogeneous nature of the Martian lithosphere, is it difficult to make any blanket statements on the nature of the collective lithosphere. Based on the reactivation criteria, we might be able to infer that the lithosphere on Mars at the study areas is "weak" enough to easily facilitate new breaks which are perfectly orthogonal to the new driving stress, rather than having to exploit the previous faulting. This is consistent with the fact that the lithosphere on Mars is generally considered weaker than Earth, due to the lower surface gravity (3.71 m/s^{-2} on Mars), resulting in a lower lithospheric pressure (Heap et al., 2017).

Concurrently, the possibility of a weak driving stress may be suggested by differences in the interpreted source of deformation. The main driver of deformation in the project study areas is dike-driven extension from local volcanic sources. In contrast, areas of Tharsis with significant fault reactivation (Tempe Terra, Noctis Labyrinthus, and Valles Marineris) typically have deformation driven by larger scale regional extension (Bistacchi et al., 2004; Orlov et al., 2022; Vallianatos & Sammonds, 2011). The only clear example of reactivation identified in this study, the oblique faulting of Group 10 in Ulysses Fossae, is also driven by regional extension. The driving stress from the formation of that fault group was so large that the resulting structure is significantly wider than the previous grabens in the area (~9 km compared to 2-4 km, see Chapter 2). The lack of observed fault reactivation may therefore be because extensional stresses generated by the local magmatic activity in the study areas, was too weak to be capable of reactivating the pre-existing faults.

There is also the possibility that there is in fact a prevalence of fault reactivation in the study areas, which simply has not been identified in this work. The sheer volume and complexity of the faults in Ceraunius Fossae could be a reason why any potential reactivation has been missed. Future work in these areas could include performing a slip and dilation tendency analysis to assess how likely the different fault populations are to reactivate in given scenarios. Nevertheless, the potential lack of reactivation in the studied locations highlights that the mechanical properties and history of faulting across Mars is distinctly complex, and that the kind of work undertaken in this thesis, where detailed analysis is performed on one piece at a time, is needed to help us understand that complexity.

5.3. The significance of magmatic processes in the surface appearance of the Tharsis Region

The key outcome of this thesis is a structural and temporal evolution of the extensional features found in Ulysses Fossae, Ceraunius Fossae and Tractus Fossae. Comparing the extension orientations through time between the areas (See Figure 5.3 below), show that the patterns are not reflected between them due to timing differences, though the last part of the Ulysses Fossae activity and the beginning of Ceraunius and Tractus Fossae activity show some similarities (highlighted in red dashed line on Figure 5.3). As discussed in this thesis, the orientations of faulting in the study area are highly influenced by the "local" magmatic activity, however it is interesting how the partial overlap of orientations correspond to the NE Tharsis-centred diking and N-S related regional extension. These are the two largest regional influences on the faulting in both study areas, and the fact that they are recognized independently in two separate studies, in similar succession, over such a large area (See Figure 5.1 for location reference), supports the interpretation that these processes were indeed active and responsible for the deformation.

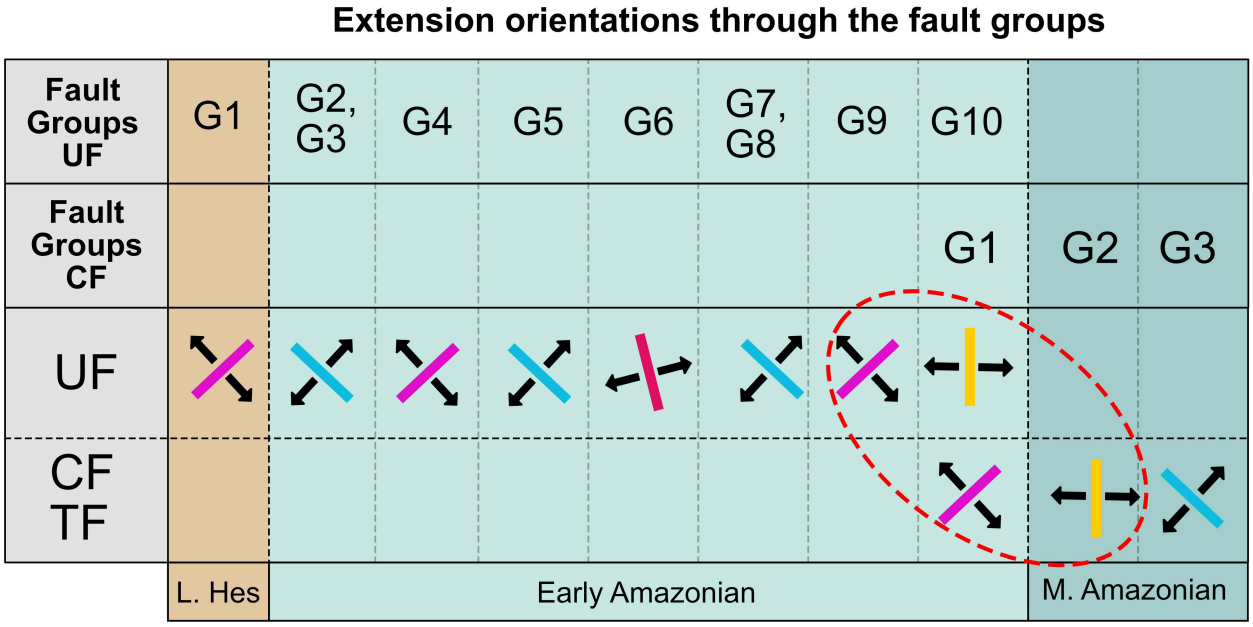

Figure 5.3: Comparison of mapped extension orientations for the fault groups in Ulysses Fossae (UF) and Ceraunius and Tractus Fossae (CF, TF). See fault groups for UF on Figure 2.5 and CF, TF fault groups on Figure 3.5, for reference. The coloured line represents the average fault orientation, and the black lines perpendicular represents the orientation of extension. The geological period in the bottom rows are Late Hesperian (L.Hes), Early Amazonian and Middle Amazonian (M. Amazonian). The red dashed line highlights the similar extension orientations for Ulysses Fossae and Ceraunius and Tractus Fossae.

The results from Chapters 2 and 3, have also given occasion to construct a timeline of volcano-centred magmatic activity in the Tharsis region. Absolute model ages are based on the crater-statistics derived ages in this study, while the assessment of individual activity among the volcanoes is based on the relative ages of the normal faulting mapped in their respective areas. See the synthesis of that in Figure 5.4 below. Together, this summarizes the extension related to 5-6 volcanoes and 2 larger magmatic sources and large-scale Tharsis diking related extension.

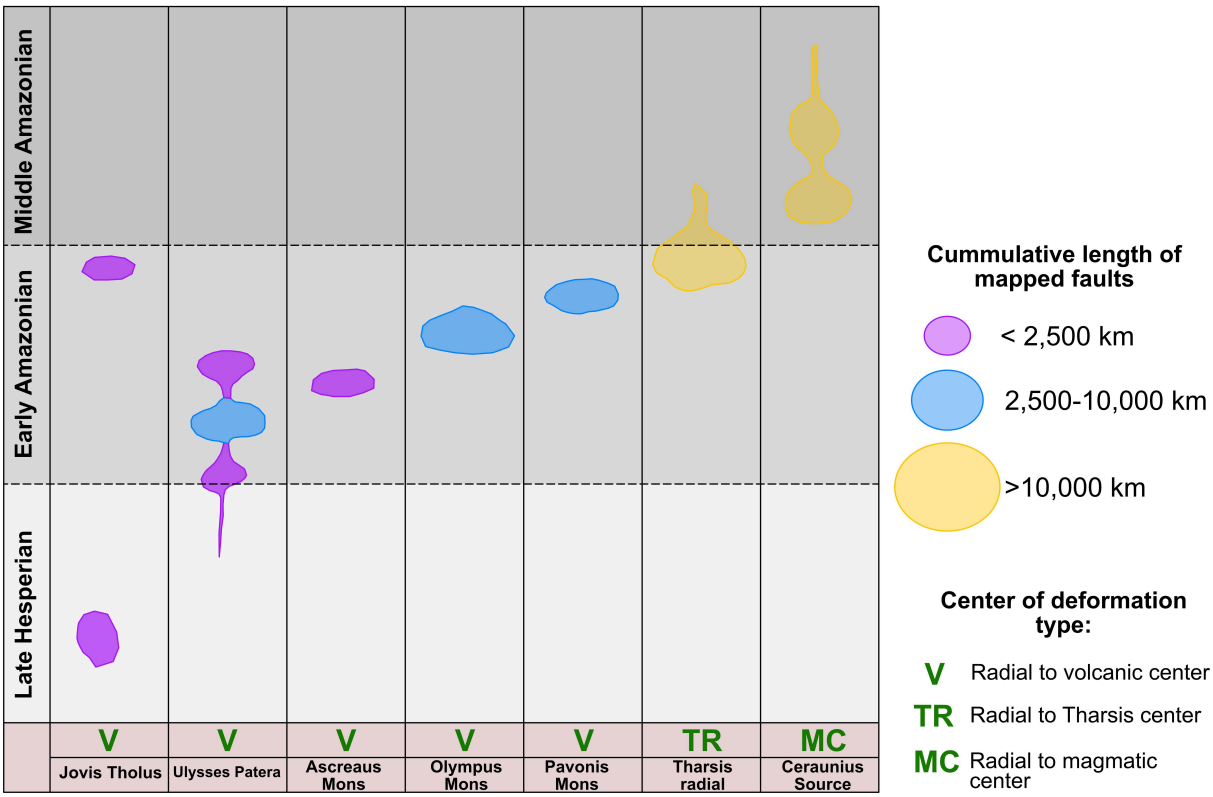

Figure 5.4: The ages of extensional activity mapped in this study, related to their centre of deformation. Purple, blue, and yellow shapes indicate the cumulative lengths of faults mapped associated with the respective centre of deformation. The deformation centres are separated into three types: V) where the mapped faults are radial to a volcano, TR) where the mapped features are radial to the centre of the Tharsis rise, and MC) where the faults are radial to a magmatic centre, in this case the proposed Ceraunius Fossae magma source.

Figure 5.4 presents an overview of the three temporal phases of extensional activity in Tharsis, as captured by the mapping and analysis of the faults in Chapter 2 and 3. It is evident that during the three geological age periods: the Late Hesperian, Early Amazonian and Middle Amazonian, the main extensional activity is separated into two latter periods. The Late Hesperian only has a minimal activity (<2500 km cumulative length) associated with the Jovis Tholus volcano (Shahrzad et al., 2023). Following that, the Early Amazonian is the main period of activity for extension due to radial diking originating from various Tharsis volcanoes, and also show the beginnings of deformation caused by Tharsis radial diking (Figure 5.4). The Middle Amazonian stage of extension is "only" recorded in the vertical diking

associated with the proposed Ceraunius Fossae magma source (CFMS). Together, the structural stages of evolution, along with the timeline of volcanic activity show a highly active, magmatically driven extensional environment in Tharsis, which was particularly active in the Early Amazonian.

5.4. Suggested future work

Within the framework and time-constraints of this thesis, I have had the opportunity to approach my research aims using both structural geology methodology as well as venturing into numerical modelling. However, even with this multidisciplinary approach, planetary geology as a research topic will always benefit from further studies. This is in no small part due to the limitations on available samples, data, and field measurements. In the following section I suggest some further work which could be explored, both to validate the results from this thesis, but also to broaden the research and make it applicable for other areas on other terrestrial planets.

5.4.1. Expanding the knowledge of the tectono-magmatic development of Tharsis and other planetary bodies

Mars' tectono-magmatic history

For Ulysses-, Ceraunius- and Tractus Fossae, the Bouley et al. (2020) revised tectonic history of Tharsis identifies 1308 extensional features in Tharsis, which are dated as Early Hesperian. Collectively this thesis has identified ~17000 extensional features, which were active mainly during in the Amazonian; this discrepancy between studies highlights the importance of approaching the Martian surface studies in higher detail. In order to understand if the local magmatic processes are exclusive to Tharsis, or if other volcanic provinces, such as Elysium (Broquet & Andrews-Hanna, 2023) or Syris Major (Hiesinger & Head III, 2004), exhibit a similar behaviour, comparative studies between the work of this thesis, and similar future work at different Martian locations is essential. This would include a comprehensive mapping of tectonic structures and different morphologies, as well as a new crater-statistics derived age for the studied units. Taking this further, performing similar studies on other terrestrial planets, such as Venus and Mercury, would add even greater clarity on this topic, though it is important to note that the quality and volume of data available for Mercury and Venus is vastly inferior to that of Mars. This variety in terrestrial planet sizes, along with different core-mantle-crust distributions are likely to reflect the surface deformation and would be beneficial to quantify for future planetary missions.

To lessen uncertainty regarding the magmatic sources for the proposed diking in this thesis, future work should include modelling of the acknowledged Tharsis plume and associated upwelling magma source. Resolving the extent of the Tharsis Superplume, the potential number of plume off-shoots, along with determining assets such as size, depth, and migration through time is an important factor in understanding the observed surface deformation in Tharsis. Due to the limited seismic surveys of Mars, numerical models would be the most appropriate approach to begin determining any details about the Martian magma chambers. Variables such as gravity, topography, and tectonics in Tharsis are comparable to Terran superplumes (Dohm et al., 2007). Though they are likely highly layered on top of each other, there are still remnants of the large lava-flows of Tharsis, along with the remnant volcanic constructions and tectonic evidence for magmatic behaviour (i.e. dikes), which can assist in determining magma flow and volatile contents. Together these may aid in creating numerical or analogue models to further define the Tharsis Superplume, whether they are geometric, thermal, or chemical models.

5.4.2. Refining techniques for tectono-magmatic evolution studies

Integrating surface structure-based analysis with existing geophysical data on Mars

Currently there are a number of subsurface detection instrument on Mars, which are able to image down to the depth of interest (>1-2 km). These are the Ground-Penetrating Radar (GPR) *SHARAD* (Shallow Radar), along with the *SEIS* (Seismic Experiment for Interior Structure). The most recent Mars rover, Perseverance, is also equipped with a GPR, the *RIMFAX* (Radar Imager for Mars' Subsurface Experiment), though it is only able to detect down to depths of ~30 cm. SHARAD is a GPR hosted on the Mars Reconnaissance Orbiter, and has a primary mission of detecting ice and water in the Martian crust; SHARAD has a max detection depth of 1 km (Seu et al., 2007). However, a recent study from 2023 became the first study to use the data to investigate the presence of dikes underneath Martian grabens (Bharti et al., 2023). In this study, reflections are detected at two different locations, where they are interpreted as dikes. However, these reflections are detected at a depth of ~34-39 m and 51-58 m respectively. This is much shallower than the depth of dikes expected for the grabens mapped in this thesis where the depth is based on their observed widths. The average graben mapped in my study is 2 km wide. Using previous estimates of graben width to dike-tip depth ratios (between 1.18 and 3.42 (Rivas-Dorado et al., 2021), would mean the shallowest dike depth for the 2 km wide grabens is 2.36 km. The SHARAD instrument will be challenged to resolve an appropriate vertical depth to detect the predicted dikes at that depth. SEIS is a single station seismometer, which was a part of NASA's InSight lander program. Though SEIS can reach the appropriate depth range, setting up a standard array of geophones crossing the grabens would be the ideal scenario. SEIS utilizes passive seismic events, such as marsquakes,

to determine the size, composition and structure of the Martian core, mantle and crust (Lognonné et al., 2019). The SEIS mission is, as of December 2020, no longer active due to the lack of power, but still serves as an indicator of the types of subsurface surveys that are possible on Mars.

5.4.3. Designing future planetary missions to maximise insight gain.

As with the majority of extraterrestrial planetary surface geology, a portion of the calculations, observations, analysis, and measurements are based on a set of assumptions and standards, agreed upon by the planetary scientific community. There are however ways to further advance the research in this thesis, along with the planetary tectonic community as a whole, specifically by the use of planetary missions. Missions to Mars have been ongoing since the first successful flyby mission by the Mariner 4 spacecraft in July 1965, which ushered in a new era of Martian exploration. Since then, 10 fly-bys, 17 orbiters, 7 landers and 6 rovers have visited Mars, all with the purpose of unravelling the planetary evolution and potential biologic past of the planet. In the following section, I list a few of the ideal main scientific missions and instruments that would greatly improve the results of this research.

1) Sample return.

Some of the main uncertainties from this thesis: the crater-statistics derived ages and the material rock properties of the lithosphere, originates from a lack of access to the material being investigated. As Tharsis is not considered a desirable location from a biosignature perspective, onsite missions to any Tharsis province locations are not prioritized by any planetary exploration organisations, such as NASA or ESA. However, sample returns are an essential part of complete scientific investigations and would highly benefit the results of this thesis. With a potential sample returned from the six study areas in this thesis (North Dome, UF North, UF South, Ceraunius North, Ceraunius South and Tractus Fossae), many outstanding unknowns can be answered. A detailed rock-type identification is essential, and by extension, identifying the mechanical properties of the rock is a main priority. Performing uniaxial tests or similar rock mechanic tests, on the sample can provide values of stresses and strains, which can be calculated into material properties. These are useful for input to the numerical model in Chapter 4.

Another main point of action would be performing an absolute age dating of the rock(s). Effective radiometric dating of Martian meteorites has utilized the well-established ^{40}Ar-^{39}Ar, K-Ar, Rb-Sr, Sm-Nd and U-Th-Pb method (*Assessment of Mars Science and Mission Priorities*, 2003). Not only will this solidify the maximum ages of the mapped grabens, combined with the detailed crater size-frequency analysis in this study, it will be possible to calibrate the Martian crater chronology, which is currently extrapolated from the Moon (See Chapter 1.2.2 for further introduction). For this purpose, it is essential to have an accurate

understanding of the location, source, and geological history of each sample, in order to relate the ages to the Martian stratigraphy.

2) Dike detection.

The second investigative aid from a planetary mission to Mars and Tharsis in particular, is using geophysical instruments to detect the presence of dikes underneath the Martian radial grabens. On Earth, dikes are detected using subsurface imaging instruments. However, on Mars the crust is considered to be basaltic, limiting the velocity and/or density contrast between the intruding basaltic body, and the crust. Building further on the preliminary work from Bharti et al. (2023), subsurface geophysical surveys are the best bet at detecting dikes under the Martian grabens. Future missions including detailed targeted seismic or magnetic studies (with adjustment for the basement material) of the subsurface below the grabens, would be essential in determining their dike-related origin.

5.4.4. Extraterrestrial dike intrusion investigations

The 2D numerical model built in PFC2D for this thesis has been a simplified for maximum computational efficiency, in order to simulate dike-intrusion and its surface deformation in a section of the Martian lithosphere. The code for the existing model is also suitable for testing a suite of additional parameters to the Young's modulus tested in this thesis. This section will highlight some key lithosphere and dike-related parameters which can be tested using the same code (Section 1.4.2.1). This section will also introduce some alternative or additional modelling approaches, as well as highlighting physical analogue models and Earth analogue fieldwork as a tool for further investigating dike-induced surface deformation on terrestrial planets (Section 1.4.2.2).

5.4.4.1. Further application of the current code

The PFC numerical model as it is set up now, is prime to test a suite of lithospheric variables, in order to expand on the investigation into surface deformation caused by dike-intrusions, and the behaviour of this process in different scenarios. Variables can both reflect the same planet through time, or the differences between terrestrial planet lithosphere and dike behaviours.

Lithosphere thickness

The influence of the depth of the Martian elastic lithosphere (T_e), on the propagation and surface detection of dikes. For time and computational strain reasons, the study in Chapter 4 is limited to one depth (25 km). However, for the current model setup a simple change of input variable makes it

straightforward to test other T_e values, with the only limitation being the longer run-times for the model for each increase of the value. T_e, has like many other Martian properties, been estimated using gravitational data and numerical modelling. The majority of the existing numerical modelling studies are based on the flexural loading of a volcanic edifice on the surface of Mars, where the lithospheric flexure will be influenced by the lithospheric parameters. These studies provide models and estimates of the lithosphere thickness for specific locations on Mars, at the time of loading (e.g. Belleguic et al., 2005; Comer, 1985; Watters, 2003). Over time the same location on Mars will have a range of lithosphere thickness values. For Olympus Mons, an early estimate comes from Comer (1985), where graben of likely flexural origin were investigated, and used together with viscoelastic relaxation and volcano growth, to estimate a lower boundary T_e at Olympus Mons to 150 km. Since then, studies by McGovern (2004), Belleguic et al.(2005) and Taylor et al. (2020) have reduced the values to >70 km, 93 ± 40 km (supported by a study by Musiol et al. (2016), and 83.3 km, respectively. Contrary to the estimates of the elastic lithosphere thickness at Olympus Mons, studies at Alba Mons have steadily increased the local T_e. Starting with the Comer (1985) study, the initial T_e estimate for Alba Mons was 33 km, which was increased by McGovern (2004) to 38-65, and then to 66 ± 20 by Belleguic in 2005. Taking these two large volcano locations into account, along with computational limitations on size, future studies using the numerical model produced for Chapter 4, can test a variety of values, with the current 25 km model as a lower boundary value, and steadily increase the value to 50, 100 and 120 km.

Lithosphere density

The 2900 kg/m^{-3} lithospheric density value used in the numerical modelling in Chapter 4 is considered an average value for crustal density on Mars, particularly in previous modelling studies (Musiol et al., 2016). Further examination of the surface deformation on Mars could vary the density between model runs, or create a more complex model, where the density varies with depth. Goossens et al. (2017) estimated a bulk crustal density of 2582 ± 209 kg/m using topography and gravity admittance, while a 2014 study of density estimations compatible with major element chemistry of Martian meteorites, and surface concentrations measured by the Mars Odyssey gamma-ray spectrometer, are consistent with an average density of 3100 kg/m^3 (Baratoux et al., 2014; Goossens et al., 2017). Future lithosphere parameter studies with the current numerical model could examine any surface deformation outcomes, while varying the density value between 2500 and 3100 kg/m^3.

Poisson's ratio

Poisson's ratio is a fundamental mechanical property of rocks and is thus an important input in modelling geological processes. Poisson's ratio, ν, describes the ratio of lateral strain to longitudinal strain of a material. As the case for to density and thickness, varying Poisson's ratio can have an effect on dike propagation and its associated deformation. A recent study from Alneasan et al. (2020), found that by increasing the value of Poisson's ratio, the material behaviour of the rock transfers gradually from brittle to ductile (Alneasan et al., 2020). The majority of numerical modelling studies of the Martian lithosphere uses a Poisson's ratio of 0.25 (Belleguic et al., 2005; Cailleau et al., 2005; Grott et al., 2005; Kronberg et al., 2007; Polit et al., 2009; Watters, 2003) similar to an average value for Earth's crust. However a more recent study by Dimitrova & Haines in 2013, suggested that a more appropriate value for Mars is 0.5. In that work, the long-term Poisson's ratio for Martian rocks is investigated from comparing forward models of lithospheric stress, with the style of faulting observed on the surface (Dimitrova & Haines, 2013). This is however not the first time that $\nu = 0.5$ was suggested for Mars, but the study in question concluded that changing Poisson's ratio to either -0 or 0.5, lead to negligibly small changes in their results (Schultz & Watters, 2001).

Testing different dike behaviours.

The numerical model is also suitable for testing a variety of dike-related parameters, which could have a potential impact on the resulting surface structures, such as dike width and intrusion depth, which is hypothesized to have an effect on the final surface deformation, with parameters such as graben width and depth (Rivas-Dorado et al., 2021).

5.4.4.2. Additional modelling approaches

The following section introduces a number of alternative or additional modelling approaches to the PFC2D discrete element numerical model used in this study.

Coupling with Finite Element Modelling software - FLAC2D

Reducing the computational time while increasing the scope of the numerical model, may be accomplished by coupling the existing PFC2D model, with a lower "layer" utilising the finite element modelling approach. The upper part of the model will reflect the near-surface of the Martian lithosphere, where PFC2D accurately represent the resulting structures, as shown in Chapter 4. The second layer of the model will lie beneath the discrete element portion and will reflect the large-scale processes occurring in the Martian lithosphere. This section of the model does not require the high resolution that the upper,

discrete modelling demands, so the lower section could be represented through a finite element modelling approach. This is an advantage, as the finite modelling will not require the computational power that the discrete element modelling does and will thus require less time to get significant results.

For the finite element model software, FLAC2D (Fast Lagrangian Analysis of Continua), also developed by Itasca, can be used. FLAC utilizes an explicit finite difference formulation which makes it possible to model complex behaviours, such as multi-stage problems, large displacements and strains, non-linear material behaviour, and unstable systems. More specifically, with FLAC code, materials are represented by elements within a grid that is manually adjusted to fit the shape of the object to be modelled; in this case FLAC would represent the lower Martian lithosphere. Each element then behaves according to a prescribed linear or non-linear stress/strain law, in response to either applied forces or boundary restraints. The material is then capable of both yield and flow, and the grid can deform (in large strain mode) and move with the represented material (Itasca Consulting Group, 2015). FLAC is based on a "Lagrangian" calculation scheme that is well suited for modelling large distortions and material collapse (Itasca Consulting Group, 2015). The equations of motion are solved to derive new velocities and displacements from stresses and forces. Velocities are then used to calculate strain rates, from which new stresses can be found through a constitutive equation (Gali, 2006). When coupling, the FLAC and PFC software runs separately, but will interact via the defined boundary between the two. The coupling will then work through cycles, where a dike intruding into the lower FLAC model will produce forces and coordinates that it will send to the boundary. PFC will then run with the input forces from FLAC, and in turn transmit velocities and forces back to FLAC, and so on. There is no loss of precision, and the transfer of data works in both directions. The FLAC code has previously been successfully applied to studies of various structural geological and tectonic problems (Lin et al., 2005; Zhang et al., 2000). Other discrete element and finite element programs are available, but none would bring the benefit of the coupled approach available for PFC and FLAC.

Considering alternative Modelling Software

As mentioned above, the Finite Element Method (FEM) is widely used when modelling geophysics and tectono-magmatic systems, where the problem to be investigated, is divided into a grid or a mesh, and models approximate solutions to differential equations (Shamey & Zhao, 2014). Compared to other numerical modelling methods, FEM has a particular precision in handling complex boundary conditions and domain geometries. One example of a commonly used FEM software for modelling large scale tectono-magmatic systems is ASPECT (Advanced Solver for Problems in Earth's ConvecTion) (Heister et al., 2017). ASPECT is a 2D and 3D Finite Element parallel code, which is used to simulate thermal

convection with a focus on the Earth's mantle. Examples of previous uses include thermomechanical modelling of the Southeast Carpathians (Şengül-Uluocak et al., 2019), upper-mantle-scale applications of subduction (Glerum et al., 2018), and 3D melt generation and migration in the mantle (Dannberg & Heister, 2016). ASPECT has been used to model large-scale deformations and thermal processes in complex rheologies.

Pylith is another FEM tool, an open-source code for modelling quasi-static crustal deformation with an emphasis on earthquake faulting (Aagaard et al., 2007). The tool is primarily used in the seismic research community and is able to calculate spatial scales ranging from meters to hundreds of kilometres with temporal scales ranging from milliseconds to thousands of years (Walker et al., 2023). Research with Pylith has involved investigating fields from simulations of coseismic and post-earthquake deformation fields, even from strike-slip faulting (Gharti et al., 2019), to estimating viscoelastic deformation in Southern Alaska due to seasonal loading of glaciers (Sauber, 2015).

Together, ASPECT and Pylith can model stress and strain analysis, fault mechanics, and heat transfer. Additionally, they have the advantage of being open-source and license free. However, these continuum-based models are not fitted to handle singularities and discontinuous problems like crack propagation (Wang et al., 2022).

An alternative to FEM is Finite Difference Modelling (FDM), which also discretizes elements into a grid. However, in FEM, the solution is approximated at the "cell" centres using a finite difference of the derivative (Bashir et al., 2022). It is considered more suitable for more "regularly" shaped domains, with no complex geometries. In general, FDM is considered to require less computational power, which in turn may reflect less accuracy in the results for complex problems. In research, FDM is suited for modelling heat transfer and fluid flow and would be more appropriate for modelling theoretical dike movement and behaviour, with less emphasis on mechanical coupling and explicit fracture-generation.

While both FEM and FDM have a documented usage in modelling large-scale magmatic systems, especially considering the typically shorter model-run times these methods have compared to DEM modelling, neither are as suitable to modelling the mechanical behaviour and explicit fracture generation possible, as DEM is (Elmo et al., 2013). While it is more difficult to accurately model dike propagation behaviour in DEM, the clear advantage of using DEM lies in its element discretization which enables clear data on fracture generation, propagation, and subsequent surface deformation.

Physical analogue modelling

Physical analogue modelling is another suitable method for understanding the mechanics of dike intrusion. While there are limitations to which material property variables that can be assigned, analogue

modelling can offer valuable insights into the deformation of different materials. An example of this was performed by Wyrick et al. (2015), where a layered sandbox model was injected with liquid paraffin to simulate a dike injection. Though this model concluded that for this example, dike-injection without pre-existing faults produced negligible deformation to the surrounding rock (Wyrick et al., 2015).

5.4.5. Using terrestrial analogues to expand planetary knowledge.

The surface of terrestrial planets is shaped by the major geologic processes that we either observe or see remnants of, and includes volcanism, tectonism, impact craters, mass movement, and aeolian-, fluvial-, and glacial processes. Terrestrial analogue field work presents itself as a very useful next step of enquiry, in order to further investigate the geological features mapped and discussed in this thesis. Different to the work presented here, looking at terrestrial analogues offer the opportunity to link directly remote sensing data to details only possible to derive from fieldwork. In addition, the geological history of landforms on Earth are generally much better known than for planetary bodies never visited by humans.

The study in this thesis concerns two main landforms, graben-forming normal faults, and pit crater chains, specifically those located within volcanic zones on Mars. The data used to investigate these locations on Mars are all remote sensing based. A location on Earth which has easy access to lava flood plains, volcanic and tectonic activity and has comparable remote sensing data to Mars, is Iceland. Iceland is located in the Northern Atlantic, and is uniquely situated on the boundary between the North American and Eurasian plates, making it one of the few places on Earth where it is possible to observe sea-floor spreading on land (Denk et al., 2011). The island is underlain by the Iceland hotspot. The Northern Volcanic Zone (NVZ) is one of 4 volcanic rift zones in Iceland, associated with divergent spreading processes (Figure 5.5). The NVZ is 200 km long and 50 km wide, and consists of 7 volcanic systems, each with a separate volcano and an accompanying fissure swarm which transects it (Hjartardóttir et al., 2016).

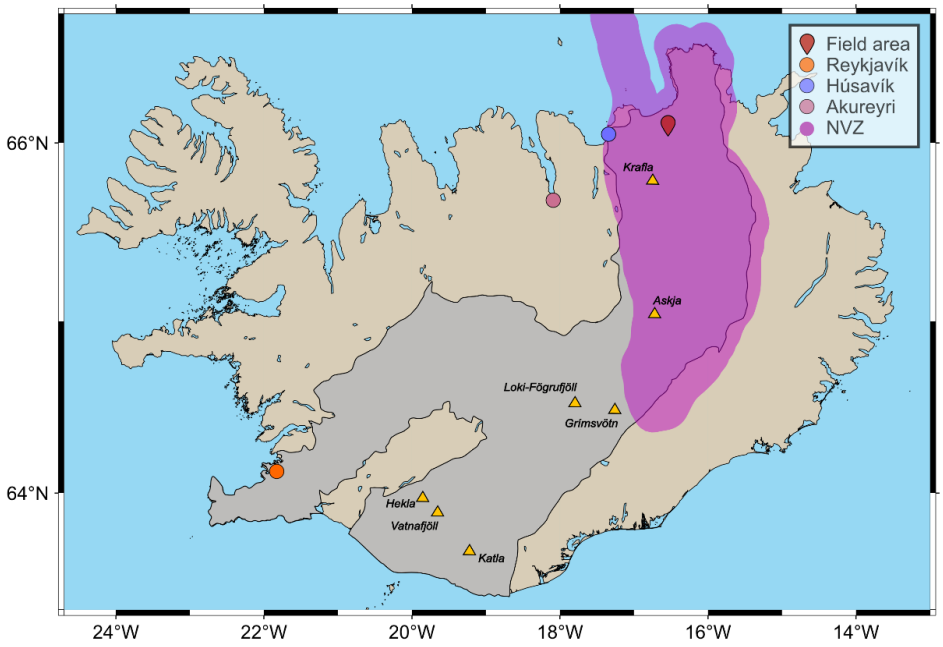

Figure 5.5: Map of Iceland with Northern Volcanic Zone (NVZ) marked in purple, and study area marked with a red pin.

Within the NVZ is the Krafla volcanic system, which inhabits all of the 3 main geological structures of interest from Mars: lava plains, normal faulting (Figure 5.6), and pit-craters. Regions of the surface of Iceland has been investigated using LiDAR (Light Detection and Ranging) surveys. LiDAR is a remote sensing method where the return-time of emitted lasers, is used to measure precise distances in order to image different objects (Bramham et al., 2021.). Airborne LiDAR functions similarly to satellite-mounted instruments orbiting Mars and is thus comparable to the MOLA-HRSC blend used to investigate the surface of Mars. See Figure 5.2 below for comparison. The DEMs derived from airborne LiDAR resolution is higher (0.5 m vertical resolution (Bramham et al., 2021), than that of the MOLA-HRSC blended data (200 m/px), which is also evident when comparing the images they produce (Figures 5.7a and 5.7b). There are two key landforms that are present both on Mars and in Iceland, which are graben-forming normal faults, and pit-crater chains. These offer the opportunity to be studied on Earth and insights can then be transferred to Mars.

Graben-forming faults:

The grabens in the study locations on Mars are very consistent in appearance; they are symmetrical and relatively narrow (1-2 km in average) grabens, considering their lengths reaching up to 3-400 km. Over these hundreds of kilometres, the faults generally maintain their orientation with strike, resulting in mainly linear, as opposed to curved, features, with some exceptions. The graben observed on the LiDAR data for the study location on Iceland, are much smaller in scale, with average lengths between 15-2000 m and

widths > 100 m (Bramham et al., 2021). Despite the change in scale, the faults on the LiDAR dataset are narrow, linear, and largely symmetrical, and display similar features to the Martian grabens, with en echelon patterns. In the field, the grabens clearly exhibited the two bounding faults, with Fault 1 exhibiting less sharp fault boundaries at some locations, possibly due to the presence of water. Fault 2 was consistently sharp through the walked trace (Figure 5.6).

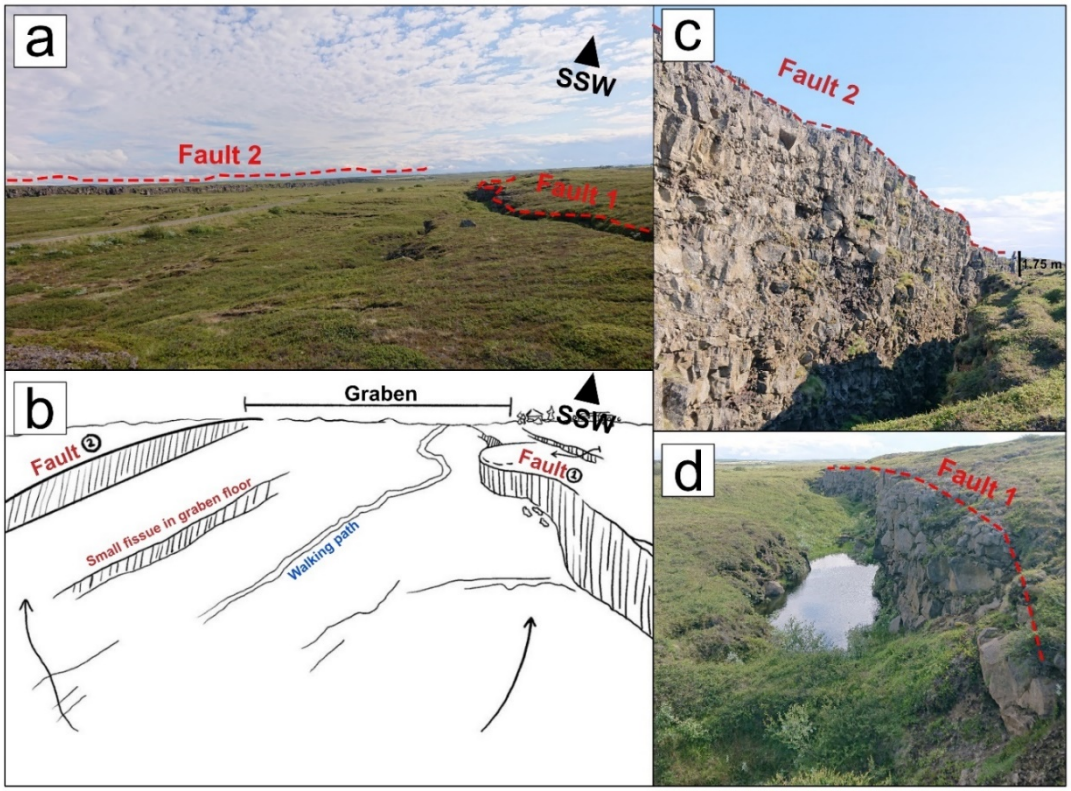

Figure 5.6: Field observations of Icelandic graben. A) image taken along strike from the middle of the graben, with the faults labelled. B) sketch of a) with geological features labelled. Two large faults are bounding this graben, which has several fissures within the graben floor. C) Zoom on Fault 2 from a). D) Zoom on Fault 1 from a).

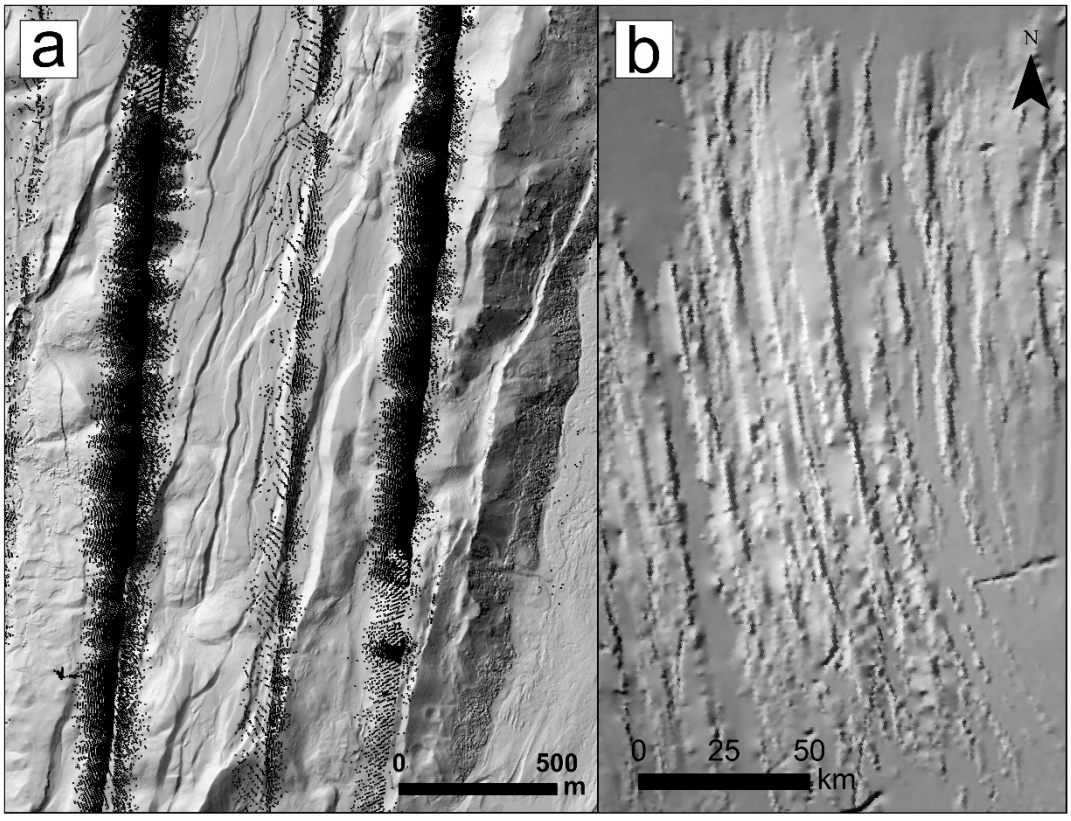

Figure 5.7: Example of graben-forming normal faulting in a) Iceland on LIDAR image and b) Mars on MOLA elecation data.. Note the difference in scale

Pit crater chains: Similar to the grabens, pit-crater chains are also observable on Mars MOLA and CTX images. As established, pit-crater chains on Mars are found both within and outside of grabens and consists of long (kilometres) chains of craters. In Iceland in the LiDAR examples, the pit-crater chains are, similarly to the grabens, much smaller features (Figure 5.8). The three pits from the example in Iceland range from circular to elliptical in shape and were closely spaced and ranged in diameter sizes from 3.5 to ~9 m (figure 5.9). They were relatively shallow (the largest crater being ~2 m deep), and all show a conical interior, though it is unclear if it is a primary feature.

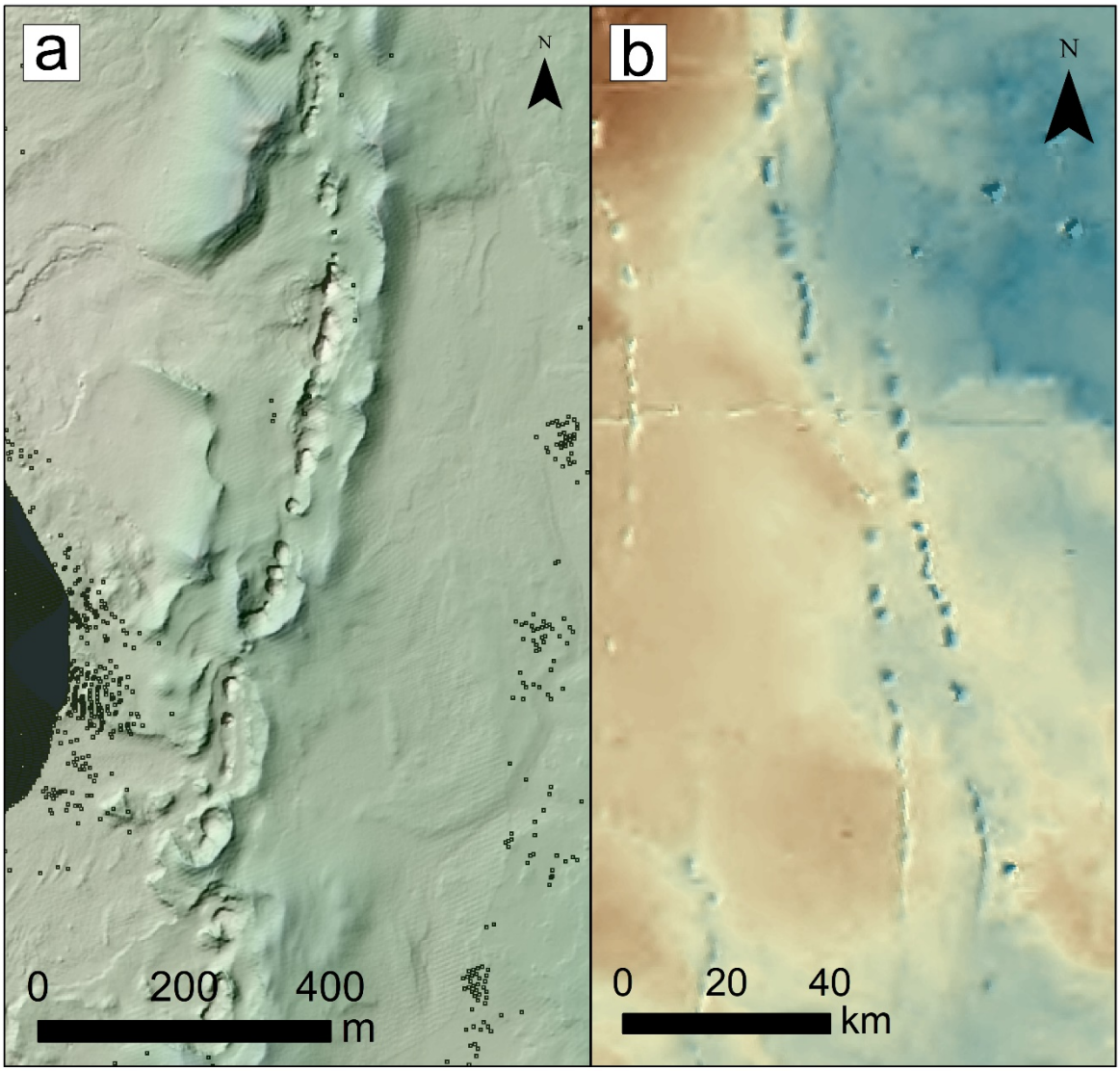

Figure 5.8: Comparison of LiDAR data for Earth showing pit-crater chains (a) and MOLA-HRSC topographic data for Mars (b) also showing pit crater chains. Note the differences in scales between the two examples.

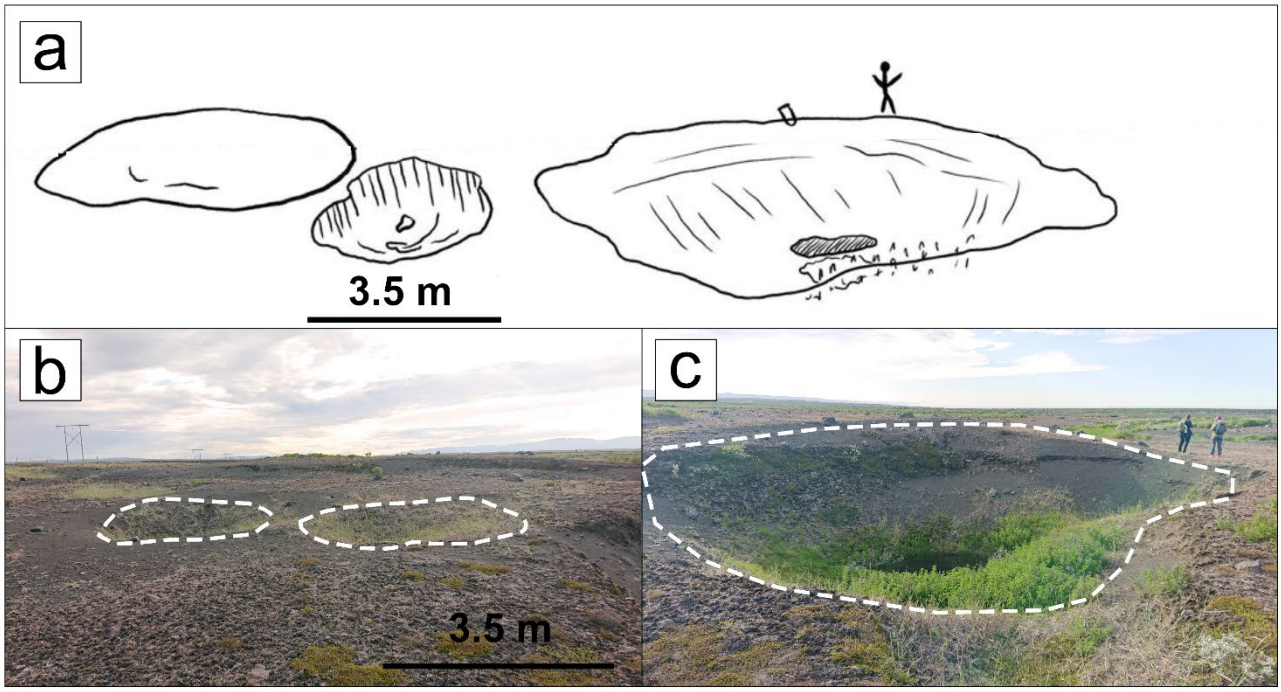

Figure 5.9: Example of pit crater chain landforms in Iceland. This example shows three craters in a row, with varying sizes.

Future analogue fieldwork:

Analogue field work has, in the case of this study, two main benefits in relation to insights we can gain on Martian magmatic processes and structures. The first insight is related to the origin of these structures. For grabens, this is related to the dike-induced origin determined for the majority of the features. Subsurface measurement for dikes underneath established grabens using radar or seismics is one possible option, while another would take advantage of the active nature of the magmatic system on Earth, using micro-seismics to determine magma-paths and evolution.

For pit-crater chains, the ambiguity surrounding their origins relates to which process which creates the cavity for the material to fall into. While this could be various different processes as highlighted in this thesis (faulting, diking, magma withdrawal, lava tubes etc.), examining terrestrial pit-crater chains with similar morphology (though smaller in scale), and in a similar magmatic environment (with a volcanic centre on the surface and a close, subsurface magma source), their accessibility on Earth allows us to further examine them.

Once features on Mars and Earth has been determined to have similar origin processes, be it diking-induced or tectonic, field measurements of Terran structures will allow us to directly compare morphology with the Martian structures. This knowledge will directly show how mechanic differences in planetary lithospheres and erosion through time, can shape extensional structures with similar origins. This is key for current and future remote sensing of the Martian surface and implications for subsurface

processes, and with well-constrained definitions, it will be hugely beneficial for examining the surface (and inferring subsurface processes based there-off) of other terrestrial planets, such as Venus.

A future, longer, and more in-depth portion of field work there would therefore include:

1) A thorough analysis of the remote-sensing LiDAR data, pre-trip. This includes size measurements of features of interests, along with topographic profiles of grabens and pit-crater chains, would serve as a comparison to any in-field data captured.
2) Measurements of the faults and pit-craters, which includes lengths, displacement, dip-angles, extension etc. which can be compared to satellite data for Mars. Do the sizes and topographic profiles from the remote-sensing data correspond to the observations and measurements in the field.
3) Ideally, any subsurface dike detection methods (e.g. GPR, magnetics, seismics).

5.5. Concluding Remarks

In this thesis, I have used detailed mapping to characterise the structural evolution of Ulysses Fossae, Ceraunius Fossae and Tractus Fossae on Mars. I have investigated and defined the volcanic, magmatic, and tectonic processes which have shaped the deformation in the Tharsis Volcanic Province. Through this work, I have produced new comprehensive structural- and impact crater mapping data (which are the most detailed datasets available as of submission date), and developed an updated understanding of the source, relative- and absolute timing, and the impact in a wider Tharsis framework.

I have produced a novel numerical model of a 2D dike intruding into the Martian lithosphere and confirmed that the process of intruding dikes can produce grabens on the Martian surface —without the aid of regional extension. Additionally, the model is primed to engage in further exploration into the enigmatic extra-terrestrial lithospheres; further exploration of how lithospheric parameters influence surface deformation will no doubt be an exciting and informative avenue to continue down along beyond this thesis.

References

Aagaard, B., Williams, C., & Knepley, M. (2007). *PyLith: A Finite-Element Code for Modeling Quasi-Static and Dynamic Crustal Deformation. 2007*, T21B-0592. AGU Fall Meeting Abstracts.

Alapieti, T. (1982). The Koillismaa layered igneous complex, Finland: Its structure, mineralogy and geochemistry, with emphasis on the distribution of chromium.

Alneasan, M., Behnia, M., & Bagherpour, R. (2020). The effect of Poisson's ratio on the creation of tensile branches around dynamic faults. Journal of Structural Geology, 131, 103950. https://doi.org/10.1016/j.jsg.2019.103950

Arkani-Hamed, J., & Riendler, L. (2002). Stress differences in the Martian lithosphere: Constraints on the thermal state of Mars. *Journal of Geophysical Research: Planets*, *107*, 2-1-2–6. https://doi.org/10.1029/2002JE001851

Assessment of Mars Science and Mission Priorities. (2003). National Academies Press. https://doi.org/10.17226/10715

Baratoux, D., Samuel, H., Michaut, C., Toplis, M. J., Monnereau, M., Wieczorek, M., Garcia, R., & Kurita, K. (2014). Petrological constraints on the density of the Martian crust. Journal of Geophysical Research: Planets, 119(7), 1707–1727. https://doi.org/10.1002/2014JE004642

Bashir, Y., Alashloo, S. Y. M., & Ghosh, D. P. (2022). Chapter 3—Seismic wave modeling and high-resolution imaging. In Y. Bashir, A. A. Babasafari, A. R. M. Arshad, S. Y. M. Alashloo, A. H. A. Latiff, R. Hamidi, S. Rezaei, T. Ratnam, C. Sambo, & D. P. Ghosh (Eds.), Seismic Imaging Methods and Applications for Oil and Gas Exploration (pp. 57–132). Elsevier. https://doi.org/10.1016/B978-0-323-91946-3.00004-3

Bazargan, M., & Gudmundsson, A. (2019). Dike-induced stresses and displacements in layered volcanic zones. Journal of Volcanology and Geothermal Research, 384, 189–205. https://doi.org/10.1016/j.jvolgeores.2019.07.010

Bellahsen, N., & Daniel, J. M. (2005). Fault reactivation control on normal fault growth: An experimental study. *Journal of Structural Geology*, *27*(4), 769–780. https://doi.org/10.1016/j.jsg.2004.12.003

Belleguic, V., Lognonné, P., & Wieczorek, M. (2005). Constraints on the Martian lithosphere from gravity and topography data. Journal of Geophysical Research: Planets, 110(E11). https://doi.org/10.1029/2005JE002437

Bharti, R. R., Smith, I. B., & Shukla, S. H. (2023). Subsurface study of the Tharsis graben system using SHARAD data. Icarus, 115681. https://doi.org/10.1016/j.icarus.2023.115681

Bistacchi, N., Massironi, M., & Baggio, P. (2004). Large-scale fault kinematic analysis in Noctis Labyrinthus (Mars). *Planetary and Space Science*, *52*(1), 215–222. https://doi.org/10.1016/j.pss.2003.08.015

Bramham, E. K. (n.d.). LiDAR and InSAR analysis of deformation in the Kra a rift zone, NE Iceland.

Bramham, E. K., Wright, T. J., Paton, D. A., & Hodgson, D. M. (2021). A new model for the growth of normal faults developed above pre-existing structures. Geology, 49(5), 587–591. https://doi.org/10.1130/G48290.1

Broquet, A., & Andrews-Hanna, J. C. (2023). Geophysical evidence for an active mantle plume underneath Elysium Planitia on Mars. Nature Astronomy, 7(2), Article 2. https://doi.org/10.1038/s41550-022-01836-3

Cailleau, B., Walter, T. R., Janle, P., & Hauber, E. (2005). Unveiling the origin of radial grabens on Alba Patera volcano by finite element modelling. Icarus, 176(1), 44–56. https://doi.org/10.1016/j.icarus.2005.01.017

Carr, M. H., & Head, J. W. (2010). Geologic history of Mars. Earth and Planetary Science Letters, 294(3), 185–203. https://doi.org/10.1016/j.epsl.2009.06.042

Comer, R. P. S. (1985). Mars—Thickness of the lithosphere from the tectonic response to volcanic loads. Reviews of Geophysics, 61–92.

Dannberg, J., & Heister, T. (2016). Compressible magma/mantle dynamics: 3-D, adaptive simulations in ASPECT. *Geophysical Journal International*, *207*(3), 1343–1366. https://doi.org/10.1093/gji/ggw329

Daniels, K. A., Kavanagh, J. L., Menand, T., & R. Stephen, J. S. (2012). The shapes of dikes: Evidence for the influence of cooling and inelastic deformation. GSA Bulletin, 124(7–8), 1102–1112. https://doi.org/10.1130/B30537.1

DeLatte, D. M., Crites, S. T., Guttenberg, N., & Yairi, T. (2019). Automated crater detection algorithms from a machine learning perspective in the convolutional neural network era. Advances in Space Research, 64(8), 1615–1628. https://doi.org/10.1016/j.asr.2019.07.017

Denk, T., Grímsson, F., Zetter, R., & Símonarson, L. A. (2011). Introduction to the Nature and Geology of Iceland. In T. Denk, F. Grimsson, R. Zetter, & L. A. Símonarson (Eds.), Late Cainozoic Floras of Iceland: 15 Million Years of Vegetation and Climate History in the Northern North Atlantic (pp. 1–29). Springer Netherlands. https://doi.org/10.1007/978-94-007-0372-8_1

Dimitrova, L., & Haines, A. (2013). Constraining the Long Term Poisson's Ratio of the Martian Lithosphere From 2D and 3D Dynamic Modeling of Lithospheric Stress and the Surface Faulting Record. 1730.

Dohm, J. M., Baker, V. R., Maruyama, S., & Anderson, R. C. (2007). Traits and Evolution of the Tharsis Superplume, Mars. In D. A. Yuen, S. Maruyama, S.-I. Karato, & B. F. Windley (Eds.), Superplumes: Beyond Plate Tectonics (pp. 523–536). Springer Netherlands. https://doi.org/10.1007/978-1-4020-5750-2_17

Elmo, D., Stead, D., Eberhardt, E., & Vyazmensky, A. (2013). Applications of Finite/Discrete Element Modeling to Rock Engineering Problems. *International Journal of Geomechanics*, *13*(5), 565–580. https://doi.org/10.1061/(ASCE)GM.1943-5622.0000238

Ernst, R., Grosfils, E., & Mège, D. (2001). Giant Dike Swarms: Earth, Venus, and Mars. Annual Review of Earth and Planetary Sciences, 29(1), 489–534. https://doi.org/10.1146/annurev.earth.29.1.489

Fassett, C. I., & Head, J. W. (2008). The timing of martian valley network activity: Constraints from buffered crater counting. Icarus, 195(1), 61–89. https://doi.org/10.1016/j.icarus.2007.12.009

Galgana, G. A., Grosfils, E. B., & McGovern, P. J. (2013). Radial dike formation on Venus: Insights from models of uplift, flexure and magmatism. Icarus, 225(1), 538–547. https://doi.org/10.1016/j.icarus.2013.04.020

Gali, M. (2006). FLAC and numerical modeling in geomechanics (pp. 1–6).

Gharti, H. N., Langer, L., & Tromp, J. (2019). Spectral-infinite-element simulations of coseismic and post-earthquake deformation. *Geophysical Journal International*, *216*(2), 1364–1393. https://doi.org/10.1093/gji/ggy495

Glerum, A., Thieulot, C., Fraters, M., Blom, C., & Spakman, W. (2018). Nonlinear viscoplasticity in ASPECT: benchmarking and applications to subduction. *Solid Earth*, *9*(2), 267–294. https://doi.org/10.5194/se-9-267-2018

Goossens, S., Sabaka, T. J., Genova, A., Mazarico, E., Nicholas, J. B., & Neumann, G. A. (2017). Evidence for a low bulk crustal density for Mars from gravity and topography. Geophysical Research Letters, 44(15), 7686–7694. https://doi.org/10.1002/2017GL074172

Grott, M., Hauber, E., Werner, S. C., Kronberg, P., & Neukum, G. (2005). High heat flux on ancient Mars: Evidence from rift flank uplift at Coracis Fossae. Geophysical Research Letters, 32(21). https://doi.org/10.1029/2005GL023894

Gudmundsson, A. (2003). Surface stresses associated with arrested dykes in rift zones. Bulletin of Volcanology, 65(8), 606–619. https://doi.org/10.1007/s00445-003-0289-7

Hahn, R. M., & Byrne, P. K. (2023). A Morphological and Spatial Analysis of Volcanoes on Venus. Journal of Geophysical Research: Planets, 128(4), e2023JE007753. https://doi.org/10.1029/2023JE007753

Heap, M. J., Byrne, P. K., & Mikhail, S. (2017). Low surface gravitational acceleration of Mars results in a thick and weak lithosphere: Implications for topography, volcanism, and hydrology. *Icarus*, *281*, 103–114. https://doi.org/10.1016/j.icarus.2016.09.003

Heister, T., Dannberg, J., Gassmöller, R., & Bangerth, W. (2017). High accuracy mantle convection simulation through modern numerical methods – II: Realistic models and problems. *Geophysical Journal International*, *210*(2), 833–851. https://doi.org/10.1093/gji/ggx195

Hiesinger, H., & Head III, J. W. (2004). The Syrtis Major volcanic province, Mars: Synthesis from Mars Global Surveyor data. Journal of Geophysical Research: Planets, 109(E1). https://doi.org/10.1029/2003JE002143

Hjartardóttir, Á. R., Einarsson, P., Magnúsdóttir, S., Björnsdóttir, Þ., & Brandsdóttir, B. (2016). Fracture systems of the Northern Volcanic Rift Zone, Iceland: An onshore part of the Mid-Atlantic plate boundary. Geological Society, London, Special Publications, 420(1), 297–314. https://doi.org/10.1144/SP420.1

Hou, G. (2012). Mechanism for three types of mafic dyke swarms. Geoscience Frontiers, 3(2), 217–223. https://doi.org/10.1016/j.gsf.2011.10.003

Itasca Consulting Group. (2015). FLAC 8 Basics (Vol. 2015).

Kneissl, T., Michael, G. G., Platz, T., & Walter, S. H. G. (2015). Age determination of linear surface features using the Buffered Crater Counting approach – Case studies of the Sirenum and Fortuna Fossae graben systems on Mars. Icarus, 250, 384–394. https://doi.org/10.1016/j.icarus.2014.12.008

Kronberg, P., Hauber, E., Grott, M., Werner, S. C., Schäfer, T., Gwinner, K., Giese, B., Masson, P., & Neukum, G. (2007). Acheron Fossae, Mars: Tectonic rifting, volcanism, and implications for lithospheric thickness. Journal of Geophysical Research: Planets, 112(E4). https://doi.org/10.1029/2006JE002780

Lin, G., Zhang, Y., Guo, F., Wang, Y., & Fan, W. (2005). Numerical modelling of lithosphere evolution in the North China Block: Thermal versus tectonic thinning. Journal of Geodynamics, 40(1), 92–103. https://doi.org/10.1016/j.jog.2005.07.011

Lognonné, P., Banerdt, W. B., Giardini, D., Pike, W. T., Christensen, U., Laudet, P., de Raucourt, S., Zweifel, P., Calcutt, S., Bierwirth, M., Hurst, K. J., Ijpelaan, F., Umland, J. W., Llorca-Cejudo, R., Larson, S. A., Garcia, R. F., Kedar, S., Knapmeyer-Endrun, B., Mimoun, D., … Wookey, J. (2019). SEIS: Insight's Seismic Experiment for Internal Structure of Mars. Space Science Reviews, 215(1), 12. https://doi.org/10.1007/s11214-018-0574-6

Magee, C., & Jackson, C. A.-L. (2020). Seismic reflection data reveal the 3D structure of the newly discovered Exmouth Dyke Swarm, offshore NW Australia. Solid Earth, 11(2), 579–606. https://doi.org/10.5194/se-11-579-2020

Mastin, L. G., & Pollard, D. D. (1988). Surface Deformation and Shallow Dike Intrusion Processes at Inyo Craters, Long Valley, California. Journal of Geophysical Research: Solid Earth, 93(B11), 13221–13235. https://doi.org/10.1029/JB093iB11p13221

McGovern, P. J. (2004). Correction to "Localized gravity/topography admittance and correlation spectra on Mars: Implications for regional and global evolution". Journal of Geophysical Research, 109(E7), E07007. https://doi.org/10.1029/2004JE002286

Morris, A., Ferrill, D. A., & Henderson, D. B. (1996). Slip-tendency analysis and fault reactivation. *Geology*, *24*(3), 275–278. https://doi.org/10.1130/0091-7613(1996)024

Musiol, S., Holohan, E. P., Cailleau, B., Platz, T., Dumke, A., Walter, T. R., Williams, D. A., & van Gasselt, S. (2016). Lithospheric flexure and gravity spreading of Olympus Mons volcano, Mars. Journal of Geophysical Research: Planets, 121(3), 255–272. https://doi.org/10.1002/2015JE004896

Okubo, C. H., & Schultz, R. A. (2005). Evidence of Tharsis-Radial Dike Intrusion in Southeast Alba Patera from MOLA-based Topography of Pit Crater Chains. 1007.

Orlov, C. J., Bramham, E. K., Thomas, M., Byrne, P. K., Piazolo, S., & Mortimer, E. (2022). Structural Architecture and Deformation History of Tempe Terra, Mars. *Journal of Geophysical Research: Planets*, *127*(11), e2022JE007407. https://doi.org/10.1029/2022JE007407

Polit, A. T., Schultz, R. A., & Soliva, R. (2009). Geometry, displacement–length scaling, and extensional strain of normal faults on Mars with inferences on mechanical stratigraphy of the Martian crust. Journal of Structural Geology, 31(7), 662–673. https://doi.org/10.1016/j.jsg.2009.03.016

Rainbird, R. H. (1993). The Sedimentary Record of Mantle Plume Uplift Preceding Eruption of the Neoproterozoic Natkusiak Flood Basalt. The Journal of Geology, 101(3), 305–318. https://doi.org/10.1086/648225

Rivas-Dorado, S., Ruiz, J., & Romeo, I. (2021). Subsurface Geometry and Emplacement Conditions of a Giant Dike System in Elysium Fossae, Mars. Journal of Geophysical Research: Planets, 126(1), e2020JE006512. https://doi.org/10.1029/2020JE006512

Rubin, A. M. (1992). Dike-induced faulting and graben subsidence in volcanic rift zones. Journal of Geophysical Research: Solid Earth, 97(B2), 1839–1858. https://doi.org/10.1029/91JB02170

Rubin, A. M. (1995). Propagation of Magma-Filled Cracks. Annual Review of Earth and Planetary Sciences, 23(1), 287–336. https://doi.org/10.1146/annurev.ea.23.050195.001443

Sauber, J. (2015). Estimating Viscoelastic Deformation Due to Seasonal Loading. *Computational Infrastructure for Geodynamics (CIG) News Elements*, *4*(3). https://ntrs.nasa.gov/citations/20150023405

Schöpfer, M. P. J., Childs, C., Manzocchi, T., Walsh, J. J., Nicol, A., & Grasemann, B. (2017). The emergence of asymmetric normal fault systems under symmetric boundary conditions. Journal of Structural Geology, 104, 159–171. https://doi.org/10.1016/j.jsg.2017.10.006

Schultz, R. A., Okubo, C. H., Goudy, C. L., & Wilkins, S. J. (2004). Igneous dikes on Mars revealed by Mars Orbiter Laser Altimeter topography. Geology, 32(10), 889–892. https://doi.org/10.1130/G20548.1

Schultz, R. A., & Watters, T. R. (2001). Forward mechanical modeling of the Amenthes Rupes Thrust Fault on Mars. Geophysical Research Letters, 28(24), 4659–4662. https://doi.org/10.1029/2001GL013468

Scott, D. H., Tanaka, K. L., & Kozak, R. (1986). Geologic map of the western equatorial region of Mars.

Şengül-Uluocak, E., Pysklywec, R. N., Göğüş, O. H., & Ulugergerli, E. U. (2019). Multidimensional Geodynamic Modeling in the Southeast Carpathians: Upper Mantle Flow-Induced Surface Topography Anomalies. *Geochemistry, Geophysics, Geosystems*, *20*(7), 3134–3149. https://doi.org/10.1029/2019GC008277

Seu, R., Phillips, R. J., Biccari, D., Orosei, R., Masdea, A., Picardi, G., Safaeinili, A., Campbell, B. A., Plaut, J. J., Marinangeli, L., Smrekar, S. E., & Nunes, D. C. (2007). SHARAD sounding radar on the Mars Reconnaissance Orbiter. Journal of Geophysical Research: Planets, 112(E5). https://doi.org/10.1029/2006JE002745

Shahrzad, S., Bramham, E. K., Thomas, M., Piazolo, S., Byrne, P. K., & Mortimer, E. (2023). Deciphering the Structural History of Ulysses Fossae, Mars, Using Fault Pattern Analysis. Journal of Geophysical Research: Planets, 128(5), e2022JE007633. https://doi.org/10.1029/2022JE007633

Shahrzad, S., Kinch, K. M., Goudge, T. A., Fassett, C. I., Needham, D. H., Quantin-Nataf, C., & Knudsen, C. P. (2019). Crater Statistics on the Dark-Toned, Mafic Floor Unit in Jezero Crater, Mars. Geophysical Research Letters, 46(5), 2408–2416. https://doi.org/10.1029/2018GL081402

Shamey, R., & Zhao, X. (Eds.). (2014). 5—Solving dynamic equations in dye transport. In *Modelling, Simulation and Control of the Dyeing Process* (pp. 100–113). Woodhead Publishing. https://doi.org/10.1533/9780857097583.100

Tanaka, K. L., Skinner Jr., J. A., Dohm, J. M., Irwin, III, R. P., Kolb, E. J., Fortezzo, C. M., Platz, T., Michael, G. G., & Hare, T. M. (2014). Geologic Map of Mars (Scientific Investigations Map) [Scientific Investigations Map].

Taylor, N. C., Johnson, J. H., Herd, R. A., & Regan, C. E. (2020). What can Olympus Mons tell us about the Martian lithosphere? Journal of Volcanology and Geothermal Research, 402, 106981. https://doi.org/10.1016/j.jvolgeores.2020.106981

Trippanera, D., Acocella, V., Ruch, J., & Abebe, B. (2015). Fault and graben growth along active magmatic divergent plate boundaries in Iceland and Ethiopia. Tectonics, 34(11), 2318–2348. https://doi.org/10.1002/2015TC003991

Urbani, S., Acocella, V., & Rivalta, E. (2018). What Drives the Lateral Versus Vertical Propagation of Dikes? Insights From Analogue Models. Journal of Geophysical Research: Solid Earth, 123(5), 3680–3697. https://doi.org/10.1029/2017JB015376

Vallianatos, F., & Sammonds, P. (2011). A non-extensive statistics of the fault-population at the Valles Marineris extensional province, Mars. *Tectonophysics*, *509*(1), 50–54. https://doi.org/10.1016/j.tecto.2011.06.001

Walker, R. L., Knepley, M. G., Aagaard, B. T., & Williams, C. A. (2023). Multiphysics modelling in PyLith: Poroelasticity. Geophysical Journal International, 235(3), 2442–2475. https://doi.org/10.1093/gji/ggad370

Wang, T., Zhang, F., Furtney, J., & Damjanac, B. (2022). A review of methods, applications and limitations for incorporating fluid flow in the discrete element method. Journal of Rock Mechanics and Geotechnical Engineering, 14(3), 1005–1024. https://doi.org/10.1016/j.jrmge.2021.10.015

Watters, T. R. (2003). Lithospheric flexure and the origin of the dichotomy boundary on Mars. Geology, 31(3), 271–274. https://doi.org/10.1130/0091-7613(2003)031

Wyrick, D., Ferrill, D. A., Morris, A. P., Colton, S. L., & Sims, D. W. (2004). Distribution, morphology, and origins of Martian pit crater chains. Journal of Geophysical Research: Planets, 109(E6). https://doi.org/10.1029/2004JE002240

Wyrick, D. Y., Morris, A. P., Todt, M. K., & Watson-Morris, M. J. (2015). Physical analogue modelling of Martian dyke-induced deformation. Geological Society, London, Special Publications, 401(1), 395–403. https://doi.org/10.1144/SP401.15

Zhang, Y., Manchtelow, N. S., Hobbs, B. E., Ord, A., & Mühlhaus, H. B. (2000). Numerical modelling of single-layer folding: Clarification of an issue regarding the possible effect of computer codes and the influence of initial irregularities. Journal of Structural Geology, 2000(22), 1511–1522.

Appendix A

Supplementary Material for Chapter 2

The materials presented in Appendix A were included as online Supplementary Material in the following publication: *Deciphering the structural history of Ulysses Fossae, Mars, using fault pattern analysis.* S. Shahrzad[1], Bramham, E. K., Thomas, M., Byrne, P. K., Piazolo, S., & Mortimer, E. Journal of Geophysical Research: Planets, 128,

Contents of this file

- Figure A1
- Tables A1 and A2

A.1 Introduction

Supporting information for "*Deciphering the structural history of Ulysses Fossae, Mars, using fault pattern analysis*". Includes one supporting Figure, A1, which shows the Crater Size-Frequency Distribution for all three Ulysses Fossae areas and two additional tables: Table A1 which is an overview over the characteristics of the 10 defined fault groups, and Table A2, which contains the strain calculations for the fault groups.

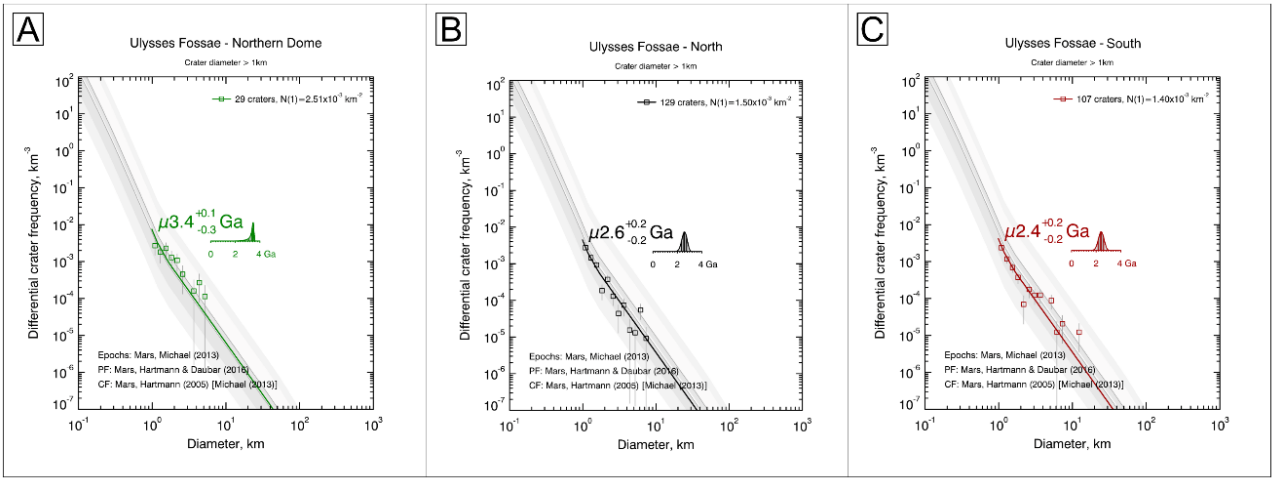

Figure A.10: Crater Size-Frequency distribution plots for all 3 areas of Ulysses Fossae.

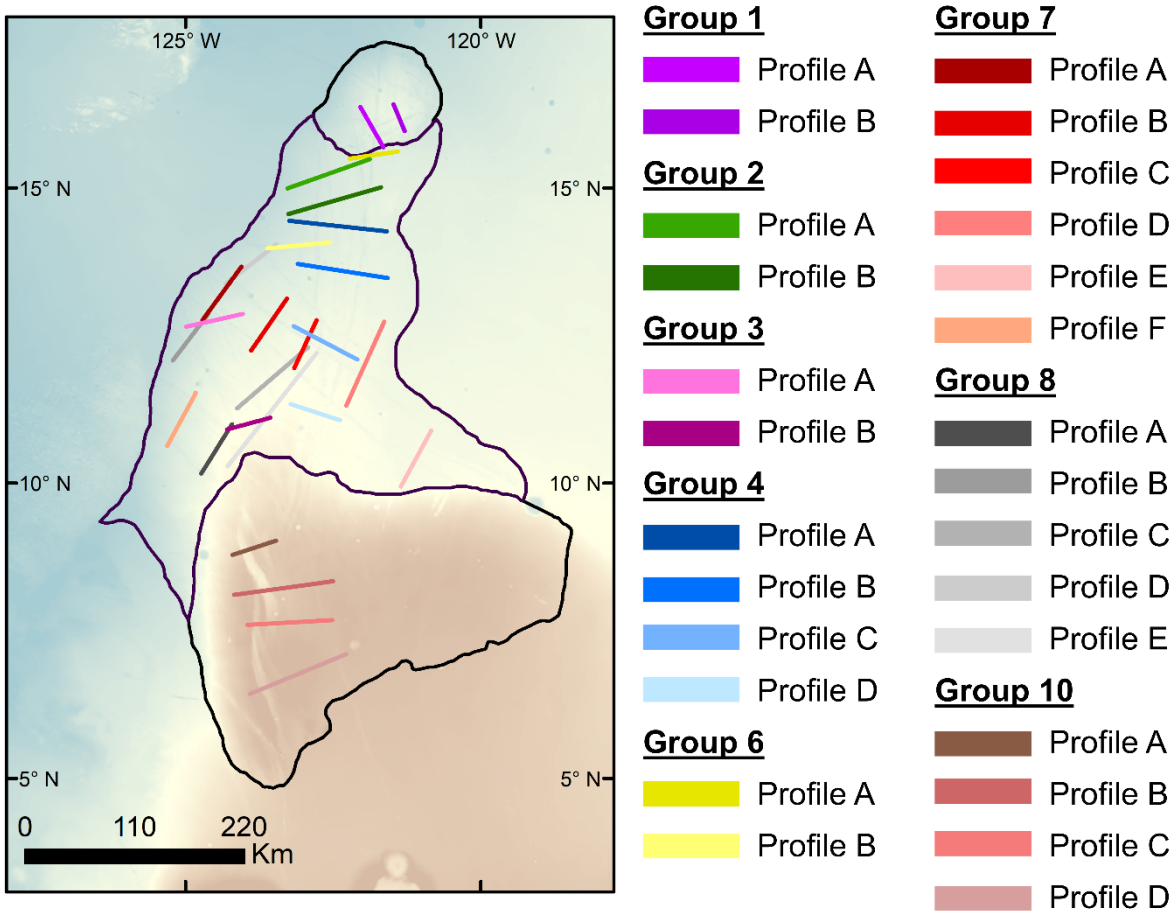

Figure A.2: Location of all topographic profiles, used to determine strain in Ulysses Fossae. Colours in the legend on the right are grouped by fault groups.

Group	*N(f)*	*Σ l (km)*	*Average length (km)*	*Age*	*Strike*	*Morphological characteristics*	*Crosscutting relationships*	*Extension source*
1	147	591.92	4.03	lH	ENE	GFNF*, linear, isolated to UF Dome.	Cross-cut by Groups 2, 4, 5, 6.	Jovis Tholus (?)
2	324	2045.18	6.31	eA	NNW	GFNF, longer faults have a curvature from NNW to N-S. Superposes UF Dome UF North.	Cross-cuts Group 1; Cross-cut by Groups 4, 5, 6 and 7	Ulysses Patera
3	631	4638.58	7.35	eA	NNW	GFNF, with slight curvature in the NW-SE orientation. Faults appear on the southern half of UF North and continue to the UF South. Some faults terminate in the north and south along the boundary of the surrounding Amazonian unit.	Cross-cut by Groups 4, 6, 7, 8, 9 and 10	Ulysses Patera
4	777	4911.36	6.32	eA	N/S	GFNF, linear and main faults are closely spaced in the middle of the UF Dome, UF North and the northern part of UF South. The northern faults terminate at the Amazonian unit boundary.	Cross-cuts Group 3; Cross-cut by Groups 5, 6, 7 and 8	Regional extension
5	357	1395.21	3.91	eA	NW/SE	GFNF, linear, mostly spatially restricted to UF Dome, with some faults crossing over to the northern part UF North.	Cross-cuts G1, G2 and G4; Cross-cut by Group 6	Ascraeus Mons
6	316	1972.73	6.24	eA	N/S	GFNF, linear, with large spacing between them. Appears on UF Dome and UF North, with a slight overlap on to UF South. The faults along the northern boundary of the UF Dome, terminate along the Amazonian unit boundary.	Cross-cuts Groups 1, 2, 3,4 and 5; Cross-cut by Groups 7 and 8	Ulysses Patera
7	1352	7261.28	5.37	eA	NW/SE	GFNF, mainly located on UF North, with some extension on to the surrounding Amazonian unit for the faults in the southeast. Along the western border of Ulysses Fossae, the faults terminate at the Amazonian unit boundary. Wide spatial distribution of faults.	Cross-cuts Groups 2, 4, 5 and 6; Cross-cut by Groups 8 and 9	Olympus Mons
8	891	6939.45	7.79	eA	NW/SE	GFNF, mainly located on UF North, with some extension on to the surrounding Amazonian unit for the faults in the southeast. A section of faults continues from UF North to the northern half of UF South. Along the western border of Ulysses Fossae, the faults terminate at the Amazonian unit boundary.	Cross-cuts Groups 4, 5, 6 and 7; Cross-cut by Group 9 and 10	Pavonis Mons
9	172	777.27	4.55	eA	NE	GFNF, faults scattered across a large area in UF North and UF South.	Cross-cuts Groups 4, 7 and 8; Cross-cut by Group 10	Jovis Tholus (?)
10	148	1563.44	10.42	eA	NNW	Normal faults creating large sigmoidal graben and large-scale en échelon features. Spatially form a narrow band and are confined within UF South. Though not mapped, the western en échelon faults continue considerably farther south onto the surrounding Amazonian unit.	Cross cuts Groups 4, 8 and 9	Regional extension/Reactivation
TOTAL	5,115	32,096.42						

Table A.1: Summary of mapped fault groups in Ulysses Fossae. Group number denotes relative age from oldest (Group 1) to youngest (Group 10). N(f) shows number of faults in each group, Σl is the cumulative length of the faults in each group. The Age is the geological period (where lH = late Hesperian and eA = early Amazonian) which the fault group is assigned in this study based on crater statistics in Section 3.3." Extension Source" has the name of a volcano if the fault group has a radial orientation to its center or is denoted as a part of the E-W regional extension of the whole Tharsis Province. *GFNF = Graben Forming Normal Fault.

Strain calculations for fault groups G1, G2, G4, G5, G6, G7, G8, G10

Group 1	**Dcum**	**ecum**	**l0 (m)**	**lfinal (m)**	**e**	**%**
Profile A	357	206.1	46643.1	46849.3	0.0044	0.44
Profile B	213	123.0	29039.0	29162.0	0.0042	0.42
	Group 1 maximum strain					**0.44**
Group 2						
Profile A	592	341.8	87352.0	87693.8	0.0039	0.39
Profile B	548	316.4	96382.6	96699.0	0.0033	0.33
	Group 2 maximum strain					**0.39**
Group 3						
Profile A	376	217.1	58136.4	58353.5	0.0037	0.37
Profile B	435	251.1	45001.5	45252.6	0.0056	0.56
	Group 3 maximum strain					**0.56**
Group 4						
Profile A	859	495.9	98203.5	98699.5	0.0051	0.51
Profile B	1086	627.0	90846.6	91473.6	0.0069	0.69
Profile C	991	572.2	71536.6	72108.8	0.0080	0.80
Profile D	561	323.9	51644.1	51968.0	0.0063	0.63
	Group 4 maximum strain					**0.80**
Group 6						
Profile A	235	135.7	48265.1	48400.8	0.0028	0.28
Profile B	33	19.1	62913.0	62932.0	0.0003	0.03
	Group 6 maximum strain					**0.28**
Group 7						
Profile A	863	498.3	66270.7	66769.0	0.0075	0.75
Profile B	1018	587.7	62771.7	63359.4	0.0094	0.94
Profile C	708	408.8	52658.0	53066.7	0.0078	0.78
Profile D	998	576.2	92119.7	92695.9	0.0063	0.63
Profile E	247	142.6	63778.4	63921.0	0.0022	0.22
Profile F	478	276.0	60545.5	60821.5	0.0046	0.46
	Group 7 maximum strain					**0.94**
Group 8						
Profile A	738	426.1	57963.3	58389.3	0.0074	0.74
Profile B	578	333.7	58094.3	58428.0	0.0057	0.57
Profile C	825	476.3	93526.3	94002.6	0.0051	0.51
Profile D	452	261.0	64896.0	65156.9	0.0040	0.40
Profile E	1347	777.7	144099.7	144877.4	0.0054	0.54
	Group 8 maximum strain					**0.74**
Group 10						
Profile A	1713	989.0	44998.2	45987.22	0.0220	2.20
Profile B	2973	1716.5	98725.7	100442.2	0.0174	1.74
Profile C	2198	1269.0	84061.7	85330.67	0.0151	1.51
Profile D	1556	898.4	103649.0	104547.3	0.0087	0.87
	Group 10 maximum strain					**2.20**

Table A.2: Strain calculations for the 8 fault groups, G1, G2, G3, G4, G6, G7, G8, G10. See main text Section 1.2.4 for equations used.

Appendix B

Supplementary Material for Chapter 3

The materials presented in Appendix B were included as online Supplementary Material in the following submitted article:
Amazonian Tectonic Evolution of Ceraunius and Tractus Fossae, Mars, and Implications for Local Magmatic Sources.

S. Shahrzad, Bramham, E. K., Piazolo, S., M. Thomas & Byrne, P. K. Journal of Geophysical Research: Planets.

Contents of this file

- Figures B.1, B.2 and B.3

B.1 Introduction

Supporting information for "Amazonian Tectonic Evolution of Ceraunius and Tractus Fossae, Mars, and Implications for Local Magmatic Sources". Includes one supporting Figure, B.1, which shows examples of topographic profiles of mapped features, Figure B.2 which show a histogram of mapped fault lengths, and Figure B.3, which show orientation rose-diagrams for the mapped faults groups based on the study area.

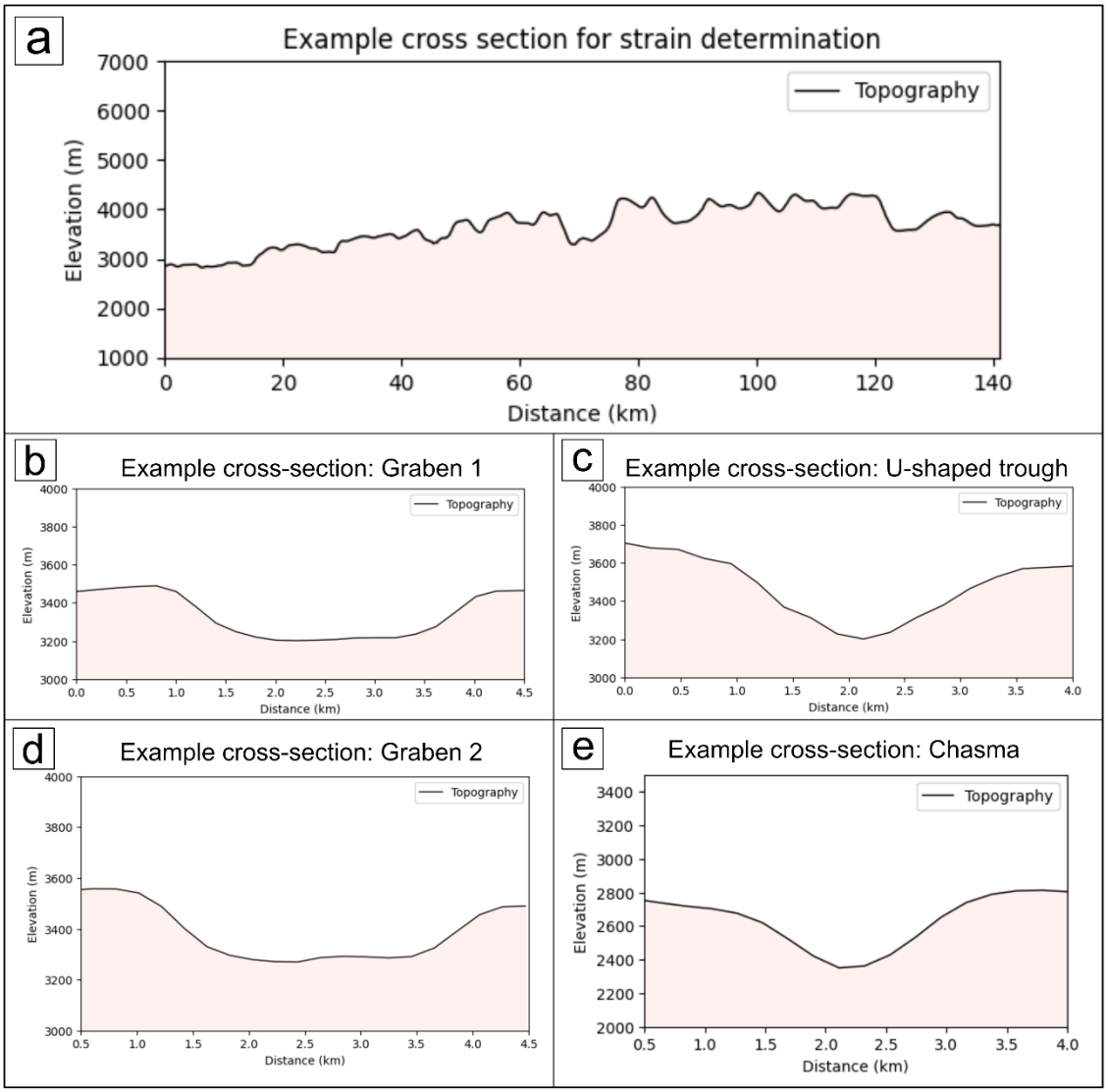

Figure B.1: Examples of various topographic features used in this study, from merged MOLA (Mars Orbiter Laser Altimeter) and HRSC (High Resolution Stereo Camera) Digital Elevation model (200 m/px) (Fergason et al., 2018). A) Example of topographic profile used to measure the strain for the 3 fault groups. B) and D) Examples of fault bounding grabens. Note the flat graben floors. C) and E) Example cross-sections of a u-shaped trough and a Chasma. Note the sloped sides and the lack of graben floor.

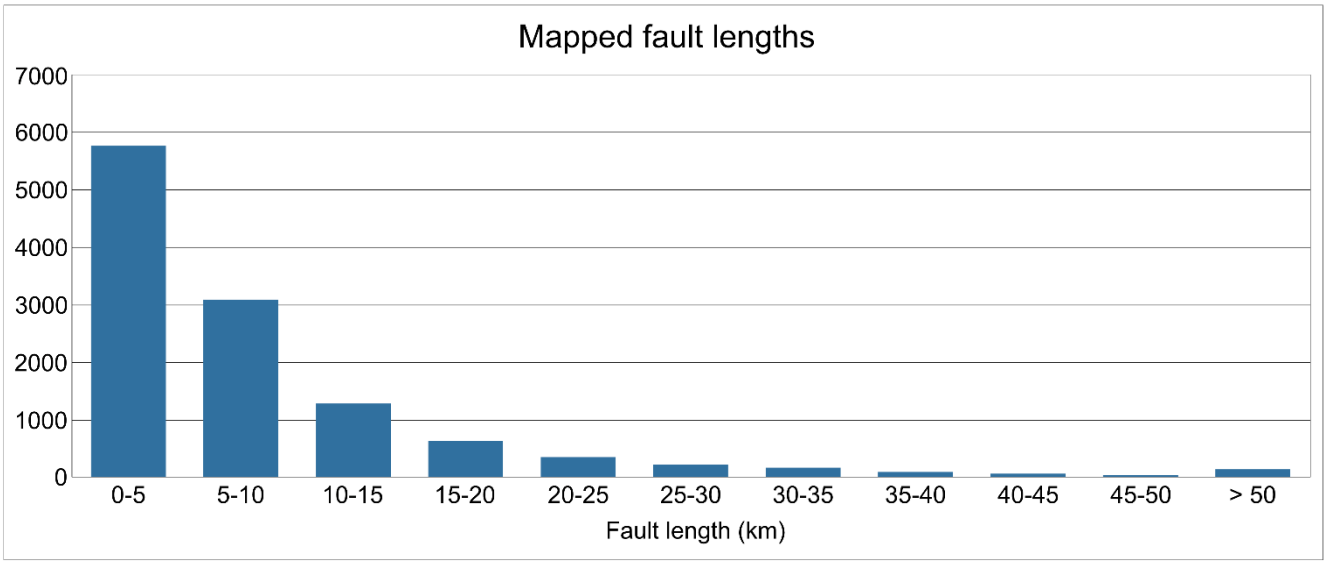

Figure B.2: Histogram showing the distribution of lengths for the mapped faults in Ceraunius North, Ceraunius South and Tractus Fossae.

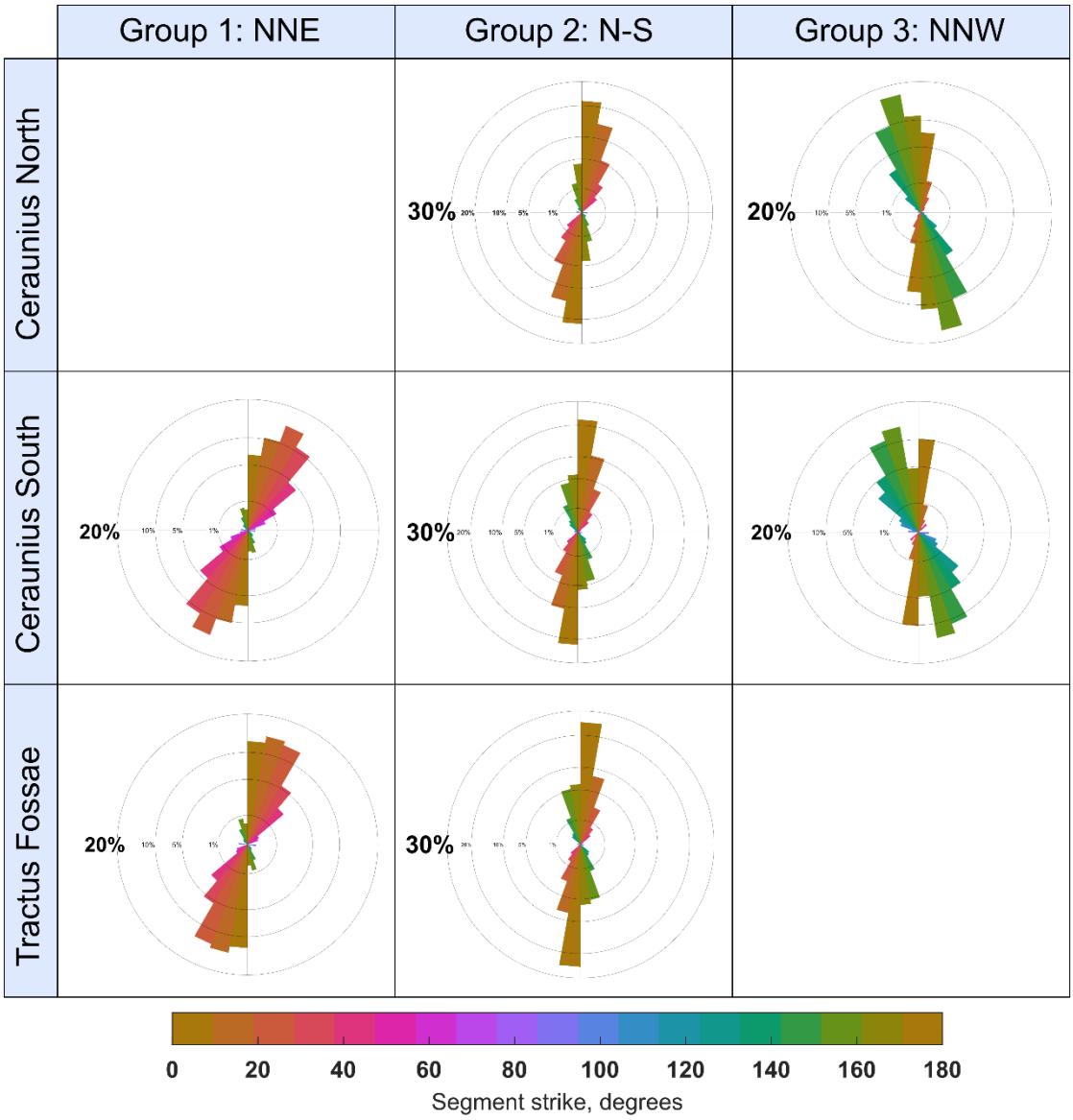

Figure B.3: Rose-diagrams showing the orientation of the mapped faults for each of the three study areas (Ceraunius North, Ceraunius South, and Tractus Fossae), divided into each group.

Appendix C

Supplementary Material for Chapter 4

Contents of this file

- Supplementary text C.1, including Supplementary Figure C.1.
- Supplementary Figures C.2, C.3, C.4.

C.1 Discrete Element Modelling Method

As described in Chapter 4, Discrete Element Modelling (DEM) is a numerical modelling methodology, which uses contact mechanics to update the forces and moments in the model. The theory behind the specific DEM used in this thesis, *Particle Flow Code (PFC)*, is described in Chapter 4.2, but here I supply further background information on DEM modelling overall, and the limitations of the method.

DEMs discretizes a material using rigid elements, usually in the form of a circle or sphere, which interact with neighboring element using the contact models assigned to them (Tavarez & Plesha, 2007). For every timestep of the model, the DEM works through a calculation cycle which provides a dynamic solution to Newton's laws of motion. A typical DEM calculation cycle will work using the assigned contact model, where the forces and moments acting on the individual particles allows the calculation of the acceleration according to Newton's second law. This acceleration determine the velocities, which is then translated into the new position for each individual particle (Potyondy, 2019).

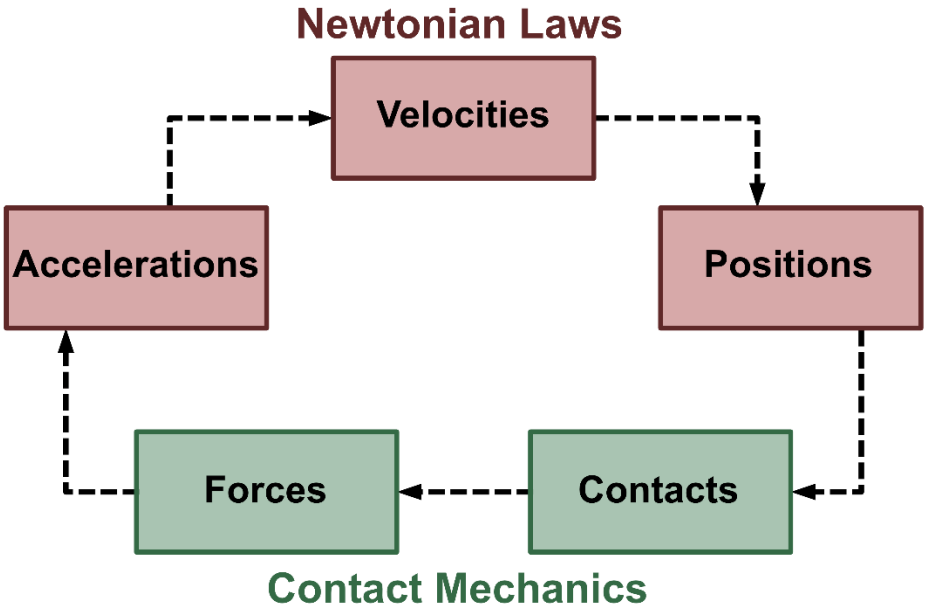

Figure C.11: Example of calculation cycle for a DEM model. Diagram modified from Tavarez & Plesha (2007) and Harnett et al,(2018).

The forces and moments used in the calculation cycle is determined by the assigned contact model. See Chapter 4.2 for the equations used in the soft-bond PFC model, used in this study. With the new, updated positions for the timestep, the DEM restarts the process after confirming the particle contacts again.

C.2. Particle Flow Code used in this thesis

The novel code developed for this thesis comprised of 2 overall sections: 1) generating the material and boundaries, and 2) creating and intruding the dike.

C.2 1. Code Part 1 – Creating the model: defining material, boundaries, and material behaviour.

```
model new
model title 'Mars_Dike'
model large-strain on
model domain extent -100000 100000
;-------------------------------------------------------------
; Model Parameters
; Model size
[mheight = 25000] ;depth in meters
[mwidth = mheight*3] ;width of model.
[mdiv = mheight/6] ;parameter for calculating coordinates.

; model width x and y coordinates
[mwx = 0]
[mwy = mwidth/2]

[mhx = 0]
[mhy = mheight]

;Block division lithosphere (3)
[block = mwidth/3]
[block2 = mwidth/6]
[bcoord = (-1*mwy)+block]
[bcoord2 = (-1*mwy)+block2]

; Varying Young's modulus between the three models
;5.4 GPa
[emod = 5.4e9]
;50 GPa
;[emod = 50e9]
;100 GPa
;[emod = 1e11]

; Particle parameters
;Porosity
[p = 0.08]
;density
[d = 2900]
```

```
;min-max particle radius
[r1min = 8]
[r1max = 20]
;min-max particle radius
[r2min = 20]
[r2max = 80]
;min-max particle radius
[r3min = 80]
[r3max = 100]
;min-max particle radius
[r4min = 100]
[r4max = 140]
;-------------------------------------------------------------

; Assign default contact model
contact cmat default model linear method deformability emod [emod]
kratio 2.5

;-------------------------------------------------------------
    ; Define the walls and section them by depth for pressure
calculation

    ; Generate walls
    wall generate plane
    wall create vertices [-1*mwy] [mhy] [mwy] [mhy]
    ;first wall ID
    [cid = 10]
    [wallList = list]
    ;Number of walls on each side
    [num=3]

    ; Create segments, by depth(height) for each side wall.
    fish define createSegments(xpos)
        local starty = mhx
        local inc = (mhy-mhx)/num
        loop local i(1,num)
            command
                wall create id [cid] vertices [xpos] [starty] [xpos]
[starty+inc]
            endcommand
             ;create extra wall variable, which is the height of the
         defined number of walls.
            wall.extra(wall.find(cid),1) = inc
            wallList = list.append(wallList,wall.find(cid))
            cid += 1
            starty += inc
        endloop
    end
    ;run the loop for each x-position.
```

```
    [createSegments(mwy)]
    [createSegments(-mwy)]


    ; Define the stresses for each side wall. If num = 1, then stress
= 2. Stress = num*2
    ; double the number of stress definitions per num.
    fish define stress1
        stress1    =    (math.abs(wall.force.contact(wall.find(10))-
>x))/wall.extra(wallList(1),1)
        stress2    =    (math.abs(wall.force.contact(wall.find(11))-
>x))/wall.extra(wallList(1),1)
        stress3    =    (math.abs(wall.force.contact(wall.find(12))-
>x))/wall.extra(wallList(1),1)
        stress4    =    (math.abs(wall.force.contact(wall.find(13))-
>x))/wall.extra(wallList(1),1)
        stress5    =    (math.abs(wall.force.contact(wall.find(14))-
>x))/wall.extra(wallList(1),1)
        stress6    =    (math.abs(wall.force.contact(wall.find(15))-
>x))/wall.extra(wallList(1),1)
    end
fish history stress1
fish history stress2
fish history stress3
fish history stress4
fish history stress5
fish history stress6

;---------------------------------------------------------------

; Distribute balls in the models, in different blocks with particles
of different radii.
model random 1001
;TOP ROW
;ball distribute block 1
ball distribute porosity [p] radius [r3min] [r3max] box [-1*mwy]
[bcoord2] [mhy/2] [mhy]
;ball distribute block 2
ball distribute porosity [p] radius [r2min] [r2max] box [bcoord2]
[bcoord2+block2] [mhy/2] [mhy]
;ball distribute block 3
ball distribute porosity [p] radius [r1min] [r1max] box [bcoord]
[bcoord+block] [mhy/2] [mhy]
;ball distribute block 4
ball distribute porosity [p] radius [r2min] [r2max] box
[bcoord+block] [(mwidth/2)-block2] [mhy/2] [mhy]
;ball distribute block 5
ball distribute porosity [p] radius [r3min] [r3max] box [(mwidth/2)-
block2] [mwidth/2] [mhy/2] [mhy]
```

```
;BOTTOM ROW
;ball distribute block 6
ball distribute porosity [p] radius [r4min] [r4max] box [-1*mwy]
[bcoord] [mhx] [mhy/2]
;ball distribute block 7
ball distribute porosity [p] radius [r2min] [r2max] box [bcoord]
[bcoord+block] [mhx] [mhy/2]
;ball distribute block 8
ball distribute porosity [p] radius [r4min] [r4max] box
[bcoord+block] [(bcoord+block)+block] [mhx] [mhy/2]

ball attribute density [d] damp 0.7

model mechanical timestep scale
model cycle 1000
model solve ratio-average 1e-5
model calm

; Define soft-bond contact model properties
history purge
contact delete
contact cmat default model softbond property dp_nratio 0.5 sb_ten
5e6 sb_coh 5e6 sb_fa 30.0 fric 0.5 sb_mode 1 method deformability
emod [emod] kratio 2.5
model clean all
contact method bond gap -1000 1000 ;range contact type 'ball-ball'
model cycle 1
model solve ratio-average 1e-5

; Assign Martian gravity and set initial stress in model.
history purge
ball attribute velocity multiply 0.0 displacement multiply 0.0
ball group 'left_end' range position-x [(-1*mwy)+20] [(-1*mwy)-20]
ball group 'right_end' range position-x [mwy-20] [mwy+20]
model save 'Bonded_Material_pregrav'
model gravity 3.721  ; Martian gravity
wall delete range id-list 2
ball tractions overburden 0 ratio 0.7 polydisperse true periodicity
false false    ...
                update-volume true update-area true              ...
                update-position false contact-create true contact-
active true output false
contact method bond gap -1000 1000; range contact type 'ball-ball'

model save 'Materal_Grav_initiated'

; Re-initialize the soft-bond model
```

```
contact cmat default model softbond property dp_nratio 0.5 sb_ten
0.0 sb_coh 0 sb_fa 30.0 fric 0 method deformability emod [emod]
kratio 2.5

; Define layers in the model to visualize deformation
ball group '1' range position-y 0 [(mdiv)-0.01]
ball group '1' range position-y [mdiv*2] [(mdiv*3)-0.01]
ball group '1' range position-y [mdiv*4] [(mdiv*5)-0.01]
ball group '2' range position-y [mdiv] [(mdiv*2)-0.01]
ball group '2' range position-y [mdiv*3] [(mdiv*4)-0.01]
ball group '2' range position-y [mdiv*5] [mheight]
model solve

model save 'Gravity_Settled'

model restore 'Gravity_Settled'

; Activate the servo walls on all side walls.
fish define setServo
    loop foreach local w wallList
        command
            wall servo activate on force-x [wall.force.contact(w)-
>x*(-1)] velocity-max 0.1 range id-list [wall.id(w)]
        endcommand
    endloop
end
[setServo]
model mechanical timestep auto
model cycle 5000

model save 'Servo_active'
```

C.2.2. Code Part 2 – Initiating the diking

```
model restore 'Servo_active'

;-----------------
;Dike parameters
;dike width
[dikew = 2000]
;dike height
[dikeh = 23000]

; Create the dike.
ball attribute disp 0 0
;Create dike walls
wall create name 'dikeleft' vertices 0 0 [-1*(dikew/2)] [-1*dikeh]
```

```
wall create name 'dikeright' vertices 0 0 [dikew/2] [-1*dikeh]

; Assign dike velocity and run model
wall attribute velocity-y 5 range name 'dikeleft'
wall attribute velocity-y 5 range name 'dikeright'
model mechanical timestep auto
;model mechanical time increment 0.1

;Run model: solve to dike height of 23 km.
model solve time 500
model save "Run1_time500"
model solve time 500
model save "Run1_time1000"
model solve time 500
model save "Run1_time1500"
model solve time 500
model save "Run1_time2000"
model solve time 500
model save "Run1_time2500"
model solve time 500
model save "Run1_time3000"
model solve time 500
model save "Run1_time3500"
model solve time 500
model save "Run1_time4000"
model solve time 500
model save "Run1_time4500"

; output the positions of top balls to construct surface topography
profile
fish define positions(numBins)
    local minV = domain.min
    local maxV = domain.max
    local dx = (maxV->x-minV->x)/numBins
    loop local i(1,numBins-1)
        local maxBall = null
        local maxVal = minV->y
        loop foreach local b ball.inbox(vector(minV->x+dx*(i-
1),minV->y),vector(minV->x+dx*(i),maxV->y))
            if ball.pos(b)->y > maxVal
                maxVal = ball.pos(b)->y
                maxBall = b
                rad = ball.radius(b)
            endif
        endloop
        if maxBall # null
            io.out(maxBall)
            io.out(rad)
            ball.group(maxBall,'top') = 'top'
```

```
        endif
    endloop
end

[positions(15000)]

    program log-file 'rad_position' truncate
    program log on

    ball list attribute radius range group 'top'
    ball list attribute position range group 'top'

    program log off

    model save '5.4GPa_end'
```

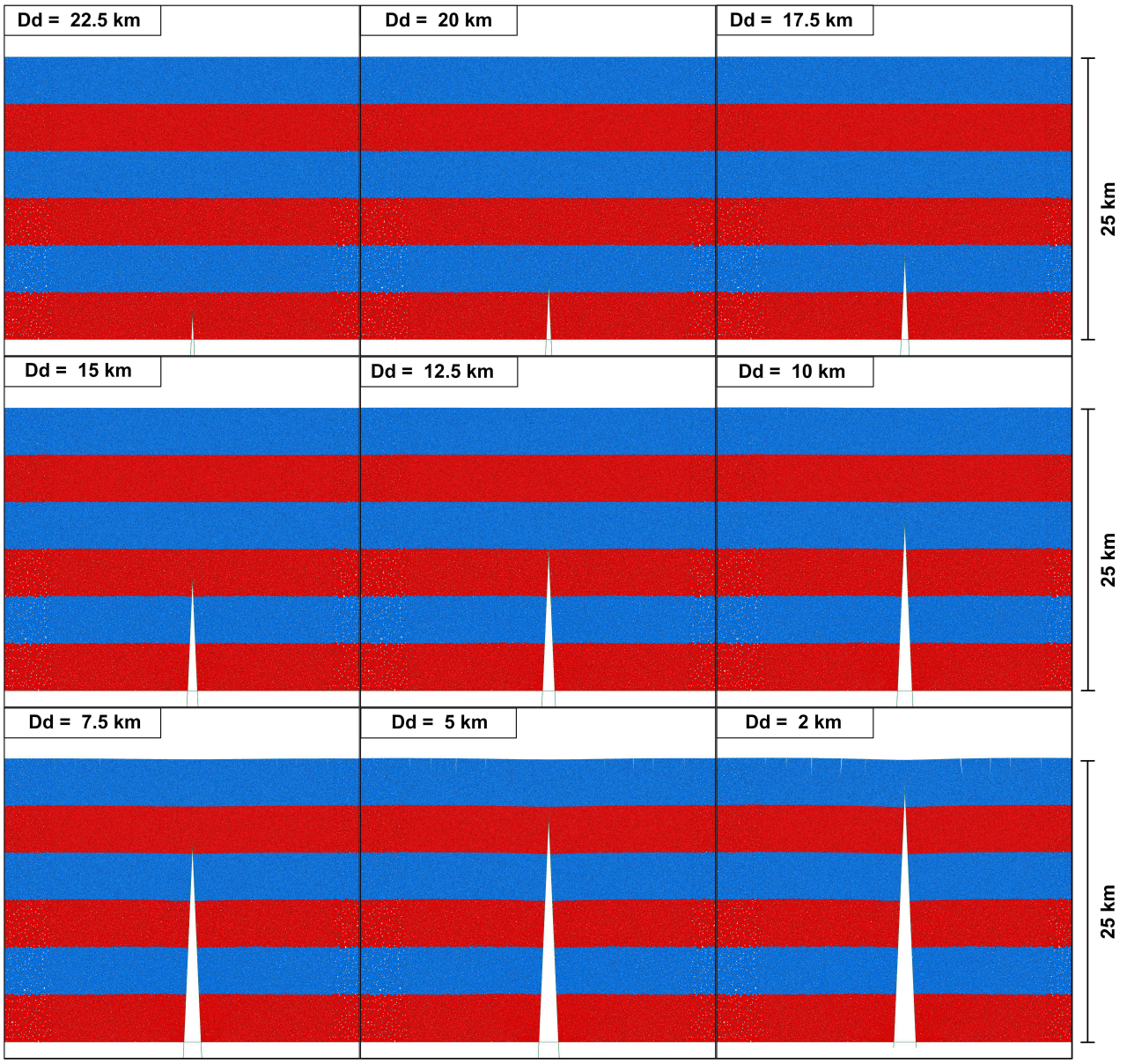

Figure C.2: Nine snapshots of the dike intrusion process for **Model A** (E=5.4 GPa). Dike-tip depth is labelled as "Dd" on each of the nine images. The red and blue colours are for visualising deformation and does not reflect a change in material properties.

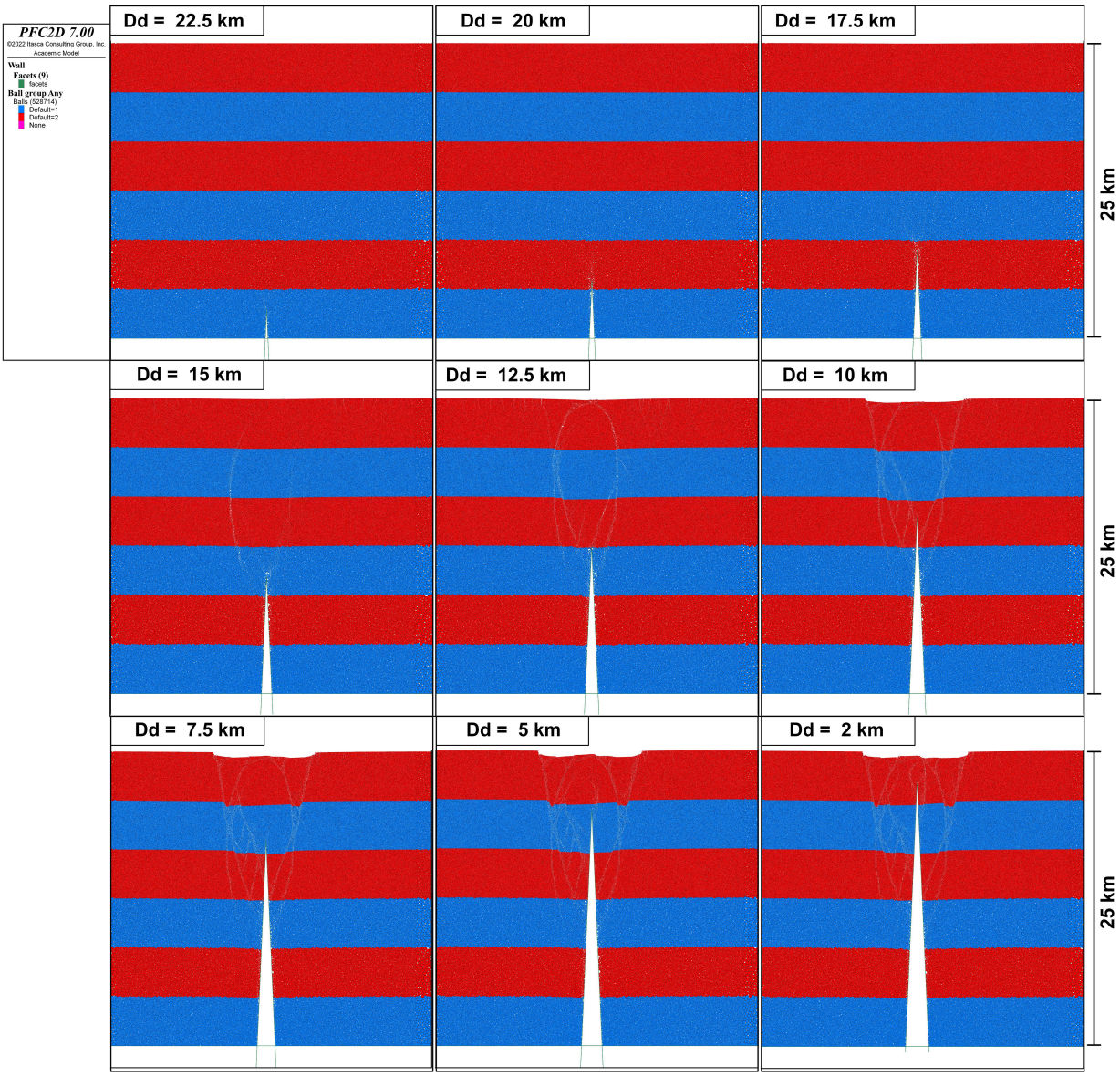

Figure C.3: Nine snapshots of the dike intrusion process for **Model B** (E=50 GPa). Dike-tip depth is labelled as "Dd" on each of the nine images. The red and blue colours are for visualising deformation and does not reflect a change in material properties.

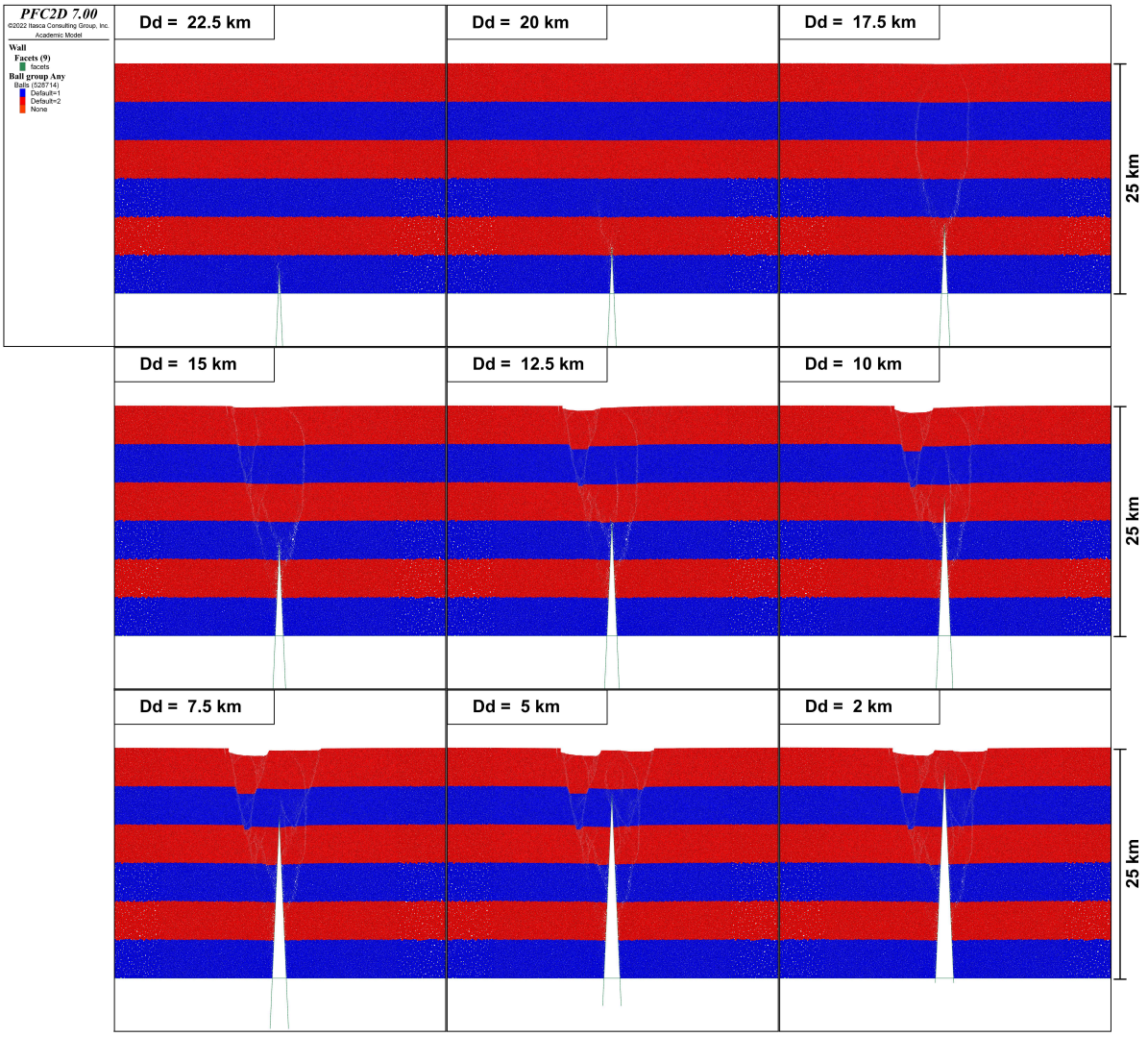

Figure C.4: Nine snapshots of the dike intrusion process for **Model C** (E=100 GPa). Dike-tip depth is labelled as "Dd" on each of the nine images. The red and blue colours are for visualising deformation and does not reflect a change in material properties.